GMe

GMe Forum 2005

Proceedings of the Seminar at the
Vienna University Of Technology

Organized by the
Society for Micro- and Nanoelectronics
(Gesellschaft für Mikro- und Nanoelektronik –
GMe)

March 17 – 18, 2005

GMe

Gesellschaft für
Mikro- und Nanoelektronik

Gesellschaft für Mikro- und Nanoelektronik

GMe Forum 2005

Proceedings of the Seminar at the
Vienna University Of Technology

Organized by the
Society for Micro- and Nanoelectronics
(Gesellschaft für Mikro- und Nanoelektronik – GMe)

March 17 – 18, 2005

Program Committee:

Emmerich Bertagnolli
Karl Riedling
Friedrich Schäffler
Michiel Vellekoop

Editor of the Proceedings:

Karl Riedling

Seminar Organization:
Karl Riedling
Claudia Benedela

Production of the Proceedings:
Claudia Benedela
Karl Riedling

Preface

The "GMe Forum" continues a long series of seminars on microelectronics technology which have been organized by the Society for Micro- and Nanoelectronics (*Gesellschaft für Mikro- und Nanoelektronik* – GMe; originally "*Gesellschaft für Mikroelektronik*") since its foundation in the mid-1980s. The original seminars addressed a purely academic audience. The new "GMe Forum" had first taken place in its current form at the Vienna University of Technology in 2001. It is designed to appeal to more application-oriented participants, particularly from Austrian industrial enterprises and governmental organizations. Most of the oral presentations are now reviews presented by top-level speakers from international industry and research facilities. The university institutions supported by the GMe also present their results, partly as oral presentations but mostly as posters.

The Society for Micro- and Nanoelectronics is mainly financed by the Federal Ministry for Traffic, Innovation and Technology (*Bundesministerium für Verkehr, Innovation und Technologie*). Its goal is to promote micro- and nanoelectronics research and technology at Austrian universities with the main aim to stimulate the transfer of know-how to the Austrian industry and by carrying out pilot projects in the GMe supported cleanroom facilities. The relatively small budget of the GMe does not allow full sponsoring of research projects. Nevertheless, the GMe supplements other research funding sources by providing contributions for creating and maintaining state of the art laboratory infrastructure.

The main goal of the GMe in recent years was the support of the two cleanroom centers at the Vienna University of Technology and at the Johannes Kepler University Linz, respectively, where internationally competitive technological equipment has been made available to researchers, students, and industry customers.

We hope that the proceedings will promote the impact of the GMe Forum 2005, and that they may contribute to an even better international cooperation of the Austrian micro- and nanoelectronics research at academic institutions and in industry.

o.Univ.Prof. Dr. Erich GORNIK   Ao.Univ.Prof. Dr. Karl RIEDLING
        President of the GMe   Secretary General of the GMe

Forum Program

Thursday, March 17, 2005

10:00 – 10:30	Welcome, Coffee
	Opening:
10:30 – 11:00	E. GORNIK (President of the GMe)
	P. SKALICKY (President of the Vienna University of Technology)
	Nanoelectromechanical Systems:
11:00 – 11.45	R. BLICK: *From Classical Mechanics to Quantum-Electro-Mechanics – **page 3***
11:45 – 12:30	Ch. HIEROLD: *From MEMS to NEMS – **page 5***
12:30 – 14:00	Lunch Break
	Micromachining with Femtosecond Lasers:
14:00 – 14:45	A. ISEMANN: *Micromachining with Femtosecond Lasers – **page 15***
	Bioelectronics:
14:45 – 15:30	H.U. DODT: *Bioelectronics and Bioimaging - New Approaches for the Investigation of Brain Microcircuits – **page 19***
15:30 – 16:00	Coffee Break
	Spintronics:
16:00 – 16:45	L. ALFF: *Spintronics: A New Spin for the World of Electronics – **page 23***
	Carbon Nanotubes:
16:45 – 17:30	W. HOENLEIN: *Carbon Nanotubes – A Successor to Silicon Technology? – **page 27***
17:30 – 17:45	Break
	Evening Session:
17:45 – 18:00	E. GORNIK: *Presentation of the Activities of the GMe*
18:00 – 19:00	Panel Discussion: "*Who supports technology in Austria?*"

Friday, March 18, 2005

	Technology:
09:00 – 09:45	R. MINIXHOFER: *Semiconductor Process Simulation* – **page 31**
09:45 – 10:30	H. OKORN-SCHMIDT: *Using Extreme Sono-Effects to Improve on the Selectivity of Particle Removal to Microelectronic Structure Damage below 65 nm* – **page 33**
10:30 – 11:00	A. LUGSTEIN: *Focused Ion Beam Technology* – **page 35**
11:00 – 11:30	Coffee Break
	Quantum Devices:
11:30 – 12:00	T. MÜLLER: *Carrier Dynamics at Quantum Dots* – **page 43**
	Opto-Electronics:
12:00 – 12:30	K. HINGERL**:** *Photonic Crystals: Optical Materials for the 21st Century* – **page 49**
12:30 – 13:00	G. SPRINGHOLZ**:** *Lead-Salt Lasers* – **page 51**
	Sensors:
13:00 – 13:30	D. ROCHA: *Sensor Interface Electronics* – **page 59**
	Poster Exhibition:
13:30	Snacks and Poster Exhibition

Poster Presentations

Opto-Electronics:

Photonic Crystals:

Spintronics:

Quantum Dots:

List of Participants

Dipl.-Ing. Stephan Abermann
TU Wien
Institut für Festkörperelektronik
A-1040 Wien

Univ.Prof. Dr. Lambert Alff
TU Wien
Institut für Sensor- und
Aktuatorsysteme
A-1040 Wien

Dr. Aaron Maxwell Andrews
TU Wien
A-1040, Wien

Erwin Auer
A-3420 Kritzendorf

Dipl.-Ing. Maximilian Austerer
TU Wien
Zentrum für Mikro- und Nanostrukturen
A-1040 Wien

Daniel Bauer
Universität Wien
A-1010 Wien

Univ.Prof. Dr. Günther Bauer
Johannes Kepler Universität
Institut für Halbleiterphysik
A-4040 Linz

Eugen Baumgartner
Johannes Kepler Universität
Institut für Halbleiter und
Festkörperphysik
A-4040 Linz

Roman Beigelbeck
ÖAW
Forschungsstelle für integrierte
Sensorsysteme
A-2700 Wr. Neustadt

Claudia Benedela
Gesellschaft für Mikro- und
Nanoelektronik
c/o Institut für Sensor- und
Aktuatorsysteme
A-1040 Wien

Alexander Benz
TU Wien
Institut für Festkörperelektronik
A-1040 Wien

Univ.Prof. Dr. Emmerich Bertagnolli
TU Wien
Institut für Festkörperelektronik
A-1040 Wien

Prof. PhD. Robert Blick
Univ. Wisconsin
Madison, WI 53706-1691, USA

Stefan Bräuer
Johannes Kepler Universität
Institut für Halbleiterphysik
A-4040 Linz

Christine Brendt
TU Wien
Institut für Festkörperelektronik
A-1040 Wien

Ass.Prof. Dr. Werner Brenner
TU Wien
Institut für Sensor- und
Aktuatorsysteme
A 1040 Wien

Mag. Wolfgang Brezna
TU Wien
Institut für Festkörperelektronik
A-1040 Wien

Dr. Hubert Brückl
Austrian Research Centers GmbH -
ARC
A-2444 Seibersdorf

Dr. Sergey Bychikhin
TU Wien
Institut für Festkörperelektronik
A-1040 Wien

Prof. Dr. Rupert Chabicovsky
TU Wien
Institut für Sensor- und
Aktuatorsysteme

Dr. Gang Chen
  Johannes Kepler Universität
  Institut für Halbleiterphysik
  A-4040 Linz

Dr. Horst Dietrich
  TU Wien
  Institut für Elektrische Mess- und
  Schaltungstechnik
  A-1040 Wien

Dr. Hans-Ulrich Dodt
  Max-Planck-Institut für Psychiatrie
  D-80804 München

Mag. Viktor Dubec
  TU Wien
  Institut für Festkörperelektronik
  A-1040 Wien

Ing. Elvira Dzigal
  TU Wien
  Institut für Festkörperelektronik
  A-1040 Wien

Univ.Prof.i.R. Dr.phil. Wolfgang
  Fallmann
  TU Wien
  Institut für Sensor- und
  Aktuatorsysteme
  A-1040 Wien

Managing Director Ernest J. Fantner
  IMS Nanofabrication GmbH
  A-1020 Wien

Gernot Fasching
  TU Wien
  Zentrum für Mikro- und Nanostrukturen
  A-1040 Wien

Dipl.-Ing. Markus Fischer
  TU Wien
  Institut für Festkörperelektronik
  A-1040 Wien

T. Glinsner
  Johannes Kepler Universität
  Institut für Halbleiterphysik
  A-4040 Linz

Sebastian Golka
  TU Wien
  Zentrum für Mikro- und Nanostrukturen
  A-1040 Wien

Univ.Prof. Dr. Erich Gornik
  TU Wien
  Institut für Festkörperelektronik
  A-1040 Wien

Martyna Grydlik
  Johannes Kepler Universität
  Institut für Halbleiterphysik
  A-4040 Linz

Mag. Dr. Margit Haas
  FFG
  Österreichische
  Forschungsförderungsgesellschaft
  A-1010 Wien

Dr. Ottfried Hafner
  A-1100 Wien

Gabriel Hairer
  TU Wien
  Institut für Sensor- und
  Aktuatorsysteme
  A-1040 Wien

Dr. Ernst Hammel
  Electrovac
  A-3400 Klosterneuburg

Michael Heer
  TU Wien
  Institut für Festkörperelektronik
  A-1040 Wien

Univ.Prof. Dr. Christopher Hierold
  ETH-Zürich CLA H 9,
  Mikro- und Nanosysteme
  CH-8092 Zürich

Doz. Dr. Kurt Hingerl
  JKU Linz
  Institut für Halbleiter- und
  Festkörperphysik
  A-4040 Linz

Ao.Univ.Prof. Dr. Gerhard Hobler
  TU Wien
  Institut für Festkörperelektronik
  A-1040 Wien

Markus Hollergschwandtner
  A-3002 Purkersdorf

Dr. Wolfgang Hönlein
  Infineon Technologies AG
  Corporate Research
  D-81739 München

Dr. Andreas Isemann
Femtolasers Produktions GmbH
A-1100 Wien

Dipl.-Ing. Farnaz Isfahani
Johannes Kepler Universität
Institut für Halbleiterphysik
A-4040 Linz

Ao.Univ.Prof. Dr. Bernhard Jakoby
TU Wien
Institut für Sensor- und
Aktuatorsysteme
A-1040 Wien

Prof. Dr. Wolfgang Jantsch
Johannes Kepler Universität
Institut für Halbleiterphysik
A-4040 Linz

Dipl.-Ing. Gerhard Karlowatz
TU Wien
Institut für Mikroelektronik
A-1040 Wien

Dr. Franz Keplinger
TU Wien
Institut für Sensor- und
Aktuatorsysteme
A-1040 Wien

Dr. Gudrun Kocher-Oberlehner
Johannes Kepler Universität
Institut für Halbleiterphysik/CD Labor
A-4040 Linz

Dr. Hans Kosina
TU Wien
Institut für Mikroelektronik
A-1040 Wien

Maksym Kovalenko
Johannes Kepler Universität
Institut für Halbleiter und
Festkörperphysik
A-4040 Linz

Dipl.-Ing.(FH) Jochen Kuntner
TU Wien
Institut für Sensor- und
Aktuatorsysteme
A-1040 Wien

PhD. Jan Kuzmik
TU Wien
Institut für Festkörperelektronik
A-1040 Wien

Dr. Samuel Kvasnica
TU Wien
Institut für Sensor- und
Aktuatorsysteme

Dr. Alois Lugstein
TU Wien
Institut für Festkörperelektronik
A-1040 Wien

Elisabeth Magerl
A-1140 Wien

Lukas Maier
Austrian Research Centers GmbH -
ARC
A-2444 Seibersdorf

Dipl.-Ing. Hans Malissa
Johannes Kepler Universität
Institut für Halbleiterphysik
A-4040 Linz

Dipl.-Ing. Giannis Meletiadis
TU Wien
Institut für Sensor- und
Aktuatorsysteme
1040 Wien

Rainer Minixhofer
austriamicrosystems AG
A-8141 Unterpremstätten

Dr. Alberto Montaigne Ramil
Johannes Kepler Universität
Institut für Halbleiter- und
Festkörperphysik
A-4040 Linz

Univ.Ass. Dr. Thomas Müller
Institut für Photonik
A-1040 Wien

Dr. Michael Nelhiebel
Infineon Technologies AG
A-9500 Villach

Dr. Harald Okorn-Schmidt
SEZ AG
A-9500 Villach

Ao.Univ.Prof. Dr. Leopold
Palmetshofer
Johannes Kepler Universität
Institut für Halbleiterphysik
A-4040 Linz

Dipl.-Phys. Christian Pflügl
TU Wien
Zentrum für Mikro- und Nanostrukturen
A-1040 Wien

Dipl.-Ing. Georg Pillwein
Johannes Kepler Universität
Institut für Halbleiterphysik
A-4040 Linz

PhD Dionyz Pogany
TU Wien
Institut für Festkörperelektronik
A-1040 Wien

Dipl.-Ing. Mahdi Pourfath
TU Wien
Institut für Mikroelektronik
A-1040 Wien

Antonia Praus
Johannes Kepler Universität
Institut für Halbleiterphysik
A-4040 Linz

Univ.Prof. Dr. Adalbert Prechtl
TU Wien
Institut für Grundlagen und Theorie der
Elektrotechnik
A-1040 Wien

Dr. Doris Rakoczy
TU Wien
Institut für Festkörperelektronik
A-1040 Wien

Dipl.-Ing. Patrick Rauter
Johannes Kepler Universität
Institut für Halbleiterphysik
A-4040 Linz

Ao.Univ.Prof. Dr. Karl Riedling
TU Wien
Institut für Sensor- und
Aktuatorsysteme
A-1040 Wien

V. Rinnerbauer
Johannes Kepler Universität
Institut für Halbleiterphysik
A-4040 Linz

Dr. Tomas Roch
TU Wien FKE
Institut für Festkörperelektronik
A-1040 Wien

Dr. Daniel Rocha
TU Wien
Institut für Sensor- und
Aktuatorsysteme
A-1040 Wien

Univ.Prof. Dr. Friedrich Schäffler
Johannes Kepler Universität
Institut für Halbleiterphysik
A-4040 Linz

Stephan Schartner
TU Wien
Institut für Festkörperelektronik
A-1040 Wien

Prof. Dr. Robert Schawarz
Institut für Sensor- und
Aktuatorsysteme
A-1040 Wien

Dipl.-Ing. Christoph Schöndorfer
TU Wien
Institut für Festkörperelektronik
A-1040 Wien

Jörg Schotter
Austrian Research Centers GmbH -
ARC

Dipl.-Ing. Matthias Schramböck
TU Wien
Institut für Festkörperelektronik
A-1040 Wien

Dr. Werner Schrenk
TU Wien
Zentrum für Mikro- und Nanostrukturen
A-1040 Wien

Dipl.-Phys. Frederik Schrey
TU Wien
Institut für Festkörperelektronik
A-1040 Wien

Univ.Prof. Dr. Siegfried Selberherr
TU Wien
Institut für Mikroelektronik
A-1040 Wien

Dipl.-Ing. Clemens Peter
Simbrunner
Johannes Kepler Universität
Institut für Halbleiter und
Festkörperphysik
A-4040 Linz

Ao.Univ.Prof. Dr. Gunther
  Springholz
  JKU Linz
  Institut für Halbleiter und
  Festkörperphysik
  A-4040 Linz

Robert Steinbach
  A-1210 Wien

Dipl.-Ing. Roland Steininger
  TU Wien
  Institut für Managementwissenschaften
  A-1040 Wien

Dipl.-Ing. Mathias Steinmair
  TU Wien
  Institut für Festkörperelektronik
  A-1040 Wien

Christoph Stepper
  Austrian Research Centers GmbH -
  ARC
  A-2444 Seibersdorf

Gottfried Strasser
  TU Wien
  Institut für Festkörperelektronik
  A-1040 Wien

Edeltraud Svasek
  TU Wien
  Institut für Sensor- und
  Aktuatorsysteme
  A-1040 Wien

Peter Svasek
  TU Wien
  Institut für Sensor- und
  Aktuatorsysteme
  A-1040 Wien

Dipl.-Ing. Alexander Szép
  TU Wien
  Institut für Computertechnik
  A-1040 Wien

Dr. Vincas Tamosiunas
  Semiconductor Physics Institute
  LT-01108 Vilnius, Lithuania

Ing. M.A. Helmut Tichy

Dipl.-Ing. Enzo Ungersböck
  TU Wien
  Institut für Mikroelektronik
  A-1040 Wien

Prof. Dr. Karl Unterrainer
  TU Wien
  Institut für Photonik
  A-1040 Wien

Dr. Gintaras Valusis
  Semiconductor Physics Institute
  LT-01108 Vilnius, Lithuania

Univ.Prof. Dr. Michael Vellekoop
  TU Wien
  Institut für Sensor- und
  Aktuatorsysteme
  A-1040 Wien

Dr. Heinz D. Wanzenboeck
  TU Wien
  Institut für Festkörperelektronik
  A-1040 Wien

Dipl.-Ing. Jarad Zarbakhsh
  Johannes Kepler Universität
  Institut für Halbleiterphysik
  A-4040 Linz

Contents

Sensors and Sensor Technology (Posters) 193

Nanoelectro-mechanical Systems

From Classical Mechanics to Quantum-Electro-Mechanics

Robert H. Blick
Laboratory for Molecular Scale Engineering
University of Wisconsin-Madison, Electrical & Computer Engineering
1415 Engineering Drive, Madison, WI 53706, USA

Classical Mechanics is what lies at the beginning of the physics curriculum as everyone will recall from numerous textbook questions. The transition to quantum mechanics is traditionally treated by looking into atomic and molecular physics. However, semiconductor processing techniques by now allow to build systems with a mechanical degree of freedom on the micron and nanometer scale. Hence, one can envision to machine systems for studying quantum electro mechanics (QEM).

In terms of applications such nano-electromechanical systems (NEMS) as compared to MEMS on the micron-scale are also found in sensor and communication components. Especially, in communication applications they are valuable additions as switching, filter, and mixer elements. The mechanical resonance frequencies for NEMS are now of the order of 1 – 2 GHz, which makes NEMS-circuits compatible with CMOS. In terms of sensor applications, I want to focus on mass sensing: NEMS implies not only microwave operating frequencies, but in addition NEMS possess extremely small masses. This inherent high sensitivity for mass sensing is of crucial importance for a number of areas such as the ever expanding field of proteomics.

Finally, I will stress the importance of quantum effects analyzed with NEMS. Prominent examples being the interaction of single electrons and single phonon modes and the observation of the Casimir force in such mechanical resonators. Similarly, the mechanical degree of freedom on the nanometer scale can also be used to shuttle single electrons at radio frequencies in a non-stochastic manner. As an outlook, I will present first results on tubular shaped NEMS with an integrated low-dimensional electron gas. Such a topology can induce a geometrical confinement potential for electrons, which can be added to the electro-magnetically induced confinement.

MEMS and NEMS

Christopher Hierold

ETH Zurich, Micro and Nanosystems
Tannenstrasse 3, CH-8092 Zurich, Switzerland,

This paper is about the impact of scaling on the system performance of mechanical inertia sensors and first activities towards nano mechanical sensors. Permanent cost pressure will result in continuous efforts to integrate more functions into further miniaturized systems. As a consequence microsystems (MEMS) may also incorporate functional nano devices such as carbon nanotubes in the future. Therefore an overview of recent activities for the application of carbon nanotubes with a focus on mechanical sensors is provided.
Keywords: microsystem, MEMS, nanosystem, carbon nano tube, sensor

Introduction

Requests for further miniaturization of microsystems may certainly result in serious efforts to integrate nano scale functional devices in microsystems. New materials with new properties on the nano scale will emerge. In this paper, limitations for microsystems scaling and current research activities in the field of nanostructures are discussed in general and first proposals to realize mechanical sensors based on carbon nanotubes (CNT) are introduced in particular. This paper is mostly about mechanical sensors and systems on the micro and nano scale.

After more than 20 years of microsystems research and development it seems inappropriate to include a definition of microsystems once again. But due to some evolution of these definitions over the years it should be mentioned that microsystems or MEMS (both phrases are used as synonyms) are considered in this paper as systems that involve electronic and non-electronic elements and functions on the micro scale. This may also include sensing functions, signal acquisition and processing, control, actuation, display functions and means for performing chemical and biochemical interactions. The system aspects comprise also system partitioning, (V)LSI of non-electronic elements, calibration, signal-to-noise-ratio, stability, reliability and first of all assembly, packaging and test. This definition follows in most points the one given by Senturia [2]. Prominent examples of such microsystems and products are TI's DMD^{TM} device [3], ADI's inertia sensors [4] or Infineon's surface micromachined integrated pressure sensors [5], [6].

Consequently, a definition for nanosystems follows: Nanosystems involve electronic and non-electronic elements and functions on the nano scale for sensing, actuation, signal processing, display, control and / or interface functions.

Today there are yet not many examples available that might fulfill this definition of nanosystems. Two examples might be IBM's "Millipede" [1] and Samsung's field emission display based on carbon nanotubes [7] the function of which is defined by electron emitting CNTs sealed in a flat vacuum package that also incorporates the picture generating phosphorus layers at a distance of 200 µm from the CNTs. Besides Samsung other companies like Motorola and Sony have been engaged in the development of field emission displays (FED). An excellent overview and summary of the state-of-the-art is provided by Itoh [8].

Scaling of Capacitive Force Sensors

Cost issues are in the foreground of the discussion about miniaturization. Researchers and product developers are spending tremendous efforts to further miniaturize integrated systems. They even accept the fate that in some cases, miniaturization does not support the physical system function per se. This is one of the most important differences between microelectronics and microsystems: While in microelectronics miniaturization and further integration, following Moore's Law, have succeeded in better performing transistors and systems until recently (smaller, faster, cheaper), inertia sensors do not benefit from scaling in general.

Table 1 summarizes the analysis of the system performance of three generalized and simplified examples of MEMS, i.e. pressure, acceleration and yaw rate sensors [9]. The performance is discussed with respect to scaling.
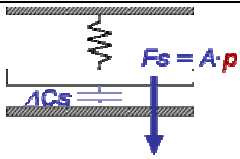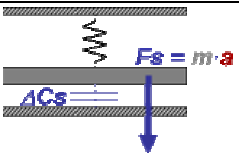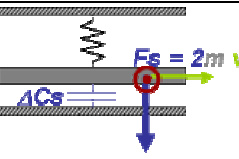
	Pressure p	Acceleration a	Yaw rate Ω
Sensing force	$F_s = \alpha^2 A_0 \, \mathbf{p}$	$F_s = \alpha^3 m_0 \, \mathbf{a}$	$F_s = 2\alpha^4 m_0 v_0 \, \mathbf{\Omega}$
SNR_{opt} $x/\alpha d_0 = const.$	~ 10log (const. α^2)	~ 10log (const. α^2)	~ 10log (const. α^2)
SNR_{opt} $\omega_{0,mech} = const.$	~ 10log (const. α^{-2})	~ 10log (const. 1)	~ 10log (const. α^2)

Table 1: Influence of miniaturization and scaling on system performance for pressure, acceleration and yaw rate sensors [9]. $\alpha < 1$ is the scaling factor for the dimensions of these simplified sensor models.

The signal-to-noise-ratio (SNR) at the output of a virtual ground amplifier is taken as a measure of the performance of all three systems. For comparison reasons all sensors, even the pressure sensor, though it would not be straight forward to realize, are assumed to be differential capacitive sensors, forming a capacitive bridge at the input of the amplifier. The following evaluation also applies if one of the sensor capacitors is fixed and considered as a reference sensor (reduced sensitivity).

All three sensors measure a sensing force F_s as a result of the physical unit applied that displaces the sensing electrode against a spring force. The change of the distance to a counter electrode is measured by the change of the respective capacitance ΔC_s.

Equation (1) gives the SNR of the sensor systems in dependence of the capacitance change and a number of constants that depend on technology, only. Furthermore, the sensor capacitance C_s is assumed to be smaller than the parasitic capacitances C_{par} of the setup, even in case of monolithic integration of MEMS and the circuit.

Numerous constraints exist when scaling a particular device, including design, process and electro-mechanical considerations. Most of them are design specific and therefore cannot be considered from a general viewpoint, but two constraints are common to all measurement systems, namely the minimum required measurement range and the minimum required measurement bandwidth. While the scaling of the mass is predefined by the scaling of the geometrical dimensions, the spring constant is considered as a free design parameter. Its choice has to satisfy these two constraints.

$$SNR_{opt} = 10\log\left(const_{tech}\frac{\Delta C_s{}^2}{C_{par}}\right) \tag{1}$$

$$C_s \ll C_{par}, \qquad const_{tech} = \frac{9\mu V_{in}{}^2 V_{d,sat}}{4k_B T B_{el} L^2}$$

B_{el}:	Electrical bandwith	μ:	Carrier mobility
V_{in}:	Input voltage	L:	Gate length
k_B:	Boltzman constant	$V_{d,sat}$:	Saturation voltage
T:	Absolute temperature		

In the case of an open loop system (case $x/\alpha d_0$ = const. in Table 1) the minimum required measurement range, which is related to the maximum relative displacement, dominates the choice of the spring constant.

Force feedback systems (case ω_{mech} = const. in Table 1) can overcome this limitation, if the feedback force can handle the measurement range. Then the minimum required mechanical bandwidth, which determines the noise bandwidth, determines the choice of the spring constant.

The results of scaling on the pressure and inertia sensors are achieved by substituting for ΔC_s in Eqn. (1) with expressions achieved by scaling down the sensors' geometry (Table 1) It is obvious that in general scaling of inertia sensors will reduce the system performance of miniaturized systems ($\alpha < 1$ is the scaling factor for the dimensions of these simplified sensor models). Only in the case of force feedback systems with reduced spring constants compensating for the reduction of size and mass accelerometers are scaling invariant. Pressure sensors are less sensitive to scaling, or may even improve, if the thickness of the sensor's membrane can be easily scaled down (reducing spring constant).

In concluding this section about scaling, it is shown that at least in the case of yaw rate sensors miniaturization will not improve the sensor's performance per se. There are possible solutions available that will help escape this scaling trap. These solutions will be implemented by complex system designs.

Nano Mechanical Sensors

CNT integration into MEMS for actuation and electrical interfacing has been proposed to characterize the electro mechanical properties of nanotubes [11], [12]. Figure 1 shows the realization of that kind of a test stand [13]. A single walled carbon nanotube (SWCNT) is assembled between two fixed Ti/Au electrodes (50 nm thick). AFM cantilevers can be used to apply forces and bending moments on the suspended SWCNT by deflecting the released cantilever structure. It is obvious that this kind of MEMS structures can also be used as electromechanical interfaces for CNT based mechanical sensors. Figure 2 shows clearly the embedded carbon nanotube (CNT).

Current research on CNT based nano transducers could be classified roughly in two categories: (i) Sensors that take advantage of the small dimensions of the tube to interact with structures and surfaces on atomic and molecular level and (ii) sensors that take advantage of unique (e.g. electronic) properties of nanotubes to interact with the macroscopic environment.
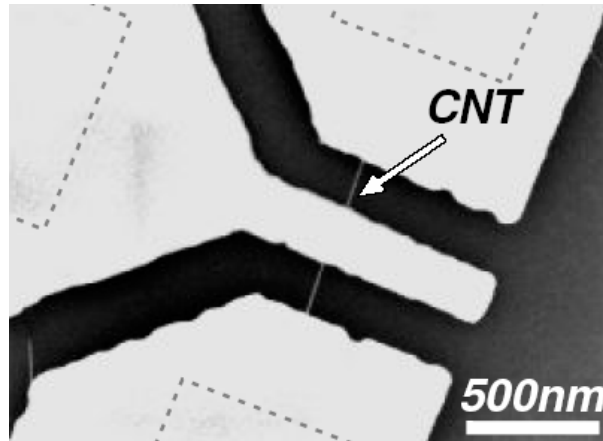
Fig. 1: SEM image of a suspended single walled carbon nano-tube, contacted by two fixed electrodes and a released cantilever (50 nm Ti/Au). The dashed lines indicate anchor areas [13].
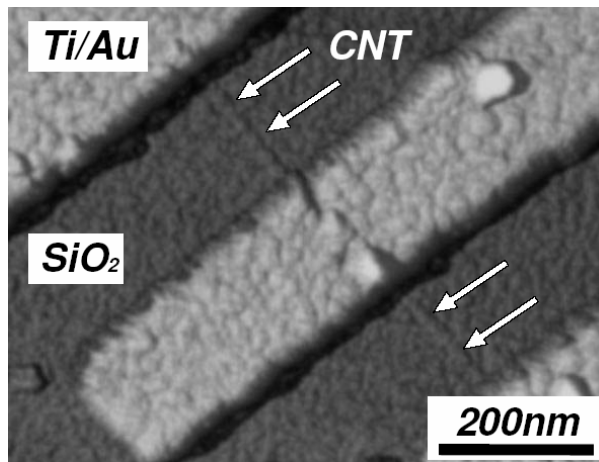
Fig. 2: AFM image of a contacted single walled carbon nanotube (diameter approx. 1.2 nm) on 1.5 µm SiO$_2$ before HF release. Gold electrodes on top are 30 nm thick [13].

Important representatives of the first category (i) are CNTs that are used as AFM probe tips [14]. CNTs are placed on the tips of conventional AFM probes either by manipulation or direct catalytic growth. The effective radii of those CNT tips are reported to be in the range of 3 nm (SWCNT) – 6 nm (MWCNT) [15] and at least of half size of etched silicon tips. An increase in lateral resolution of up to 70% was achieved by imaging gold nanostructures compared to the resolution achieved with silicon tips. Additional advantages are the typical high aspect ratio of the cylindrical CNT that is advantageous for imaging narrow and steep features and the elastic buckling of the tube above a low critical force that avoids the damage of the device under test (e.g. organic and biological samples). Furthermore it was shown [16] that the CNT tip's end can be modified to create probes that can sense matter on the molecular level by very distinct chemical functionality.

Mechanical sensors of category (ii) are reported in the area of strain sensors. A substrate (matrix) material (e.g. polymer) is filled with CNTs and investigated by Raman spectroscopy [17]. In SWCNT the position of the D* Raman band strongly depends on the strain transferred from the substrate to the nanotubes. The spatial resolution of the

measurement is around 1 µm and is limited by the spot of the Raman laser. This method is used to measure stress fields around defects in polymers and tensile strain in materials.

A new approach to apply SWCNTs as stress sensors on the macro scale is reported in [18]. SWCNTs mixed with DMF (N,N-dimethylformamide), filtered and dried, resulting in a 10 µm thick film of randomly oriented SWCNT bundles (buckypaper) is fabricated and attached to a device under test. The resistance of the CNT layer is measured by a four point probe technique. The measured voltage shift is proportional to the applied stress or strain. Unfortunately there is no discussion about the performance of those CNT strain sensors compared to conventional strain gauges. However, the authors claim that the described approach allows incorporating CNTs directly into various materials (e.g. composites) to realize integrated strain sensors.

Very recently a PMMA-based micro pressure sensor was reported [19] using bulk multi walled CNTs as piezoresistive sensing elements. The MWCNTs are attached to gold electrodes on top of the membrane by AC electrophoretic manipulation of the nanotubes. By applying pressure to the membrane the tubes are strained and the resistance of the tubes is increasing. The gauge factor of the tubes is estimated and reported to be 235.

The direct integration of CNTs into MEMS devices could result in the next generation of nanotransducers for the evaluation of mechanical loads. To realize these nanotransducers, it is mandatory to control and reproduce the assembly, or better the growth, of nanostructures from one point of catalyst to another. Self assembly of nanostructures instead of structuring by photolithographic means will be the preferred process technology approach for manufacturing of these structures. Recently [20], [21], field assisted growth of CNTs was demonstrated to control the alignment of CNTs between two separate areas of Fe catalysts on silicon or molybdenum electrodes, respectively.

Fabrication of nanostructures by means of self-assembly instead of planar photolithography and etch steps will reduce fabrication complexity and costs significantly. In concluding this section about nanosystems one should emphasize that nanosystems are not just miniaturized microsystems. New process technologies towards self-assembly and the utilization of new sensing principles based on quantum effects will help to avoid the scaling trap of microsystems. Basic research is needed to integrate nanostructures into MEMS on wafer level to characterize performance based on statistical data and to provide defined electrical and mechanical interfaces of nanostructures to the micro and macro world.

Acknowledgments

References

[1]   P. Vettiger, et. al.: "The "Millipede" - Nanotechnology Entering Data Storage", IEEE Transactions on Nanotechnology, Vol. 1, No. 1 , March 2002, pp. 39 – 55.

[2]   S.D. Senturia "Microsystem Design". Kluwer, Boston 2002[4].

[3]   P.F. van Kessel, L.J. Hornbeck, R.E. Meier, M.R. Douglass: "A MEMS-Based Projection Display", Proceedings of the IEEE , Vol. 86, No. 8, Aug. 1998, pp. 1687 – 1704.

[4]   J.A. Geen, et.al.S.J. Sherman, J.F. Chang, S.R. Lewis: "Single-Chip Surface Micromachined Integrated Gyroscope With 50 /h Allan Deviation". IEEE Journal of Solid State Circuits, Vol. 37, No. 12, December 2002, pp. 1860 – 1866.

[5]   C. Hierold: "Intelligent CMOS Sensors". IEEE MEMS 2000, Myazaki, Proceedings IEEE Thirteenth Annual International Conference on Micro Electro Mechanical Systems, IEEE 2000, pp. 1-6.

[6]   T. Scheiter, H. Kapels, K.G. Oppermann, C. Hierold, W.M. Werner, H.J. Timme,: "Full integration of a pressure-sensor system into a standard BiCMOS process". Sensors and Actuators A Physical, 15 May 1998; A67(1-3): pp. 211-214.

[7]   W.B. Choi, et. al.: "Carbon-Nanotube Based Field-Emission Displays for Large Area and Color Applications", J. of Information Display, Vol. 1, No. 1, (Dec 2000), pp. 59-62,

[8]   S. Itoh, M. Tanaka, "Current Status of Field-Emission Displays", Proc. of the IEEE, Vol. 90, No. 4 (April 2002), pp. 514-520.

[9]   C. Hierold, "From micro to nano systems: mechanical sensors go nano", J. Micromech. Microeng., 14, pp. 1-11, September 2004. www.iop.org/journals/jmm

[10] B.E. Boser, R.T. Howe: "Surface Micromachined Accelerometers". IEEE Journal of Solid-State Circuits, 31(3), March 1996, pp. 366-375,.

[11] R.S. Ruoff, D. Qian, and W.K. Liu, "Mechanical properties of carbon nanotubes: theoretical predictions and experimental measurements" C.R. Physique 4 (2003), pp. 993-1008.

[12] P. A. Williams et. al., "Controlled placement of an individual carbon nanotube onto a microelectromechanical structure", Applied Physics Letters, Vol. 80, No. 14, 2002, pp. 2574-2576.

[13] C. Stampfer, A. Jungen, C. Hierold, "Fabrication of discrete carbon nanotube based nanoscaled force sensors", Proc. IEEE Sensors 2004, Vienna, Oct. 24-27, 2004.

[14] C.L. Cheung, J.H. Hafner, C.M. Lieber: "Carbon nanotube atomic force microscopy tips: Direct growth by chemical vapor deposition and application to high-resolution imaging", Proc. of the National Academy of Science of the USA, Vol. 97, No. 8 (Apr. 11, 2000), pp. 3809 – 3813.

[15] S.S. Wong, et. al., "Single-walled carbon nanotube probes for high resolution nanostructure imaging", Appl. Physics Letters, Vol. 73, No. 23 (7 Dec 1998), pp. 3465 – 3467.

[16] S.S. Wong, E. Joselevich, A.T. Wooley, C.L. Cheung, C.M. Lieber, "Covalently functionalized Nanotubes as nanometer-sized probes in chemistry and biology", Nature (letters), Vol. 394, 2 July 1998, pp.52 – 55.

[17] Q. Zhao, M.D. Frogley, H.D. Wagner, "Direction-sensitive strain-mapping with carbon nanotube sensors", Composites Science and Technology 62 (2002), pp. 147 – 150.

[18] P. Dharap, Z. Li, S. Nagarajaiah, E.V. Barrera, "Nanotube film based on single-wall carbon nanotubes for strain sensing", IoP Nanotechnology Vol. 15 (2004), pp. 379 – 382.

[19] Carmen K. M. Fung, Maggie Q.H. Zhang, Rosa H. M. Chan, Wen J. Li, "A PMMA-Based Micro Pressure Sensor Chip Using Carbon Nanotubes as Sensing

Elements", Technical Digest, 18th IEEE Int. Conf. on Micro Electro Mechanical Systems, MEMS 2005, pp. 251 – 254, 2005

[20] H. Miyashita, T. Ono, M. Esashi, "Nanomechanical Structures With An Integrated Carbon Nanotube". The 12 Int. Conf. on Solid-State Sensors, Actuators and Microsystems, Transducers'03, Boston, Digest of Technical Papers Vol. 1, IEEE 2003 pp. 182

[21] A.Ural, Y. Li, H. Dai, "Electric-field-aligned growth of single-walled carbon nanotubes on surfaces". Appl. Phys. Letters Vol. 81, No. 18, 28. October 2002, pp. 3464 – 3466

Micromachining with Femtosecond Lasers

Micromachining with Femtosecond Lasers

Andreas Isemann
Femtolasers Produktions GmbH, 1100 Vienna, Austria

Laser sources have been used for machining for some time now. With conventional continuously emitting or long pulsed laser sources in the nanosecond regime, however, limited precision in the range of some micrometers is possible. The heat deposited in the material during the absorption also makes the machining of delicate materials impossible. The shockwaves associated with the absorption of the pulse may also cause damage.

The mechanism of the ablation changes drastically when going from the nanosecond to the femtosecond pulse duration regime. Some background of the mechanism of the essentially cold ablation is given, explaining how the fascinating precise results have become possible. The difference in the mechanism for metals and dielectrics will be explained. Since with short pulses, less energy is needed for ablation than with long pulses, also the shock waves are reduced.

Among other things, shape memory alloys, delicate polymers and structured thin films will be shown as well as results from two photon polymerization

Also, using ultrashort pulses, it has become possible to create structure sizes below the diffraction limit of the beam, which is in the range of one micrometer for a laser operating in the near infrared region. By operating the laser close to the ablation threshold, only the central part of the beam initiates ablation, which is thus below the diffraction limit.

Machined samples will be shown providing some insight into possibilities of processing with ultrashort pulses.

Up to now, amplified femtosecond laser systems were necessary to do micro machining. A roadmap of possible developments is laid out and discussed. A new category of oscillator is introduced filling the gap of conventional oscillators and amplified systems to address the needs of micromachining. First experimental results of machined samples with this oscillator will be shown.

Bioelectronics

Bioelectronics and Bioimaging - New Approaches for the Investigation of Brain Microcircuits

Hans-Ulrich Dodt
Max-Planck-Institute of Psychiatry, D-80804 Munich, Germany

Bioelectronics and bioimaging are new approaches for the investigation of the brain and its microcircuits. They complement each other, as bioelectronics investigates the function, whereas bioimaging is mainly concerned with the morphology of the brain. For the study of neuronal microcircuits, neurons in rather opaque brain slices have to be visualized. This allows the recording of the electrical potentials of these neurons with microelectrodes. The development of the necessary optical techniques will be described. By using these techniques, electrophysiological phenomena, which may be the basis of information storage in the brain, could be studied. A new approach for nonlinear correlation analysis revealed unknown synchronization phenomena between nerve cells, which can lead to the generation of epilepsy.

The wiring of neurons in neuronal networks could be investigated by laser stimulation of single neurons. We found that the connectivity in neuronal networks is dependent on external information input. To visualize neurons in the intact brain we started to inject quantum dots into nerve cells and detect them by their fluorescence. This approach offers new perspectives for the visualization of neurons in the intact brain.

A technique was developed to visualize brain microcircuits in 3-D with high resolution which renders fixed mouse brains by chemical means completely transparent. The method was combined with a new kind of microscopy. With this combination the neuronal network could be visualized with cellular resolution.

The results from these different approaches should help to understand the microcircuits of the brain and may ultimately allow the implementation of the underlying principles in technical solutions.

Spintronics

Spintronics: A New Spin for the World of Electronics

Lambert Alff

Institute of Sensor and Actuator Systems, Applied Electronic Materials
Vienna University of Technology, A-1040 Vienna, Austria

Electronic applications are based on the properties of electrons in solid bodies. While currently employed devices operate with the positive or negative charge of electrons, the spin of electrons has been neglected so far. The use of this purely quantum mechanical degree of freedom might be the next development of modern electronics: spintronics. What are the basic principles of spintronics, what are the advantages compared to conventional electronics? Which progress has already been made in the field, which problems are ahead? One focus of the talk will be the development of suited new materials for spintronics.

Carbon Nanotubes

Carbon Nanotubes – A Successor to Silicon Technology?

W. Hoenlein, F. Kreupl, G.S. Duesberg, A.P. Graham, M. Liebau, W. Pamler, R. Seidel, E. Unger
Infineon Technologies AG, Corporate Research, D-81730 Munich, Germany

Carbon nanotubes (CNTs) exhibit a number of interesting properties that make them viable candidates for applications in microelectronics. In particular, the availability of both metallic and semiconducting species for transistors and interconnects, respectively, means that the most important building blocks of microelectronics are accessible. However, silicon technology has set some definite conditions for large scale integration and manufacturing that have to be satisfied by any competing technology: Devices must be adequate for integration, a large number of devices must be fabricated at the same time, downscaling of lateral dimensions must be feasible, and modular processing must be possible at yields close to 100% for each individual processing step. In this paper state-of-the-art carbon nanotube production and placement procedures will be assessed with respect to these requirements. The first application result for interconnects will be presented that involves the replacement of metal via plugs between two conductive layers by carbon nanotubes. Likewise, semiconducting single-walled carbon nanotube field effect transistors will be compared to advanced silicon MOSFETs. The scaling of lateral dimensions is the most successful principle in microelectronics. We will also address the scalability of one dimensional CNT devices and show recent experimental results of very short CNTFETs. Finally, a stand alone CNT power device is presented that is produced with state-of-the-art deposition techniques and is capable of driving LEDs and small motors.

Technology

Semiconductor Process Simulation

Rainer Minixhofer
austriamicrosystems AG, A-8141 Unterpremstätten, Austria

Semiconductor technology and industry has enormously advanced in the past decades. Starting from a plastic triangle, a slab of germanium, some gold foil and gold contacts (the first bipolar transistor in 1947), as of 2004 the typical transistor density per circuit is around 140 million transistors/cm² for micro processor applications, doubling every year.

Semiconductor industry is the main driving force for technology innovation and "New Economy" markets. The ongoing development of faster integrated circuits with higher device density has led to highly complex and sophisticated products which are widely accepted by the society. A modern integrated circuit cannot be developed without the massive use of computer aided design (CAD) in any step of the complex flow from the idea to the final product. This presentation concentrates on technology computer aided design (TCAD) and its use for the simulation of the semiconductor fabrication process flow.

Semiconductor process simulation aims to model the physical systems of single semiconductor fabrication steps and their sequence which form the overall process flow. This task implies the modeling of the single process steps with differential equations and solving them on mesh-grids, which represent a cross-section through the interesting area of the integrated circuit.

The final outcome is the topography of the overall structure (boundary of the cross-section consisting of different materials) and the doping distribution inside the semiconducting materials. This information can be used to model the electrical behavior of the structure in a subsequent device simulation step. Since the physical structure and the doping concentrations can be hardly obtained by experiments, process simulation gains even more value at nanometer scale process technologies.

This presentation aims to describe some aspects of the implementation of process simulators. Furthermore the benefits of process modeling are shown with a couple of examples.

Using Extreme Sono-Effects to Improve on the Selectivity of Particle Removal to Microelectronic Structure Damage Below 65 nm

Harald F. Okorn-Schmidt *et al.*
SEZ Research Centers, A-9500 Villach, Austria

Development work for the next generation of microelectronic devices, 65 and especially 45 nm, is under full steam, and major challenges for 32 nm and beyond are being tackled one-by-one by scientists and engineers working in pre-development, corporate and academic research centers. It seems that the red brick wall painted a couple years ago has become a little porous again as novel, sensitive substrates and materials finally find themselves being implemented or are close to introduction in the manufacturing process, e.g. strained silicon, high-k dielectrics, new silicides or maybe even metal gates. The excitement related to this seemingly everlasting move towards the ultimate nano-structured device however should not let us forget to explore in detail and understand the added process complexity and especially the increased requirements for contamination control and surface preparation.

In this presentation one major challenge microelectronic device manufacturers are facing will be especially highlighted: selective removal of nm sized particles without damage to equally or just slightly larger device structures. A novel approach to understand and improve on "physically assisted" chemical cleaning will be discussed.

A New Approach for the Formation of Size and Site Controlled Metallic Nano Dots Seeded by Focused Ion Beams

A. Lugstein, E. Bertagnolli

Institute of Solid State Electronics
Vienna University of Technology, A-1040 Vienna, Austria

We present a new approach for the generation of metallic nano pattern, which in contrast to conventional bottom up or top down processes is based on a subtractive self organization process relying on material decomposition induced by focused ion beam (FIB) exposure. Two dimensional ordered arrays of embedded as well as freestanding nanometer sized Ga dots were fabricated by a site control technique relying on preformed craters and an irradiation mediated migration and agglomeration. The formation of these dots is discussed in terms of selective etching of arsenic due to the local energy injection by the gallium ions and further minimization of the excess free energy of the surfaces.

Further we have shown that FIB bombardment of InAs produces indium crystallites. The influence of the ion dose, the beam energy, the sample temperature and the dose rate on the surface evolution has been investigated for further III/V compound semiconductors by atomic force microscopy, scanning electron microscopy, auger electron spectroscopy and X-ray diffraction measurements.

In summary, the surface topography resulting from FIB bombardment is being investigated for possible use in nano-technology applications. This technique, based on a subtractive self organization process, may lead to a new fabrication process for three dimensional metallic nanostructures.

Introduction

Nanoscale structuring opportunities are prerequisites for any nanoscale engineering. The main bottleneck in the application of nano dots for quantum devices [1] – [3] is the difficulty of creating ordered arrays of size controlled dots in the nanometer range with a high uniformity in size. Low-dimensional nanostructures are usually fabricated using either a top down or a bottom up strategy. The former technique is extremely flexible, but suffers from limitations in minimum feature size and uniformity. The latter one, utilizing spontaneous self-ordering effects, is limited by the broad size distribution and the lack of control of the positioning of the self-organized nanostructures. In this context the discovery of the appearance of periodic structures with dimensions in the nanometer regime induced by ion bombardment [4] – [7] has attracted growing interest due to the possibility of obtaining a self-organized formation of nanostructures. In particular resist-less focused ion beam techniques are most suited for the combination of top-down structuring with selective bottom-up self-assembling techniques. To keep up with the trend of structures to shrink in dimensions, the response of ion induced material modifications will have to be controlled on a nanometer scale. A prerequisite thereof is a deep understanding of the ion beam interaction with the processed substrate material. In this paper, we present a new approach for the generation of metallic nano dots based on a subtractive self organization process, relying on compound semiconductor decomposition induced by FIB exposure.

Experimental

The samples exposed to the FIB were cleaved from mirror polished (100) InAs and (100) GaAs wafers. All machining experiments were carried out using the Micrion twin lens FIB system equipped with a Ga liquid metal ion source. The FIB system was operated with a 200 μm beam-limiting aperture corresponding to a nominal beam diameter of 120 nm and a beam current of 4.7 nA at an acceleration voltage of 50 kV. To investigate the morphological evolution, the samples were irradiated in a single scan with ion fluences between 6.25×10^{15} ions/cm^2 and 7.25×10^{16} ions/cm^2. After FIB irradiation, post-exposure annealing is performed at 200 °C in forming gas. For the formation of the regular Ga dot structures we generated an array consisting of 50 x 50 nominally identical 80 nm deep holes. The pattern evolution was observed by FIB-Secondary Electron Microscopy (FIB-SEM), Atomic Force Microscopy (AFM), Auger Electron Spectroscopy (AES) and X-ray diffraction (XRD).

Results and Discussion

Our FIB system enables the in-situ monitoring of the pattern evolution of the GaAs surface during FIB bombardment. Figure 1(a) shows a FIB-SEM image of a (50 x 50) μm^2 box on the GaAs surface after FIB exposure with 50 keV Ga+ ions and an ion fluence of 3.75×1016 ions/cm^2. Droplet like features appears on the GaAs surface and the diameter of the dots varies between 120 nm and 640 nm. The AFM image in Fig. 1(b) reveals a perfect calotte shape of one single dot with a diameter of 190 nm and a height of 75 nm, resulting in an aspect ratio of about 0.4 and the smooth surface surrounding of the dot.

(a)   (b)
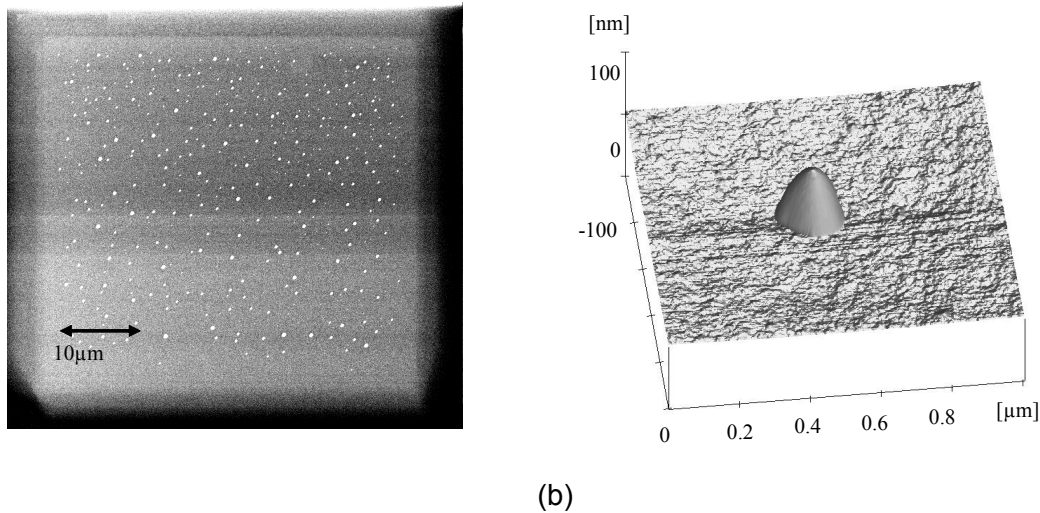
Fig. 1:   FIB-SEM image of a GaAs surface after 50 keV Ga$^+$ FIB exposure with an ion dose of 3.75×10^{16} ions/cm^2 (a) and the topographic AFM image of one single dot (b).

AES investigations point toward Ga enrichment in the protrusion after FIB exposure and reveal the formation of nearly pure gallium dots after a moderate annealing. We assume that the irradiation leads to decomposition of GaAs and selective etching of arsenic due to the local energy injection by the gallium ions [8]. The excess Ga atoms are produced by preferential sputtering of the arsenic atoms, and because of enhanced diffusion, the Ga atoms agglomerate into the observed Ga-rich precipitates. The development of the new heterogeneous phase leads to an increase in the total surface energy of the system. Thus, in case of preferential FIB sputtering of GaAs, the minimization of surface energy calls for a spherical shape of the small Ga dots, as we did ob-

serve. After formation of Ga dots the most crucial issue is to locate dots at predicted sites. In case of pre-patterning of the surface by milling holes in the GaAs surface the Ga-rich dots are formed at designated sites. The AFM image in Fig. 2 shows a part of the FIB generated array consisting of 50 x 50 nominally identical 80 nm deep holes, with the Ga droplets at the center of the craters.
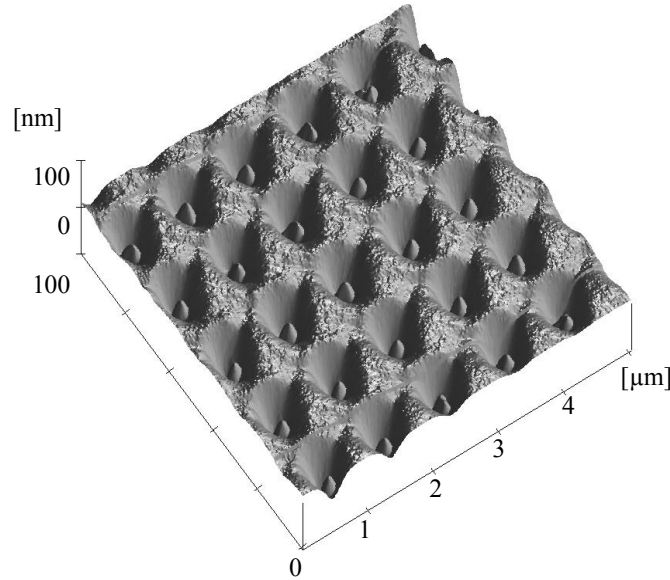
Fig. 2: AFM image of an array of embedded Ga dots generated by FIB milling of nominally identical 80 nm deep holes with a spacing of 1 µm between them.

From a section analysis of the AFM image we have measured an average diameter of the dots of 250 nm and a height of 55 nm. Besides the site controllability, the size uniformity is also improved, as each potential well in which the migrating Ga atoms are collected is uniform.
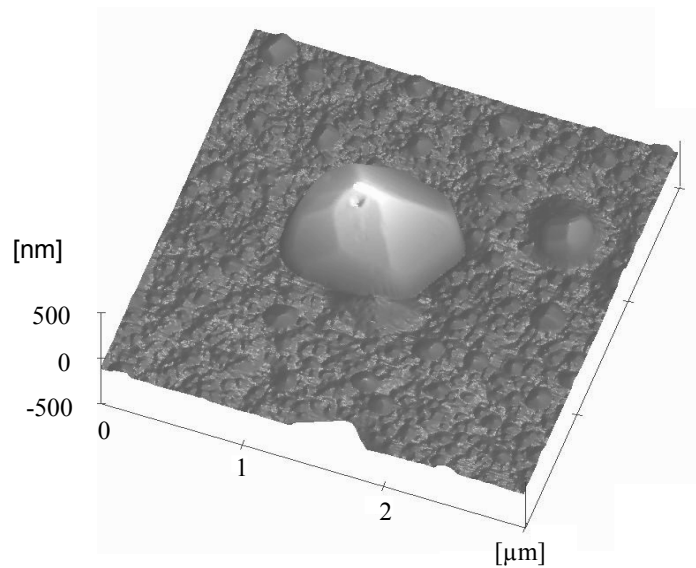
Fig. 3: AFM image of an indium crystallite on the InAs surface after FIB exposure with an ion dose of 5×10^{16} ions/cm^2

In case of InAs randomly distributed micro-protrusions are formed due to FIB exposure with diameters ranging from 30 nm to 2 µm. The AFM image in Fig. 3 indicates that the protrusions are nearby perfect crystallites with obvious facets, in close contact with the substrate. A two-dimensional AES mapping points towards the enrichment of indium in the crystallites, whereby the calculated composition of the ion bombarded neighborhood aside the crystallites is very close to the ratio of the undisturbed InAs surface. The XRD measurements shown in Fig. 4 prove the assumption of indium crystallite formation, as the three most intense reflections of crystalline indium are clearly visible in the X-ray diffractograms after FIB treatment. Relative intensities and *d* spacings of these reflections are in perfect agreement with reference material [8].
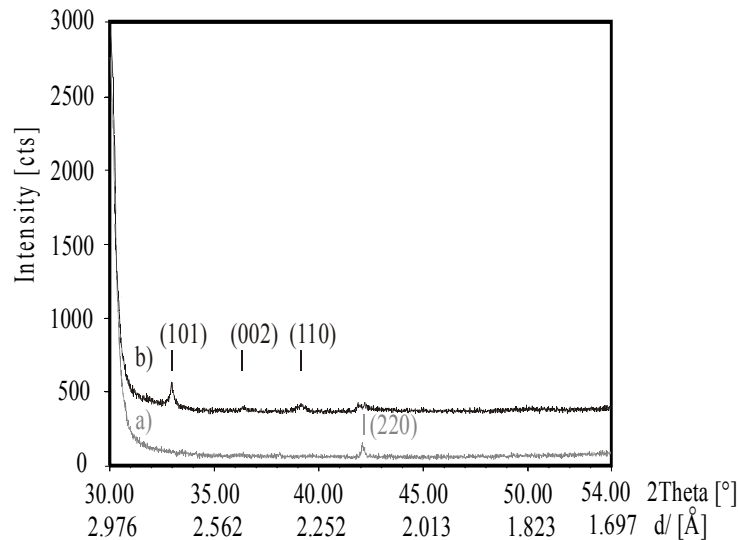
Fig 4:   X-ray diffractograms of an InAs wafer before (a) and after (b) Ga$^+$ ion beam irradiation.

Conclusions

Concluding, we have shown that 50 keV FIB-Ga$^+$ ion bombardment at normal incidence produces droplet like Ga dots on a GaAs substrate and indium crystallites on the InAs surface. The formation of these dots is discussed in terms of selective etching of arsenic due to the local energy injection by the gallium ions and further agglomeration because of enhanced diffusion of the remaining species. In case of GaAs, regular patterns can be obtained by a new site control technique using ion beam surface potential modification. This technique is a promising way to obtain three dimensional metallic nanostructures with uniform dot sizes and high packaging densities. Furthermore, this method is expected to apply to various metals apart from gallium and indium.

Acknowledgement

References

[1]   K. Mukai, N. Nishioka, M. Sugawara, S. Yamazaki, Jpn. J. Appl. Phys. 33, L1710 (1994)

[2]   J.N. Randall, Nanotechnology, 4, 41 (1993)

[3]   P.D. Dresselhaus, L. Ji, S. Han, J.E. Lukens. K.K. Likharev, Phys. Rev. Lett. 72 3226 (1994)

[4]   G. Carter, V. Vishnyakov, Phys. Rev. B 54, 17647 (1996)

[5]   J. Erlebacher, M.J. Aziz, E. Chason, M.B. Sinclair, J.A. Floro, Phys. Rev. Lett. 82, 2330 (1999)

[6]   S. Rusponi, G. Constantini, C. Boragno, U. Valbusa, Phys. Rev. Lett. 81, 4184 (1998)

[7]   S. Habenicht, W. Bolse, K.P. Lieb, K. Reimann, U. Geyer, Phys. Rev. B 60, R2200 (1999)

[8]   J. G. Pellerin, D. P. Griggis, P. E. Russel, J. Vac. Sci. Technol. B8, 1945 (1990).

Quantum Devices

Carrier Dynamics in Quantum Dots

T. Müller, F.F. Schrey, G. Fasching, L. Rebohle, G. Strasser, K. Unterrainer

Institut für Photonik & Zentrum für Mikro- und Nanostrukturen, TU-Wien
Floragasse 7, A-1040 Wien, Austria

The electron capture and relaxation dynamics in self-assembled InAs/GaAs quantum dots is investigated by means of interband pump – intraband probe spectroscopy. By tuning femtosecond infrared pulses into resonance with intraband transitions between confined quantum dot states and the wetting layer continuum, the electron population of the quantum dot ground state is determined as a function of time-delay after the interband pump.

Introduction

The capture and relaxation of carriers in semiconductor quantum dots (QDs) has attracted much attention during the last decade, since a profound understanding of these processes is essential for the development of novel optoelectronic devices. A drastic slow-down of the relaxation compared to higher-dimensional structures has been predicted because of the so-called phonon bottleneck effect [1], [2]. However, it has turned out that a number of scattering processes, including multi-phonon emission [3] – [7], electron-electron scattering [8] – [10] and electron-hole scattering [11], [12], can circumvent the phonon bottleneck, leading to capture and relaxation times from approximately one to several tens of picoseconds. Most of the experiments have been performed by using interband techniques, such as time-resolved photoluminescence (PL) spectroscopy [4], [5], [7], [9] and differential transmission spectroscopy [6], [11], where the signal reflects the combined electron-hole dynamics. In this letter we report an interband pump – intraband probe experiment, which is sensitive to the capture and relaxation of electrons only. The pump excites electrons and holes in the GaAs matrix surrounding the QDs, while the infrared (IR) probe is tuned into resonance with electronic intraband transitions [13] between the bound QD states and continuum states in the wetting layer (WL).

Results and Discussion

The investigated sample was grown by molecular beam epitaxy on a semi-insulating GaAs substrate. It consists of 30 layers of InAs QDs separated by 50 nm thick GaAs barriers and a 50 nm GaAs cap layer. The dot density was estimated from an atomic force microscopy study to be around 2×10^{10} cm^{-2} per layer. For IR absorption measurements, the sample was polished at 58° to the growth axis in order to form a single-pass waveguide for the IR radiation.

Room-temperature PL spectra for two different excitation densities were recorded using a continuous-wave Ti:sapphire laser (740 nm excitation wavelength) and are presented in Fig. 1. At low excitation density (25 W/cm^2) we observe two transitions corresponding to $e1h1$ luminescence at 1.081 eV and $e2h2$ luminescence at 1.137 eV. At higher excitation (1 kW/cm^2) the QD states are filled up and luminescence corresponding to the $e3h3$ transition at 1.194 eV is also observable, as well as luminescence at 1.333 eV from the underlying InAs WL. The inhomogeneous broadening of the transitions (~50 meV full width at half maximum (FWHM)) mainly reflects the size distribution of the InAs QDs. At T = 5 K the PL shifts by ~90 meV towards higher energy which is

due to the temperature-dependence of the GaAs and InAs bandgaps. The energy differences between the QD states, however, are not affected. From the PL we determine an energetic difference of 252 meV between the QD ground state $e1h1$ and the WL. Approximately two thirds of this energetic difference occur between the conduction band offsets [6]. Thus, we estimate the intraband transition energy between the QD ground state $e1$ and the WL to be ~160 meV.
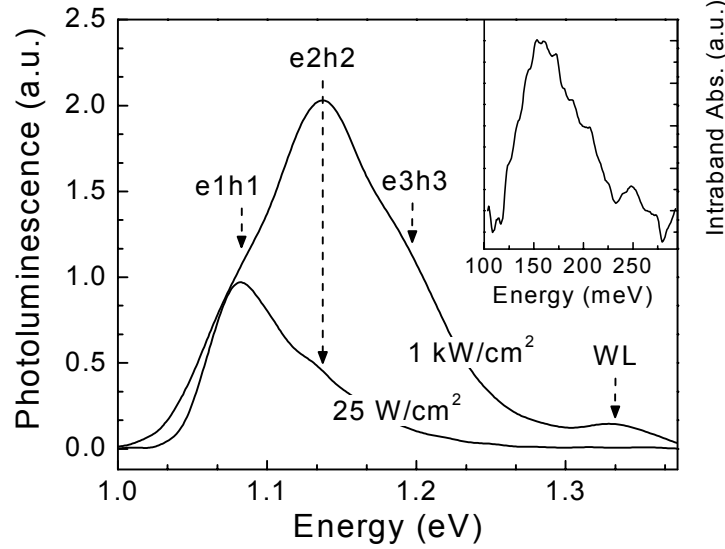
Fig. 1:   Room-temperature photoluminescence spectra at two different excitation
          densities. Inset: Photoinduced intraband absorption spectrum at T = 5 K.

For time-resolved probing of the intraband transitions we used a mode-locked Ti:sapphire laser that delivers 12 fs pulses centered at a wavelength of 780 nm. Half of the laser intensity served as an interband pump to inject electrons and holes in the GaAs barriers. The other part was used to generate the linear polarized IR probe pulses by phase-matched difference frequency mixing in a 0.5 mm thick GaSe crystal [14]. The probe pulses are tunable in the E_{pr} = 75 – 155 meV range (10 – 20 meV FWHM) with pulse durations between ~100 and ~200 fs.

Figure 2 (a) shows typical pump-probe signals (E_{pr} = 155 meV, I_p = 25 W/cm^2) at room-temperature when the probe is tuned into resonance with the $e1$–WL transition. When the probe is polarized perpendicular to the growth direction (s-polarization) we observe a step-like increase of the absorption, which rises within the time resolution of the experiment and decays within several hundred picoseconds. This signal is attributed to free-carrier absorption in the substrate and barriers and its decay to free-carrier recombination. When the probe is polarized in growth direction (p-polarization) a slowly rising absorption superimposed on the free-carrier signal is observed. Relaxation and thermalization in the GaAs barriers and the InAs WL occur on a time scale <1 ps. Thus, the slow rise of the absorption reflects the effective electron capture into the QD, more precisely into the QD ground state. From the absorption data we deduce the capture time τ_c by an exponential fitting procedure.

The inset of Fig. 2 (a) displays the excitation density dependence of the capture time τ_c at room-temperature. We observe two regimes exhibiting a different density dependence of the capture time. τ_c decreases with increasing excitation density above 25 W/cm^2. In contrast, the capture time changes only slightly at low excitation densities. The high-power dependence can be explained by electron-electron scattering: An electron is scattered into the QD ground state by transferring its energy to a hot electron in the barrier or the WL. A sequence of scattering processes where the electron relaxes

through excited QD states is even more probable [8]. Assuming that the electron-electron scattering rate is proportional to the excitation density and taking another density-independent scattering process (described by the scattering rate τ_i^{-1}) into account we can write for the overall capture rate [9] $\tau_c^{-1} = \tau_i^{-1} + \sigma \cdot I_p$, where σ is a fitting parameter. Using this simple expression we can fit the experimental results, as shown by the solid line in Fig. 2 (a).
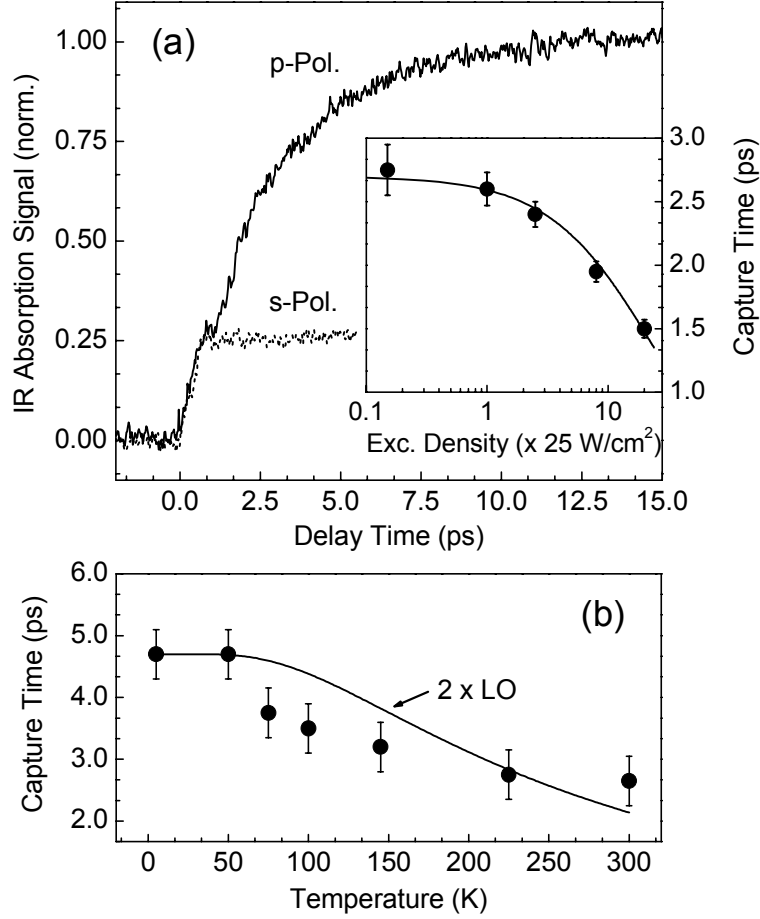
Fig. 2: (a) Photoinduced IR absorption signals of the QD sample as a function of pump-probe delay for a probe energy of 155 meV. Inset: excitation density dependence of the capture time at room-temperature. (b) Temperature-dependence of the capture time at an excitation density of 25 W/cm^2.

Let us now turn our attention to the low-density regime where electron-electron scattering can be ruled out as a relaxation mechanism. Figure 2 (b) shows the temperature-dependence of the capture time at I_p = 25 W/cm^2. We find an increase of τ_c from 2.7 ps to 4.7 ps upon decreasing the temperature from 300 K to 5 K. Two scattering mechanisms could explain such short capture times at low excitation density:

(i) Multi-phonon emission: One possible explanation for the observed short capture times could be that electrons scatter between subsequent QD states via repeated emission of two LO phonons. The corresponding two-phonon scattering rate for this process can be written as [7] $\tau_c^{-1} = \Gamma_0 \times [N_{LO}(T) + 1]^2$, where Γ_0 is the scattering rate at T = 0 K and $N_{LO}(T)$ is the Bose-Einstein distribution function for LO phonons. The calculated curve can roughly account for the experimental temperature dependence, as shown in Fig. 2 (b) by the solid line. Although LO phonons can relax electrons in a QD

only for a narrow range of dot sizes (because of their weak dispersion), emission of energetically different LO phonons (from the GaAs barriers, the WL, the QDs, and the respective interfaces) and also broadening of the phonons (due to strain and alloy inhomogeneities) could enlarge this energetic window [14].

(ii) Electron-hole scattering: Another fast relaxation mechanism in QDs is electron-hole scattering. Since this process involves only a single electron and a single hole in a QD it can occur even at very low excitation densities [11]. Due to the high effective hole mass the QD level separation in the valence band is in the range of a few meV. This allows holes to thermalize within several hundred femtoseconds. Electrons in the conduction band can transfer their energy to holes, which then lose their energy via phonons.

Acknowledgements

References

[1] U. Bockelmann and G. Bastard, Phys Rev. B **42**, 8947 (1990).

[2] H. Benisty, C. M. Sotomayor-Torres, and C. Weisbuch, Phys Rev. B **44**, 10945 (1991).

[3] T. Inoshita and H. Sakaki, Phys. Rev. B **46**, 7260 (1992).

[4] B. Ohnesorge, M. Albrecht, J. Oshinowo, A. Forchel, and Y. Arakawa, Phys. Rev. B **54**, 11532 (1996).

[5] R. Heitz, M. Veit, N. N. Ledentsov, A. Hoffmann, D. Bimberg, V. M. Ustinov, P. S. Kopev, and Zh. I. Alferov, Phys. Rev. B **56**, 10435 (1997).

[6] J. Feldmann, S. T. Cundiff, M. Arzberger, G. Böhm, and G. Abstreiter, J. Appl. Phys. **89**, 1180 (2001).

[7] M. De Giorgi, C. Lingk, G. von Plessen, J. Feldmann, S. De Rinaldis, A. Passaseo, M. De Vittorio, R. Cingolani, and M. Lomascolo, Appl. Phys. Lett. **79**, 3968 (2001).

[8] U. Bockelmann and T. Egeler, Phys. Rev. B **46**, 15574 (1992).

[9] D. Morris, N. Perret, and S. Fafard, Appl. Phys. Lett. **75**, 3593 (1999).

[10] S. Sauvage, P. Boucaud, F. Glotin, R. Prazeres, J.-M. Ortega, A. Lemaître, J.-M. Gérard, and V. Thierry-Flieg, Appl. Phys. Lett. **73**, 3818 (1998).

[11] T. S. Sosnowski, T. B. Norris, H. Jiang, J. Singh, K. Kamath, and B. Bhattacharya, Phys. Rev. B **57**, R9423 (1998).

[12] R. Ferreira and G. Bastard, Appl. Phys. Lett. **74**, 2818 (1999).

[13] S. Sauvage, P. Boucaud, F. H. Julien, J.-M. Gérard, and V. Thierry-Mieg, Appl. Phys. Lett. **71**, 2785 (1997).

[14] R. A. Kaindl, D. C. Smith, and T. Elsaesser, Opt. Lett. **23**, 861 (1998).

Opto-Electronics

Photonic Crystals: Optical Materials for the 21st Century

Kurt Hingerl
Institute for Semiconductor and Solid State Physics,
Christian Doppler Laboratory for Surface Optics
Johannes Kepler University, A-4040 Linz, Austria

Progress in photonics is closely connected to development of optical materials which allow controlling the flow of light. Photonic Crystals represent a novel class of materials which elevates the concept of steering of light to a new level: A spatially periodic varying index of refraction leads to the formation of a photonic bandstructure that may exhibit ranges of frequencies for which ordinary propagation of electromagnetic radiation is forbidden. As a consequence, these artificial materials profoundly influence the propagation characteristics of light as well as the radiation dynamics of optically active materials embedded in Photonic Crystals.

In this talk I will introduce the basic physical concepts of Photonic Crystals. This will be followed by a discussion of some of the most promising fabrication techniques of these materials. Based on this, I will give illustrative examples of both experimental and theoretical characterizations of Photonic Crystals. Finally, I will discuss selected applications of Photonic Crystals from the fields of integrated photonics and also highlight possibilities to localize light in nonperiodic systems. Especially it is shown that adhering to some restrictions in the acceptable lattice transformations one can achieve omnidirectional photonic bandgaps for an entire sub-class of such structures. We demonstrate, designing an efficient arbitrary-angle waveguide bend, that curvilinear-lattice photonic crystals can be employed for the creation of original types of nano-photonic devices.

Continuous Wave Mid-Infrared IV–VI Vertical Cavity Surface Emitting Lasers

G. Springholz, T. Schwarzl, M. Böberl, W. Heiss,

Institut für Halbleiter und Festkörperphysik, Universität Linz, Altenbergerstraße 69, 4040 Linz, Austria

J. Fürst, H. Pascher

Experimentalphysik I, Universität Bayreuth, D-95447 Bayreuth, Germany

Continuous wave emission of mid-infrared IV-VI vertical-cavity surface-emitting laser structures with PbSe as active medium is demonstrated for the 6 to 8 µm wavelength region. The lasers are based on ultra-high finesse microcavity structures formed by high reflectivity EuSe/PbEuSe Bragg mirrors. Optically pumped cw laser emission is observed up to temperatures of 120 K. We achieved internal threshold pump intensities of down to 25 W/cm^2, which is two orders of magnitude smaller than reported so far. The line width of the laser emission is only 18 µeV (0.9 nm) with a strong narrowing as compared to the line width of the cavity resonance. Continuous wave output powers are up to 4.8 mW.

Introduction

Narrow bandwidth coherent mid-infrared emitters are extremely useful for ultrahigh-sensitive chemical gas analysis and atmospheric pollution monitoring [1] because most strong absorption lines of molecular gases are found in the mid-infrared spectral region. Due to their nearly symmetric conduction and valence bands and their very small non-radiative Auger recombination rates [2], the IV-VI semiconductors or lead salt compounds are very well suited for such applications. Therefore, edge emitting IV-VI semiconductor laser diodes have long been used for MIR gas spectroscopy and detection with operation temperatures up to 223 K in continuous wave (cw) [3] and above room temperature in pulsed mode [4]. As compared to edge emitting lasers, vertical cavity surface emitting lasers (VCSELs) offer several advantages such as very small beam divergences, single mode operation, and the possibility of monolithic integration and potentially lower threshold pump powers. For IV-VI lasers, another important advantage of VCSELs is that they can be grown on readily available BaF2 substrates, which have a much higher thermal conductivity and mechanical hardness than the usual high-cost IV-VI substrates. Since their first demonstration [5], [6], the performance of optically pumped IV-VI semiconductor vertical-cavity surface-emitting lasers (VCSELs) has been continuously improved [7], and pulsed laser emission has been obtained up to 65°C [8]. In contrast, cw operation of mid-infrared VCSELs at higher temperatures has not been achieved so far, and the longest wavelength for cw-operating mid-infrared VCSELs reported has been 2.9 µm for a type-II antimonide active region [9]. In the present work, we report the fabrication and operation characteristics of cw PbSe VCSEL samples for long-wavelength emission between 6.7 and 8 µm.

Structure and Design

As our previous photoluminescence studies have shown that PbSe exhibits superior luminescence efficiency as compared to PbTe [10], Se-based compounds were used

for all VCSEL layers. The microcavity structures were designed by matrix transfer calculations [5] – [8]. Due to the strong temperature dependence of the band gap, IV-VI VCSELs have to be tailored for a certain operation temperature [7], [8]. As PbSe emits at 6.5 µm or longer only at cryogenic temperature, the lasers were designed for an operation temperature of around 90 and 4 K. Thus, the VCSEL structure is formed by two high-reflectivity Bragg mirrors consisting of five $\lambda/4$ EuSe/$Pb_{0.94}Eu_{0.06}$Se layer pairs. Due to the high refractive index contrast of 50% between these mirror materials, only five layer pairs are required to obtain a reflectivity well above 99%.

The 2 λ thick cavity region between the mirrors consists of a 2.2 µm $Pb_{0.94}Eu_{0.06}$Se buffer and a 1.1 µm PbSe active region. The cavity design ensures that neither the PbSe laser emission nor the 5.3 µm pump laser is absorbed in the mirror layers, and that the pump wavelength does not coincide with the mirror stop band. The complete laser structure was grown by molecular beam epitaxy onto (111) BaF_2 substrates at a substrate temperature of 250 °C. Two cw-VCSELs were fabricated for different operation temperatures and emission wavelengths. The first one was designed for operation at liquid He temperature, and thus, the cavity resonance wavelength was set to the 7.9 µm PbSe band gap emission at 4 K. The second VCSEL was designed for 85 K operation with a corresponding PbSe emission at about 6.7 µm. A cross sectional electron microscopy image of this VCSEL is shown in the insert of Fig. 1 (b).
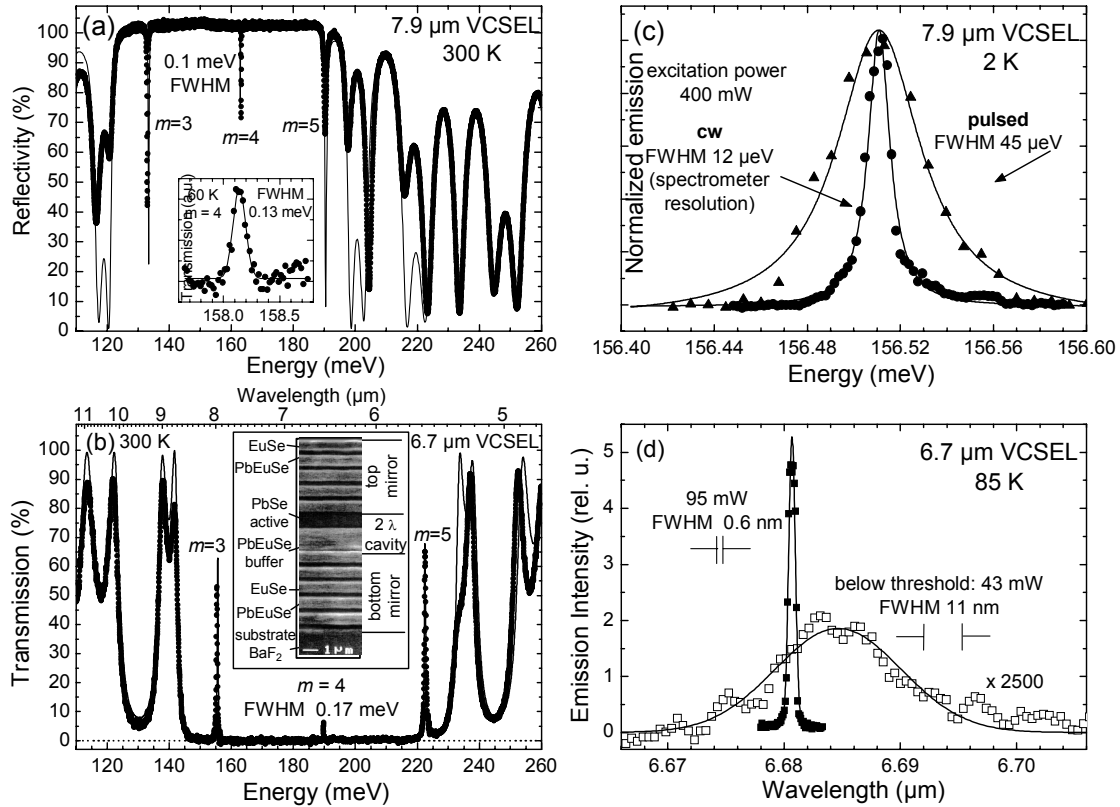
Fig. 1: (a) Reflectivity of the 7.9 µm cw-VCSEL, and (b) transmission of the 6.7 µm cw-VCSEL, both measured at 300 K. The solid lines correspond to the theoretical spectra calculated using the transfer matrix method. The insert in (a) shows the transmission around the central cavity mode at 60 K on an enlarged scale, and the insert in (b) the cross-sectional scanning electron microscopy image of the VCSEL structure. Right hand side: (c) Emission spectra of the 7.9 µm VCSEL at 2 K in cw (dots) and pulsed mode (triangles), both at 400 mW pump power. (d) Emission of the 6.7 µm VCSEL at 85 K at a pump power of 95 mW (■) above threshold and 43 mW (□) below threshold.

Optical Properties

Figure 1 (a) shows the reflectivity spectrum of the 7.9 μm VCSEL measured at 300 K. At this temperature, the spectrum exhibits three narrow cavity resonances of m = 3rd, 4th, and 5th order at 133, 163, and 190 meV (9.33, 7.61, and 6.53 μm), respectively. The measured line width of the 3rd resonance mode is 0.25 meV, whereas that of the central 4th order mode is only 0.10 meV, demonstrating a high cavity finesse of about 400, taking into account the order of the mode. The calculated reflectivity spectrum, shown by the solid line in Fig. 1 (a), is in very good agreement with the experimental data. Owing to the decrease of the energy band gap of PbSe from 279 meV at 300 K to 146 meV at 2 K, at low temperature the higher energy cavity resonances are damped by the interband PbSe absorption. Thus, at 60 K (see insert of Fig. 1 (a)), the 4th order cavity resonance is broadened from 0.10 meV at room temperature to 0.13 meV. At even lower temperatures, the 4th order resonance completely disappears because this wavelength is completely absorbed by the PbSe active region. Comparing the 300 K and 60 K spectra one can see that the spectral position of the resonances shifts to lower energies at a rate of 22 μeV/K to 158 meV or 7.8 μm at 60 L due to the increasing refractive index of the cavity material. For the room temperature transmission spectrum of the 6.7 μm VCSEL (Fig. 1 (b)), again, three cavity resonance peaks are observed, but now at energies of 155, 190 and 223 meV or λ = 8.0, 6.53, and 5.23 μm, respectively. The line width of the central 4th order cavity mode is only 0.17 meV or 7 nm, indicating a cavity finesse of about 300. As the temperature is lowered, again the resonance positions are red-shifted due to the increasing refractive index and below 100 K the central cavity mode becomes damped due to the PbSe absorption.

Laser Emission

Both VCSELs were optically pumped with a cw-CO laser emitting at a 5.28 μm wavelength (235 meV). The pump beam was focused onto the sample surface to a spot size of about 200 μm and the emitted light was detected with an HgCdTe detector through a grating spectrometer using the lock-in technique. The total emitted power was measured with a calibrated detector using an InSb long pass filter. Figure 1 (c) shows the emitted laser line for cw as well as pulsed excitation with 400 mW pump power in both cases. At 2 K, the stimulated emission of the 4th order resonance of the 7.9 μm VCSEL is found at 156.51 meV, *i.e.,* λ = 7.92 μm. This represents the longest emission wavelength of all VCSELs reported to date. For cw operation, an extremely narrow line width of only 12 μeV (0.6 nm) is observed, as found from the Lorentzian line fits shown as solid lines in Fig. 1 (c). This line width is 10 times smaller than the 130 μeV width found for the unpumped cavity resonance in the 60 K transmission measurements of Fig. 1 (a); and it is also much narrower than that observed for pulsed mode emission that is shown by the solid triangles in Fig. 1 (c). At 400 mW peak power excitation, the FWHM of the pulsed laser emission is 45 μeV (2.3 nm), but increases up to 100 μeV when the pump power is increased. This is still below the width of the unpumped cavity and is attributed to dynamical broadening effects. For cw-excitation, the measured line width is exactly the resolution of the spectrometer setup. Thus, the true cw line width must be actually much smaller than 0.6 nm.

The emission spectra of the 6.7 μm VCSEL at 85 K are shown in Fig. 1 (d). At a low pump power of 43 mW, a weak emission at 6.685 μm with an 11 nm FWHM is found (open squares in Fig. 1 (d)), which corresponds to the expected wavelength and line width of the 4th order cavity resonance at 85 K. Therefore, this signal is attributed to spontaneous emission, filtered out by the cavity mode. At a doubled excitation power of 95 mW (filled squares in Fig. 1 (d)), the emitted intensity increases drastically by a factor of 5000 and it is a factor of 20 narrower. The line width as determined by a Gaussian line fit (solid line) is only 0.6 nm or 16 μeV, again limited only by the spectrometer resolution (denoted by –||– in the figure). Thus, above threshold we observe a very

strong spectral narrowing not only with respect to the width of the passive cavity mode, but also compared to the spontaneous emission signal.
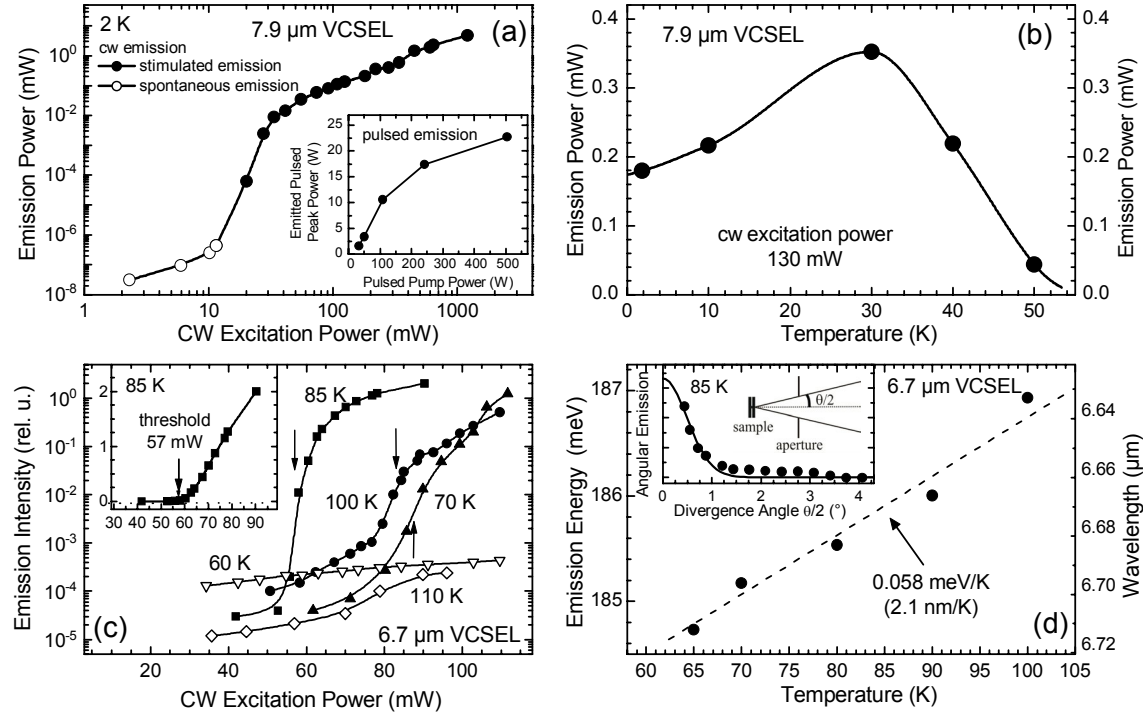
Fig. 2: (a) Cw output power of the 7.9 µm VCSEL plotted as a function of pump power at 2 K: (o) spontaneous emission, (●) laser emission. The 25 mW laser threshold is determined from the inflection point. Inset: pulsed laser output versus excitation power. (b) Cw output power of the same VCSEL at 130 mW pump power plotted versus operation temperature. (c) Cw output intensity of the 6.7 µm VCSEL plotted versus pump power at temperatures between 60 and 110 K: full symbols: stimulated emission, open symbols: spontaneous emission. Insert output intensity versus pump power at 85 K on a linear scale, with the thresholds indicated by arrows. (d) Tuning characteristics of the 6.7 µm VCSEL: emission energy and emission wavelength plotted versus operation temperature. This yields a linear tuning coefficient of +0.058 meV/K or -2.1 nm/K. The insert shows the measured angular emission characteristics of the laser (dots). The solid line represents the Gaussian line fit to the data points.

Figure 2 (a) shows the cw power emitted by the 7.9 µm VCSEL as a function of excitation power. For weak excitation, only spontaneous emission (open circles) is observed. Above threshold, the emitted power rapidly increases (full circles). As can be seen by the inflection point of the S-shaped curve of the double logarithmic plot in Fig. 2 (a), the external laser threshold is 25 mW. Since the pump laser was focused to a diameter of 200 µm, this corresponds to an internal threshold of 25 W/cm^2, where the 63 % reflectivity of the laser structure at the pump energy is taken into account. At an excitation power of 1.2 W, the cw power emitted through one Bragg mirror is 4.8 mW. This is the highest observed from any cw VCSEL in the mid-infrared. For higher excitation powers, pulsed mode excitation was used in order to prevent thermal damaging of the sample. The inset of Fig. 2 (a) shows the emitted pulse peak power as a function of pump power. For 500 W pump pulses, a peak power of 23 W is emitted from one side of the VCSEL. Due to the symmetric cavity design, the total emitted power is twice the power measured from one side. Therefore, the conversion efficiencies for cw and pulsed ope-

ration at maximum output powers are 0.8 % and 9 %, respectively. The maximum pulsed mode efficiency is 20 %, at 100 W pump power. Below 100 W, the slope efficiency determined by linear fits is 24 % whereas for CW operation a value of 1% was found.

The temperature dependence of the 7.9 µm VCSEL emission is shown in Fig. 2 (b) for a constant 130 mW excitation power. Up to 30 K, the spontaneous emission of the PbSe active material shifts closer to the 4th order cavity mode. Thus, the emitted intensity increases. At 30 K, the maximum of the spontaneous emission coincides with the cavity resonance, manifested in best laser performance. Above 30 K, the emitted intensity is reduced because the maximum of the spontaneous emission shifts above the cavity mode. At 57 K, the laser emission is quenched due to complete detuning of resonance and spontaneous emission.

The threshold behavior of the 6.7 µm VCSEL sample is shown in Fig. 2 (c) for different temperatures. Again, the data is plotted on a logarithmic scale to reveal also the sub-threshold signals. For clarity, the measurement for 85 K is also plotted in the inset on a linear scale. The threshold pump power was evaluated for operation temperatures of 70 (triangles), 85 (squares) and 100 K (circles) to be 87, 57 and 83 mW, respectively, as indicated by the arrows at the inflection points of the logarithmic plots. Thus, the minimum threshold is at the design temperature, where the maximum of the spontaneous emission and the cavity mode position coincide. The minimum pump threshold of 57 mW at 85 K corresponds to an internal threshold power density of 67 W/cm^2. In the logarithmic plots one can not only see the sub-threshold signals, but also the emission at 60 and 110 K (open symbols in Fig. 2 (c)), at which only weak and much broader spontaneous emission is observed. Thus, this VCSEL operates only at temperatures between 65 and 100 K because at higher as well as lower temperatures, the PbSe emission is above or below the cavity mode. The maximum observed total cw output power at 85 K is 1.2 mW at a pump power of 230 mW, which corresponds to a conversion efficiency of 0.5 %. We have also fabricated a third VCSEL with a design wavelength of 6.5 µm. This laser shows essentially the same performance as the 6.7 µm laser, but due to the shorter wavelength it lases up to a temperature of 120 K.

For applications of the lasers for molecular spectroscopy, the tuning ability and beam divergence are of crucial importance. These are characterized in detail in Fig. 2 (d) for the 6.7 µm VCSEL. The total tuning range by temperature variation was found to be 70 nm, with a linear tuning coefficient of +0.058 meV/K or –2.1 nm/K. This large tuning range is particularly advantageous for spectroscopy and it is substantially larger as compared to that of III-V quantum cascade lasers operating in the same wavelength range with a typical tuning coefficient of 0.01 meV/K [11]. In addition, we have recently shown that the emission wavelength can also be tuned quite elegantly by applying external magnetic fields [12]. In this case, we have found that the laser emission splits into two circularly polarized lines with opposite polarization. Therefore, the lasing action involves only spin polarized electronic states, *i.e.*, these VCSELs can be viewed as a novel kind of spin laser. We have also determined the angular emission characteristic of the cw VCSELs. As demonstrated in the inset of Fig. 2 (d) for an emission angle of only 1° off the surface normal (see sketch in the inset), the emission intensity (filled squares) essentially drops to zero, and the Gaussian line fit to the emission profile (solid line) yields a half width at half maximum of only 0.5°. This narrow forward directed emission is a clear advantage of the VCSELs as compared to edge emitters. Up to now, the cw-operation temperatures were limited by the pump laser wavelength as well as the temperature dependence of the PbSe photoluminescence emission. It is therefore anticipated that already minor changes in the cavity structure and active region design as well as the use of other pump sources will soon lead to higher cw-laser operation temperatures.

Conclusion

In conclusion, lead salt vertical-cavity surface-emitting lasers offer attractive properties as coherent infrared laser sources. They feature single mode operation, emit circularly shaped parallel beams with extremely small beam divergence, and exhibit very sharp emission lines widths below 12 µeV. Based on the use of high finesse infrared microcavity structures, cw-operation up to 120 K was demonstrated, which is expected to be significantly increased in the near future. In comparison with quantum cascade lasers, the lead salt VCSELs show a substantially larger wavelength tunability, which is of crucial importance for spectroscopy applications.

Acknowledgements

References

[1]   M. Tacke, in: Long Wavelength Infrared Emitters Based on Quantum Wells and Superlattices, edited by M. Helm (Gordon and Breach Science, Amsterdam, 2000), pp. 347–396

[2]   P. C. Findlay, C. R. Pidgeon, R. Kotitschke, A. Hollingworth, B. N. Murdin, C. J. Langerak, A. van der Meer, C. M. Ciesla, J. Oswald, A. Homer, G. Springholz, and G. Bauer, "Auger recombination dynamics of lead salts under picosecond free-electronlaser excitation" Phys. Rev. B 58, 1998, 12908 – 12914

[3]   Z. Feit, M. McDonald, R. Woods, V. Archembault, P.Mak, "Single-mode molecular beam epitaxy grown PbEuSeTe/PbTe buried-heterostructure diode lasers for CO_2 high-resolution spectroscopy" Appl. Phys. Lett. 68, 1996, 738 – 740

[4]   U. P. Schiessl and J. Rohr, "60°C lead salt laser emission near 5 µm wavelength" Infrared Phys. Technol. 40, 1999, 325 -330.

[5]   T. Schwarzl, W.Heiss, G.Springholz, M.Aigle, H.Pascher, "6 µm vertical cavity surface emitting laser based on IV-VI compounds" Electron.Lett. 36, 2000, 322 – 324

[6]   W. W. Bewley, C. L. Felix, I. Vurgaftman, J. R. Meyer, G. Xu, and Z. Shi, "Lead salt vertical-cavity surface-emitting lasers operating at λ = 4.5 − 4.6 µm with optical pumping" Electron. Lett. 36, 2000, 539–540

[7]   J. Fürst, H. Pascher, T. Schwarzl, M. Böberl, W. Heiss, G. Springholz, G. Bauer. "MIR IV-VI vertical cavity surface-emitting lasers with zero-, two-, and three-dimensional systems in the active region", Appl. Phys. Lett. 81, 2002, 208 – 210

[8]   W. Heiss, T. Schwarzl, G. Springholz, K. Biermann, K. Reimann. "Above-room-temperature mid-infrared lasing from vertical-cavity surface-emitting PbTe quantum-well lasers", Appl. Phys. Lett. 78, 2001, 862 – 864

[10]   M. Böberl, W. Heiss, T. Schwarzl, K. Wiesauer, G. Springholz, "Mid-infrared continuous-wave photoluminescence of lead salt structures up to temperatures of 190°C" Appl. Phys. Lett. 82, 2003, 4065-4067

[11]   T. Allen, S. Blaser, M. Beck, D. Hofstetter, J. Faist, and E. Gini, "Continuous-wave distributed-feedback quantum-cascade lasers on a Peltier cooler" Appl. Phys. Lett. 83 (2003) 1929-1931.

[12]   J. Fürst, H. Pascher, T. Schwarzl, G. Springholz, M. Böberl, G. Bauer, W. Heiss, "Magnetic field tunable circularly polarized emission from midinfrared IV-VI vertical emitting lasers" Appl. Phys. Lett. 86, 2005, 021100-2

Sensors

Sensor Interface Electronics

Daniel Rocha

**Industrial Sensor Systems, Institute of Sensor and Actuator Systems
Vienna University of Technology, Austria**

The importance of tailored electronic readout circuits in biosensing applications has in the past often been neglected. In this contribution we demonstrate the relevance of the issue considering a practical example of closely coupled co-design of micro- and nanosystems: a high-quality recording platform for single ion channel measurements on functionalized artificial lipid membranes.

Introduction

Ion-channels on cell membranes play crucial roles in physiology and pathophysiology and are important drug targets [1]. Microelectrode-based electrophysiological techniques which access the interior of a cell and can directly measure the minute currents through these channels have been employed in the past for the study of ion-channels.

The most successful of these techniques and the current golden standard is the patch-clamp technique [2]. Although traditionally performed manually and thus yielding very low throughputs in the order of 10 data points/technician/day, during the last decade several automated high-throughput screening (HTS) lab-on-a-chip systems have been proposed which have throughput rates going up to 20.000 data points/day [3]. The quality of the data produced by these systems is however not yet high enough to resolve single ion-channel currents in a repeatable manner.

Recording the sub-picoampere currents flowing through single ion channels in cell membranes with sub-millisecond resolution has up to date been difficult and often impossible due to both the limitations of the readout electronics and the difficulty of establishing a repeatable clean interface between the cell and the biosensor so as to form a so-called gigaseal. Yet, such recordings would yield valuable information in the study of the highly dynamic processes occurring upon e.g. channel gating or the membrane relaxation after potential steps and phase transitions and thus open way to significant advances in ion channel research.

In this paper we describe a low-noise amplifier design which is part of a planar patch-clamp chip being developed at our institute in cooperation with the Centre of Nanobiotechnology (CNB, University of Natural Resources and Applied Sciences, Vienna, Austria) for the recording of single ion channel currents on arrays of functionalized supported artificial lipid bilayer membrane (BLM) patches The topic of this contribution is the design of an amplifier for optimal noise performance to be employed in single ion channel current measurements.

Envisioned system

Together with the CNB [4] we are developing a low-noise single ion-channel recording platform in which an array of functionalized artificial lipid membrane patches with implanted ion channels will be patterned on a solid support (see Fig. 1) including provision for a clean interface to the electronic measurement setup.
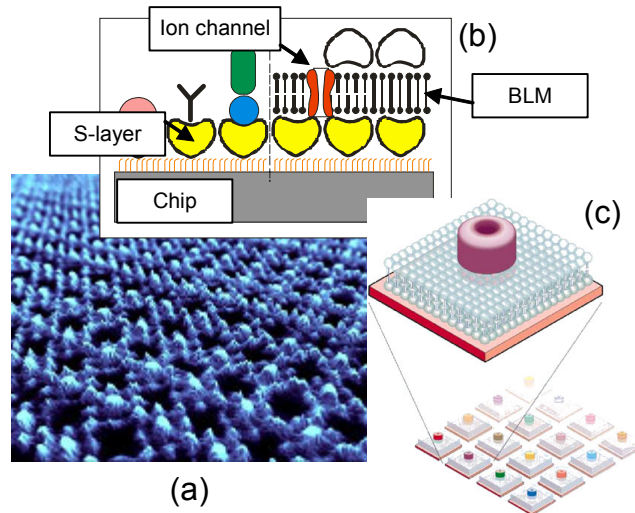
Fig. 1: Functionalized supported lipid bilayer membranes (BLM) [4]. (a) AFM of BLM support layer based on S-layer proteins. (CNB/BoKu), (b) and (c) schematic representations of respectively a supported BLM and an array of BLMs with implanted ion channels.
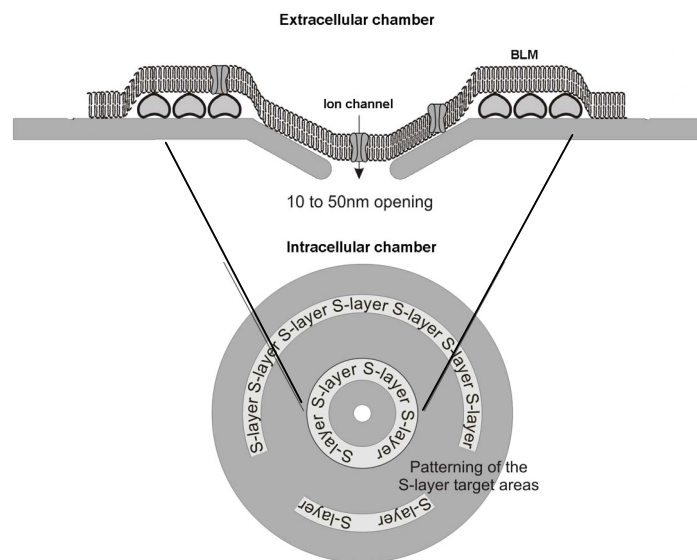
Fig. 2: Biomimetic cell-chip interface for improved adhesion of the cell membrane to the substrate so as to reach seal resistances in the order of 100 GΩ and above. Side view (top figure). Top view (bottom figure).

When looking at the minimization of noise, one of the most important features for high quality single ion channel recordings is a good seal between the intra and extracellular measurement chambers. Any current path having a conductance comparable to a single ion channel's conductance (1 – 150 pS) would generate an excessive amount of noise and lead to it being impossible to discern the minute signal current flowing through the ion channel from the noise generated by the leakage conductance.

On the one hand, we intend to improve the seal impedance by one order of magnitude when compared to traditional on-chip patch-clamp measurement setups so as to reach seal resistances in the order of 100 GΩ and above. For that purpose we will employ a

biomimetic interface based on S-layer proteins (see Fig. 2). By providing conditions which closely match the cell's natural environment, we expect the adhesion to the substrate to be vastly improved thus yielding better quality seals.

On the other hand, low-noise electronics need to be delivered, which will amplify the low-power signals to more robust levels that may easily be transported off-chip for further processing. The design of such an amplifier is the subject of the following section.

Optimal low-noise amplifier design

In the quest towards studying singular ion channels artificially implanted into engineered BLM patches having widths and lengths in the range of a few hundred nanometers, the need arises for optimal interfacing between the biosensor and the readout electronics.

In order to reach input-referred noise levels well below 100 fA in a band from 0 to 20 kHz, one must necessarily match the amplifier's input stage to the source impedance. An electrical lumped-element model corresponding to a membrane patch including the seal impedance and the access resistance is given in Fig. 3. This impedance is seen to be mainly capacitive in the frequency range of interest.
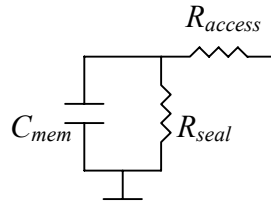
Fig. 3: Lumped element model of a membrane patch. C_{mem} has a typical density of 1 µF / cm^2, for the 1 µm^2 patches we are targeting $C_{mem} \approx$ 10 fF. A good seal will have resistances of R_{seal} > 100 GΩ and R_{access} will typically be a few MΩ. For the frequencies of interest, the one dominant component is C_{mem}.

Eq. 1

$$S_{i,n,tot} = \ldots \frac{L^2}{I_{C0}C_{g,tot}}\omega^2\left(C_f + C_s + C_{g,tot}\right)^2\left(1 + \frac{f_k}{f}\right)$$
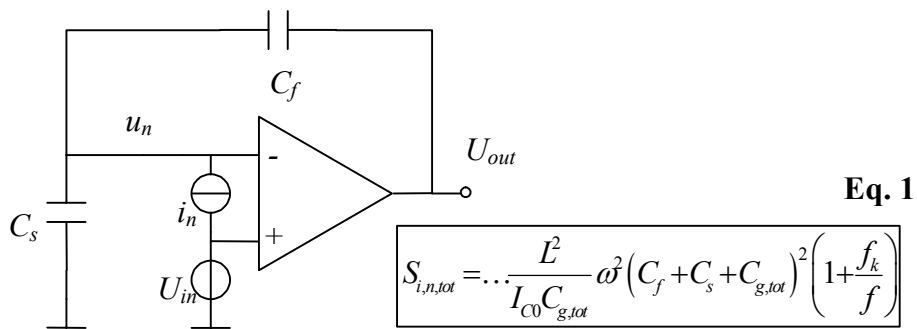
Fig. 4: Feedback configuration including noise sources u_n and i_n. Equation 1 shows the dependence of the total input-referred noise current power spectral density with C_s, C_f, the total gate capacitance $C_{g,tot}$, the gate length of the input transistor L and the inversion coefficient I_{C0}. One can see that L should be chosen to be minimal, the transistor should biased deep in strong inversion and $C_{g,tot}$ should be equal to $C_f + C_s$

One possible feedback configuration for the amplifier would be the transimpedance amplifier shown in Fig. 4. Notice that capacitive feedback has been used in order to

eliminate noise contributions stemming from the passive elements. The main source of noise thus comes from the amplifier itself and is originated mainly by the drain noise current. It can be modeled by the two equivalent sources i_n and u_n at the amplifier's input port (see Fig. 4), where it can be shown that i_n is proportional to $C_{g,tot} = C_{gs} + C_{gd}$ and u_n is inversely proportional to $C_{g,tot}$. Both noise sources have a component stemming from the drain current's thermal noise and another due to its 1/f noise. The thermal noise component is minimized for a minimal gate length L, $C_{g,tot} = C_f + C_s$ and when the input stage is biased deep in strong inversion ($I_{C0} \gg 1$, see Equation 1 in Fig. 4 and Fig. 6).
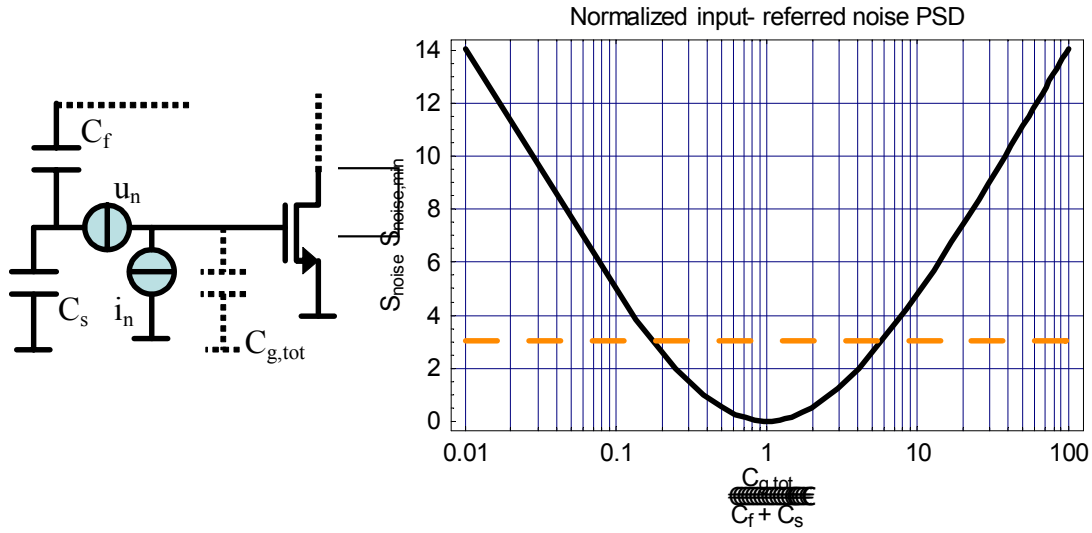
Fig. 5: Normalized input-referred noise power spectral density (PSD) as a function of the ratio of the input stage's capacitance ($C_{g,tot}$) and the sum of the feedback and source capacitances ($C_f + C_s$).
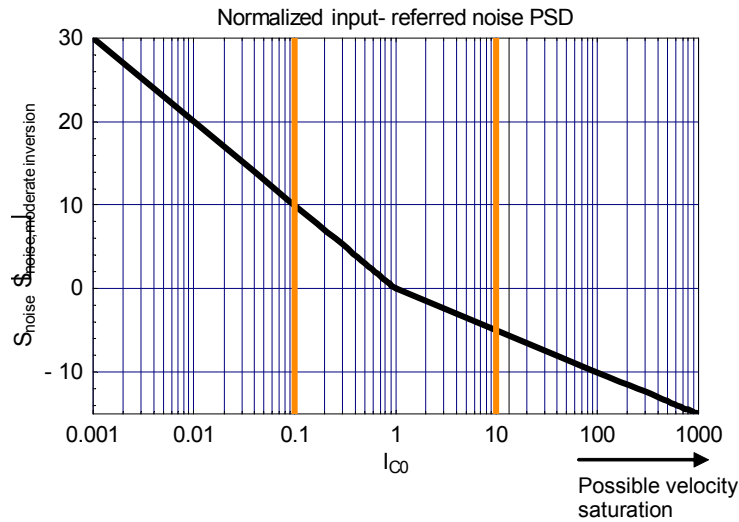
Fig. 6: Normalized input-referred power spectral density (PSD) as a function of the inversion coefficient (where $I_{C0} = 1$ corresponds to the center of moderate inversion)

For the very small source capacitances corresponding to nanosized BLM patches, the optimal input stage transistor sizes will thus become very small, consequently yielding

an increase in 1/f noise. In order to reduce the 1/f noise component, the autozeroed architecture depicted in Fig. 7 has been employed [5]. It uses an auxiliary amplifier for reducing the 1/f noise component of the main amplifier and has the advantage that both input terminals of the main amplifier are permanently usable, as needed for the feedback configuration depicted in Fig. 4. On phase Φ_2, the auxiliary amplifier autozeroes itself in order to become a very low-offset amplifier which is subsequently used for measuring the main amplifier's offset and 1/f noise, canceling it via a low-frequency feedback path.
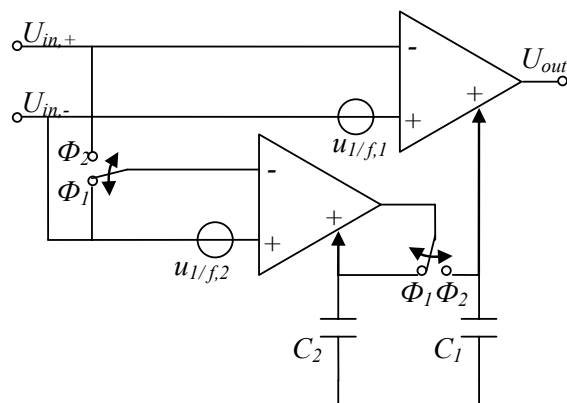
Fig. 7: Autozeroed amplifier. Both the main and the auxiliary amplifiers have an additional control input for offset cancellation. $U_{out}=A (U_{in+} - U_{in-}) + A_{Az} U_{1/f}$. On phase Φ_1 the auxiliary amp autozeroes itself, thus becoming a very low offset sense amplifier for the main amp's offset voltage which is detected on phase Φ_2. The control voltages are held on capacitors C_1 and C_2 respectively during phases Φ_1 and Φ_2 respectively.
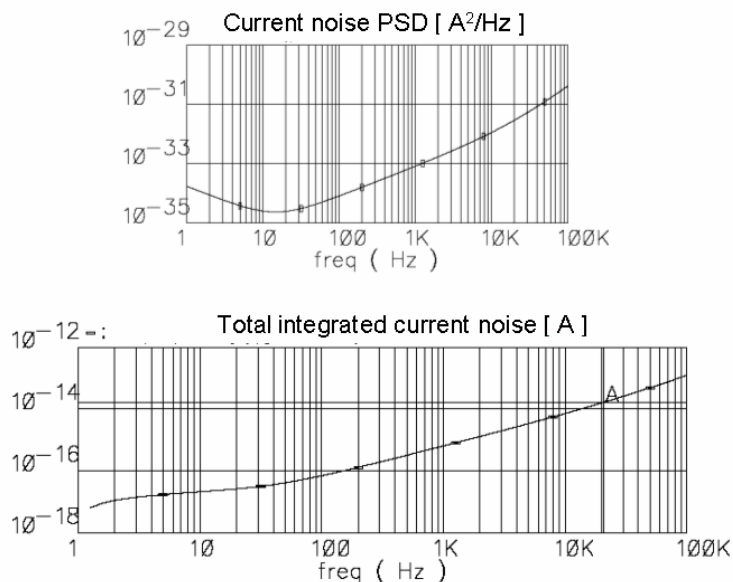
Fig. 8: Simulated noise power spectral density (top) total input-referred noise current. Results obtained with periodic noise analysis using Spectre RF simulator. At 20 kHz a total inband noise of 16.4 fA was obtained.

Simulation results show that it is possible to reach noise levels of about 17 fA for 1 µm x 1 µm patches using a standard 0.8 µm CMOS process from austriaMicrosystems (see Fig. 8).

Conclusion

The design of a low-noise amplifier for optimal noise performance to be employed in a state-of-the-art recording platform for the measurement of sub-picoampere currents flowing through single ion channels implanted on artificial lipid bilayer membrane (BLM) patches has been presented. The resulting amplifier features a simulated total inband noise of 16.4 fA in a band spanning from 0 to 20 kHz, which represents about one order of magnitude improvement in noise performance when compared to current state-of-the-art patch-clamp amplifiers.

Acknowledgements

References

[1]   Hille, B., *Ion Channels of Excitable Membranes*. 3rd ed. 2001: Sinauer Associates.

[2]   Sakmann, B. and E. Neher, *Single-Channel Recording*. 2nd ed. 1995: Kluwer Academic Publishers.

[3]   Comley, J., *Patchers vs. Screeners.* Drug Discovery World, 2003: pp. 47-57.

[4]   Pum, D.; Schuster, B.; Sara, M.; Sleytr, U.B., *Functionalisation of surfaces with S-layers*, IEE Proceedings - Nanobiotechnology, vol. 151 (3), pp. 83-86, Jun. 2004.

[5]   Coln, M.C.W., *Chopper stabilization of MOS operational amplifiers using feed-forward techniques*, IEEE J. Solid-State Circ., vol. 16, pp. 745-748, Dec. 1981.

Opto-Electronics (Posters)

Epitaxial Bragg Mirrors with Broad Omnidirectional Stop Band in the Mid-Infrared

E. Baumgartner, T. Schwarzl, G. Springholz, W. Heiss

Institut für Halbleiter und Festkörperphysik, Universität Linz, Altenbergerstraße 69, 4040 Linz, Austria

We present laser-quality low-loss Bragg mirrors exhibiting a broad omnidirectional stop band in the mid-infrared around 6.9 µm. Due to the high refractive index contrast of 80%, Bragg mirrors made from only three layer pairs of PbTe and EuTe are demonstrated to achieve reflectances higher than 99 % for angles of incidence up to 40° and higher than 98% for angles of incidence up to 70°. The relative omnidirectional stop band width is 50%.

Introduction

Similar to metallic mirrors, omnidirectional Bragg reflectors offer high reflectivity independent of the angle of incidence, but combined with the low-loss behavior and transparency of dielectric multilayer stacks. Such devices are advantageous for applications in laser resonators where light is incident from oblique directions, as in low-loss ring resonators or in two-dimensional planar-mirror resonators. They enable also the realization of highly-efficient corner-cube retro reflectors. Bragg mirrors exhibiting omnidirectional stop bands in the mid-infrared were demonstrated both theoretically and experimentally with relative stop band widths up to 45 % [1].

In our work, a high-finesse microcavity formed by two omnidirectional PbTe/EuTe Bragg mirrors for the mid-infrared was used for detailed optical analysis of the mirror properties. The appearance of a cavity resonance facilitates the accurate determination of the mirror reflectance from the quality factor of the resonator [2]. Similar mirrors have successfully been used for cw operating mid-infrared vertical-cavity surface-emitting lasers with divergence angles of 1° [3].

Theory

In modeling the transmittance behavior of a half wavelength microcavity enclosed between Bragg mirrors the characteristic matrix description is preferred [4], because it provides insight into the energetic position and extent of the photonic band gap.

An omnidirectional Bragg mirror will remain reflective throughout all angles of incidence, whenever the refractive indices of the environment and the mirror dielectrics are such that light impinging at grazing incidence will be refracted strong enough to avoid the Brewster angle on all subsequent refractions (Fig. 1 (d)). For a given microcavity structure (Fig. 1 (b)), the simulated angular dependence of the transmittance spectra (Fig. 1 (e), (f)) displays the stopband of almost vanishing transmission, lined by the Fabry-Perot interference fringes of the microcavity structure as a whole. Figs. 1 (c), (d) show the calculated photonic band structure of the Bragg mirrors forming the cavity.

The finesse F_m of a Fabry-Perot resonator of order m can be expressed as (Fig. 1 (a); R is the geometrical mean of the reflectances of the enclosing mirrors):

$$\frac{1}{m}\frac{k_0}{FWHM(k_0)} = F_m \approx \pi \frac{\sqrt{R}}{1-R}$$

Therefore, reflectances that are derived from the resonance line width FWHM (k_0) will always provide a worst-case estimate for the reflectance of one mirror.

(a)

(b)

(c)

(d)

(e)

(f)
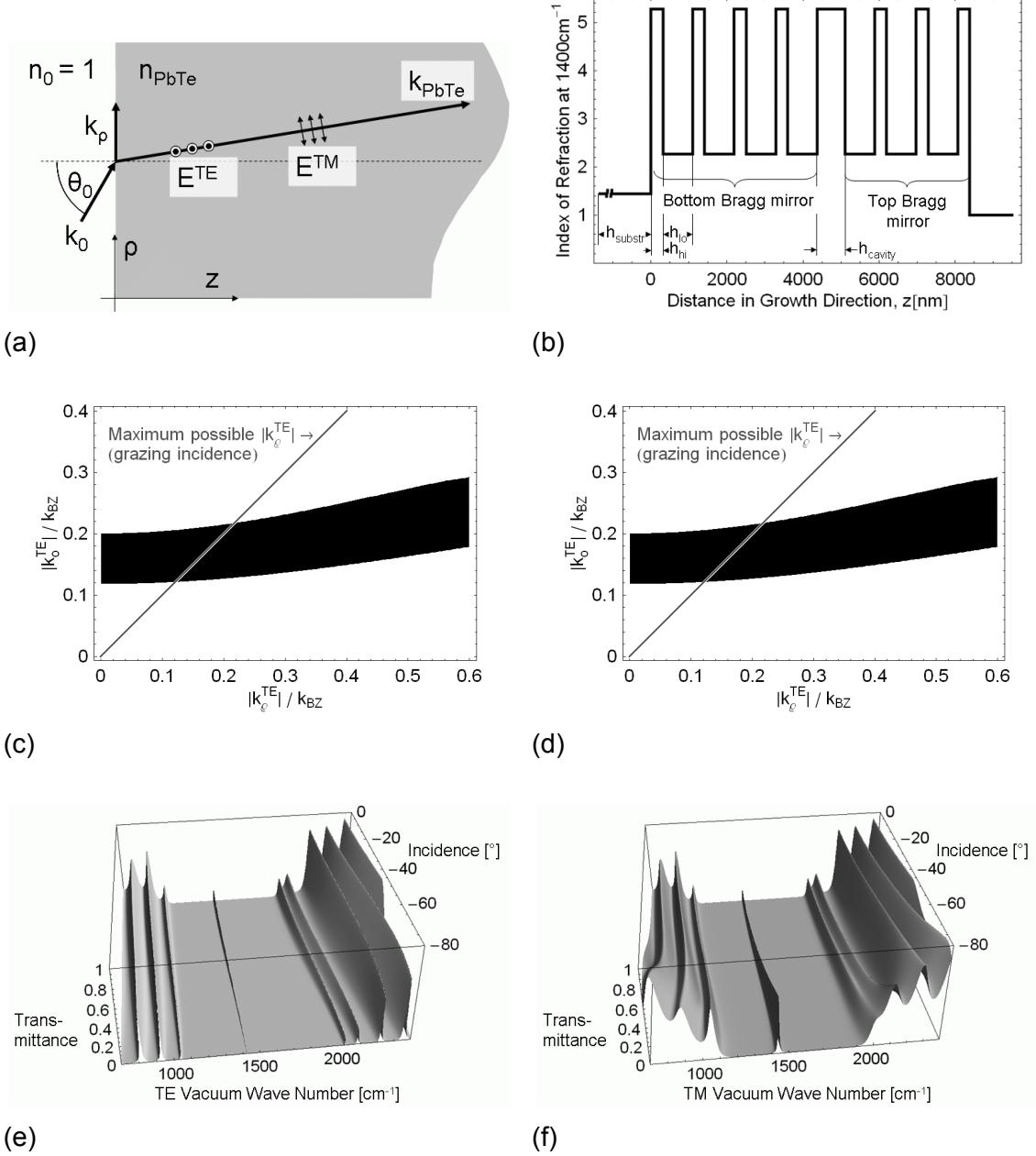
Fig. 1: (a) Terminology and coordinate system used; (b) target microcavity structure by index of refraction of its components; (c) and (d): Calculated angular dependence of the stopband width (black) for one of the mirrors as described in Fig. 1(b). By expressing the angle of incidence in terms of the in-plane wave vector component $k\rho$ (Fig. 1(a)) the angle dependence is transformed into a dispersion relation $\omega(k_\rho) = c_0 k_0(k_\rho)$. $k_{BZ} \equiv 2\pi/(h_{lo}+h_{hi})$. The region below the light line (grazing incidence) corresponds to unphysical system states. (e), (f): Angular dependence of calculated transmittance spectra for the model structure (b).

Experimental

Sample Preparation

On a ‹111› BaF$_2$ substrate the half wave cavity structure targeted at a wavelength of 6.9 µm was grown by molecular beam epitaxy. As indicated in Fig. 1 (b), the overall structure consisted of four PbTe/EuTe mirror layer pairs of width h_{hi} = 317 nm and h_{lo} = 777 nm respectively, a PbTe cavity layer of width h_{cavity} = 732 nm and three top mirror layer pairs. With the special choice of materials, even at grazing incidence all angles of refraction within the mirror structure will remain smaller than the Brewster angle for TM polarized light (Fig. 1 (d)).

Measurements and Results

The angular dependence of the transmittance spectrum was determined by Fourier transform infrared (FTIR) spectroscopy. Probing the sample through a 2 mm aperture made a compromise over the need for a large aperture to proceed to high angles of incidence and the desire to measure the true resonance line width by avoiding the influence of lateral sample inhomogeneities. From the Lorentzian shaped resonance of the 0° spectrum through a pinhole aperture and through the 2 mm aperture an apparatus function was calculated, which afterwards was used to deconvolve the resonance line shapes of the angle scan with the 2 mm aperture (see insert in Fig. 2 (b)).

In Fig. 2 (a) the angular dependence of the stop band edges (triangles) and the resonance position (squares) are plotted. Theoretical predictions made by matrix methods (lines) are evidently in good agreement to the experimental findings. At 3% transmittance level a broad omnidirectional stopband of 727 cm^{-1} width around a center frequency of 1440 cm^{-1} could be found. This corresponds to a relative omnidirectional stopband width of 50%.

In Fig. 2(b) the angular dependence of the halfwidth of the resonance linewidth is plotted for TE, TM polarization. Taking into account the penetration of the light into the mirrors, an effective cavity finesse (Fig. 2 (c)) of well over 100 for angles of incidence up to 70° can be deduced from this. The lower limit mirror reflectance data in Fig. 2 (d) clearly show reflectances higher than 99% for angles of incidence up to 40° and higher than 98% for angles of incidence up to 70°.

Conclusion

By means of an epitaxially fabricated half-wave microcavity for the mid-infrared formed by Bragg mirror layers made from PbTe and EuTe, we have experimentally and theo-retically demonstrated the omnidirectionality of these Bragg mirrors for angles of inci-dence up to 70°. Around 6.9 µm, we have achieved a relative stopband width of 50% and have demonstrated effective reflectances higher than 99% for angles up to 40° and higher than 98% for angles of incidence up to 70°, indicating the suitability for laser applications.

Acknowledgements
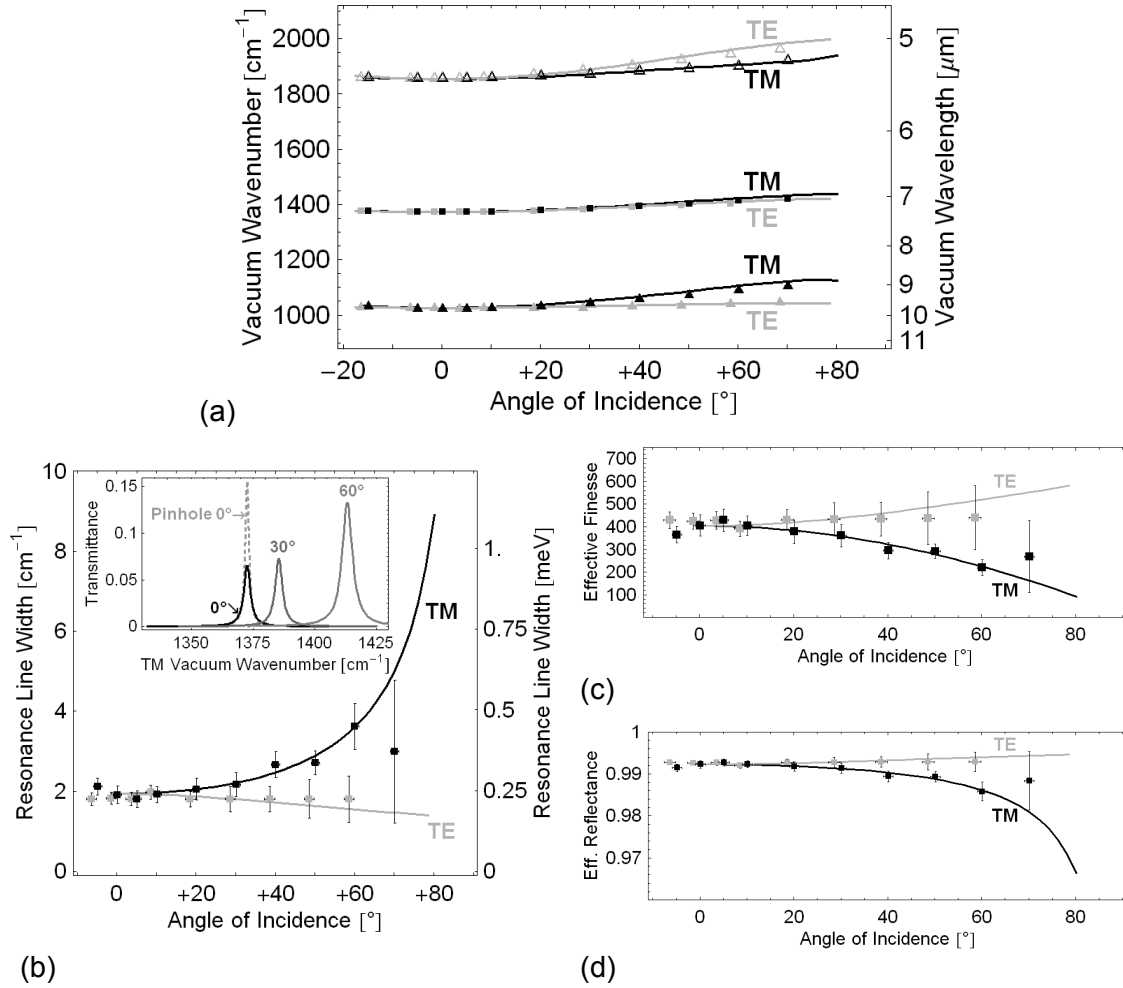
Fig. 2: (a) Angular dependence of Bragg mirror stopband edge (triangles) and cavity resonance (squares) position, compared to model prediction (lines). (b) Experimentally determined TE, TM resonance line widths. Insert: Angle scan TM resonance line shapes compared to that measured through a pinhole aperture (dashed line). (c) Effective finesse of the microcavity, as derived from the effective order of the cavity resonance and its line width. (d) Angular dependence of the lower limit of the effective Bragg mirror reflectance, as deduced from (c).

References

[1]   Y. Fink, J. N. Winn, S. Fan, C. Chen, J. Michel, J. D. Joannopoulos, E. L.Thomas: "A Dielectric Omnidirectional Reflector", Science 282, 1998, pp. 1679-1682

[2]   T. Schwarzl, W. Heiss, G. Springholz: "Ultra-high-finesse IV-VI microcavities for the midinfrared", Appl. Phys. Lett. 75 (9), 1999, pp. 1246-1248

[3]   T.Schwarzl, G.Springholz, M.Böberl, E.Kaufmann, J.Roither, W.Heiss, J.Fürst, H.Pascher: "Emission properties of 6.7 μm continuous-wave PbSe-based vertical-emitting microcavity lasers operating up to 100 K", Appl. Phys. Lett. 86, 2005, pp. 31102

[4]   A. D. Rakic, M. L. Majewski in H. Li, K. Iga (Eds.): "Vertical-Cavity Surface-Emitting Laser Devices", Springer-Verlag, Berlin 2003, pp. 259 – 301

Terahertz Quantum Cascade Lasers Operating in Magnetic Fields

G. Fasching[1], R. Zobl[1], V. Tamošiunas[1], J. Ulrich[1], G. Strasser[1],
K Unterrainer[1], R. Colombelli[2], C. Gmachl[2], L.N. Pfeiffer[2], K.W. West[2], and
F. Capasso[3]

[1]Institute of Photonics and Center for Micro- and Nanostructures,
Vienna University of Technology, A-1040 Vienna, Austria

[2]Bell Laboratories, Lucent Technologies,
600 Mountain Avenue, Murray Hill, NJ 07974

[3]Harvard University, Division of Engineering and Applied Sciences,
Cambridge, MA 02138

We have measured the emission intensity and spectra of Terahertz Quantum Cascade Lasers in an external magnetic field applied normal to the epilayers. We have observed a reduction of the threshold current, an enhancement of laser emission intensity and shifts of the emission line. A wider operating range was predicted for the selected waveguide design according to our finite-difference time-domain simulation results. The intensity enhancement and the threshold current reduction are attributed to the suppression of nonradiative Auger-intersubband transitions by Landau-quantization of the in-plane electron motion, to the modulation of the injection rate via resonant inter-Landau-level transfer, and to the modulation of waveguide properties.

Introduction

The first Quantum Cascade-Laser (QCL) in the Terahertz range was recently demonstrated by Köhler et al [1] proving that QCL concept can be successfully implemented also in far-infrared region. The continuous wave operation of the THz QCL was also reported [2]. However, the further improvement of THz QCLs and lasing at even longer wavelengths is a challenge for different reasons related to the intersubband population dynamics and the waveguide properties. Electron-electron scattering and interface roughness are the main scattering mechanisms at low temperatures in this range of intersubband energies. They lead to fast carrier relaxation, counteracting population inversion. An external magnetic field applied normal to epilayers should lead to an additional quantization of the in-plane electron motion [3] and to the modification of the scattering. The recently observed enhancement of the luminescence intensity of GaAs/AlGaAs [4] and InGaAs/InAlAs [5] Terahertz quantum cascade structures confirms such effect.

Experimental

The system used in the emission experiments consists of a FTIR spectrometer (NICOLET Magna IR 850) equipped with a Si beamsplitter and a 4.2 K Si bolometer. For the magnetic field measurements, the THz QCL is mounted in a magnet cryostat with two superconducting magnets. In this cryostat, detection is possible by a magnetic field tunable InSb cyclotron resonance detector, by a broadband Ga doped Ge detector, or by the external FTIR (Fig. 1).

The magnetic field at the location of the sample (oriented perpendicular to the epitaxial layers) can be adjusted independently from 0 T to 6.7 T by a second magnet. A closed light pipe guides the radiation from the sample to the detector. This narrow band InSb detector [4] is tuned by the magnetic field of the second (detector) superconducting magnet. The whole spectrometer is immersed in liquid He, so that room temperature background radiation cannot distort the measurements.
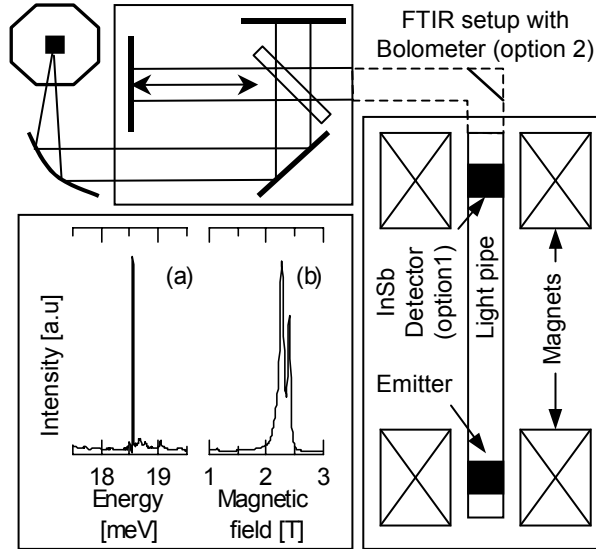
Fig. 1:   Set-up for high resolution spectral measurements: cryostat with superconducting magnets, high resolution (0.0155 meV) Fourier spectrometer and Si bolometer. (a) High-resolution spectrum of the laser without applied magnetic field at the emitter sample. (b) Response of the InSb detector versus applied detector magnetic field when illuminated by the THz laser (one line corresponds to the free electron cyclotron resonance, the other one to the impurity bound resonance).

Measurements

A 4.5 THz Quantum Cascade Laser, based on the active structure design proposed in [1] was used for the measurements in a magnetic field. 100 periods of the active structure were sandwiched between two n$^+$-doped contact layers (the bottom layer was d = 500 nm thick with n = 4×10^{18} cm^{-3} doping, the top layer was d = 100 nm thick with n = 7×10^{18} cm^{-3} doping) grown on a semi insulating GaAs substrate using molecular beam epitaxy (MBE).

A 100 µm wide device was selected for the intensity measurements in magnetic field due to its broadest lasing range. The broadband Ge detector was used to obtain the laser intensity as a function of different sample magnetic fields which is presented in Fig. 2. The laser emission intensity increases substantially for certain values of the magnetic field when compared to B = 0 T. For increasing magnetic fields we observe oscillations with a larger period. The application of a magnetic field increases the laser intensity by a factor of more than five at B = 4.2 T (see Fig. 2). This effect is understood as a consequence of the discretization of the energy spectrum. In the parabolic dispersion relation in the absence of a magnetic field the energy conservation requirement for intersubband Auger-scattering processes is fulfilled for a continuum of energy changes ΔE (meaning one electron suffers an energy change of $+\Delta E$, the other one a change of $-\Delta E$). However, for a non-vanishing magnetic field the only allowed energy changes ΔE are multiples of the cyclotron resonance energy $\hbar\omega_c$. Since the Auger-scattering rate

scales inversely with the associated change in energy and momentum, it is more and more suppressed with increasing Landau-level splitting. The laser intensity is proportional to the inversion which is directly proportional to the injection rate and inversely proportional to the non-radiative relaxation rate.
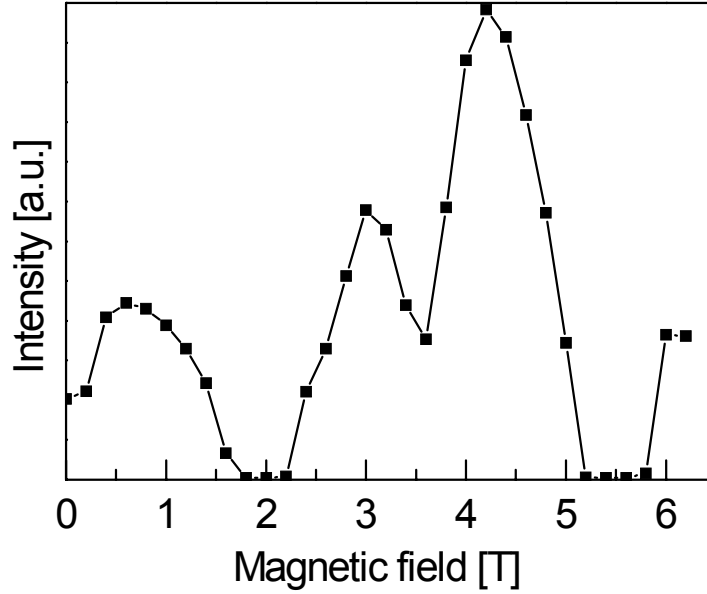
Fig. 2: Maximal laser emission intensity versus magnetic field. Laser emission intensity was recorded for every given magnetic field flux density value by adjusting pulse generator settings to obtain the maximum intensity. Clear emission intensity maxima are observed for N = 2.5 (4.2 T) and N = 3.5 (3 T).

We first assume that the injection rate is not influenced by the magnetic field. We would expect an oscillatory increase of the laser emission with minima where the magneto-intersubband resonance condition is met:

$$E_2 - E_1 = \frac{\hbar e B_N}{m^*} N$$

Here $E_2 - E_1$ is the energy difference between the lowest Landau-levels of the upper and lower laser transition, $\hbar$ - the Planck constant, e - the elementary charge, B_N - magnetic flux density , m^* - effective mass, N – an integer. Resonant tunneling between Landau levels opens up an additional non-radiative relaxation channel via the Landau ladder ($|1,N\rangle$, $|1,N-1\rangle$, ...$|1,0\rangle$) and by reducing the population inversion leads to the decrease of the laser emission intensity. It should be pointed out that a theoretical model proposed by Raikh and Shahbazyan [9] well describes a momentum transfer caused by interface roughness or impurities, which is required for resonant transfer between Landau levels of different subbands. It is clearly seen from the figure that the laser stops working at these magneto-intersubband resonances.

The energy difference between the injector states is small (~3.1 − 3.8 meV [10]) and the condition for complete magnetic quantization

$$\frac{\hbar e B}{m^*} > \Delta E_{injector}$$

is reached at relatively low magnetic fields. Optimum performance of the laser should be achieved for $\frac{\hbar e B}{m^*} M = \Delta E_{injector}$ and $\frac{\hbar e B}{m^*} N \neq \Delta E_{laser}$, where N and M are integers.

The interplay between increased injector efficiency and reduced non-radiative relaxation determines the detailed dependence of the laser intensity on the magnetic field.

The laser intensity increase and oscillatory behavior was consistently observed for all lasing devices independently of device width.

Conclusion

In summary, we have observed a reduction of the threshold current, an enhancement of laser emission intensity and shifts of the emission line in an external magnetic field applied normal to epilayers. An operating range of the selected waveguide design is consistent with our finite-difference time-domain simulation results. The intensity enhancement and the threshold current reduction are attributed to the suppression of nonradiative Auger-intersubband transitions by Landau-quantization of the in-plane electron motion, to the modulation of the injection rate via resonant inter-Landau-level transfer and to the modulation of waveguide properties.

Acknowledgements

References

[1] R. Köhler, A. Tredicucci, F. Beltram, H.E. Beere, E.H. Linfield, A.G. Davies, D.A. Ritchie, R.C. Iotti, F. Rossi, *Nature* **417**, 156 (2002).

[2] L. Ajili, G. Scalari, D. Hofstetter, M. Beck, J. Faist, H. Beere, G. Davis, E. Linfield, D. Ritchie, *Elect. Lett.* **38**, 1675 (2002).

[3] A. Blank and S. Feng, *J. Appl. Phys.* **74**, 4795 (1993).

[4] J. Ulrich, R. Zobl, K. Unterrainer, G. Strasser, and E. Gornik, *Appl. Phys. Lett.* **76**, 19 (2000).

[5] S. Blaser, M. Rochat, M. Beck, D. Hofstetter and J. Faist, *Appl. Phys. Lett.* **81**, 67 (2002).

[6] K. S. Yee, *IEEE Trans. Antennas Propagat.*, vol. AP-14, pp. 302-307, May 1966.

[7] A. Taflove, *Computational Electrodynamics: The Finite-Difference Time-Domain Method.* Norwood, MA: Artech House, 1995.

[8] R. W. Ziolkowski, J. M. Arnold, D. M. Gogny, *Phys. Rev. A*, vol. 52, 4, pp. 3082-3094, 1995.

[9] M. E. Raikh and T. V. Shahbazyan, *Phys. Rev. B* 49, 5531 (1994).

[10] R. Köhler, R. C. Iotti, A. Tredicucci, F. Rossi, *Appl. Phys. Lett.* **79**, 3920 (2001).

[11] V. Tamosiunas, R. Zobl, J. Ulrich, K. Unterrainer, R. Colombelli, C. Gmachl, K. West, L. Pfeiffer, F. Capasso, *Appl. Phys. Lett.* **83**, 3873 (2003).

Resonator Fabrication for Cavity Enhanced, Tunable Si/Ge Quantum Cascade Detectors

M. Grydlik[1], P. Rauter[1], T. Fromherz[1], G. Bauer[1], L. Diehl[2], C. Falub[2], G. Dehlinger[2], H. Sigg[2], D. Grützmacher[2]

[1] Institute for Semiconductor and Solid State Physics, University of Linz, Altenbergerstraße 69, A-4040 Linz

[2] Laboratory for Micro- and Nanotechnology, Paul-Scherrer Institute, CH-5232 Villigen PSI

A process for integrating SiGe quantum well infrared photodetectors (QWIPs) grown on SOI substrates into a vertical cavity resonator has been developed. The process is based on a low temperature (T < 250°C) etch mask deposition and, therefore, is applicable for novel QWIP structures grown by low temperature Si MBE.

Introduction

Infrared detection employing optical transitions in quantum wells has attracted a lot of research interest in the past several years. Due to the design freedom a variety of detector figures like for example the spectral region of sensitivity, the response time, the detector noise etc. can be adjusted over a large parameter range [1], [2] and optimized detector performance can be achieved for several areas of applications. In a recent work on Si/Ge QWIPs, we have demonstrated that in addition a large wavelength tunability can be achieved by employing the injector concept originally developed for quantum cascade electro-luminescence and laser structures [3]. The detectivity of these tunable SiGe QWIPs at 77K is approximately 1.5×10^9 cmHz$^{0.5}$/W, typically 1 – 2 orders of magnitude smaller than the detectivity of group III-V based devices. One concept to increase the detectivity of SiGe QWIPs in a narrow detection bandwidth consists of integrating the QWIP into a resonator. In Si/Ge QWIPs, typically the absorption of valence band quantum wells (QWs) is the basis for photocurrent generation. Since for valence band QWs, absorption is also allowed for radiation propagating parallel to the growth direction, vertical cavities can be used to enhance the absorption efficiency of these devices. Moreover, since for QWIPs based on SiGe cascade structures, an extremely large tuning range from for example 200 meV to 400 meV was demonstrated [3], the integration of this novel detectors into a properly designed vertical cavity will allow resonator enhanced detection for 2 narrow bands at wavelengths λ and 2λ that can be addressed by the externally applied voltage.

Experimental

For integrating a tunable QWIP into a vertical cavity resonator, 15 periods of nominally the same QW sequence as described in Ref. [3] (5 SiGe valence band quantum wells with 39, 26, 24, 23, and 35 Å well width and 0.42, 0.42, 0.40, 0.37, and 0.28 Ge concentration, respectively, separated by 30, 25, 25, and 25 Å Si barriers) have been grown on a SOI substrate by low temperature (T = 300 °C) solid source MBE. Detector mesas (typically 300 x 300 µm^2) with bottom and top contacts were formed by reactive ion etching and Al:Si metallization. A schematic sketch of the detector structure is

shown in the inset of Fig.1. The photocurrent spectra shown in Fig. 1 clearly demonstrate that the detectors grown on SOI substrate show a similar tunability as reported previously [3] for detectors grown on Si substrate.
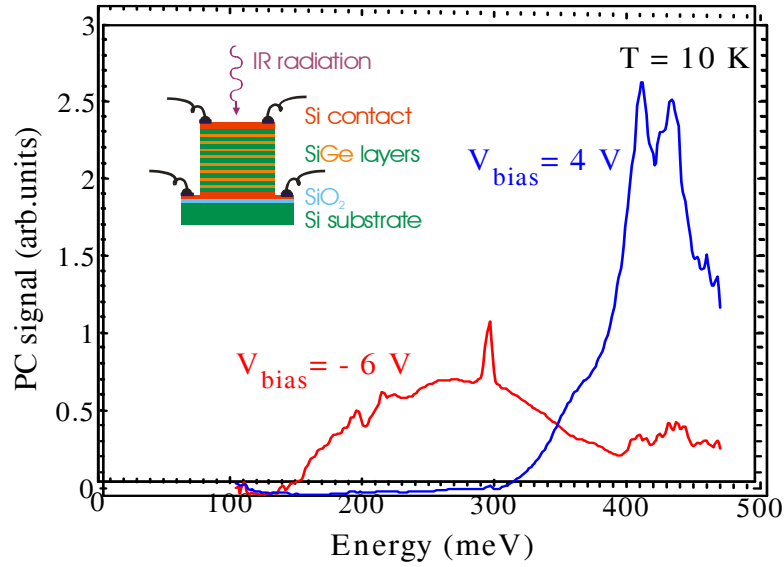
Fig. 1: Photocurrent spectra of SiGe cascade QWIPs measured at the bias voltages indicated in the plot.
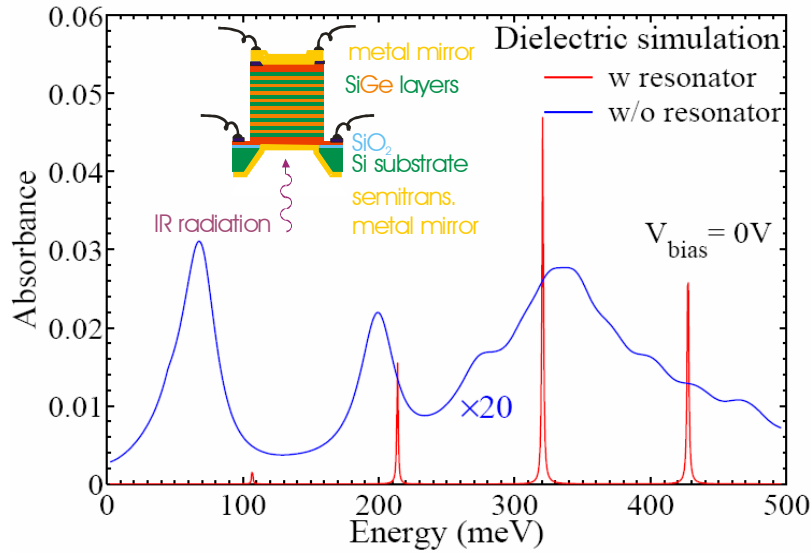
Fig. 2: Simulation of the QWIP absorbance with (red line) and without (blue line) resonator mirrors. Note that the result obtained for the case without mirrors is multiplied by 20.

In Fig. 2 a simulation of the effect of a resonator on the absorption efficiency is shown. Using the absorption spectrum calculated for the QWIP structure by k.p band structure simulations [3], the sample transmission, reflection and absorption including multireflections at all interfaces in the sample was calculated for radiation propagating perpendicular to the sample surface by the transfer matrix method [4]. The intensity absorbed by the QWIP layer sequences is shown by the blue line in Fig. 2. Using the same band

stucture for the QWIP and assuming a free standing membrane consisting of the QWIP layers coated with a thick gold layer on top of the membrane and a thin (for example 20 nm), semitransparent gold layer at the opposite side of the membrane through that radiation can be coupled into the QWIP (for a sketch, see inset of Fig. 2), the QWIP absorption was simulated by the transfer-matrix method [4] for comparison. In this simulation, the dielectric function of the gold was described by a Drude dispersion according to [5]. The simulated QWIP absorbance is shown by the red line in Fig. 2. It is evident from this plot that at the resonance wavelengths the QWIP absorption is enhanced by at least an order of magnitude.

For fabricating vertical cavity resonator as sketched in the inset of Fig. 2, openings aligned to the detector mesas have to be etched from the backside of the sample through the substrate. The buried oxide layer of the SOI substrate is used as an etch-stop. After removing the remaining SiO_2 layer by an HF etch, a free standing film consisting of the detector QW sequences results. On the top and bottom side of this detector film, broadband, high-reflectivity metal or Bragg mirrors will be deposited that finally form the resonator.

From the previous paragraph it is clear that the choice of a proper etchant is crucial for successful resonator fabrication. In our work, TMAH (Tetramethylammonium Hydroxide) at 90 °C was used as etchant for the following reasons: (a) TMAH has reasonably large etch rate (30 µm/h) for the Si (001) lattice plane that allows to etch free the buried oxide layer of a thinned SOI substrate (200 µm) in approximately 7 h. (b) In addition, the TMAH etch rate for Si (111) lattice planes is approximately an order of magnitude smaller than in (001) direction. Therefore, TMAH etch grooves are bound by (111) planes and negligible underetching of the etch mask occurs. (c) The etch rate of TMAH for thermally grown oxide is virtually vanishing. Therefore the etching process is effectively stopped by the 200 nm thick buried oxide of the SOI substrate. Even after a 2 h long over-etching the exposed SiO_2 layer showed no indication of an etch attack and remained optically flat. (d) TMAH is compatible with the standard Si technology as it is contained in most of the photoresist developers.

For the long etch times required to etch from the wafer backside to the buried SiO_2, an etch mask with high resistance against TMAH is required. In standard Si MEM technology, a structured Si_3N_4 layer deposited by LPCVD at approximately 900 °C is commonly used as mask for long TMAH etches. However, due to the high deposition temperature necessary for the LPCVD process, this mask material can not be used for samples with QWIP structures grown on the wafer front side. On the other hand, a 300 nm thick Si_3N_4 deposited at lower temperatures (250 °C) in a plasma enhanced CVD (PECVD) process was destroyed by the TMAH etch after approximately 100 nm etch depth. Increasing the thickness of the Si_3N_4 to 400 nm and 500 nm did not improve the results most probably due to increased number of strain induced cracks in the thicker Si_3N_4 layers.

The best results were obtained by a mask consisting of a double layer of Si_3N_4 (200 nm) and the spin-on polymer BCB (Bencocyclobutene, Dow Chemicals brand name: "Cyclotene" [6]) with a thickness of 6 – 8 µm. BCB can be structured by reactive ion etching in a mixed O_2 and CF_4 plasma. The Si_3N_4 layer acts as an adhesion promoter for the BCB film. With this mask and a 10 h long TMAH etch, free standing Si membranes could be produced on a test wafer consisting of a Si layer grown on an SOI substrate instead of the Si/Ge QWIP structure. Electron and optical microscope pictures of the membrane are shown in Figs. 3 (a) – (d). In the optical microscope (Figs. 3 (a), (b)) no surface roughness of the membrane and the (111) sidewalls are visible. The sample shown in Figs. 3 (a), (b) was illuminated from the backside resulting in a bright appearance of the Si membranes, indicating that the membranes are transparent in the visible spectral region due to their small thicknesses. Also the electron microscope pictures (Figs. 3 (c), (d)) do not show significant surface roughness of the membranes and the sidewalls. The etch mask shown in Fig. 3 (d) is evidently not

attacked by the TMAH etch and only a small underetching due to the non-vanishing etch rate in (111) direction is shown. Infrared transmission through a Si membrane was measured with an infrared microscope. The transmission spectrum plotted in Fig. 3 (e) shows strong Fabry-Perot oscillations with a periodicity corresponding to a membrane thickness of 1.42 µm. In future work, the line width of these oscillations will be decreased by increasing the cavity Q-factor with high-reflectivity broadband mirrors deposited on the membrane surfaces.
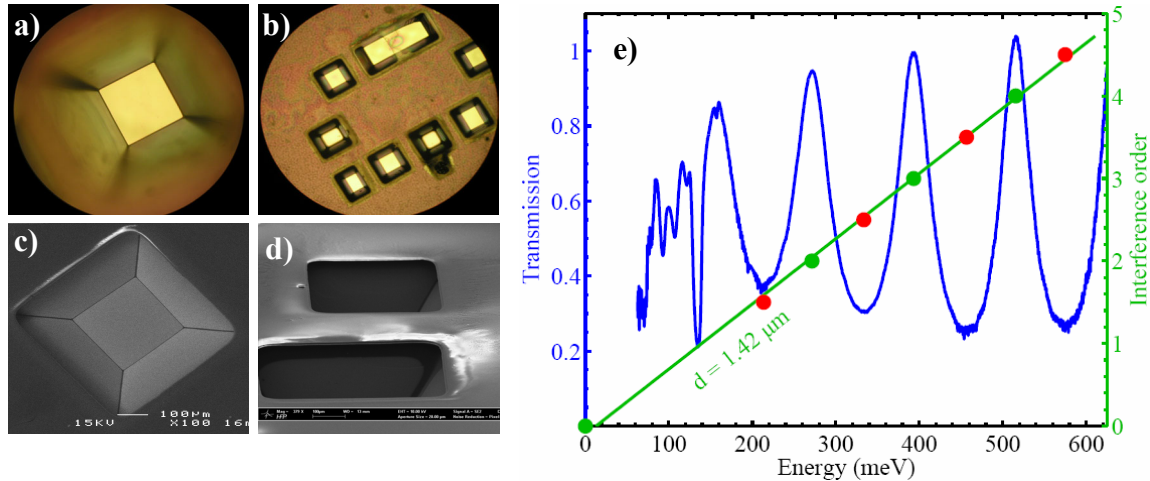
Fig. 3: Results obtained by visible ((a), (b)), electron ((c), (d)) and infrared microscope (e) experiments revealing an optically flat Si membrane with thickness of 1.42 µm fabricated by the process described in the text.

Conclusions

A process for fabricating a thin, free standing Si membrane by etching grooves from the backside of an SOI wafer has been developed, where the buried SiO_2 layer acts as an effective etch stop. Since only low temperature (T< 250°C) process steps are involved, the process is perfectly suited for integrating Si/Ge based QWIPs grown on SOI substrates into vertical cavity resonators.

Acknowledgements

References

[1]   B. F. Levine, "Quantum-well infrared photodetectors", J. Appl. Phys. **74**, R1-R81 (1993).

[2]   H. Schneider, P.Koidl, M. Walther, J. Fleissner, R. Rehm, E. Diwo, K. Schwarz, G. Weimann, "Ten years of QWIP development at Fraunhofer IAF", Infrared Phys. Technol**. 42**, 283-289 (2001).

[3]   P. Rauter, T.Fromherz, G. Bauer,L. Diehl, G. Dehlinger, H. Sigg, D. Grützmacher, H. Schneider, "Voltage tuneable, two-band MIR detection based on Si/SiGe quantum cascade injector structures", Appl. Phys. Lett. **83**, 3879-3881 (2003).

[4]   see for example: B. Harbecke,” Coherent and Incoherent Reflection and
       Transmission of Multilayer Structures”, Appl. Phys. B **39**, 165 (1986).

[5]   M.A. Ordal, et. al, “Optical properties of fourteen metals in the infrared and far
       infrared..”, Appl. Optics **24**, 4493 (1985).

[6]   http://www.dow.com/cyclotene/

Nanocrystal Based Microcavity Light Emitting Devices

J. Roither, M. V. Kovalenko, S. Pichler, T. Schwarzl, W. Heiss

Institut für Halbleiter- und Festkörperphysik, Universität Linz, Altenbergerstraße 69, 4040 Linz, Austria

D. V. Talapin, N. Gaponik, A. Eychmuller

Institut für Physikalische Chemie, Universität Hamburg, D-20146 Hamburg, Germany

Highly luminescent, colloidally synthesized semiconductor nanocrystals are used to fabricate microcavity light emitting devices operating around 650 and 1540 nm. They consist of a Bragg interference mirror from standard optical materials, an active layer consisting of either CdSe nanocrystals for operation in the visible or HgTe nanocrystals with a strong emission in the telecommunication wavelength range, a spacer layer to achieve the desired cavity length, and a metallic top mirror. Both types of devices give highly directional, narrow mode emission with a beam divergence below 2° clearly evidencing that the nanocrystal emission couples to the microcavity resonances. Furthermore, operation up to 75°C is demonstrated without degradation of the nanocrystals, which is promising for potential applications.

Introduction

Semiconductor nanocrystals (NCs) synthesized by wet-chemical methods have been investigated because of their strongly size-dependent electrical and optical properties. The high flexibility of the synthesis processes allows one to obtain NCs with different shapes and with energy band gaps ranging from the mid-infrared to the UV depending on both the elemental composition and the size of the particles. Moreover, the very high photoluminescence (PL) quantum efficiencies close to unity achieved at room temperature make NCs ideal candidates to improve the performance of light emitting devices. Therefore, NCs have been used to increase the efficiency of plastic light emitting diodes and to obtain single photon sources operating at room temperature. In addition, the operation of NC-based laser devices such as distributed feedback- and micro-ring lasers has been demonstrated. Recently, NCs have not only been used to realize spherical resonators with tremendously high quality factors but also to achieve ultra-low threshold continuous wave lasing at room temperature. While the emission of single NCs, films of NCs and spherical resonators is evenly distributed over all directions in space, in the present work we investigated microcavity light emitting devices, giving strongly directional emission from NCs in continuous wave operation mode. The microcavity devices contain as active material either CdSe NCs for operation in the visible at wavelengths around the damping minimum in plastic optical fibers or HgTe NCs with a strong emission in the telecommunication wavelength range.

Design and Fabrication

In the microcavity structures either CdSe or HgTe NCs are placed between a Bragg interference mirror and a metallic mirror. The devices were designed by transfer matrix calculations using the optical constants of the individual layer materials, determined by transmission spectroscopy of single reference layers.

Primarily, for the HgTe based microcavity devices (MC-HT), dielectric Bragg interference mirrors consisting of five pairs of TiO_2 and SiO_2 layers with a thickness of a quarter of the design wavelength of 1540 nm were deposited on a glass substrate by ion assisted electron beam evaporation. This results in mirror reflectivities of 95.5% in the center of the stop band. On top of the reflector ending up with a SiO_2 Bragg layer, a densely packed film of HgTe NCs was deposited by the layer-by-layer assembly method. A sequence of 20 bilayers of poly(diallyldimethylammonium chloride) and HgTe NCs results in a smooth and closely packed film with a thickness of 50 nm. The NC-film was covered by a spacer layer of SiO_2 to achieve (a) the desired cavity length for a single resonance right at the center of the Bragg mirror stop band as well as (b) a small refractive index at the interface to the metallic mirror on top of the structures to obtain a high overall reflectivity. The thickness of the spacer layer is varied to tune the wavelength of the cavity resonance. On top of the structures a 200 nm thick silver mirror was deposited by DC magnetron sputtering.

For the CdSe based devices (MC-CS), Bragg mirrors also consisting of five pairs of TiO_2 and SiO_2 layers but designed for a wavelength of 650 nm were deposited on a 22 microns thick, freshly cleaved sheet of pristine mica, whose surfaces are parallel to each other. On the other side of the mica substrate a film of CdSe NCs acting as the optical active material in our devices was deposited and covered by PMMA to protect them during deposition of the metallic top mirror.

Results

All devices were characterized by reflectivity measurements clearly showing a broad Bragg mirror stop band with a maximum reflectivity at the stop band center of 95.5% in perfect agreement with the expected value from our design simulations.

For the MC-HT devices a SiO_2 spacer layer thickness of 170 nm results in single resonator mode right at the center of the Bragg mirror stop band at 1540 nm with a full width at half maximum (FWHM) of only 19.5 meV. By increasing the spacer layer thickness and thus the cavity length, the resonance can be deliberately detuned to lower photon energies [1].

In contrast to that, more than 30 narrow modes are found within the stop band around 650 nm in the MC-CS devices due to the mica sheet thickness of 22 microns [2]. Each resonator mode consists of a double peak structure with a width of 8.5 meV and a spacing of 5.8 meV whose energy splitting is found to scale with the thickness of the mica sheets [2], [3], indicating that it is solely caused by the birefringent properties of the used mica sheets.

For PL experiments, the samples were optically excited by commercially available laser diodes in cw operation mode at wavelengths of 980 and 532 nm at room temperature. For the MC-HT devices a single peak is found, with a FWHM close to 20 meV, which is about eight times smaller than the emission of a NC reference sample (Fig. 1 (a) (solid curves)). The peak energy coincides with the resonance energy deduced from the reflectivity experiments, clearly evidencing that the NC emission couples to the microcavity mode. By increasing the cavity length from 170 nm to 220, 270 and 320 nm SiO_2 spacer layer thickness, the emission of the microcavity can be spectrally tuned over a large range of nearly 90 meV towards lower energies, as shown in Fig. 1 (a).

Decreasing the cavity length results in the same tuning range but towards higher energies (not shown here). Thus, the microcavity emission can be tuned over a total range of 177 meV (1400-1750 nm), only limited by the width of the NC PL (Fig. 1 (a) (dashed curve)) which is comparable to that of the Bragg mirror stop band. Furthermore, temperature dependent PL experiments reveal only a moderate decrease of the device emission, so that at 75 °C still one third of the intensity at 25 °C is observed [1]. This decrease is solely caused by an increase of nonradiative recombination and not by

decomposition of the NCs, because after cycling the temperature several times up and down the same PL intensities are obtained.

The PL spectrum of a MC-CS device is presented in Fig. 1 (b) (solid curve) together with that of a NC reference layer (dashed curve). Obviously, the envelope of the device emission matches well to that of the reference layer, both exhibiting its maximum around 1.9 eV (650 nm).
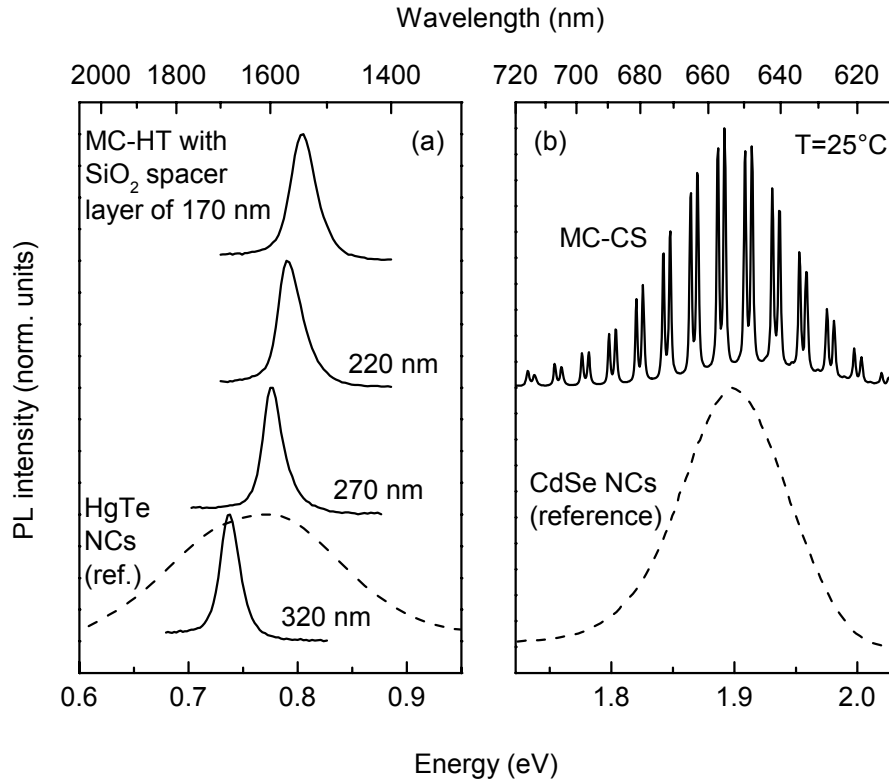
Fig. 1: Room temperature PL spectra of (a) four HgTe based devices (MC-HT) with different cavity lengths (SiO$_2$ spacer layer thicknesses of 170, 220, 270 and 320 nm, respectively) and (b) a CdSe based device (MC-CS) with a cavity length of approximately 22 microns. For clarity the spectra are shifted in vertical direction with respect to each other. In (a) as well as in (b) the PL spectrum of a NC reference layer is shown as a dashed curve.

The device spectrum, however, shows 30 pronounced resonator modes with a spacing of only 19 meV and a width of each double peak of 8.5 meV so that almost 50 % of the NC PL spectrum is covered by the modes. Therefore, a large fraction of the NC PL is extracted from the device.

As a final point we discuss the angular dependence of the spontaneous emission which was determined in the same way as described in Ref. [2]. As depicted in Fig. 2, the experimental angular dependence can be well fitted by a Gaussian function with a half width at half maximum of 0.65° for the MC-CS device (MC-HT devices show similar results). For emission angles of only 2° off from the surface normal (see sketch in the inset), the emission intensities essentially drop to zero. Therefore, the narrow forward directed emission in combination with the symmetric beam profile and the narrow spectral width, resulting from the geometry of our cavities, is very promising for future applications of such devices.
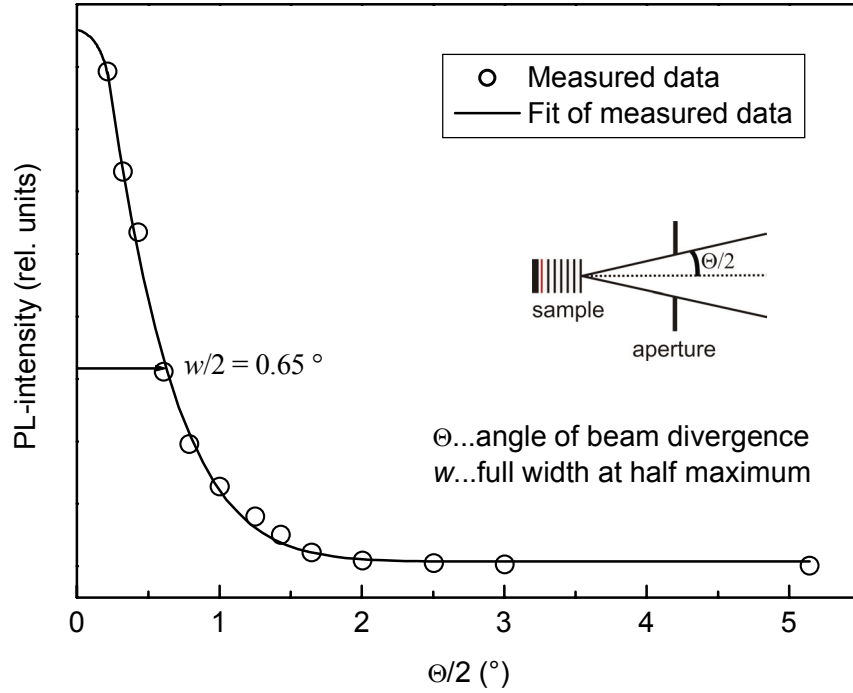
Fig. 2: PL intensity in dependence of half-angle of divergence. Measured data is represented by circles and the fit of measured data by a solid curve. This Gauss distribution results in a total beam divergence of 1.3°.

Conclusion

In conclusion, we have demonstrated microcavity light emitting devices containing either CdSe NCs for operation in the visible at wavelengths around the damping minimum in plastic optical fibers or HgTe NCs with a strong emission in the telecommunication wavelength range. The CdSe based devices show emission from several resonances around 650 nm, with a small mode spacing, solely caused by the large cavity length of 22 microns. This allows one to extract a large fraction of the nanocrystal luminescence from the cavity. In contrast, the optical distance between the mirrors of the HgTe based devices is reduced to obtain a single resonance at the Bragg mirror stop band center. By varying the length of the microcavity, the resonator mode can be well tuned within the Bragg mirror stop band. Since the width of the NC PL is almost as large as the width of the stop band, also the microcavity emission can be tuned between 1.4 and 1.75 microns. This easily enables the adaptation of our devices to applications demanding a certain emission wavelength. Furthermore, the microcavity emission is strongly forward directed and a beam divergence of only 1.3° is demonstrated. Due to the simple and cost effective fabrication of the microcavity devices combined with their favorable optical emission properties with excellent stability also above room temperature, such devices might be attractive alternatives to currently available commercial laser diodes operating in this spectral range. For this electrical excitation is envisaged in the near future.

Acknowledgements

References

[1]   J. Roither, M. V. Kovalenko, S. Pichler, T. Schwarzl and W. Heiss, "Nanocrystal based microcavity light emitting devices operating in the telecommunication wavelength range" submitted to Appl. Phys. Lett.

[2]   J. Roither, D. V. Talapin, N. Gaponik, A. Eychmuller and W. Heiss, "Highly directional emission from colloidally synthesized nanocrystals in vertical cavities with small mode spacing" Appl. Phys. Lett. 84, 2004, 2223 – 2225

[3]   J. Roither, D. V. Talapin, N. Gaponik, A. Eychmuller and W. Heiss, "Colloidally synthesized semiconductor nanocrystals in resonant cavity light emitting devices" Electronics Lett. 38, 2002, 1373 – 1374

Surface-Emitting Single-Mode Quantum Cascade Lasers

M. Austerer, C. Pflügl, W. Schrenk, S. Golka, G. Strasser

Zentrum für Mikro- und Nanostrukturen, Technische Universität Wien, Floragasse 7, A-1040 Wien

We present high power surface-emitting single mode GaAs-based quantum cascade lasers (QCLs) in the mid-infrared. By using an air-AlGaAs waveguide combined with second-order distributed feedback processing, we obtained optical output via the surface above 3W. Surface-normal dual-lobe light emission exceeds the emission from one as-cleaved facet by a factor of six.

Introduction

Significant improvements during the last decade made quantum cascade lasers [1] (QCLs) interesting for many applications, where coherent light emitters in the mid- and far-infrared are required. An important step for the use of these devices was the achievement of single mode emission. This was first demonstrated by processing the lasers as first order distributed feedback (DFB) lasers, where a grating which is imposed on top of the laser selects a single mode within the gain spectrum of the device [2], [3]. Recently, tunable single mode emission was also achieved by grating-coupled external cavity QCLs [4].
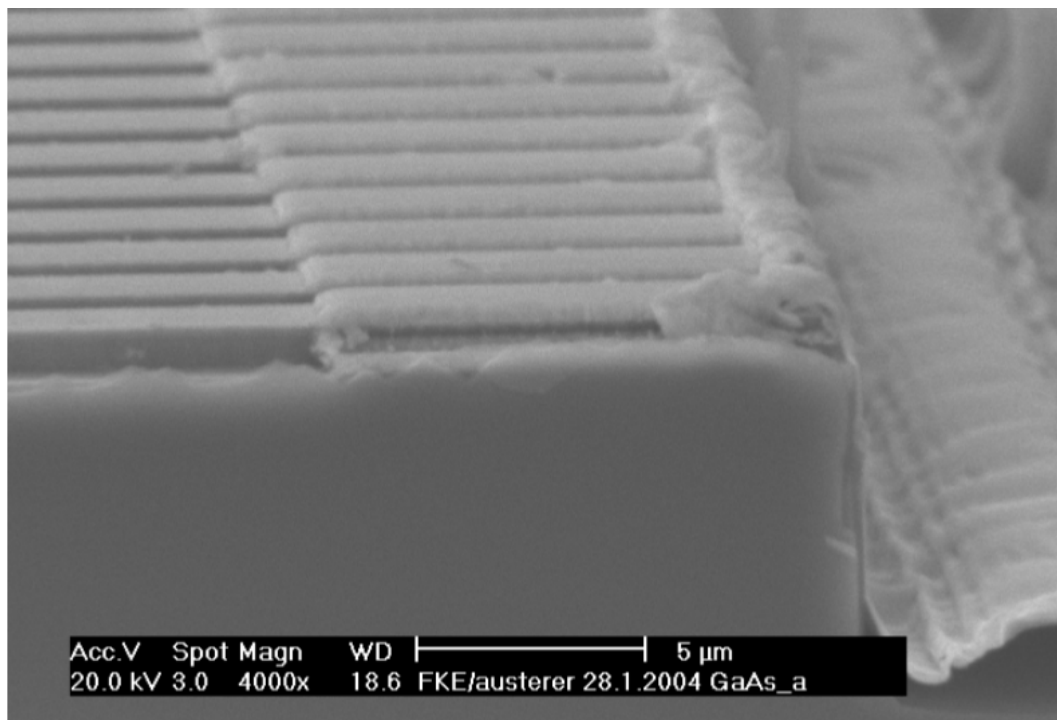

Fig. 1: REM image of the processed DFB laser ridges.

QCLs are based on intersubband transitions. Selection rules for transitions in quantum wells allow gain only for TM polarized electromagnetic waves. Therefore conventional vertical cavity surface emitting laser design is not suitable for QCLs. If one wants to exploit the advantages of surface normal emission another approach must be taken. One successful way to achieve surface emission is to use two-dimensional photonic crystals [5]. We have chosen a distributed feedback design where the feedback is given through a second-order Bragg grating etched into the surface of the laser ridge. Such surface emitting QCLs have been realized both in the InGaAs/InAlAs/InP and also in the GaAs/AlGaAs material system [6], [7]. Appropriate etch depths, a low loss top air cladding and metallization of the grating peaks only, lead to high power surface emission. Surface emitting QCLs have the big advantage that the radiation field could be increased significantly and the beam divergence is reduced.

Design and Characterization

The laser material is grown by molecular beam epitaxy on (100) GaAs substrates. The gain media is embedded in the most cases in a double plasmon enhanced waveguide. Such a waveguide consists of ~1 μm thick highly doped cladding layers ($~4 \times 10^{18}$ cm^{-3}), and ~3.5 μm thick low doped spacer layers ($~4 \times 10^{16}$ cm^{-3}). The highly doped layers are used for light confinement and the spacer layers reduce the penetration of the guided mode into the cladding layers as they show huge free carrier absorption. A surface plasmon waveguide is usually used for long wavelength material ($\lambda > 20$ μm) because of the reduced thickness, which is important for MBE growth.

Different cavity types such as Fabry Perot (FP), distributed feedback (DFB), and cylinder lasers were fabricated. Reactive ion etching was used for directional etching to obtain vertical etch profiles (Fig. 1). SiN is used for insulation and the extended contacts are sputtered. The grating for the DFB lasers was etched into the surface of the top cladding layer and covered with metal. The light is confined by total internal reflection in the case of cylinder shaped lasers. The lasers were soldered with In on Cu plates and wire bonded.

Our laser material is grown by solid source molecular beam epitaxy on n-doped GaAs (Si, 2×10^{18} cm^{-3}. The active region consists of 40 cascades of a GaAs/Al$_{0.45}$Ga$_{0.55}$As three well design [8]. As a waveguide we have chosen an air/AlGaAs cladding in order to reduce absorption losses compared with a typical double-plasmon waveguide. Our calculations yield a waveguide loss coefficient of $\alpha = 3.8$ cm^{-1}, whereas the structure with a double-plasmon waveguide has α-values of 12 cm^{-1}. The significant reduction of the losses was investigated by comparing the threshold current density of this device with a device (both fabricated as Fabry-Perot lasers) with the same active region but a double plasmon waveguide. The threshold was reduced from 4.1 kA/cm^2 to 2.7 kA/cm^2 at 78 K and from 11.8 kA/cm^2 to 7.8 kA/cm^2 at 240 K, whereas we have comparable output powers and emission spectra. A reduction of the threshold current is favorable concerning the strong self-heating due to the applied current of electrically pumped lasers. In the case of 2nd order DFB lasers a low loss top waveguide is particularly important because the light is coupled out via the surface.

Taking the waveguide structure and the desired wavelength of 8.9 microns into account, a suitable grating period ($\Lambda = 2.8$ μm), duty cycle ($\sigma = 0.5$) and grating depth (1.1 μm) were calculated. The grating was exposed on top of the MBE grown material by means of optical lithography and reactive ion etching (RIE) (see Fig.1). The grating peaks were covered with a metal to provide a homogenous lateral current distribution even for wide ridges. Then the ridges (30 to 70 μm) were defined also by RIE (depth 10 μm). The metal on the grating peaks is actually contacted by side contacts with an overlap of about 8 μm on both sides, resulting in a width of the surface emission window w_{wind} between $w_{wind} = 14$ μm (w = 30 μm) and $w_{wind} = 54$ μm (w = 70 μm). The extended contacts are insulated with SiN. The cleaved laser facets are left uncoated and

the laser bars are mounted epilayer up on a temperature controlled cold finger in a flow cryostat.
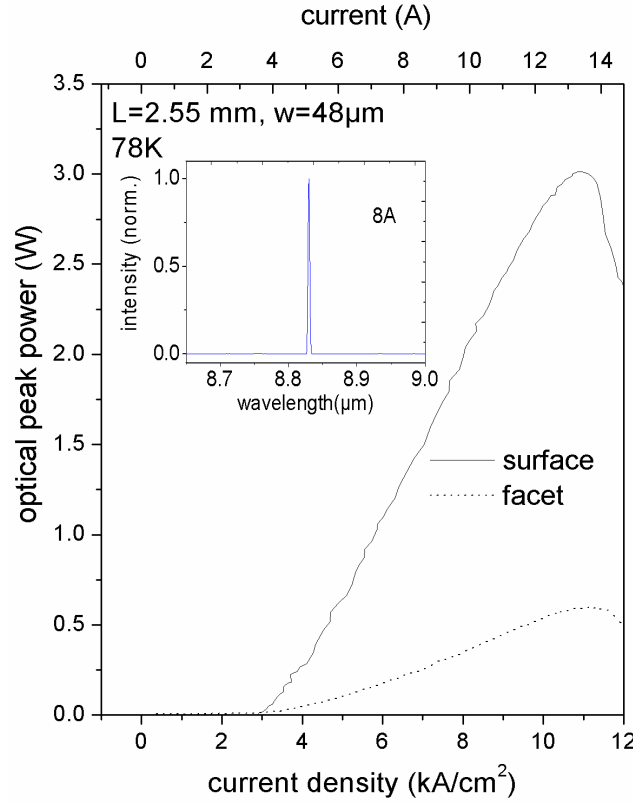
Fig. 2: Absolute light output power versus bias current density for a 2.55 mm long laser at 78 K. The inset shows the spectrum for an applied current of 8 A.

The laser ridges were cleaved to different lengths in order to investigate the critical DFB coupling length. Lasers that are shorter than 1.4 mm, thus having a product of DFB coupling coefficient $\kappa = 7$ cm^{-1} and length (cm) smaller than one, do not experience sufficient feedback from the surface grating and are showing typical Fabry-Perot modes. The samples were mounted substrate-down on a turnable cold finger and operated under pulsed bias (100 ns, 5 kHz) at 78 K. By turning the cold finger we could observe both edge and surface emission.

The far field of such lasers exhibits an asymmetric dual lobe pattern, because the near field close to the emitting surface also includes interference terms. An in-detail investigation shows that the relative position of the grating and the end mirrors determines the ratio of the two lobe intensities [9]. The single mode emission wavelength is continuously tunable by the heat sink temperature.

In Fig. 2 absolute light output power versus bias current density for a 2.55 mm long laser is plotted. Single mode emission is observed for all bias currents above threshold (inset of Fig. 2). Light power was measured using a calibrated thermopile detector. We obtained peak output power at 78 K above 3 W via the surface. In the case of edge emission an f/1 AR-coated ZnSe lens was used to collect the light from the highly divergent beam. In both cases the light power was focused onto the thermopile detector by means of a gold coated off-axis parabola. The ratio between surface emission and single-facet emission is determined to be six for this device.
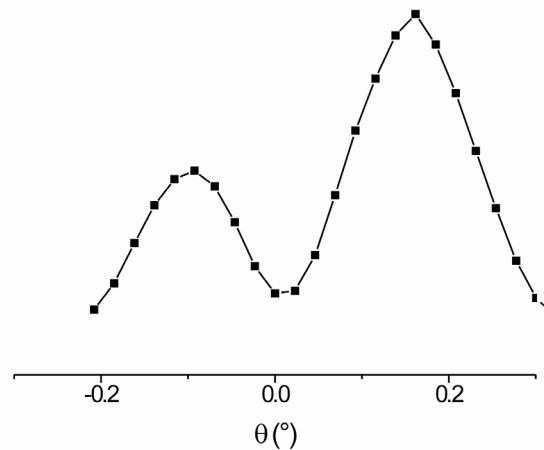
Fig. 3:   Far field distribution of the laser emission.

The far field distribution (Fig. 3) of the laser emission was measured using a 1 mm x 1 mm sensitive area liquid-nitrogen cooled HgCdTe detector at a distance of 124 cm away from the laser chip. Lateral resolution of 1 mm results in an angular resolution of 0.046°. The two beam lobes are separated by 0.25° and have an FWHM beam divergence of 0.2° in laser ridge parallel direction. Beam divergence in ridge normal direction is determined by the ridge width, here FWHM beam divergences are in the range of 10° to 20°.

Conclusions

We have shown the high-power capabilities of surface emitting DFB quantum cascade lasers. Single lobe emission surface emission of second order DFB QCLs is proposed by introducing a phase shift into the surface grating. Such low divergence emission pattern would further improve practical usability. In contrary to facet emitters, for many applications no collimating lens would be necessary.

Acknowledgements

References

[1]   J. Faist, F. Capasso, D. L. Sivco, C. Sirtori, A. L. Hutchinson and A. Y. Cho, Science 264, 553 (1994)

[2]   J. Faist, C. Gmachl, F. Capasso, C. Sirtori, D. L. Sivco, J. N. Baillargeon, A. Y. Cho, Appl. Phys. Lett. 70, 2670 (1997)

[3]   W. Schrenk, N. Finger, S. Gianordoli, L. Hvozdara, G. Strasser, E. Gornik, Appl. Phys. Lett. 76, 253 (2000)

[4]   R. Maulini, M. Beck, J. Faist, and E. Gini, Appl. Phys. Lett. 84, 1659 (2004)

[5]   R. Colombelli, K. Srinivasan, M. Troccoli, O. Painter, C. F. Gmachl, D. M. Tennant, A. M. Sergent, D. L. Sivco, A. Y. Cho, F. Capasso, Science 302, 1374 (2003)

[6]   D. Hofstetter, J. Faist, M. Beck, U. Oesterle, Appl. Phys. Lett. 75, 3769 (1999)

[7]   W. Schrenk, N. Finger, S. Gianordoli, L. Hvozdara, G. Strasser, E. Gornik, Appl. Phys. Lett. 77, 2086 (2000)

[8]   H. Page, C. Becker, A. Robertson, G. Glastre, V. Ortiz, and C. Sirtori Appl. Phys. Lett. 78, 3529 (2001)

[9]   H. Kogelnik, C. V. Shank, J. Appl. Phys. 43, 2327 (1972)

Photonic Crystals (Posters)

UV-Nanoimprinting –
A Potential Method for the Fabrication of
3D-Photonic Crystals

T. Glinsner, F. Isfahani, K. Hingerl

Institute of Semiconductor and Solid State Physics
Johannes Kepler University, A-4040 Linz, Austria

This contribution presents results achieved in ultraviolet nanoimprint lithography (UV-NIL) recommending this process as a potential fabrication method for photonic crystals.

In photonic crystals the periodic arrangement of two materials with dissimilar dielectric properties exhibits a band of forbidden frequencies for the propagation of light (photonic band gap). Several techniques for the fabrication of 3D photonic crystals were proposed. Among them can be found wafer bonding, silicon micromachining, self-assembly, two-photon absorption, 3D holography as well as subsequent sputtering, DUV lithography and etching of consecutive planes.

UV-NIL offers a low cost opportunity for the fabrication of nm-scale pattern transfer in single or multiple step application if compared to mainstream optical lithography. In UV-NIL processes, soft (PDMS) or hard stamps (quartz glass) are used to imprint features into a UV-curable low viscosity material at room temperature. The Industrial Technology Roadmap for Semiconductors (ITRS) calls for nanoimprint lithography to be employed for the 32 nm node, which may be reached in 2010. This next generation lithography technique is using quartz glass stamps, fabricated by e-beam lithography and subsequent dry etching techniques, which can be repeatedly imprinted in spin-on material layers on silicon substrates.

A concept for the fabrication of the woodpile structure will be demonstrated as well as achieved results. The woodpile structure consists of aligned rods where every subsequent layer is rotated 90° above the former layer so that the fifth layer is exactly above the first one and the piles of the third shall be located exactly between the piles of the first row.

Polarization Splitting Based on Planar Photonic Crystals

V. Rinnerbauer[1,2], J. Schermer[2], and K. Hingerl[1]

[1]Christian Doppler Labor für oberflächenoptische Methoden, Johannes-Kepler-Universität Linz, A-4040 Linz

[2]Photeon Technologies, A-6900 Bregenz

Planar polarization splitting devices based on photonic crystal slabs have been developed, their main advantages being the planar design and their possible integration into PLCs. Three different principles are demonstrated and results from numerical simulations shown.

Introduction

The use of polarization multiplexing to double the existing fiber capacity has been demonstrated successfully in a recent field trial on an installed DWDM metropolitan area network in Berlin, Germany [1]. Together with the growing number of polarization preserving devices, in particular photonic crystal (PhC) devices, this experiment shows us the importance of effective polarization demultiplexers.

Due to their inherent polarization sensitivity, photonic crystals offer convenient solutions on a length scale of several tens of micrometers in silicon-based or other high index material systems. In a 2D photonic crystal slab, the presence of a horizontal symmetry plane allows us to decompose the guided modes into TE-like and TM-like polarization states, which are even and odd with respect to reflections through this plane [2]. In this paper, we will show three different principles that exploit the polarization dependency of these guided modes.

Polarization Splitter Design

Reflection at a Photonic Crystal Interface

At the interface of a photonic crystal, an impinging wave is either transmitted or reflected, depending on whether there are allowed states for its frequency. The absence of allowed states can result either from a bandgap for this frequency, or else for symmetry reasons, which prohibit the excitation of the photonic crystal modes. Therefore reflection and transmission depend on the photonic crystal structure and the wavelength, the polarization and the incident angle of the impinging wave.

For this polarization splitter we have designed a photonic crystal structure that reflects one polarization while transmitting the other. The reflection and transmission spectra of a photonic crystal have been calculated using a plane wave expansion technique [3] based on a method proposed by K. Sakoda [4]. The results for a hexagonal lattice with 16 rows of air holes in silicon with a radius to period ratio $r/a = 0.29$ are shown in Fig. 1.

The effective refractive index of the silicon background was set to $n_{eff} = 2.76$, which corresponds to a slab height h of $h/a = 0.6$. This effective index was derived using the scaling laws, preserving the position of the bandgap for the transition from 2D to 3D

cases. The angle of incidence in this example is 10 degrees. It can be seen that for these parameters there are frequency regions where one polarization is transmitted but the other is reflected. We use the parameter $\omega a/2\pi c = 0.293$. In Fig. 1 this parameter, whereby the power reflection is 0.990 for TE and the power transmission for TM is 0.998, is indicated by an arrow. The plane wave calculations were performed with 5 plane waves (n) parallel to the interface and 50 plane waves (m) perpendicular to it [notation of 4]. The results have been verified with 2D and 3D FDTD simulations of PhC slabs.
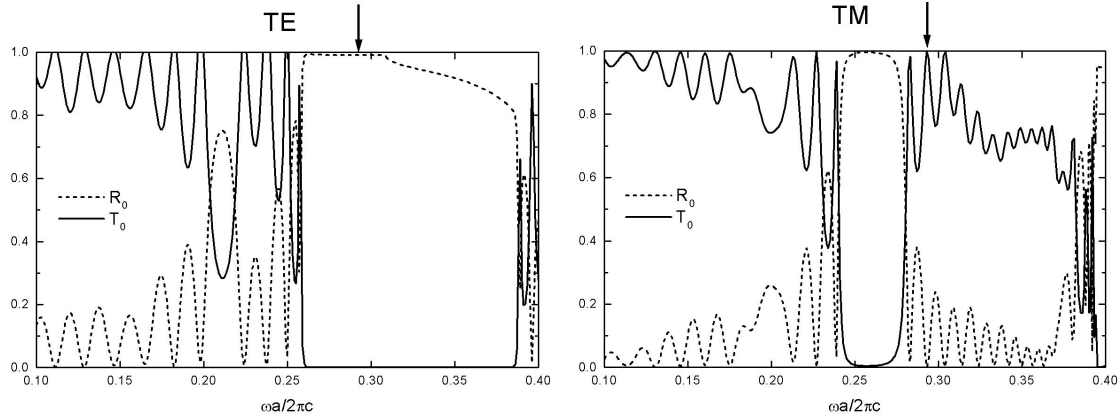
Fig. 1:   Reflection at and transmission through a photonic crystal for TE (left) and TM polarization (right) as a function of normalized frequency
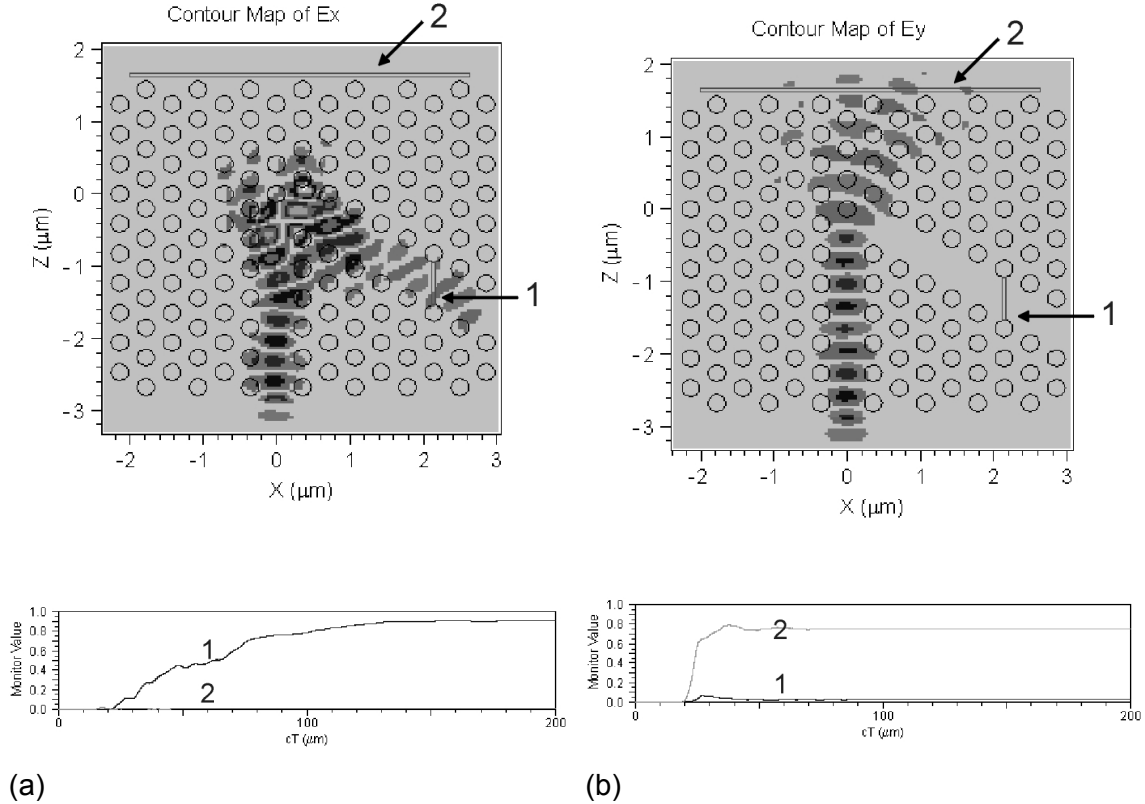
Fig. 2:   FDTD simulation of a PhC bend for (a) TE and (b) TM polarization

Guided Modes and Free Propagation

In this example, a defect waveguide is introduced into a photonic crystal structure exhibiting a bandgap for TE polarization only. Because the bandgap prohibits propagation in the bulk, a bend in this photonic crystal waveguide redirects TE light with frequencies in the bandgap. However, the other polarization is not guided around the bend by the defect waveguide, and continues propagating straight through the crystal.

Once again, a hexagonal lattice of air holes in silicon with r/a = 0.29 is used. The period a is 415 nm and the height of the slab is 320 nm. This lattice has a bandgap for TE polarization for normalized frequencies of about 0.24 ≤ ωa/2πc ≤ 0.31.

The results of 3D FDTD simulations with a wavelength of 1.55 μm for such a structure are shown in Fig. 2. The time evolution of power is monitored at positions 1, 2 and the results shown below the picture of the field are a measure of the output power at the waveguide output on the right (position 1, dark gray) and at the top edge of the photonic crystal (position 2, light gray). The power output for TE polarization is about 90% (insertion loss of 0.45 dB), and 75% (1.25 dB) for TM.

The geometry of the bend was then optimized to obtain maximum output for both polarizations for a broad bandwidth. Simulations of the optimized bend show an output power of 93% (insertion loss of 0.3dB) for both polarizations at 1.55 mm, with a crosstalk below 16 dB for TM and below 24 dB for TE. The non-uniformity in the C-band is less than 0.5 dB for both polarizations.

Polarization-dependent defect modes

In this case the polarizations are separated at a Y branch in a photonic crystal connecting three defect waveguides with polarization-dependent modes. The defect modes of the photonic crystal waveguides are designed in such a way that each output waveguide of the Y-branch supports only one polarization whilst the input waveguide supports both.
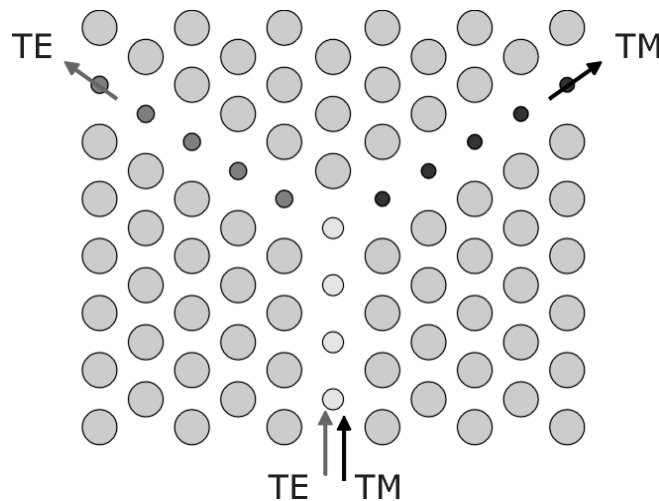
Fig. 3: Y-branch structure with polarization-dependent defect modes in the branches

In a 2D example we use a hexagonal lattice of air holes in silicon with r/a = 0.45. The lattice exhibits a bandgap for both polarizations for normalized frequencies of about 0.41 ≤ ωa/2πc ≤ 0.45.

Line defect waveguides are formed in this lattice by reducing the radius of the holes in one row. The input waveguide has a defect radius r/a = 0.33, which supports modes of

both polarizations in the bandgap, whereas one output waveguide with a defect radius of r/a = 0. 2365 supports only TE modes (Fig. 4 (a)) in a frequency region of about $0.430 \leq \omega a/2\pi c \leq 0.434$, and the other output waveguide with r/a = 0.1925 supports only TM modes in this frequency region (Fig. 4 (b)).

(a)   (b)
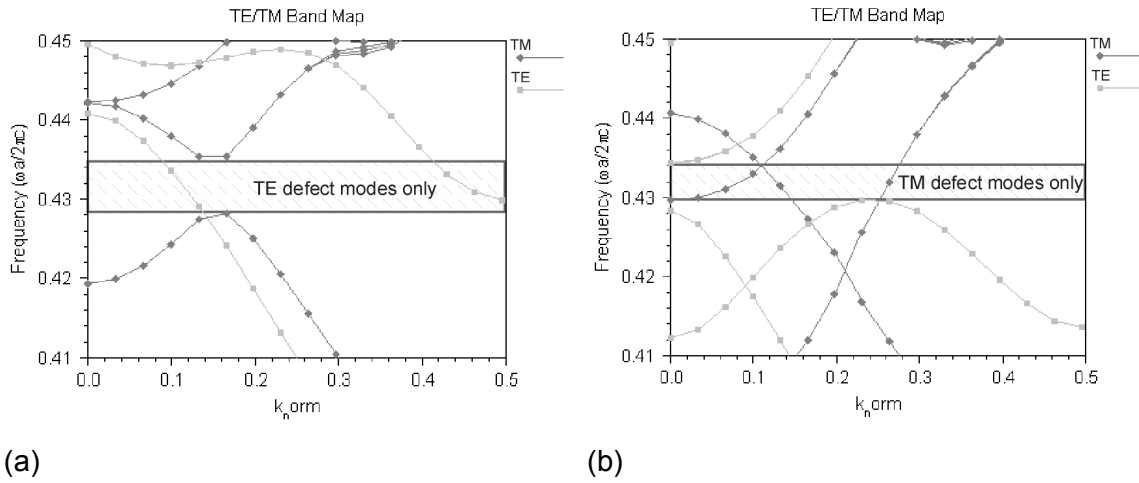
Fig. 3: Defect bands for (a) r/a = 0. 2365 and (b) r/a = 0.1925, parameters as explained in the text

In this example, the design of the Y-branch junction is of crucial importance for good transmission.

Conclusion

We have demonstrated three different designs of polarization splitting devices in photonic crystal slabs, exploiting the inherent polarization sensitivity of 2D photonic crystal slabs. The main advantages of all designs are the planar geometry and the ability to be integrated into PLCs with high integration density.

References

[1] N.E.Hecker-Denschlag, W. Schairer, W. Fischler, A. Richter, T. Auernhammer, B. Lankl: "Polarization multiplexing in a remotely-configureable photonic network", ECOC 2002, Vol.3, 6.4.5

[2] S.G. Johnson, Shanhui-Fan, P.R. Villeneuve, J.D. Joannopoulos, L.A. Kolodziejski: "Guided modes in photonic crystal slabs", Phys. Rev. B, Vol. 60(8), 1999, pp 5751-8

[3] K. Hingerl, L. Mao, V. Holy,V. Rinnerbauer, J. Schermer: "Reflection and Transmission of Finite 2D Photonic Crystals", ECOC 2003, Vol.3, pp 672-3

[4] K. Sakoda: "Optical Properties of Photonic Crystals", Springer, Berlin 2001, Chapter 4

Spintronics (Posters)

Electronic and Magnetic Properties of GaN:Fe

A. Bonanni [1], H. Przybylinska [1,2], A. Wolos [1], C. Simbrunner [1], H. Sitter [1],
W. Jantsch [1], M. Kiecana [2], M. Sawicki [2], T. Dietl [2],
P. Granitzer [3], K. Rumpf [3], and H. Krenn [3]

[1] Institut für Halbleiter- und Festkörperphysik, Johannes Kepler Universität, Linz, Austria

[2] Institute of Physics, Polish Academy of Sciences, Warsaw, Poland

[3] Karl Franzens Universität, Graz, Austria

Here we report on metal-organic chemical vapor deposition growth of GaN:Fe and its characterization by means of high-resolution X-ray diffraction, secondary ion mass spectroscopy, photoluminescence, electron spin resonance, and magnetization measurements. Both electron spin resonance and photoluminescence demonstrate the existence of Fe in the isolated $3d^5$ (Fe^{3+}) state. The magnetization measurements show, apart from Curie paramagnetism due to Fe^{3+}, a temperature independent contribution which we attribute tentatively to van Vleck paramagnetism of Fe in the 2+ state. We conclude that the Fe ions coexist in two charge states in the investigated samples. The fraction of Fe^{3+} ions was found to increase upon additional co-doping with Mg acceptors, both in ESR as well as in magnetization. In the latter one a significant reduction of the temperature independent magnetic moment was simultaneously observed. High field magnetization data yield Fe concentration in the $x \approx 10^{-3}$ range, which compares well with secondary ion mass spectroscopy results.

Introduction

Transition metal doped GaN is one of the predicted candidates for obtaining Zener-type ferromagnetism with $T_c > 300K$. As a necessary condition, the transition metal ion should be incorporated on isolated (*i.e.* not clustered) substitutional sites and exhibit a high-spin ground state. So far, the Mn dopant in GaN has been investigated thoroughly, as it was expected to act as an acceptor providing besides the S = 5/2 spin also the high hole concentration necessary to mediate the exchange coupling among the Mn ions. More recently it has been shown, however, that unlike Mn in GaAs the 3+/2+ acceptor level of Mn in GaN is deep (>1.7 eV above the valence band edge) and the hole is localized on Mn, leaving it in the $3d^4$ state. Hence, Zener magnetism is not expected for the GaN:Mn system. In this respect the GaN:Fe seems to be more promising, especially with p-type co-doping.

Experimental

Sample Preparation

All samples have been fabricated in an AIXTRON 200RF horizontal tube metal-organic chemical vapor deposition (MOCVD) reactor. The growth of the device quality layers was carried out on c-plane sapphire substrates by using TMGa, NH, Cp Fe, Cp Mg and SiH as precursors and H as carrier gas. The deposition process has been performed according to a well established procedure consisting of substrate nitridation, low temperature (540 °C) GaN nucleation layer growth, annealing of the nucleation layer under

NH leading to re-crystallization and GaN buffer growth (1 µm). On top, iron doped GaN layers (1 µm) were grown at different temperatures (800 – 1050°C) and Cp_2Fe fluxes (50 – 200 scams).

Measurements

Crystal Quality

High-resolution x-ray diffraction measurements were performed routinely on the grown samples. Rocking curves showed a full width at half maximum (FWHM) of the order of 260 up to 320 deg, which is comparable to the state-of-the-art device material. Increasing the iron flux resulted in a broadening of the GaN (0002) reflex.
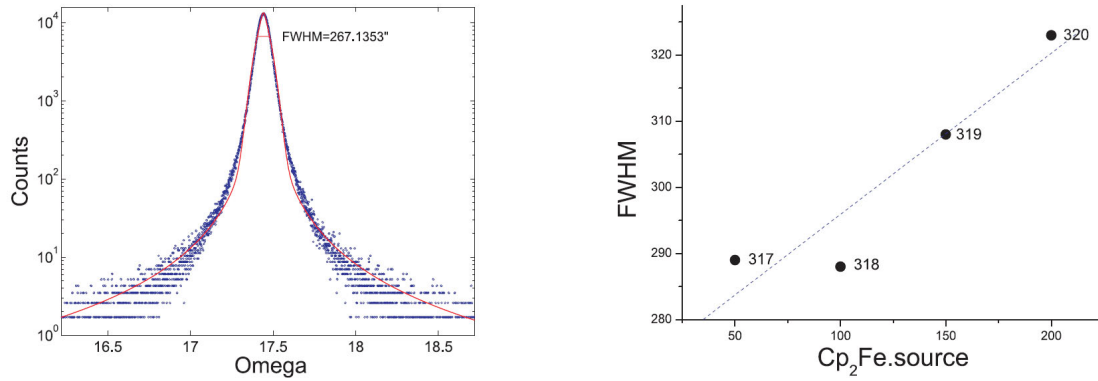
Fig. 1: Rocking curve of the GaN (0002) reflex measured for GaN:Fe epilayers (left panel) and the FWHM as a function of Fe flux (Cp_2Fe) (right panel).
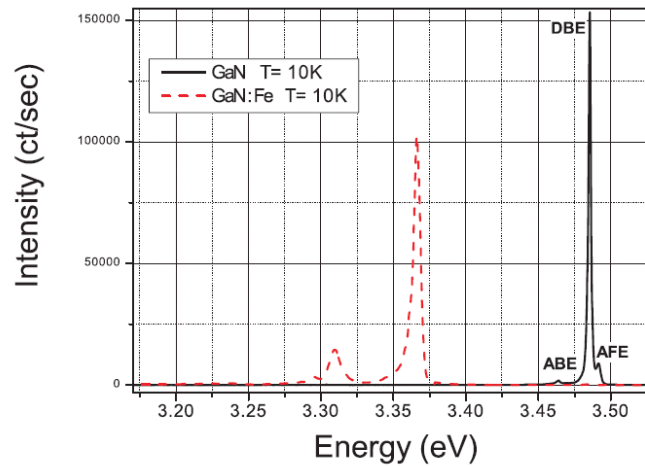
Fig. 2: Photoluminescence spectra of GaN and GaN:Fe samples showing excitonic transitions: AFE, DBE, ABE, as well as unidentified lines due to the Fe dopant.

Photoluminescence Measurements

Figure 2 shows a comparative photoluminescence (PL) study of pure GaN and GaN:Fe. The peaks were identified as an acceptor-free exciton (AFE), a donor bound

exciton (DBE) as well as an acceptor bound exciton (ABE). The DBE may be bound to Si or O, which lead to the unintentional n-type behavior of pure GaN, the ABE may be bound to Mg [1]. The peaks assigned to iron have not been identified so far.

Figure 3 shows an infrared PL band at 1.289 eV, that is assigned to a $^4T_1(G)$ - $^6A_1(S)$ crystal field transition of Fe^{3+} (d^5 configuration) [2]. The strong crystal field is typical for GaN due to its small lattice constant and the high electronegativity of nitrogen.
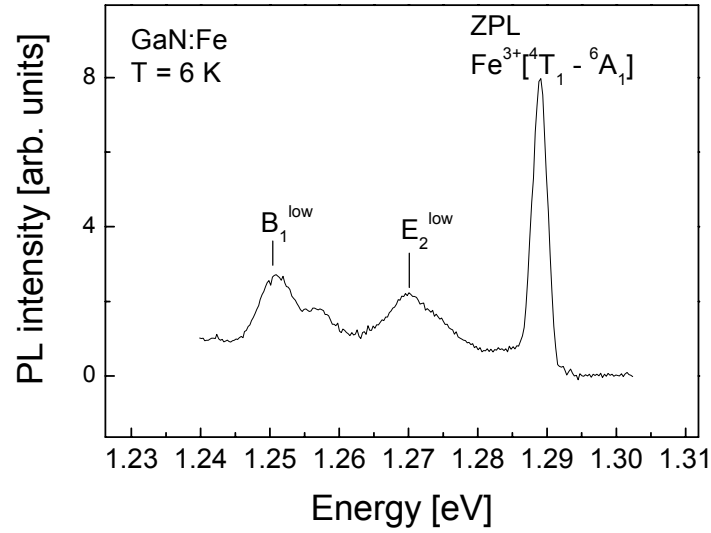
Fig. 3: Photoluminescence spectrum of an intracenter transition $^4T_1(G)$ - $^6A_1(S)$ within $Fe^{3+}(d^5)$ configuration of iron in GaN. The zero-phonon line at 1.289 is accompanied by GaN phonon replicas. E_2^{low} and B_1^{low} GaN phonons are marked.
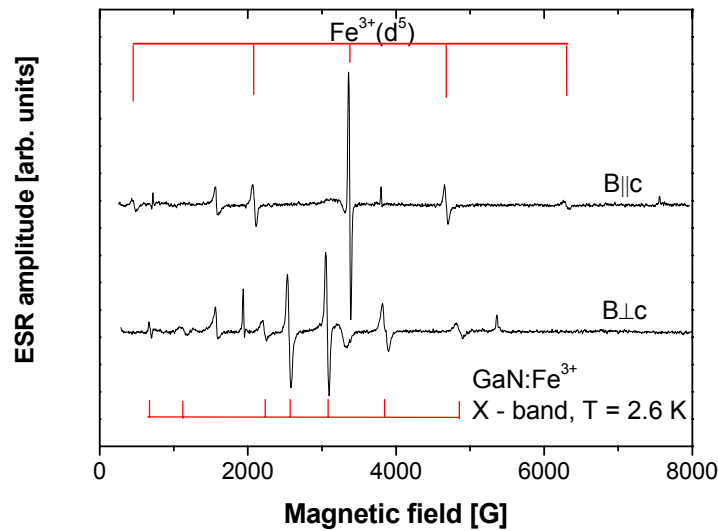
Fig. 4: ESR spectra of $Fe^{3+}(d^5)$ in wurtzite GaN epilayers collected in B || c and B ⊥ c configuration.

Electron Spin Resonance Measurements

Electron spin resonance (ESR) experiments show the presence of $Fe^{3+}(d^5)$ substituting Ga in all studied GaN samples. The examples of ESR spectra collected at the magnetic field parallel or perpendicular to the GaN c-axis are shown in Fig. 4. The amplitude of the ESR signal (proportional to the number of Fe^{3+} centers), increases after co-doping with Mg acceptors. This is the indication of a mixed valence state of the Fe impurity in GaN samples – *i.e.*, the co-existence of the $Fe^{3+}(d^5)$ and most probably the $Fe^{2+}(d^6)$ charge states.

Magnetic Properties

Magnetization measurements of GaN:Fe epilayers were performed by a superconducting quantum interference device magnetometer (SQUID). Figure 5 shows the temperature dependence of the magnetization as obtained from measurements at constant magnetic field on GaN:Fe with different Fe content. In addition to a Curie type of magnetism due to $Fe^{3+}(d^5)$ there is clearly a temperature independent contribution which we attribute to Van-Vleck magnetism, most possibly originating from $Fe^{2+}(d^6)$ configuration of iron. In some of the measured samples an additional ferromagnetic contribution to the magnetization was observed. However, there is no experimental evidence so far that this fraction originates from the homogeneously doped GaFeN layer.
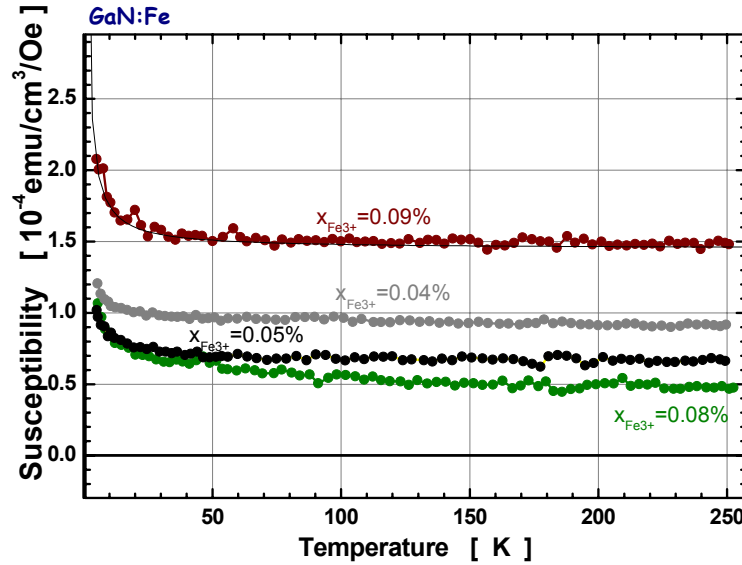
Fig. 5: Susceptibility (M/H) of GaN:Fe as a function of temperature measured at 10000 Oe. The paramagnetic contribution due to Fe^{3+} and the Van Vleck paramagnetism due to Fe^{2+} may be distinguished.

Conclusion

Both ESR and PL demonstrate the existence of Fe in the isolated $3d^5$ (Fe^{3+}) state. The magnetization measurements show, apart from Curie paramagnetism due to Fe^{3+}, a temperature independent contribution which we attribute tentatively to van Vleck paramagnetism of Fe in the 2+ state. The fraction of Fe^{3+} ions was found to increase upon additional co-doping with Mg acceptors, both in ESR as well as in magnetization. In the latter one a significant reduction of the temperature independent magnetic moment was

simultaneously observed. High field SQUID data yield Fe concentration in the $x \cong 10^{-3}$ range, in agreement with SIMS results. A small ferromagnetic contribution to magnetization was also observed, but as far there is no evidence that this fraction originates from homogeneous GaFeN.

References

[1] B. Monemar: "Bound excitons in GaN", J. Phys: Condens. Matter, Vol. 13, 2001, pp. 7011-7026.

[2] R. Heitz, P. Maxim, L. Eckey, P. Thurian, A. Hoffmann, I. Broser, K. Pressel, and B. K. Meyer: "Excited states of Fe^{3+} in GaN", Phys. Rev. B, Vol. 55, 1997, pp. 4382–4387.

High Mobility Si/SiGe Heterostructures for Spintronics Applications

D. Gruber [1], H. Malissa [1], G. Chen [1], D. Pachinger [1], H. Lichtenberger [1], T. Fromherz [1], F. Schäffler [1], G. Bauer [1], W. Jantsch [1], A. M. Tyryshkin [2], and S. A. Lyon [2]

[1] **Institute of Semiconductor and Solid State Physics Johannes Kepler University Linz, A-4040 Linz**

[2] **Department of Electrical Engineering, Princeton University, Princeton, NJ 08544 USA**

We investigate techniques for using Silicon-Germanium as material for solid-state quantum computing. Two topics are presented: First, the use of quantum well structures with different Ge content which can be used to shift the g-factor of conduction band electrons via voltages applied to gates above and below the structure. The change in g-factor allows then to put the electrons in and out of resonance in an Electron Spin Resonance experiment. Second, measurement of spin relaxation times of electrons confined in the strain field above Ge dots in a SiGe heterostructure. Photoluminescence (PL) shows indirect transitions from the VB of the Ge dots to the confined Si CB states. A single line is seen in ESR with $g \approx 2.0000$ during illumination.

Introduction

The Silicon Germanium (SiGe) material system is a promising candidate for solid-state spintronics applications due to its very long spin relaxation times and its compatibility to standard Si process technology. There are proposals (*e.g.* [1]) for spin transistors in the SiGe material system which could be used for Quantum Computing. For this application very long spin coherence times and the ability to control and to read spin orientation is necessary. We address the topic with two different experiments: One is to demonstrate the ability to control the g-factor of electron spins in SiGe Quantum well structures by applying electrical fields, which can be used for selective spin manipulation. The second is the measurement of spin relaxation times of electrons confined in the strain fields above Ge dots in a SiGe matrix.

g-Factor Tuning in SiGe Quantum Wells

Our samples are grown in a Molecular Beam Epitaxy (MBE) system with electron beam evaporators for Si and Ge. The channels are n-type modulation-doped with Sb. High mobilities of up to μ_e = 250,000 cm^2/Vs have been reached in pure Si channels without back gate. The spin lifetimes are extremely long as well: Spin-echo measurements give T_1 = 2.3 µs and T_2 = 3 µs for a magnetic field perpendicular to the 2DEG plane [2]. The high quality of our samples was also shown in recent magneto-transport experiments, where the v = 1/3, 4/7 and 4/9 composite fermion states in the fractional quantum Hall effect were seen for the first time in the SiGe material system [3].The samples are either pure Si wells or double quantum well (QW) structures with a pure Si well and one with 5% Ge, which are separated by a barrier with 15% Ge content. The second structure is designed in a way that by applying electrical fields relative to the quantum wells one can completely shift the electronic wave function from one well to the other as depicted in a self-consistent band structure simulation in Fig. 1. Hand in hand with the change in the surrounding material goes a change in g-factor of the electrons [4] and

hence a change in resonance frequency in an Electron Spin Resonance (ESR) experiment. Spin manipulation via pulsed ESR techniques is then possible on the spins which have been shifted into resonance.
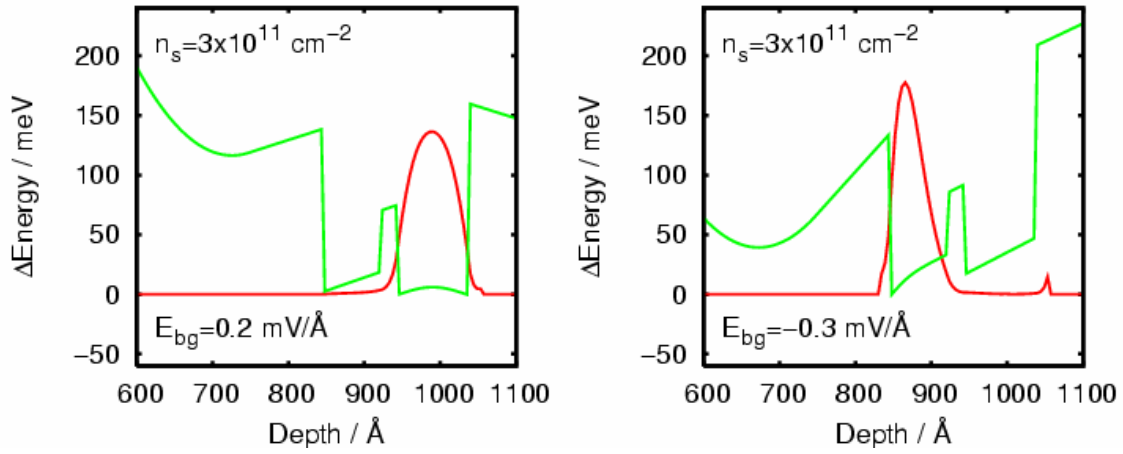
Fig. 1: Self-consistent band structure calculation of the double quantum well structure (as shown above and right) with different applied backgate fields: A front gate was used to keep the carrier concentration at a constant density of n_s = 3×10^{11} cm^{-2}. The calculated change in g-factor can be estimated as Δg = 2.5×10^{-4}, which is enough to separate the resonances and allow spin manipulation.

The required electrical fields are created by applying voltages to a Schottky-type topgate and either a grown-in n-type backgate or an evaporated Al backgate on the backside of the sample. Figure 2 shows how the carrier density and the mobility can be changed in a pure Si channel with Schottky topgate and evaporated Al backgate. Our next goal is the combination of front- and backgate and the double QW structure.
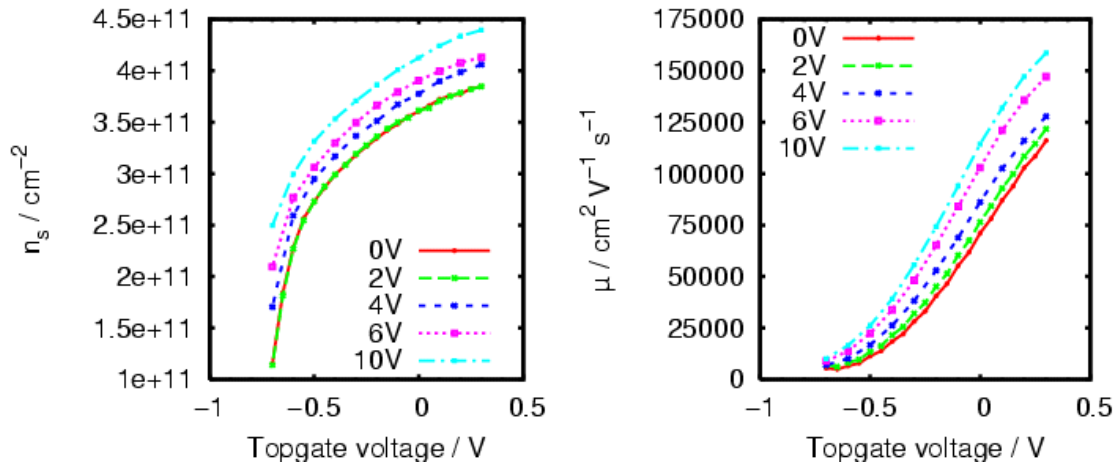
Fig. 2: Carrier density and mobility of a sample with pure Si channel with a Pd Schottky gate on top and an evaporated Al backgate on the back side plotted as a function of the topgate voltage for different backgate voltages. Both mobility and carrier density can be influenced by shifting the wave function away from the interface (higher backgate voltages).

In summary, we report about a SiGe double QW structure designed for tuning the electronic g-factor of electrons. Simulations show that it is possible to completely shift the electronic wave function between two wells with different Ge content and hence the g-factor which is a requirement for quantum computing in SiGe. The process for top- and backgate electrodes is established, and demonstrated on a single Si well sample. The next step will be the combination of double QW structure and front- and backgate.

Spin Relaxation Times in SiGe Islands

In III-V compounds it was shown that the confinement in low dimensional structures such as dots leads to a significant increase of spin lifetimes [5]. In order to achieve confinement in the SiGe material system, we grow Ge islands on Si(100) substrates (i) in a self-organized Stranski-Krastanov growth mode, which leads to an inhomogeneous distribution of island sizes and locations, and (ii) by prepatterning the substrate by either electron beam or holographic lithography. In the first type of samples (i) the density of dots is about 5 times higher than in the prestructured samples (ii), which we estimate from AFM measurements. The Ge dots were overgrown with Si which is locally strained due to the buried Ge dots. The strain causes an attractive potential for electrons. Repeating this procedure, Ge dots grow exactly on top of the strained Si areas. Up to 12 periods of dots were grown in that way which yielded a total of $>10^{10}$ dots.

In photoluminescence experiments a wide band appears around 0.8 eV which corresponds to transitions from the valence band of the Ge dots to conduction band states in the strained silicon (Fig. 3 (a)). This feature is much stronger in the samples with inhomogeneous size distribution (i), which can be attributed to the higher dot density. In EPR experiments a sharp line at g = 1.998 with a line-width of 0.25 G appears under illumination with sub-bandgap light (Fig. 3 (b)). The amplitude of this signal scales with the estimated total number of spins in the sample and also with the PL signal, and is very weak in the structured samples.

(a)   (b)
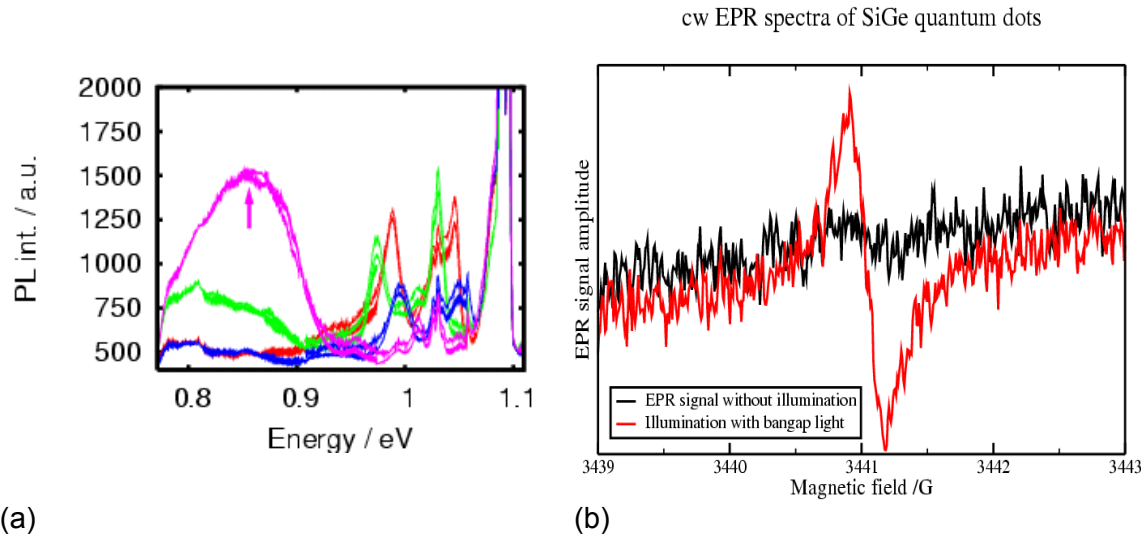
Fig. 3: (a) photoluminescence data from structured and unstructured (marked) samples; (b) EPR line at g = 1.998 with and without illumination with bandgap light.

The spin relaxation times were measured in time-resolved EPR experiments. In such experiments, the sample is not continuously irradiated by microwaves (MW). Instead, short high power MW pulses are applied. At resonance, these pulses cause the spins to rotate out of their thermal equilibrium orientation parallel to the direction of the static

external magnetic field H_0 by an angle that is proportional to the pulse duration around the direction of H_1, where H_1 the value of magnetic component of the MW field. Applying a π/2 pulse causes the spins to rotate into the plane perpendicular to the H_0, and a π pulse rotates the spins by 180°, thus inverting the spin orientation. Interaction with the surrounding lattice (longitudinal relaxation) and with other spins (transverse relaxation) causes the spins to dephase and to return to their thermal equilibrium value.

Specific pulse sequences are applied in order to observe longitudinal (T_1) and transverse (T_2) relaxation [6]. A π/2 pulse puts the overall magnetization in a plane perpendicular to H_0 where it decays due to spin-spin interaction (transverse relaxation) which is observed as free induction decay (FID). Some time τ after the first pulse a π pulse is applied to rotate the spins by 180°. As a consequence, a second FID appears after a time τ, 2τ after the initial π/2 pulse (Hahn echo). By varying τ, T_2 results from:

$$M = M_0 e^{-2t/T_2} ,$$

where M is the echo amplitude at time τ and M_0 at τ = 0.

When a π pulse is applied, the magnetization is rotated opposite to its thermal equilibrium orientation. Due to interaction with the environment the spins will relax back to their initial orientation parallel to H_0 (longitudinal spin relaxation). After a time T, a π/2 pulse is applied to put the magnetization into the plane perpendicular to H_0, and a π pulse is used to observe the Hahn echo as described above. T_1 results from:

$$M = M_0 \left(1 - 2 e^{-T/T_1} \right) .$$

Only the sample containing self-organized dots could be measured with time resolved EPR. We obtain a value of 0.8 μs for T_2 which is isotropic, whereas T_1 depends on sample orientation: in the case where H_0 is perpendicular to the sample plane, T_1 is 0.7 μs; in the case where H_0 is oriented in-plane, T_1 is 1.2 μs which is roughly what one expects for spin orbit coupling. Expressed in terms of line width, the homogeneous transverse line width is 0.082 G (isotropic) and the longitudinal line width is 0.070 G for perpendicular H_0 and 0.022 G for in-plane H_0. For comparison, the inhomogeneously broadened line width from cw EPR is 0.220 G for perpendicular and 0.350 G for in-plane H_0, which is considerably larger than the homogeneous contributions. The large inhomogeneous line width is attributed (i) to a fluctuation of the g-factor for different dot sizes and (ii) the hyperfine interaction with ^{29}Si.

References

[1]   R. Vrijen, E. Yablonovitch, K. Wang, H.W. Jiang et al.: "Electron-spin-resonance transistors for quantum computing in silicon-germanium heterostructures", Phys.Rev.A, Vol. 62, 2000, pp. 012306

[2]   A. M. Tyryshkin, S. A. Lyon, W. Jantsch, and F. Schäffler: "Spin Manipulation of Free Two-Dimensional Electrons in Si/SiGe", Phys. Rev. Lett. 94, 2005, 12802

[3]   K. Lai, W. Pan, D.C.Tsui, S. Lyon, et al.: "Two-Flux Composite Fermion Series of the Fractional Quantum Hall States in Strained Si", Phys. Rev. Lett. 93,2004,156805

[4]   H. Malissa, W. Jantsch, M. Mühlberger, F. Schäffler, Z. Wilamowski, M. Draxler, and "Anisotropy of g-factor and electron spin resonance linewidth in modulation doped SiGe quantum wells", Apl. Phys. Lett. 85, 2004, 1739

[5]   M. Kroutvar, Y. Ducommun, D. Heiss, M. Bichler, et al.: "Optically programmable electron spin memory using semiconductor quantum dots", Nature 432, 2004, 81

[6]   A. Schweiger and G. Jeschke: "Principles of Pulse Electron Paramagnetic Resonance" (Oxford University Press, Oxford, 2001)

Quantum Dots (Posters)

Quantitative Scanning Capacitance Spectroscopy on GaAs and InAs Quantum Dots

W. Brezna, T. Roch, G. Strasser, J. Smoliner

Institute of Solid State Electronics
Vienna University of Technology, A-1040 Vienna, Austria

In this work, quantitative scanning capacitance spectroscopy studies on bulk GaAs and InAs quantum dots are carried out in ambient atmosphere. The experimental results are well described by a simple spherical capacitor model, and the corresponding barrier heights and sample dopings are determined from the measured data. We further find a strong dependence of the C(V) data on the applied tip force. The barrier height is decreasing significantly with increasing pressure.

Introduction

Scanning Capacitance Microscopy/Spectroscopy (SCM/SCS) is an extension of conventional Atomic Force Microscopy (AFM) and a promising tool for two-dimensional carrier profiling in semiconductor devices. In SCM/SCS, a conductive AFM tip is used to measure the local capacitance between the tip and the sample. The current state of the art of this technique can be found in the review articles [1] – [4].

In scanning capacitance spectroscopy (SCS), the tip-sample capacitance is recorded during a DC voltage sweep to obtain a capacitance versus voltage (C(V)) curve [5]. However, quantitative SCM/SCS measurements are still a major challenge for technical and physical reasons. First, the capacitance between the AFM tip and the sample is in the aF regime only. To obtain a reasonable signal size at reasonable data collection speed for imaging, lock-in techniques are normally used. Thus, commercial SCM systems usually yield qualitative dC/dV data only. To obtain quantitative results, these data have to be calibrated. This, however, is technically complicated due to large difficulties with the reproducibility of the reference sample preparation process. In addition, the currently commercially available SCM systems do not operate at small signal conditions, which further complicates the data evaluation and makes sophisticated simulation methods almost inevitable [1] – [4].

To circumvent at least the reproducibility problems with reference samples, quantitative scanning capacitance spectroscopy can be used. In our previous work [6] we have demonstrated that this method is e.g. useful for a nanoscale analysis of high-k dielectric materials such as ZrO_2 and a pointwise calibration of capacitance images obtained by commercial SCM systems.

While a large amount of literature exists on SCM measurements on silicon samples, significantly fewer publications can be found on SCM on GaAs and other III-V materials. Besides very innovative approaches such as X-ray absorption measurements by SCM [7] and local capacitance measurements on InAs dot-covered GaAs surfaces by scanning capacitance microscopy [8] under high vacuum conditions, most of the SCM work on GaAs was devoted to the SCM characterization of laser structures [9], [10]. Douheret, e.g., has shown that SCM can provide a complete 2D map of the device structure, including doping variations, the location of p-n junctions, and regrown interfaces.

In this paper, bulk GaAs and InAs quantum dots are studied by scanning capacitance spectroscopy in ambient atmosphere. It is found that the experimental data agree well with capacitance spectra calculated from a simple spherical capacitor model. The donor concentrations obtained from this model are in excellent agreement with the sample parameters and the measured Schottky barrier heights are consistent with data obtained by Ballistic Electron Emission Microscopy on similar samples [12]. The influence of illumination and tip force is found to be very critical.

Experimental Preliminaries

All samples we used for our experiments were MBE grown GaAs layers on semi insulating GaAs substrates. The layer thickness was 1 µm for all samples and the doping was $N_d = 1 \times 10^{16}$ cm^{-3} and $N_d = 1 \times 10^{17}$ cm^{-3} for the GaAs bulk samples, respectively. The "on surface" quantum dot sample we used had the same layer structure and was also doped at a level of $N_d = 1 \times 10^{16}$ cm^{-3}.

For all capacitance measurements, an ultrahigh precision, low frequency (1 kHz) capacitance bridge (*Andeen Hagerling* 2550) was used, which allows capacitance and loss measurements under well controlled, small signal conditions down to the aF regime. A (*Keithley*) source measure unit was used to provide the DC voltage component. External coax cables from the capacitance bridge were attached on both the sample and the AFM tip holder. The AFM was only used for tip positioning and for the tip-sample approach. As tips we used highly doped (p-type 1×10^{20} cm^{-3}) conductive diamond tips (*Nanosensors*, Germany). The spring constant of the cantilevers was 42 N/m and the typical tip radius was 100 nm according to the data sheet. Note that this type of cantilevers is normally used for scanning spreading resistance measurements only; the reasons for using these tips are described below.

In contrast to standard SCM/SCS measurements, where the applied frequencies are so high (≈1 GHz) that light induced charge carriers cannot follow the HF fields, our setup operates at a frequency of 1 kHz. Here, the measurement turned out to be extremely sensitive to the influence of light. Therefore, the AFM hardware was modified in order to switch off the laser and all other illumination and the feedback loop was controlled externally during the C(V) measurements [11]. To minimize vibrations and acoustic noise, the AFM system was placed on an air suspended table and put into an acoustic hood. This also allowed an operation under temperature stable conditions which turned out to be crucial. In detail, the temperature variations were kept below ±10 mK during the measurements. Due to improved shielding measures and larger signals compared to our earlier experiments [6], a reasonable signal to noise ratio was already obtained at moderate averaging times and a typical C(V) spectrum took 20 minutes.

Results and Discussion

Figure 1 (a) shows typical C(V) curves, which were obtained in complete darkness. The force we used for these measurements was 2.9 µN. Curve (1) was recorded on bulk GaAs with a doping of $N_d = 1 \times 10^{16}$ cm^{-3}. Curve (2) was bulk GaAs too, with $N_d = 1 \times 10^{17}$ cm^{-3}, and curve (3) was obtained on a InAs quantum dot on GaAs substrate with a doping of $N_d = 1 \times 10^{16}$ cm^{-3}. Obviously, the onset of these C(V) spectra is shifted to lower bias for higher substrate doping and the onset of the C(V) curve obtained on a quantum dot is even lower.

As already found by Yamamoto [8], a simple parallel plate capacitor model cannot be used to describe AFM based capacitance spectra on GaAs. The reason for this lies in the nature of the Schottky contact between the tip and the GaAs underneath. In a Schottky contact, the extent of the depleted space charge region determines the capacitance of the contact. As the depletion length easily reaches several hundred na-

nometers on low doped samples and the tip radius is much smaller, a simple parallel plate capacitor model is not appropriate for geometric reasons. In contrast to that, the active region in Metal-SiO$_2$-Silicon (MOS) junctions is always directly at the Si-SiO$_2$ interface directly underneath the tip, which is the reason why simple parallel plate capacitor models on Si samples normally yield results which are correct at least within an order of magnitude.
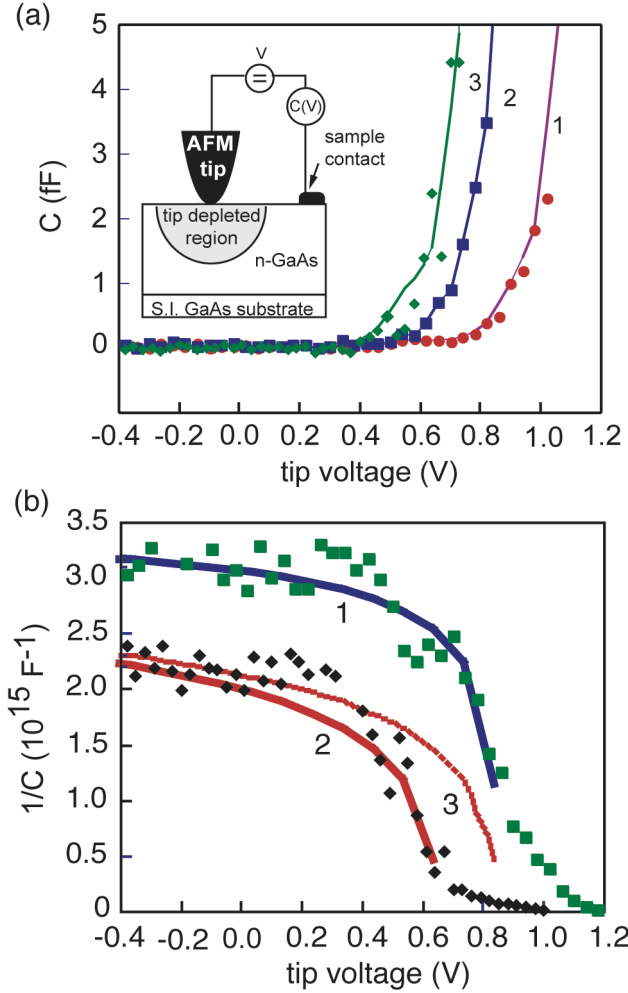
Fig. 1: (a) Capacitance – voltage (C(V)) spectra measured on three different samples (curves 1 – 3). (1): bulk GaAs with N_d = 1x10^{16} cm^{-3}, (2): bulk GaAs with N_d = 1x10^{17} cm^{-3}, (3): InAs dots on GaAs with N_d = 1x10^{16} cm^{-3}. The solid lines connecting the data points are only a guide for the eye. A schematic view of the experimental setup is shown in the inset. (b) Capacitance data for the high and low doped bulk sample plotted as 1/C over bias. The solid lines were calculated using a spherical capacitor model. Details are found in the text.

To analyze our data, we therefore applied a simple model assuming a capacitor consisting of two concentric spheres. The capacitance of such a spherical capacitor is calculated as $C = 4\pi\varepsilon_r\varepsilon_0\left(\dfrac{r_1 r_2}{r_2 - r_1}\right)$, where ε_0 is the dielectric constant of vacuum, ε_r is the relative dielectric constant and r_1 and r_2 are the radii of the inner and outer sphere. To estimate the capacitance of our tip-semiconductor system we simply set $r_1 = r_{tip}$, where r_{tip} is the tip radius and r_2 is set to $r_2 = (r_{tip} + d)$, where d is the depletion layer thickness in GaAs. We further assume that ε_r =13 and ignore all influence of the dielectric con-

stant of the diamond tip and the surrounding air. For a given Schottky barrier height V_b, the depletion layer thickness d is calculated as: $d = \left(2(V - V_b)\varepsilon_r\varepsilon_0/(eN_D)\right)^{\frac{1}{2}}$, where V is any applied external voltage, and N_D the doping concentration. Finally we take for the tip-sample capacitance C_{TS} a value of $C_{TS} = C/2$ only, because we just consider the lower half sphere of the capacitor. As long as $d > r_1$, which is easily achieved on low doped substrates, this will be a reasonably good approximation.
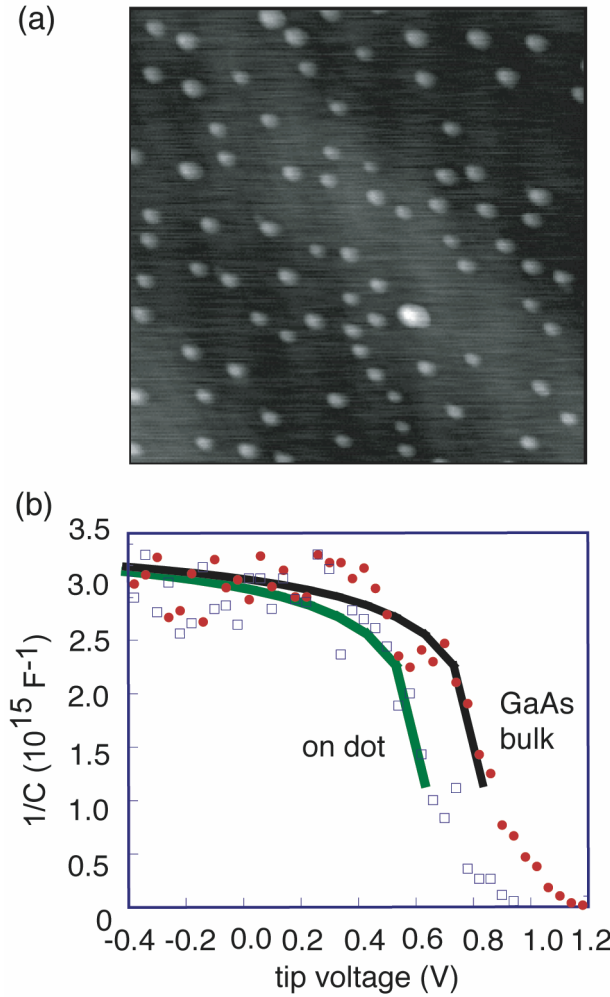
Fig. 2: (a): AFM image of the quantum dot sample. Scan size is 1µm x 1µm. The typical dot diameter is 40 nm. (b): 1/C(V) curves obtained on the low doped bulk sample and on quantum dot positions. The solid lines were calculated using a spherical capacitor model. Details are found in the text.

To compare the model with the experimental data, it is helpful to plot $1/C_{TS}$ versus tip-bias similar like the $1/C_2$ versus bias plots, which are usually made for C(V) curves on Schottky junctions assuming parallel plate capacitors. For the low doped sample, the agreement between the experimental data and the primitive model is amazing. Figure 1 (b) shows a comparison of the measured and calculated curves. Curve (1) shows the result for a substrate doping of $N_d = 1 \times 10^{16}$ cm^{-3}, a tip radius of 90 nm, and a Schottky barrier height of Vb = 0.9 eV. The background stray capacitance was also subtracted. Below the barrier height, the agreement is really excellent. For bias values above the barrier height, the model can not be applied. Curve (2) shows the result for the sample with the higher doping ($N_d = 1 \times 10^{17}$ cm^{-3}). In agreement with our simulation, the recip-

rocal of the measured signal becomes smaller with increased doping level. To fit the shifted onset position, an "effective" barrier height of $V_b = 0.7eV$ was assumed to account for the tunneling effects through the thinner Schottky barrier at higher doping levels. However, the overall agreement between the calculation and the experiment is still not as good as for the low doped substrate. In our opinion, this is due to the smaller extension of the depleted region, where the primitive spherical capacitor approximation becomes less accurate. For comparison, the result of an equivalent simulation assuming a barrier height of 0.9 eV is also shown in curve (3).

Motivated by the good agreement between theory and experiment on bulk GaAs, the same measurements were also carried out on InAs quantum dots. An AFM topography of our sample can be seen in Figure 2 (a). The dots have a typical diameter of 40 nm on this sample. Figure 2 (b) shows the corresponding capacitance data.
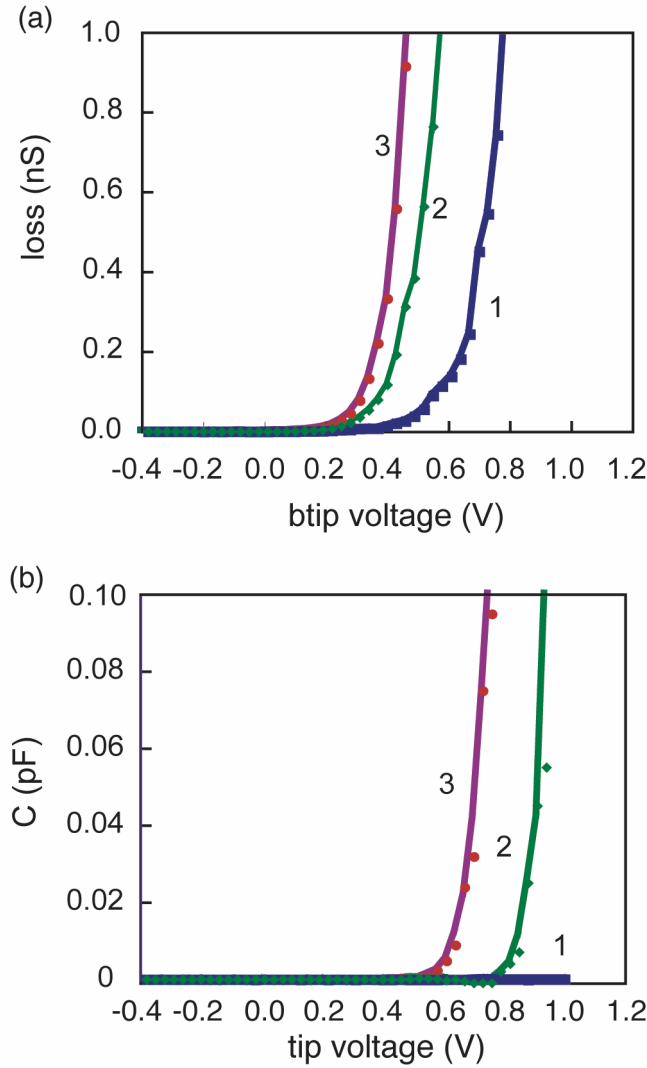
Fig. 3: (a) Loss curves recorded on bulk GaAs ($N_d = 1 \times 10^{16}$ cm^{-3}) using forces of 2.0 µN, 3.8 µN and 6.1 µN, for curves (1 – 3), respectively. (b) Simultaneously measured C(V)-spectra.

Compared to the GaAs bulk data, the "on dot" curve looks qualitatively the same and is just shifted to the left. The calculated "on-dot" curve was obtained using a barrier height of $V_b = 0.65$ eV, which is in excellent agreement with the band offset between InAs dots and GaAs determined earlier [12] by Ballistic Electron Emission Microscopy (BEEM).

This indicates, that the InAs dot acts as intermediate contact to the tip and that the capacitance is dominated by the behavior of the InAs-GaAs system and not the tip. A similar behavior was already found by Yamamoto et al. [8].

As final point we want to discuss the influence of the tip-sample force, which turned out to have a significant influence on the results. Figure 3 (a) shows typical loss (differential conductance) spectra on the low doped GaAs bulk sample as a function of tip-force. Curves (1) – (3) were measured using tip forces of 2.0 µN, 3.8 µN and 6.1 µN, respectively. As in conventional spreading resistance measurements, the loss increases with increasing force between tip and sample. It must be pointed out, however, that the minimal force (F ≈ 1 µN) to obtain reproducible loss data is surprisingly high. For all our measurements we had to use diamond coated "scanning spreading resistance cantilevers" with a high spring constant (C = 42 N/m). With conductive diamond coated "contact mode cantilevers" (C = 1 N/m) the forces turned out to be too low to achieve reliable conductance data. The physical origin for this behavior is probably found in the ambient conditions where the measurements were carried out. Under ambient conditions, all samples are usually covered with a thin film of water. Especially on semiconductors, one can expect an additional native oxide, too. Thus, the existence of a force threshold to penetrate these films with an AFM tip is not that surprising, the rather high amount of force, however, is.

For local capacitance measurements, the situation is even worse. Even at tip forces where a clear local conductance via the tip is already observed (Figure 3 (a), curve (1)), no capacitance signal can be detected (Figure 3 (b), curve (1)). At a tip force of 3.8 µN, which turned out to be the minimum value for reproducible capacitance measurements on our sample, we obtain typical data as they are shown in curve (2). Under these conditions, we obtain a barrier height of V_b = 0.9 eV as discussed above. At a tip force of 6.1 µN (curve (3)), the capacitance curve is shifted to the left and the barrier height is reduced and our model yields a significantly reduced value of V_b = 0.55 eV. Going to higher pressures was impossible, since this normally led to tip destruction before further significant changes could be detected.

On the reasons why the threshold force for reproducible capacitance measurements is even higher than for conductance measurements, we can only speculate. Most probably, however, any intermediate layer (water, oxide) had to be penetrated completely by the tip before a reasonable Schottky contact is established. In contrast to that, thin oxide layers would show a finite conductance already much earlier due to tunneling effects.

On the quantum dot sample, systematic pressure studies were unfortunately impossible, since the dots were considerably damaged at higher tip forces. In addition, we noticed that tip forces greater than 4.7 µN had to be used before any capacitance signal could be recorded on off-dot positions on the wetting layer. Since the samples were not grown freshly, the wetting layer was probably oxidized completely. However, we have no explanation why an oxidized InAs wetting layer is significantly thicker or less conducting than native GaAs oxide and we also found no information in the literature on this topic.

Summary

In summary, quantitative AFM based capacitance studies were carried out in air on bulk GaAs and InAs quantum dots. All C(V) data were well described by a simple spherical capacitor model on all samples, and substrate doping as well as the corresponding barrier heights were determined and in agreement with reference data. We also found a force threshold for reproducible capacitance measurements and a significant influence of the tip sample force on the obtained results.

Acknowledgements

References

[1]   V.V. Zavyalov, J.S. McMurray, C.C. Williams, Rev. Sci. Instr. 7, 158 (1999)

[2]   R. Stephenson, P. DeWolf, T. Trenkler, T. Hantschel, T. Clarysse, P. Jansen, W. Wandervorst, Vac. Sci. Technol. B18, 555 (2000)

[3]   D.D. Bugg, P.J. King, J. Phys. E21 147 (1988)

[4]   V.V. Zavyalov, J.S. McMurray, C.C. Williams, Rev. Sci. Instr. 7, 158 (1999)

[4]   P. De Wolf, R. Stephenson, T. Trenkler, T. Clarysse, T. Hantschel, W. Vandervorst, J. Vac. Sci. Technol. B18, 361 (2000)

[5]   E.H. Nicollian, J.R. Brews, MOS (metal oxide semiconductor) physics and technology, John Wiley & Sons Ltd, New York 1982

[6]   W. Brezna, M. Schramboeck, A. Lugstein, S. Harasek, H. Enichlmair, E. Bertagnolli, E. Gornik, J. Smoliner, Appl. Phys. Lett. 83 4253 (2003)

[7]   M. Ishii, T. Uchihashi, Physica B 340-342, 1142 (2003)

[8]   H. Yamamoto, T. Takahashi, I. Kamiya, Appl. Phys. Lett. 77, 1994 (2000)

[9]   O. Douheret, S. Anand, C. Angulo-Barrios, S. Lourdudoss, Appl. Phys. Lett. 81, 960 (2002)

[10] M.W. Xu, N. Duhayon, W. Vanderworst, 2002 GaAs MANTECH Conference Digest of Papers, 173 (2002)

[11] for more technical details please send email to : juergen.smoliner@tuwien.ac.at

[12] D. Rakoczy, G. Strasser, J. Smoliner, J. Vac. Sci. Technol. B20, 373 (2002)

Self-Organization of Ripples and Islands with SiGe-MBE

G. Chen, H. Lichtenberger, G. Bauer, and F. Schäffler

**Institute of Semiconductor and Solid State Physics,
Johannes Kepler University, A-4040 Linz, Austria**

We explored two methods to obtain laterally ordered Ge/Si quantum dot arrays. For the first we exploit the two independent growth instabilities of the SiGe/Si(001) hetero-system, namely kinetic step bunching and Stranski-Krastanov (SK) island growth, to implement a two-stage growth scheme for the fabrication of long-range ordered SiGe islands. The second approach is to deposit Ge/SiGe onto prepatterned Si substrates, which are prepared via lithography and subsequent reactive ion etching (RIE). It results in perfectly ordered, 2D dot arrays that can be extended into 3D by strain-ordering of a Ge-dot superlattice.

Introduction

The self-organized growth of Ge/Si quantum dot hetero-structures has attracted considerable interest because of its potential for electronic and optoelectronics devices, and its compatibility with the well-explored Si-technology. Recently, laterally ordered Ge/Si quantum dots have also been suggested for the implementation of quantum computing functions, as well as quantum information storage, which both require the separate identification and external addressability of each quantum dot. To obtain laterally ordered Ge/Si quantum dot arrays, we explored two methods. (i) A route which is only based on self-organization to achieve ordering is based on a slightly vicinal Si(001) surface, which is intrinsically unstable against kinetic-step-bunching during homoepitaxial growth. The resulting ripple morphology serves as a one-dimensional template for preferential Ge dot nucleation. (ii) Another approach is to deposit Ge/SiGe onto two-dimensionally prepatterned Si-substrates, which are prepared via lithography and subsequent reactive ion etching (RIE).

Results and Discussion

The Si(001) surface is intrinsically unstable against kinetic step bunching during Si homo- and SiGe heteroepitaxy [1] – [4]. This phenomenon was originally attributed to lattice-mismatch strain [5], but it is now clear that it is of purely kinetic origin. Recent kinetic Monte Carlo simulations in connection with a basic stability analysis provide strong evidence for step bunching being caused by the interplay between the adsorption/desorption kinetics at single atomic height steps and the pronounced diffusion anisotropy on the reconstructed Si(001) surface [6], [7]. The simulations show excellent agreement with STM experiments, and qualitatively reproduce the pronounced temperature dependence of the step bunching phenomena.

The detailed understanding of homoepitaxial step bunching on Si(001) allowed us to tailor the period and height of the bunches by controlling substrate miscut, growth temperature, deposition rate and layer thickness (Fig. 1). This way, homoepitaxial layers with ripple periods of 100 ± 10 nm were prepared on Si(001) substrates with 4° miscut along [110] (Fig. 2).
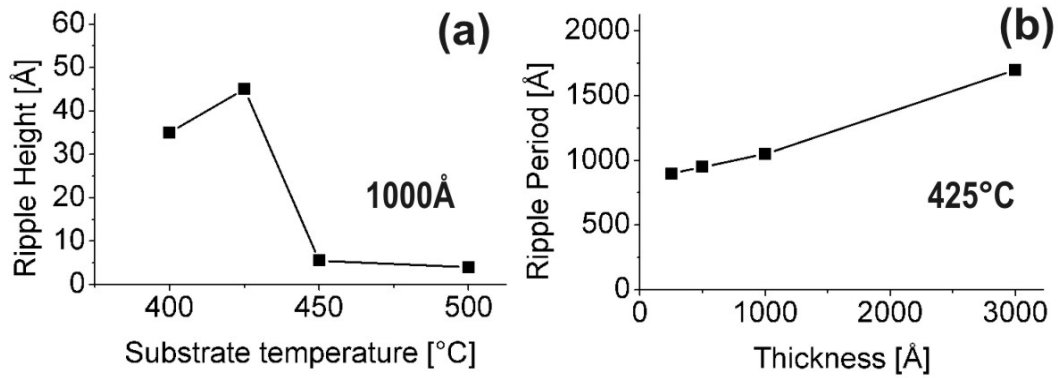
Fig. 1: (a) Dependence of the step-bunching ripple height on substrate temperature for a 1000Å Si-buffer. The maximum of the instability for 4° miscut and a Si-rate of 0.2Å/s occurs around 425°C; (b) Increase of the ripple period with thickness for the optimum Si-buffer temperature at 425°C.
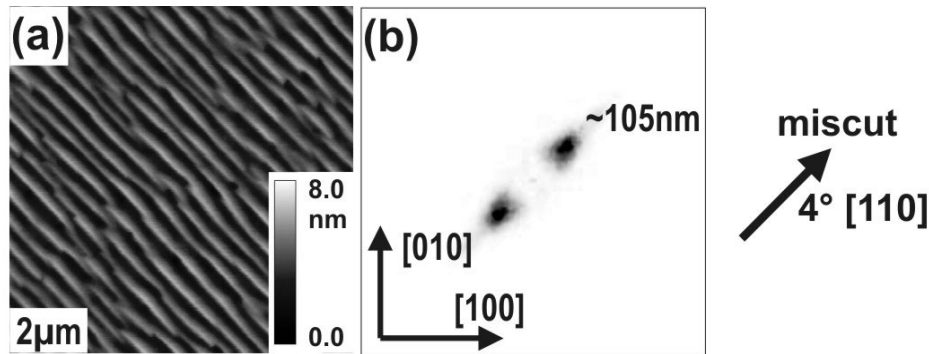
Fig. 2: (a) Kinetic step bunching of a homoepitaxial Si layer on a vicinal Si(001) substrate with 4° miscut along [110]. (b) Fast Fourier Transform showing a spacing for the step bunches of 100 ± 10 nm.

These were then employed as templates for the ordering of SiGe or Ge dots grown in the strain-driven Stranski-Krastanov mode. When the period length of the template complies with the mean spacing of the dots, only one dot row fits into one period (Fig. 3).

We could show that the dots then nucleate at the step bunches, where the energetically favorable {1 0 5} facets of the dots are most easily created by step-meandering [8] – [11]. Considering growth further away from thermal equilibrium, the $Si_{0.55}Ge_{0.45}$ film deposited at 425 °C does not completely disintegrate into individual islands, but reveals how and where island nucleation commences: Upon SiGe deposition the flanks of the step bunches are converted into a zigzag train of adjacent (1 0 5) and (0 1 5) facets.

The originally smooth flanks match quite well the slope of the [5 5 1] intersection line between two adjacent {1 0 5} facets and thus can easily be converted into a {1 0 5} faceted SiGe ridge structure, which is perpendicular to the step-bunches. This is a step-meandering instability induced by strain and the low-energy {1 0 5} facets of SiGe on Si(001). It marks the transition (Fig. 4) from conformal Si/SiGe epilayer growth to strain-driven, ordered 3D-growth which is observed at 625°C for the $Si_{0.55}Ge_{0.45}$ epilayer. This leads to a fair degree of 2D rectangular, face-centered ordering of the SiGe dots (Fig. 3 (d)) in an approach that employs self-organization mechanisms only [9] – [12].
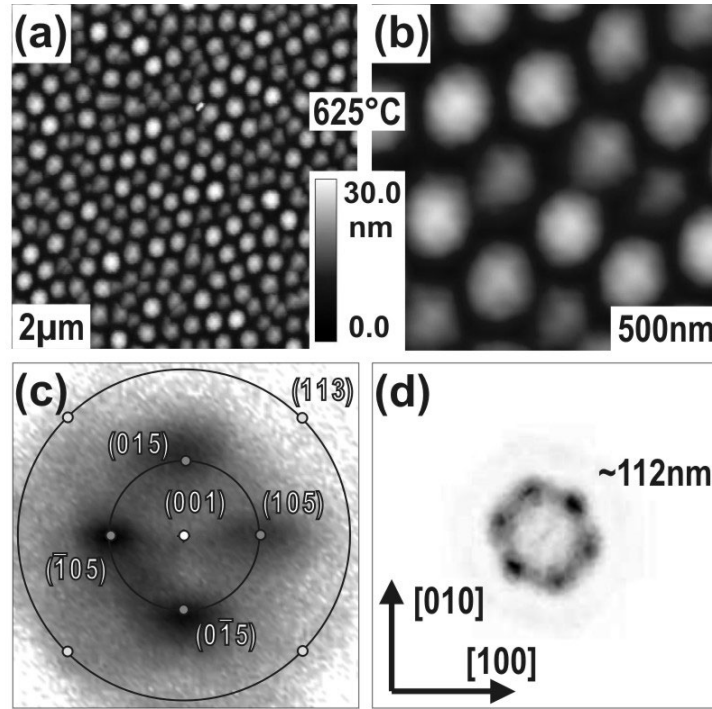
Fig. 3: (a), (b) Self-organized SiGe dots on the Si template from Fig. 2 with the 50 Å Si$_{0.55}$Ge$_{0.45}$ epilayer deposited @ 625°C; (c) Surface orientation maps derived from Fig. 2 (a). The dots show preferentially {1 0 5} facets (inner circle). (d) Fast Fourier Transform of Fig. 3 (a), revealing rectangular, face-centered ordering of the dots.
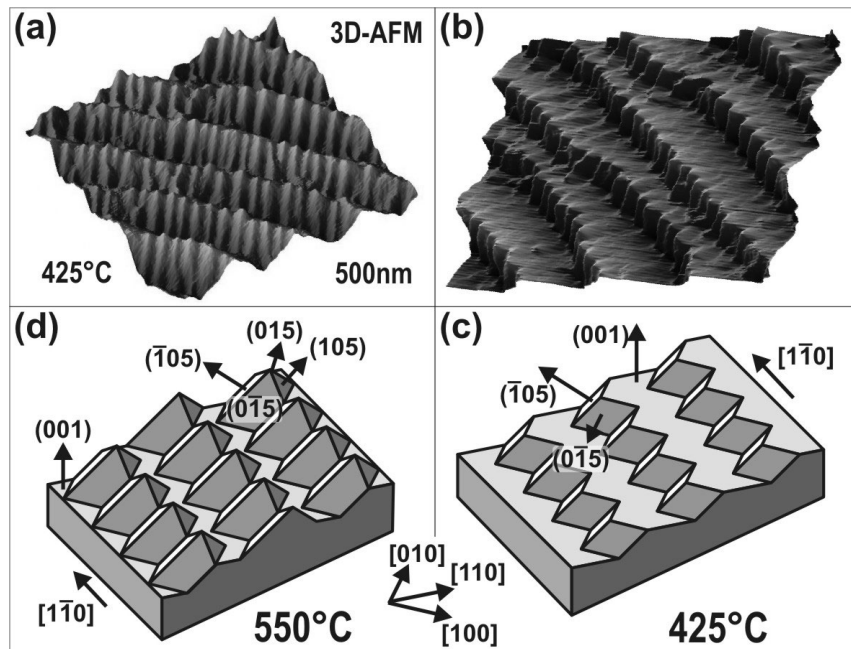
Fig. 4: (a), (b) 3D-AFM representations of a 50 Å Si$_{0.55}$Ge$_{0.45}$-layer grown @ 425 °C showing a strain-induced {1 0 5} zigzag structure decorating the bunch flanks. The dominant facets for SiGe layers deposited at 425 and 550 °C are depicted schematically in (c) and (d) respectively. At 550 °C also retrograde {1 0 5} facets appear which are necessary to form 3D-islands as depicted in Fig. 3.

To realize perfectly ordered SiGe and Ge dots in 2D and 3D, we used lithographically defined pit arrays. For small enough periods, only one dot per unit cell is created, which nucleates at the lowest point of the pit (Fig. 5).

XTEM images reveal that the nucleation site is defined by the intersection of neighboring facets, which form during Si buffer layer deposition on the nano-structured templates [13]. Thus, by combining nano-structuring with self-organized growth, arbitrarily large areas of perfectly ordered 2D SiGe and Ge dot arrays can be implemented [14] –[16]. On this base we also realized perfect 3D Ge dot arrays by additionally exploiting the strain-driven vertical ordering of Ge dots in a Si/Ge dot super-lattice [17].

Lithographically defined ordering of SiGe and Ge dots fulfills an essential precondition for all but the most elemental applications of self-organized dots, namely their addressability. Vertical stacking of such arrays provides the option to use the topmost dot layer as a self-aligned mask for selective ion implantation.
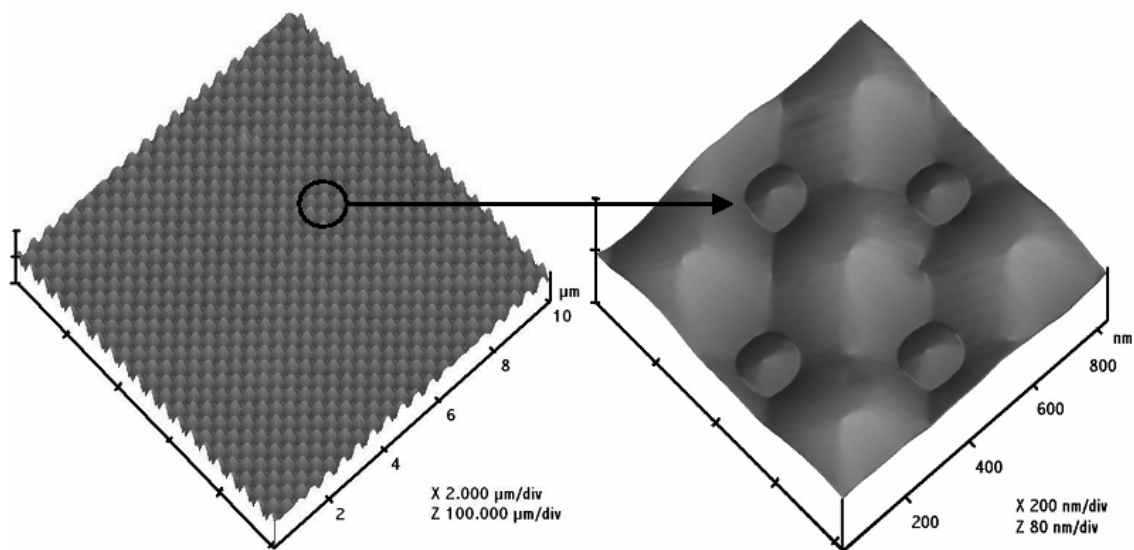
Fig. 5: 3D-AFM representations of a perfect 2D array of self-organized Ge with a periodicity of 350 nm on a Si template defined by lithography and reactive ion etching.

Acknowledgements

References

[1] C. Schelling *et al* , *Phys. Rev. Lett.* **83**, 995 (1999).

[2] C. Schelling *et al* , *Phys. Rev. B* **64**, 041301(R) (2001).

[3] M. Mühlberger *et al* , *Surf. Sci.* **721**, 532 (2003).

[4] A. Ronda *et al* , *Physica E* **23**, 370 (2004).

[5] J. Tersoff *et al* , *Phys. Rev. Lett.* **75**, 2730 (1995).

[6] J. Myslivecek *et al* , *Surf. Sci.* **520**, 193 (2002).

[7] J. Myslivecek *et al* , *cond-mat/* 021231.

[8] H. Lichtenberger *et al* , *J. Cryst. Growth*, in print.

[9] H. Lichtenberger *et al* , *Appl. Phys. Lett.* **86**, 131919 (2005)

[10] C. Teichert et al , Appl. Phys. A: Mater. Sci. Process. **67**, 675 (1998).

[11] J.-H. Zhu et al , Appl. Phys. Lett. **33**, 620 (1998).

[12] C. Teichert et al , Phys. Rep. **365**, 335 (2002).

[13] Z. Zhong et al , J. Appl. Phys. **93**, 6258 (2003).

[14] Z. Zhong et al , Appl. Phys. Lett. **82**, 445 (2003).

[15] Z. Zhong et al , Appl. Phys. Lett. **82**, 4779 (2003).

[16] Z. Zhong et al , Appl. Phys. Lett. **83**, 3695 (2003).

[17] Z. Zhong et al , Physica E **21**, 588 (2004).

Photocurrent Spectroscopy of Single InAs/GaAs Quantum Dots

G. Fasching, F.F. Schrey, T. Müller, and K. Unterrainer

Institute of Photonics, Vienna University of Technology, Floragasse 7, A-1040 Vienna, Austria

W. Brezna, M. Austerer, T. Roch, M.A. Andrews, J. Smoliner, and G. Strasser

Institute of Solid State Electronics, Vienna University of Technology, Floragasse 7, A-1040 Vienna, Austria

In this work, we present a carrier escape study from InAs/GaAs self assembled QD's by the use of photocurrent measurements. As a function of the applied field, we detect a shift of the exciton ground state transition due to the quantum-confined Stark shift. From the measured Stark shift S = 4.3 meV we deduce a exciton dipole moment of p = (4.3 ± 0.2)×10^{-29} Cm. The tunneling time, which is directly related to the observed photocurrent linewidth due to τ ~ ℏ/(2Γ), changes by a factor of five in the photocurrent regime. The measured linewidth dependency on the electric field is modeled by a simple 1D WKB approximation for the tunneling process, which shows that the energetic position of the wetting layer is important for the measured tunneling time out of the dot.

Introduction

Since the first proposal of quantum dots in 1982 [1] a great deal of research has been dedicated to the study of the optical and electrical properties of QD's. The improved understanding of the excellent properties of this quantum system made it already possible to implement QD's in devices like lasers [2], [3], MIR photodetectors [4], single-photon turnstile devices [5], [6] or single-electron turnstile devices [7]. In previous work [7], [8] a decay of the coherent excitation was observed due to competing mechanisms like carrier-carrier scattering, Coulomb scattering, phonon scattering and tunneling escape.

In this contribution we investigate the influence of these scattering processes on the scattering rate of the observed exciton ground state transition. In our experiments we resonantly excite the exciton interband ground state transition of single InAs/GaAs self-assembled QD's embedded in an *n-i*-Schottky photodiode. QD's provided with both electric contacts and optical access allow us to vary independently the electric field while measuring the electrical or optical response of a single QD. Complementary to the photoluminescence (PL), the collected photocurrent (PC) provides information about the absorption spectrum and the tunneling escape times of single QD's.

Experimental

Sample and Experimental Setup

The sample investigated was grown using molecular beam epitaxy on semi-insulating GaAs (100). Nominally, 1.55 ML of InAs are deposited at 500 °C on *i*-GaAs 40 nm above an *n*-doped GaAs layer (10^{18} cm^{-3}) which forms the bottom contact. During the

growth of the QD's the rotation of the wafer has been stopped to produce an InAs deposition gradient across the wafer, resulting in a variation of the corresponding InAs QD density. Atomic force microscopy (AFM) studies of a similar sample with uncapped dots could determine the density gradient from ~500 μm^{-2} to zero. The growth of the self-assembled QDs is followed by 80 nm *i*-GaAs, a 40 nm thick $Al_{0.3}Ga_{0.7}As$ barrier, and a 10 nm *i*-GaAs cap layer. After the growth the sample was processed by photo-lithographic methods into photodiodes. Ohmic contacts were established to the doped n^+ region and semitransparent Ti-Schottky contacts were deposited on the top surface to achieve a homogeneous electric field in the region of the investigated QD's. The Schottky contact was in addition covered with an opaque Au mask where 2 μm^{-2} apertures were opened to allow optical access to the QDs. The results reported in the present work were obtained from a region of the wafer where the QD density I < 1 μm^{-2}.

The PL and the PC measurements were performed at 4.2 K using the 760 nm line of a cw Ti:Sapphire laser for PL spectroscopy and a tunable Ti:Sapphire laser to resonantly excite the QD energy levels for PC spectroscopy. The sample was placed in a low drift Oxford LHe flow cryostat. The PL and PC excitation paths as well as the PL detection path lead through a confocal laser scanning microscope (LSM) with a lateral and axial resolution below 500 nm. The PL signal is filtered by an 850 nm long pass filter and dispersed in a 0.5 m spectrometer, which allows a spectral resolution better than 50 μeV with a liquid nitrogen cooled CCD detector. The PC signal is detected by a sensitive photodiode amplifier which is capable to bias the photodiode and standard lock-in technique. The spectral resolution of the PC measurements determined by the laser linewidth is ≈30 μeV.

Measurements

The band structure under negative bias condition is shown schematically in Fig. 1. Changing the bias voltage from positive to negative voltage reduces the tunneling barrier thickness in the direction of the applied field and therefore the tunneling time τ_t of the photoexcited carriers out of the dot. When τ_t becomes equal or even smaller than the radiative lifetime of the exciton τ_r ~ 1 ns one changes from the PL measurement regime to the PC measurement regime.
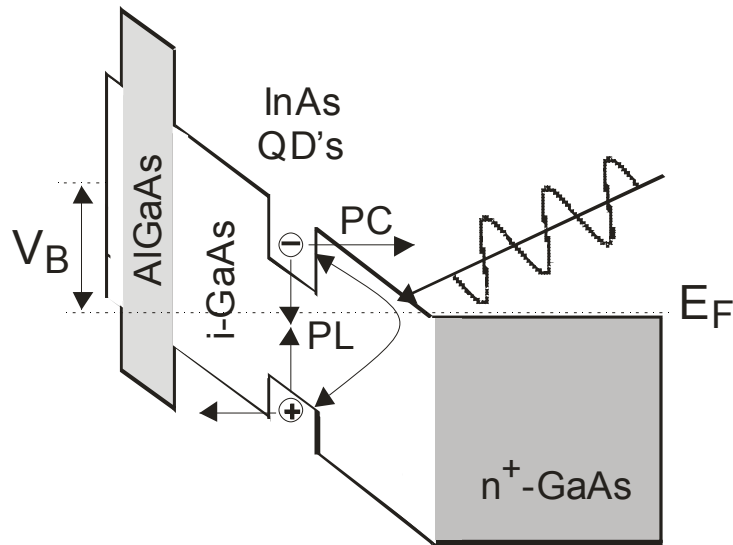

Fig. 1: Schematic band diagram of the investigated Schottky photodiode under negative bias voltage V_B

Figures 2 (a) and (b) show PL and PC spectra at the same aperture of the shadow mask under different bias conditions. In both cases sharp single peaks are observed attributed to single QD emission (PL) and absorption (PC). The PC line in Fig. 2 (b) is measured at higher electric field than the PL line in Fig. 2 (a) and is therefore shifted to a lower energy due to the QCSE. Under the measurement conditions shown in the inset of Fig. 2 (b) the observed PC peak magnitude is 2.5 pA. This current corresponds to a generation rate of 10^7 e-h pairs per second. The fact that no biexciton lines are observed, which have typically about 3 meV binding energies, leads to the conclusion that the used excitation power was low enough that occupation of the QD with more than one exciton can be excluded. The FWHM of the PL line corresponds (according to $\tau \sim \hbar/(2\Gamma)$) to an exciton lifetime τ of about 6 ps which is approx. three orders of magnitude smaller than the radiative lifetime of 1 ns mentioned above. This effective lifetime is given by $\tau^{-1} = \tau_r^{-1} + \tau_t^{-1} + \tau_c^{-1}$, where τ_r is the recombination time, τ_t is the tunneling time and τ_c^{-1} describes Coulomb scattering by free carries (due to the nonresonant excitation for PL), defects, impurities, and alloy fluctuations. The PC linewidth is limited to ~100 µeV for low electric fields where also PL can be measured. Due to these findings we claim that the FWHM of the measured PC and PL lines is limited due to the Coulomb interactions mentioned above. The PC signal can be observed in the electric field range of 30 kV/cm to 80 kV/cm.
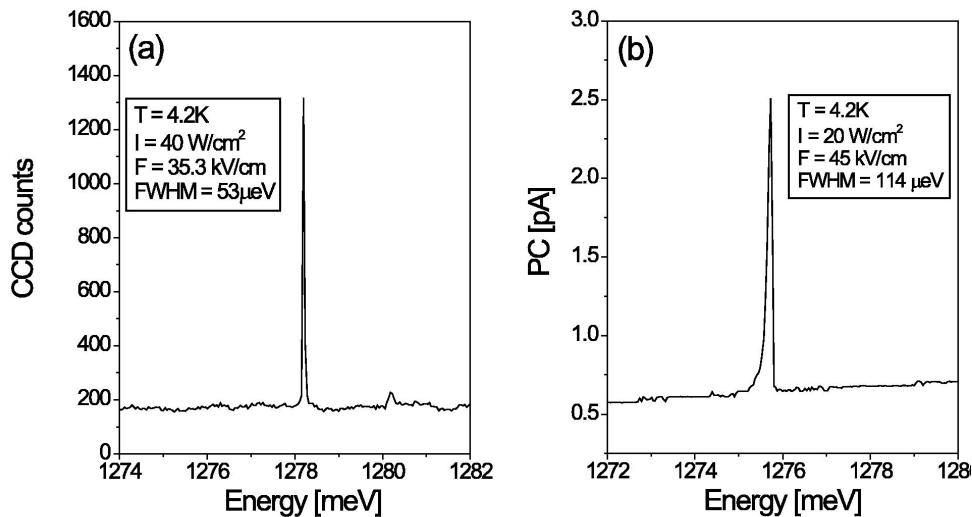
Fig. 2: Photoluminescence (a) and photocurrent (b) spectrum of a single QD. The energetic shift is due to the Stark shift and bias-controlled charging of the QD at low electric fields where the QD ground state level is shifted below the Fermi level [9].

Conclusion

In this contribution we report on field-dependent photocurrent measurements of the excitonic interband transitions of single InAs/GaAs self-assembled QD's. The application of an external electric field allows controlling the transition energy due to the QCSE. The measured Stark shift S = 4.3 meV/V of the exciton transition can be used for the realization of a single QD spectrometer. From the measured Stark shift we obtain a dipole moment p = (4.3 ± 0.2)×10^{-29} Cm. The decrease of the PC linewidth for low electric fields is limited to a value of Γ ~ 100 µeV, which is attributed to Coulomb interaction of the exciton with carriers surrounding the QD.

Acknowledgements

References

[1]   Y. Arakawa and H. Sakaki, *Appl. Phys. Lett.* **40**, 939 (1982).

[2]   G. Park, O.B. Shchekin, D.L. Huffaker, D.G. Deppe, *IEEE Photon. Tech. Lett.* **12**, 230 (2000).

[3]   N.N. Ledentsov, A.R. Kovsh, A.E. Zhukov, N.A. Maleev, S.S. Mikhrin, A.P. Vasil'ev, E.S. Semenova, M.V. Maximov, Yu.M. Shernyakov, N.V., Kryzhanovskaya, V.M. Ustinov, D. Bimberg, *IEEE Electron. Lett.* **39**, 1126 (2003).

[4]   L.Rebohle, F.F. Schrey, S. Hofer, G.Strasser, K. Unterrainer, *Appl. Phys. Lett.* **81**, 2079 (2002).

[5]   P. Michler, A. Kiraz, C. Becher, W.V. Schoenfeld, P.M. Petroff, Lidong Zhang, E. Hu, A. Imamoglu, *Science* **290**, 2282 (2000).

[6]   Z. Yuan, B.E. Kardynal, R.M. Stevenson, A.J. Shields, C.J. Lobo, K. Cooper, N.S. Beattie, D.A. Ritchie, M. Pepper, *Science* **295**, 102 (2002).

[7]   A. Zrenner, E. Beham, S. Stufler, F. Findeis, M. Bichler, G. Abstreiter, *Nature* **418**, 612 (2002).

[8]   X. Li, Y. Wu, D. Steel, D. Gammon, T.H. Stievater, D.S. Katzer, D. Park, C. Piermarocchi, and L.J. Sham, *Science* **301**, 809 (2003).

[9]   F. Findeis, M. Baier, E. Beham, A. Zrenner, and G. Abstreiter, *Appl. Phys. Lett.* **78**, 2958 (2001).

Lateral Quantum Dots in High Mobility Heterostructures

G. Pillwein [1], T. Berer [1], G. Brunthaler [1], F. Schäffler [1], and G. Strasser [2]

[1] Institute for Semiconductor Physics, University Linz, Austria

[2] Institut für Festkörperelektronik TU Vienna, Austria

We have fabricated single lateral quantum dots in the two-dimensional electron gas (2DEG) of modulation doped GaAs/AlGaAs and Si/SiGe heterostructures, which are basic elements for more sophisticated devices. Electrical measurements were carried out at temperatures down to 30 mK. The technology of the GaAs structures has been adapted to Si/SiGe-based lateral quantum dots. We report Coulomb blockade measurements of lateral quantum dots formed by the split-gate technique on MBE grown modulation doped GaAs/AlGaAs and Si/Si$_{0.75}$Ge$_{0.25}$ heterostructures.

Introduction

In several recent proposals [1] – [3] lateral quantum dots were discussed as a promising option to realize the quantum entanglement necessary for quantum computation. As an approach to this topic we have chosen to fabricate single quantum dot devices in the two-dimensional electron gas (2DEG) of GaAs/AlGaAs and Si/SiGe heterojunctions. These dots are the basic building blocks of more complex structures (e.g. [4]), which we plan to investigate in the near future.

The technology of the GaAs structures has been adapted to Si/SiGe based lateral quantum dots. Recently, several lateral quantum dots in silicon/silicon-germanium heterostructures have been reported [5], [6]. However, none of these were achieved by the classical split-gate technique that is necessary for the coupling of quantum dots and for high integration.

Sample Preparation

GaAs/AlGaAs

High mobility modulation doped GaAs/AlGaAs heterostructures were grown by MBE at TU Vienna. The 2DEG in these samples is typically situated 70 – 100 nm below the surface. Further processing of the samples was done in the cleanroom in Linz. Hall bars were structured by optical lithography. Ohmic contacts to the 2DEG were made by depositing Cr, Au, Ge, Ni, Au and annealing at 450 °C. The mesa was wet chemically etched.

The electrical properties of the 2DEG were determined by quantum Hall effect and SdH measurements. Typical carrier densities were in the range from 2 to 4×10^{11} cm^{-2} with mobilities between 0.3 and 2×10^6 cm^2/Vs.

The area of the quantum dot is defined by Cr/Au gates on top of the Hall bar mesa, which were written by e-beam lithography. The top center gate electrode acts as a plunger gate. Gold connections from the bond pads to the small gates are structured by optical lithography.

Si/SiGe

High mobility modulation doped Si/SiGe heterostructures were grown by MBE in Linz. The 2DEG in these samples is situated about 85 nm below the surface. Hall bars were structured by optical lithography. Ohmic contacts were formed by deposition of Au/Sb and subsequent annealing at 350 ºC. A Hall bar structure was prepared by reactive ion etching (RIE) with SF_6.

Electrical measurements (SdH and QHE) at 1.5 K showed an electron mobility of 150,000 cm²/Vs at an electron density of 3.2 x 10^{11} cm^{-2}

The split gate structures were written by e-beam lithography and defined by lift-off of the Schottky-gate metal Pd. The top center gate electrode acts as a plunger gate. Connections from the bond pads to the small gates are made of Palladium.
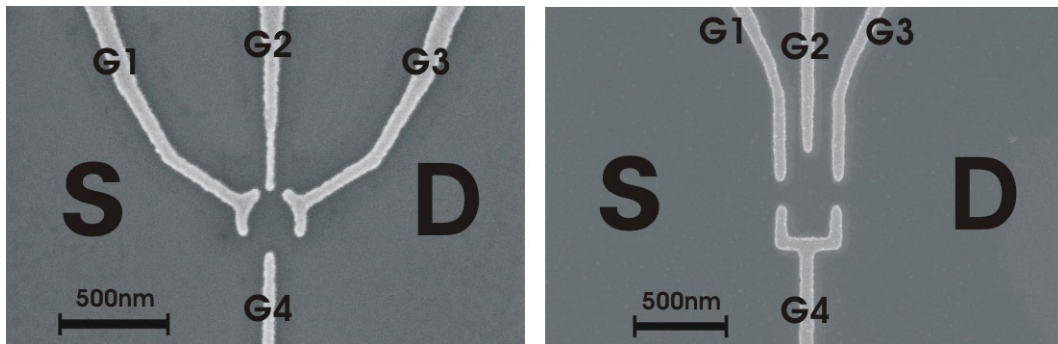
Fig. 1: Scanning electron micrograph of (a) the Cr/Au top gates on a GaAs/AlGaAs sample and (b) the Pd split gates on a Si/SiGe sample. The pitch between the upper gates is 185nm.

Measurements

When applying a negative voltage to the gates the underlying 2DEG is depleted and the dot area is defined in the center. By varying the plunger gate voltage, the energy levels inside the quantum dot can be moved into and out of resonance with the Fermi level in the leads. The conductance will increase whenever the energies are aligned and decrease in between, forming the so called Coulomb oscillations. If a large DC bias is applied at the source drain contacts the transport blockade can be overcome and excited energy states of the quantum dot can be probed.

GaAs Quantum Dots

By measuring the conductance versus both the plunger gate voltage V_G and the source drain voltage V_{SD}, we obtain the so-called quantum dot spectrum. It gives access to a lot of information about the quantum dot. Such a measurement is shown in Fig. 2 (a) below.

From the size and shape of the rhombic regions indicated by lines we obtain electrical properties such as capacitances of the gates and leads with respect to the dot. It is also possible to estimate the electrically active size of the dots from these data. This will differ from the actual geometrical size of the dot because of a depletion region, which extends around the gates. The difference between structural diameter and electrically active diameter indicates that the depletion region extends about 80 – 90 nm around the gates.

By changing the plunger gate voltage the tunnel barriers are also influenced, which limits the number of measurable Coulomb oscillations. Counteractive changing of the voltage on the outer gates allows us to stabilize the tunnel barriers and therefore increase the range of occupation numbers accessible by measurement.

In a few of the investigated samples we have observed conductance fluctuations superimposed upon the usual Coulomb oscillations. What at a first glance looked like random noise, turned out to be a reproducible fluctuation on a very small gate voltage scale, which was preserved over several sweeps in both directions (see Fig. 2 (b)).

Fig. 2: (a) Differential Conductance of the AlGaAs quantum dot as a function of gate voltage and applied dc source-drain voltage; (b) reproducible conductance fluctuations.

Interestingly, these fluctuations still occur on an energy scale smaller than 3 µeV, which is an order of magnitude smaller than the thermal energy at 300 mK (k_{BT} = 26 µeV), and would therefore be assumed to be smeared out.

Further measurements will be required to investigate the exact origin of these fluctuations.

Si/SiGe Quantum Dots

A lateral quantum dot formed by a split-gate technique was realized on a modulation doped $Si/Si_{0.75}Ge_{0.25}$ heterostructure and Coulomb blockade was measured up to 1 K. Figure 3 shows the quantum dot spectrum ("Coulomb diamond") taken at 30 mK and 1 K.

By analyzing the measured Coulomb diamonds we estimated the gate and the source capacity to be 6.4 aF and 30 aF respectively and the total dot capacity to be 65 aF. Therefore the dot diameter is approximately 160 nm resulting in less than 70 electrons in the dot.

These results show that SET functionality can be achieved in modulation-doped Si/SiGe heterostructures with a standard split-gate approach that can easily be integrated into an array of coupled SETs as suggested in Ref. [3].
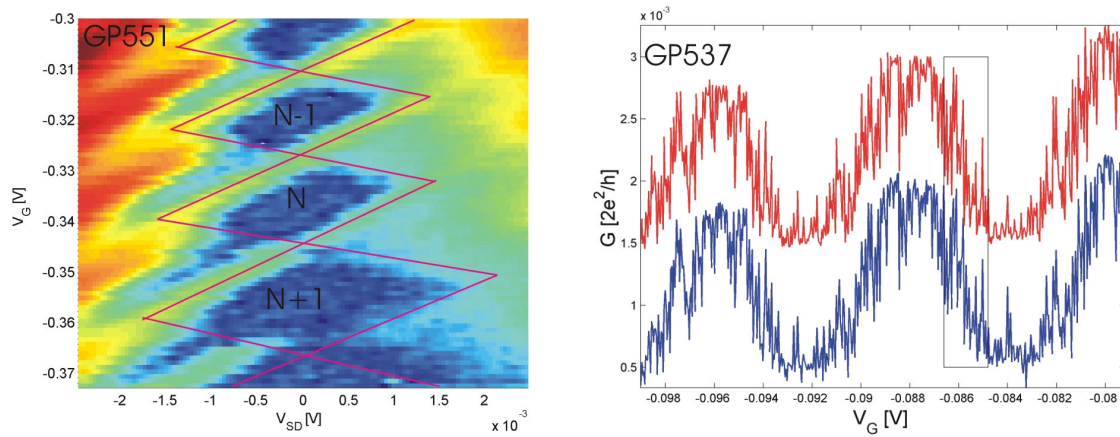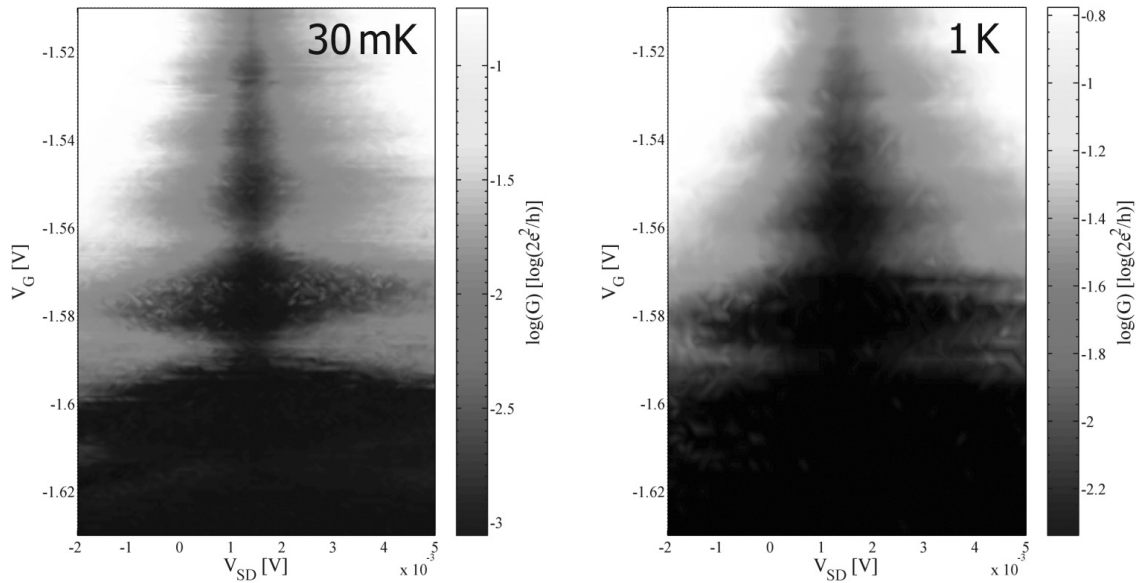
Fig. 3: Differential Conductance of the Si/SiGe quantum dot as a function of gate voltage and applied dc source-drain voltage at a) 30mK and b) 1K. Coulomb blockade diamonds are clearly visible.

Conclusion and Outlook

Single lateral quantum dots in the 2DEG of modulation doped GaAs/AlGaAs and Si/SiGe heterostructures have been realized with a split-gate technique. Coulomb blockade measurements, which prove the functionality of our devices, were performed down to a temperature of 30 mK. Based on these results we will fabricate quantum dot circuits consisting of two or more dots, which may be combined with quantum point contacts for charge readout.

Acknowledgements

References

[1]   D. Loss, D.P. DiVincenzo: "Quantum computation with quantum dots", Phys. Rev. A 57, 1998, 120 – 126

[2]   L.M.K. Vandersypen et al., quant ph/0207059 (unpublished)

[3]   M. Friesen et al: " Practical design and simulation of silicon-based quantum-dot qubits", Phys. Rev. B, 67, 2004, 1213010-1 – 1213010-4

[4]   J. Elzerman et al.: "Few-electron quantum dot circuit with integrated charge read out", Phys. Rev. B 67, 2003, 161308-1 – 161308-4

[5]   A. Notargiacomo et al: "Single-electron transistor based on modulation-doped SiGe heterostructures", APL, 83, 2003, 302 – 304

[6]   L. J. Klein et al: "Coulomb blockade in a silicon/silicon–germanium two-dimensional electron gas quantum dot", APL, 84, 2004, 4047 – 4049

Self Organized InAs Quantum Dot Arrays on Patterned GaAs Substrates

M. Schramböck, W. Schrenk, T. Roch, A. M. Andrews, M. Austerer, and G. Strasser

Center for Micro- and Nanostructures
Vienna University of Technology, A-1040 Vienna, Austria

Self-assembled semiconductor nanostructures such as quantum dots (QDs) have been under intense investigation during the last years due to their appealing electronic and optical properties. Unique physical properties have been observed in QD structures, and device applications using QDs, such as lasers, detectors and memories, have been explored. However, for novel QD devices like single photon sources or transistor structures, it is desirable to control the lateral position of the QDs. To achieve this, nanoscale grid patterns can be used to laterally align the QDs.

In this work, the self organization of InAs quantum dots grown with molecular beam epitaxy (MBE) on pre-patterned GaAs substrates was investigated. To create the grid patterns on the substrates, holographic lithography has been used.

Holographic lithography was studied because it provides an easy and efficient way to create nanosized patterns over large areas. For holographic lithography a He-Cd laser at a wavelength of 325 nm was used as an ultraviolet (UV) light source. After coating the GaAs substrate with photoresist it was then exposed in a holographic apparatus. The nanoscale grid patterns were then transferred onto the GaAs using wet chemical etching.

After preparing the substrates they were thoroughly cleaned, inserted into the MBE chamber and prepared for the growth. After growing a GaAs-based buffer layer on the substrates, they were consequently covered with self assembled QDs. These dots are either embedded into GaAs or serve as surface dots for further investigations.

The dot density, lateral and size distribution is measured using atomic force microscopy (AFM). Photoluminescence (PL) measurements performed on the samples with and without patterns give further information on dot size and size distribution. Furthermore, the influence of different dot growth conditions on dot quality and density is examined.

Ultrafast Intersublevel Spectroscopy of Quantum Dot Ensembles and Single Quantum Dots

F.F. Schrey, G. Fasching, T. Müller, G. Strasser, and K. Unterrainer

Zentrum für Mikro- und Nanostrukturen, Technische Universität Wien, Floragasse 7, A-1040 Wien

Based on ultrafast interband pump intraband probe spectroscopy we measure electron capture and relaxation times into the discrete dot energy levels within a few picoseconds and discuss possible relaxation mechanisms. Further we present an approach to rule out dot ensemble related effects within the time resolved measurements by combining interband micro-photoluminescence measurements with the intersublevel pump and probe spectroscopy. We show preliminary results for time-resolved, mid infrared induced direct electron transfer between electron intersublevels, which is monitored by changes in the interband luminescence of a single quantum dot.

Introduction

The strong interest in semiconductor quantum dots (QD) is based on their macroscopic quantum mechanical properties. Their low dimensionality within the surrounding 3D semiconductor matrix reduces phase scattering within the quantum mechanical wavefunctions of the QDs and leads to atomlike eigenstates in their energetic structure. Within the last decade, many attempts were made to exploit these properties in order to optimize the performance of optoelectronic devices like mid- and far-infrared photodetectors [1] or QD based near-infrared band-gap lasers [2]. Furthermore, it became possible to directly address single QDs, which led to optically and electrically driven single photon turnstile devices [3]. QDs can even be regarded as candidates for quantum-bit operations since its eigenstates could be entangled and basic q-bit operations have been carried out [4].

However many questions concerning carrier dynamics in QDs still remain open. Especially where only the electrons within the dots contribute to the device performance, the existing interband techniques to study exciton dynamics within these nanostructures deliver only ambiguous results, which complicate or even prevent the correct design of the device. Hence, getting access to the electron properties separated from hole contributions and ensemble related effects will allow accurate predictions how far QDs can improve devices working in the MIR and FIR regions.

We will demonstrate how ultrafast interband pump intraband probe spectroscopy will access these informations.

Experiments

Both samples were grown by MBE on semi-insulating GaAs substrates. The first one, for QD ensemble experiments, consists of 30 layers of InAs QDs separated by 50 nm thick GaAs barriers and a 50 nm GaAs cap layer. The dot density was estimated from an atomic force microscopy study to be around 2×10^{10} cm^{-2} per layer. For IR absorption measurements, the sample was polished at 58° to the growth axis in order to form a single-pass waveguide for the IR radiation and to enable a considerable electric field

component along the growth axis. The second sample for single dot (SQD) experiments contains only one QD layer with a density gradient between 10^7 dots/cm^2 and 5×10^{10} cm^{-2}. In the low-density area, the sample was processed into 8.5 μm tall micropillars with diameters between 1 and 10 μm. This assures the illumination and detection of one QD only in the micro-photoluminescence (μPL) experiments below.

For the first sample room-temperature photoluminescence (PL) spectra for two different excitation densities were recorded using a continuous-wave Ti:sapphire laser (740 nm excitation wavelength). From the PL we determine an energetic difference of 252 meV between the QD ground state e1h1 and the wetting layer (WL). Approximately two thirds of this energetic difference occur between the conduction band offsets [5]. Thus, we estimate the intraband transition energy between the QD ground state e1 and the WL to be ~160 meV. Accordingly, we expect intraband transitions from the excited states e2 and e3 to the WL at energies of ~105 meV and ~50 meV, respectively. Thus, the intraband absorption into the WL at probe energies of 160, 105 and 50 meV can be interpreted in terms of e1, e2 and e3 QD level electron populations, respectively.

For time-resolved probing of the intraband transitions, we used a mode-locked Ti:sapphire laser that delivers 12 fs pulses centered at a wavelength of 780 nm. Half of the laser intensity I_p served as an interband pump to inject electrons and holes in the GaAs barriers. The other part was used to generate the linear polarized IR probe pulses by phase-matched difference frequency mixing in a 0.5 mm thick GaSe crystal [6]. The probe pulses are tunable in the 75 – 155 meV range with pulse durations between ~100 and ~200 fs.

Absorption signals were measured at two different IR probe beam polarizations: When the probe is polarized perpendicular to the growth direction (s-polarization) we observe a step-like increase of the absorption, which rises within the time resolution of the experiment and decays within several hundred picoseconds. This signal is attributed to free-carrier absorption in the substrate and barriers and its decay to free-carrier recombination. When the probe is polarized in growth direction (p-polarization) a slowly rising absorption superimposed on the free-carrier signal is observed. Relaxation and thermalization in the GaAs barriers and the InAs WL occur on a time scale <1 ps. Thus, the slow rise of the absorption reflects the effective electron capture into the QD, more precisely into the QD ground state. From the absorption data, we deduce the capture time τ_c by an exponential fitting procedure.

Let us turn our attention to an excitation regime where electron-electron scattering can be ruled out as a relaxation mechanism [7]. Recording the temperature-dependence of the capture time at I_p = 25 W/cm^2 we find an increase of τ_c from 2.7 ps to 4.7 ps upon decreasing the temperature from 300 K to 5 K. Two scattering mechanisms could explain such short capture times: (i) multi-phonon emission and (ii) electron-hole scattering.

(i) Multi-phonon emission: The most efficient capture pathway in our sample is the step-wise relaxation through the excited QD states. The longitudinal optical (LO) phonon energy in InAs amounts to E_{LO} = 29 meV and the average electron level separation in our QDs is ~55 meV. Thus, one possible explanation for the observed short capture times could be that electrons scatter between subsequent QD states via repeated emission of two LO phonons [7], [8]. Although LO phonons can relax electrons in a QD only for a narrow range of dot sizes (because of their weak dispersion), emission of energetically different LO phonons (from the GaAs barriers, the WL, the QDs, and the respective interfaces) and also broadening of the phonons (due to strain and alloy inhomogeneities) could enlarge this energetic window [6]. This "continuum" of LO phonons could relax the entire distribution very efficiently.

(ii) Electron-hole scattering: since this process involves only a single electron and a single hole in a QD, it can occur even at very low excitation densities [9]. Due to the high effective hole mass, the QD level separation in the valence band is in the range of

a few meV. This allows holes to thermalize within several hundred femtoseconds. Electrons in the conduction band can transfer their energy to holes, which then lose their energy via phonons. Holes can be scattered depending on their initial energy either into higher QD hole states or into the WL.

Our understanding of the capture process is the following: Electrons are generated by the pump pulse in the GaAs barrier and are then transferred very fast into the WL. This process, which is mediated by LO phonons, occurs on a sub-picosecond timescale [10]. Afterwards the electrons relax between subsequent QD states either via repeated emission of two LO phonons or via subsequent electron-hole scattering processes.
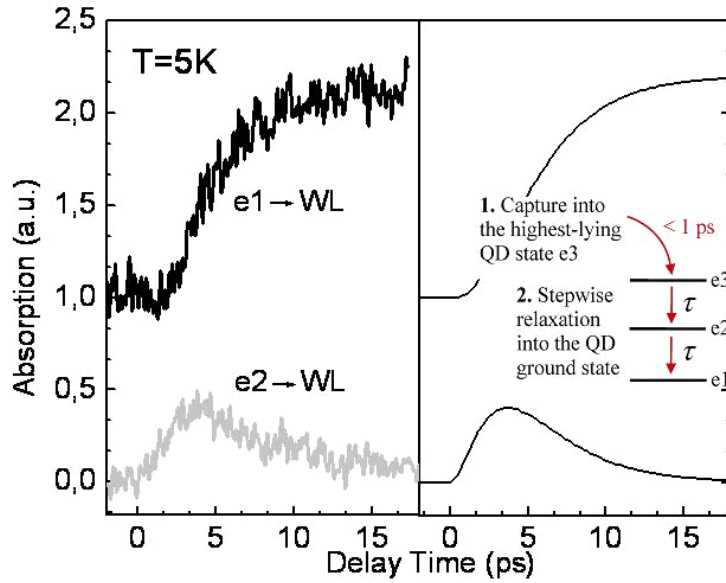

Fig. 1: (a) Photoinduced IR absorption signals for the E1-WL transition at 155 meV and the E2-WL transition at 105 meV (lower curve) as a function of pump-probe delay at 5K. (b) Results from the three level model sketched between the curves.

In order to support this interpretation we compare in Fig. 1 (a) the IR absorption at energies of 155 meV and 105 meV, corresponding to the e1-WL and e2-WL intraband transitions, respectively (T = 5 K). Note that in this figure the free-carrier absorption signals have been subtracted for better clarity. Since the absorption signals can be interpreted in terms of QD level populations it is clear that the QD ground state e1 gets populated via the excited state e2, because the electrons leave e2 with the same time constant as they arrive in e1. In Fig. 1 (b) we present results obtained by solving the rate equations for a simple three-level model, shown in the inset. In this model it is assumed that electrons populate the highest-lying QD state e3 within 1 ps after the pump and relax afterwards via e2 to the ground state e1. Good agreement with the experimental data is obtained for τ = 2.5 ps. These results suggest that not only the capture, but also the relaxation of electrons in our QDs occurs on a picosecond timescale [7].

However, these experiments cannot completely satisfy question concerning the relaxation processes. The ensemble broadening in PL as well as in the absorption signal might cover important aspects within the dynamic behavior of the dots. To rule out ensemble related processes or contributions from the surrounding material these time resolved studies have to be extended into the SQD regime. Since direct MIR pump and probe measurements on SQDs are impossible due to the small sensitivity of absorption measurements, another radiative process has to be used to monitor the intersublevel dynamic. We suggest using the recombination NIR radiation of excitons and excited

excitons within the SQD for this purpose. By combining P&P with the µPL setup, we obtain all necessary tools for our time resolved investigation.

Preliminary results from NIR excitation of a SQD within a micromesa structure superimposed with cw MIR radiation indicate a direct electron transfer between the s- and p-levels of the SQD [11], [12]. Corresponding to the electron occupation the photon count rate of the exciton lines is changed if MIR excitation is superimposed on the NIR excitation.

In case of a time resolved experiment we expect changes in the photon count rate in dependence of the NIR-pump-MIR-probe delay. Such an experiment is depicted in Fig. 2 (a) where we recorded the delay dependent count rate for an exciton ground state in a SQD within a 5 µm micropillar.
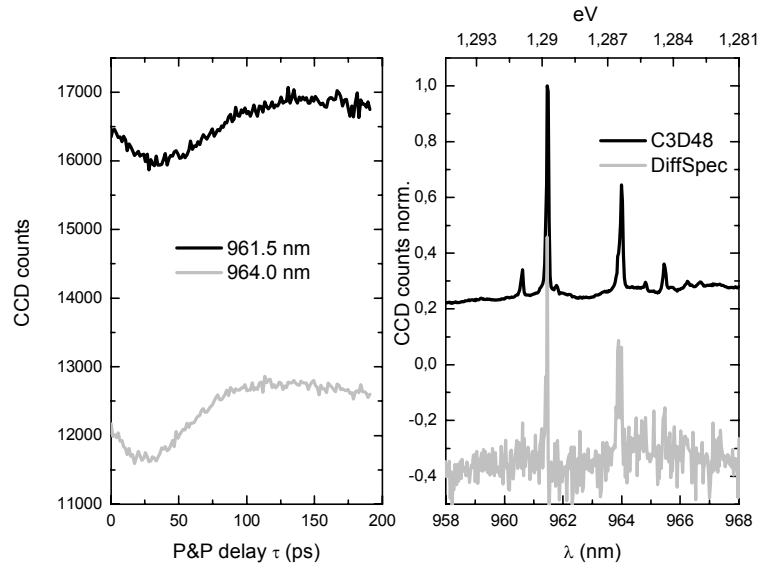

Fig. 2: Intersublevel dynamics in a SQD: (a) Photon count rate in dependence of P&P time delay τ. (b) Spectrum of QD ground state (upper curve) and difference spectrum after NIR/MIR superposition at τ = 30 ps.

In this case, the electron is transferred via the 95 meV MIR probe pulse from the ground state into the WL continuum and thus removed from the recombination channel of the SQD. Consequently, the PL count rate decreases for the observed transitions at 961.5 nm and 964 nm. As control experiment we recorded the SQD spectrum for NIR excitation with and without superimposed MIR radiation at delay τ = 30 ps. Afterwards we subtracted both spectra from each other as depicted in the lower curve of Fig. 2 (b). Again the count rate was decreased if an appropriate delay interval was chosen while no effect could be monitored if a very large time delay (>400 ps) was chosen. Further investigations of these MIR induced electron transfers will follow and new insights into the relaxation effects within SQDs are expected in the near future.

Conclusions

We suggest exploiting the capacity of ultrafast interband pump intraband probe spectroscopy combined with µPL tools for the investigation of QD dynamics. We could monitor the electron capture and relaxation dynamics of a QD ensemble on a low picosecond timescale. In addition, we could demonstrate a P&P procedure that allows studying electron dynamics in a single QD.

Acknowledgements

References

[1] L. Rebohle, F. F. Schrey, S. Hofer, G. Strasser, and K. Unterrainer, Appl. Phys. Lett. 81, 2079 (2002).

[2] D. Bimberg, N. N. Ledentsov, N. Grundmann, N. Kirstaedter, O. G. Schmidt, M. H. Mao, V. M. Ustinov, A. Y. Egorof, A. E. Zhukov, P. S. Kopev, Z. I. Alferov, S. S. Ruvimov, U. Goesele, and J. Heydenreich, Phys. stat. sol. (b) 194, 159 (1996).

[3] P. Michler, A. Kiraz, C. Becher, W. V. Schoenfeld, P. M. Petroff, Lidong Zhang, E. Hu, A. Imamoglu, Science 290, 2282 (2000)

[4] Xiaoqin Li, Yanwen Wu, Duncan Steel, D. Gammon, T. H. Stievater, D. S. Katzer, D. Park, C. Piermarocchi, and L. J. Sham, Science 301, 809 (2003)

[5] D. Wasserman and S. A. Lyon, Appl. Phys. Lett. 81, 2848 (2002).

[6] R. A. Kaindl, D. C. Smith, and T. Elsaesser, Opt. Lett. 23, 861 (1998).

[7] T. Müller, F.F. Schrey, G. Strasser, and K. Unterrainer, Appl. Phys. Lett. 83, 3572 (2003)

[8] M. De Giorgi, C. Lingk, G. von Plessen, J. Feldmann, S. De Rinaldis, A. Passaseo, M. De Vittorio, R. Cingolani, and M. Lomascolo, Appl. Phys. Lett. 79, 3968 (2001).

[9] T. S. Sosnowski, T. B. Norris, H. Jiang, J. Singh, K. Kamath, and B. Bhattacharya, Phys. Rev. B 57, R9423 (1998).

[10] R. Ferreira and G. Bastard, Appl. Phys. Lett. 74, 2818 (1999).

[11] F.F. Schrey, G. Fasching, T. Müller, G. Strasser, and K. Unterrainer, phys. stat. sol. (c) 1, 434 (2004)

[12] F.F. Schrey, T. Müller, G. Fasching, S. Anders, C. Pflügl, W. Schrenk, G. Strasser, and K. Unterrainer, Physica E 25, 271 (2004)

X-Ray Diffraction from a SiGe Island Quasicrystal

J. Stangl, J. Novak, E. Wintersberger, V. Holy, G. Bauer

Institute for Semiconductor and Solid State Physics, University of Linz, A-4040 Linz

Introduction

Nanometer-sized semiconductor islands and quantum dots have opened up the route to novel optoelectronic and electronic applications. The growth of islands by self-assembly in the Stranski-Krastanow growth mode is a well-established method. In general, self-assembled islands are inhomogeneous in size. An improvement of the size homogeneity can be achieved by growing islands in regular two dimensional (2D) arrays [1] – [5]. Such a 2D island lattice can be extended into a three dimensional (3D) island crystal by stacking island layers separated by spacer layers using appropriate growth conditions [6], [7]. Shape and size of the islands as well as their chemical composition undergo substantial changes during capping mainly due to interdiffusion with the spacer material. Direct images of the morphology of buried islands can be obtained by cross-section transmission electron microscopy (TEM) and scanning tunneling microscopy (STM) (see Ref. [8] and references therein). Alternatively, structural properties of buried islands can be studied by x-ray diffraction (XRD), which yields information on a much larger ensemble of the islands and is particularly sensitive to lattice strains.

We used coplanar high-angle XRD to investigate the size and the chemical composition of Ge/Si islands in a 3D island crystal. The evaluation of the experimental data was based on calculations of diffusely scattered intensity for a model island. For the calculations of the elastic strain fields caused by lattice mismatch between Si and Ge, we refined an analytical solution of continuum elasticity equations, which was used in Refs. [9] – [11] for the calculation of strain fields in two dimensions, for SiGe wires and laterally modulated $InAs_nAlAs_m$ short period superlattices.

Experimental

The investigated sample was grown by solid-source molecular beam epitaxy on Si(001), which was prepatterned with a square grid of pits using electron beam lithography and reactive ion etching. The pit grid is oriented along $\langle 110 \rangle$ directions and has a period of 400 nm. The size of the patterned area is 0.5 x 0.5 mm^2. After growth of a 150 nm thick Si buffer layer, further deposition of 6 ML of Ge at 700 °C resulted in 2D ordered islands, with one island per pit. After depositing 30 nm of Si as a spacer layer 12 double-layers of Ge islands and Si spacer layers of about 25 nm were deposited at 650 °C. The topmost island layer was left uncapped for atomic force microscopy (AFM) investigations. The islands grew in the same 2D grid in each island layer due to their preferential nucleation in strain energy minima above the underlying islands in the pits.

A nearly perfect 3D island crystal was produced in this way. Details on growth and atomic force microscopy (AFM) images of the topmost island layer are shown in Ref. [7]. The aspect ratio of the uncapped island sidewalls height/width = 0.2 corresponds to {105} sidewall orientation, which is characteristic for pyramidal islands.
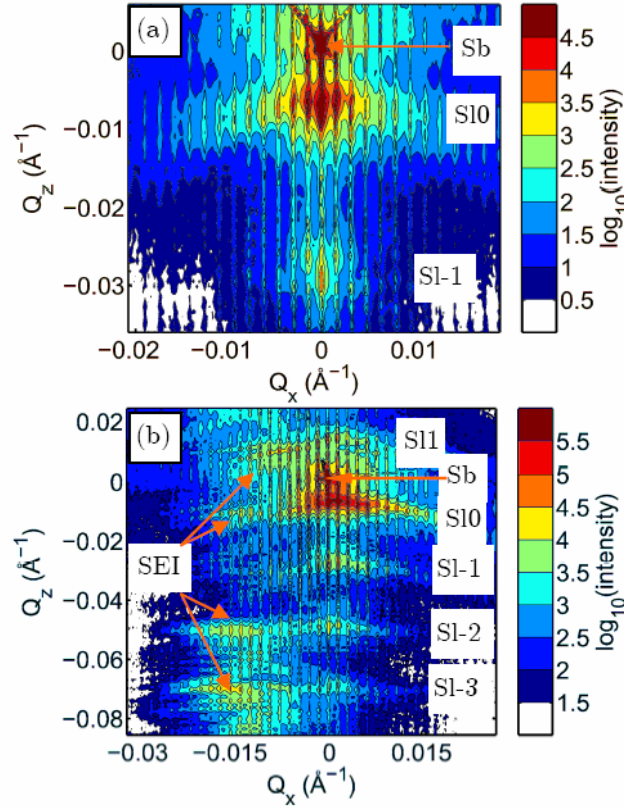
Fig. 1: Measured reciprocal space maps around the (224) (a) and (004) (b) reciprocal lattice points. Vertical satellites, originating from the periodicity of the island layers along the growth direction, are denoted Sl-3 to Sl1. Substrate peaks are denoted by Sb, and SEI denotes stripes of enhanced intensity (see text).

The measurements were carried out at beamline ID10B at the European Synchrotron Radiation Facility (ESRF), Grenoble, at a wavelength of 1.547 Å. High-resolution XRD was measured in coplanar geometry using a Si (111) analyzer in front of a point detector in order to resolve the lateral satellites. Diffusely scattered intensity around the symmetrical (004) and asymmetrical (224) substrate lattice points was measured, the resulting reciprocal space maps (RSMs) are shown in Fig. 1. The Si substrate peaks are denoted by Sb, horizontal stripes of enhanced intensity, denoted Sl-3 to Sl1 in Fig. 1, are vertical satellites due to the periodically repeated motif of island layers / spacer layers. Their distance corresponds to a vertical period of $L_\perp$ = 30.0 ± 0.5 nm.

For the simulations of scattered intensity we used kinematical approximation, as we fitted the intensity distribution beside the crystal truncation rods, where dynamic scattering effects are not important. The expressions used involve the displacement field in the sample, which we calculated by means of an analytic solution of the elasticity equations. We assume that the islands in each island layer form a perfect 2D lattice and that the islands are perfectly stacked above each other. Additionally, the size, shape, and chemical composition of all islands in the 3D island crystal are assumed to be identical. We neglected the uncapped island layer on top of the sample, but rather assume a flat sample surface. In coplanar diffraction geometry, the existence of the uncapped island layer has no significant influence on the scattered intensity.

Due to the lateral periodicity of the island pattern, we performed a Fourier transformation in the expressions of the scattered intensity as well as in the displacement fields and the elastic constants, allowing for an analytic solution of the equilibrium equations of elasticity. Details can be found in Ref. [12].
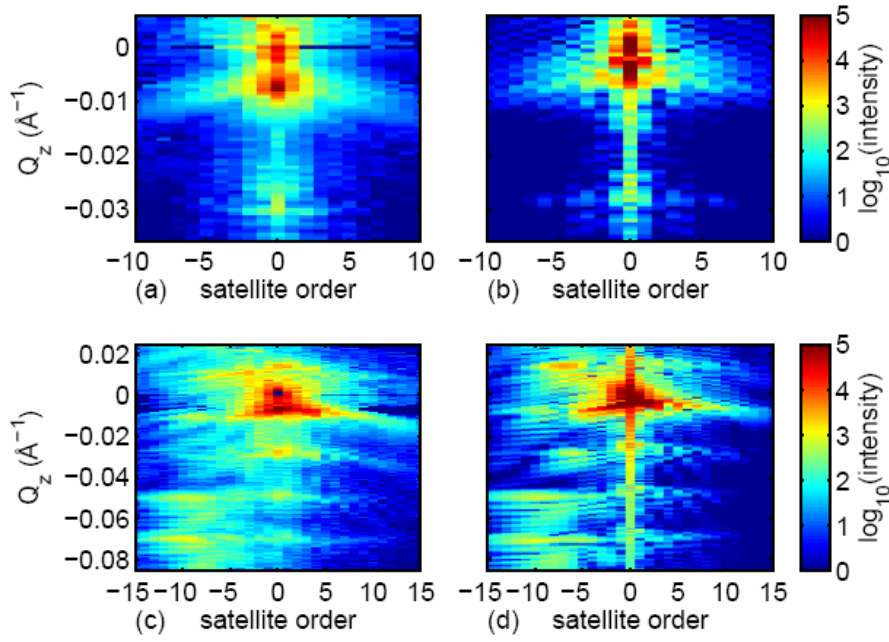
Fig. 2: 2D map of the lateral satellite intensities extracted from RSMs measured around the (004) (a) and (224) (c) reciprocal lattice points. Simulations of diffusely scattered intensity for the (004) (b) and (224) (d) diffractions.

Results

In order to evaluate x-ray data we first fitted the measured intensity profiles along the Q_x axis by series of Lorentzians. Their amplitudes are plotted in Figs. 2 (a), (c) as a function of the satellite order along the [110] direction and Q_z for (004) and (224) diffractions, respectively. The Q_x position of a given lateral satellite order is constant along Q_z, implying vertical replication of the lateral island positions in subsequent layers. The FWHM of the satellites as a function of satellite order is constant and comparable to the instrumental resolution, indicating the excellent long-range order of island positions.

For the simulations of the diffuse intensity and the strain fields all islands were assumed to have the same shape of a truncated cone, characterized by its bottom radius R_{bot}, top radius R_{top}, and height h_i. The Ge content x_i was assumed to be constant within islands. Additionally, a wetting layer (WL) of a constant thickness h_w and a constant Ge content x_w throughout the lateral unit cell was used. A rotational symmetry of the island shape was chosen in accordance with Ref. [13], where the preferential alloying of the island corners due to the surface diffusion of the Si atoms was observed, corresponding to an effective rounding of the islands during capping.

During fitting we made the following observations. (i) The lower the Ge content in the islands, the more intense are the lateral satellites close to the substrate peak. Furthermore, stripes of enhanced intensity within the vertical satellites move closer to the truncation rod. This can be explained by the decrease of the island lattice strain for lower Ge content. (ii) The higher the islands, the further away from the truncation rod the stripes of enhanced intensity are within the vertical satellites. This effect is connected with the larger degree of lattice relaxation in the island layers closer to the top surface. (iii) The vertical shift of the 0th order vertical satellite with respect to the substrate Bragg peak increases with the total amount of Ge in the WL. (iv) Finally, the tilt of the vertical satellites with respect to the Q_x axis increases with the island base radius.

The best simulation (see Figs. 2 (b), (d)) was obtained for island bottom and top radii of R_{bot} = 85 ± 10 nm and R_{top} = 10 ± 10 nm, island height of h_i = 19 ± 4 nm, and a Ge content of x_i = 40 ± 10%. The WL height was h_w = 0.8 nm and its Ge content x_w = 10% (only the product $h_w x_w$ can be determined from the fitting). We obtain an aspect ratio of $\eta = h_i / (R_{bot} - R_{top})$ = 0.25 ± 0.06, close to η = 0.2 of {105} facets typical for Ge pyramids, and different from η = 0.47 of {113} facets typical for Ge domes.

From the simulations also the lateral (ε_{xx}) and vertical (ε_{zz}) strains within the island stack follow (zero strain corresponds to the non-deformed Si lattice). The strain field is almost periodic in the vertical direction only in the region from 4th to 7th island layers; above and below the surface relaxation and influence of the Si substrate destroy the periodicity. The maximum lateral strain of ε_{xx} = 0.9% is observed in compressed SiGe in the top edges of the islands, corresponding to a degree of relaxation of 55% $Si_{0.6}Ge_{0.4}$. The lateral strain minimum of ε_{xx} = −0.5% is observed in compressed Si around the bottom edges of the islands. The vertical strain ε_{zz} increases in the lateral direction from the center of the islands towards their sidewalls. The maximum of ε_{zz} = 3.4% is observed in expanded SiGe in the bottom edge of the islands, and the minimum of ε_{zz} = −2% is observed in compressed Si just above the center of the top island facets.

Conclusion

An analysis of coplanar high-angle x-ray diffraction data was performed and structural information on buried Ge islands was obtained, which form a 3D island crystal. Combining an analytical solution of equilibrium equations of linear elasticity and kinematical scattering theory we successfully simulated the experimental x-ray diffraction data. Comparing the measured reciprocal space maps of the diffracted intensity with simulations, we found that the islands have {105} facets after Si capping, i.e., they have pyramidal shape. The Ge content in the islands is as low as 40 ± 10%. From the fits, also the strain state in and around the buried islands was determined.

References

[1]   O.G. Schmidt *et al.*, Appl. Phys. Lett. **77**, 4139 (2000).

[2]   G. Jin, J.L. Liu, K.L. Wang, Appl. Phys. Lett. **76**, 3591 (2000).

[3]   M. Borgström, V. Zela, W. Seifert, Nanotechnology **14**, 264 (2003).

[4]   Bin Yang, Feng Liu, M.G. Lagally, Phys. Rev. Lett. **92**, 25502 (2004).

[5]   Zh. Zhong, G. Bauer, Appl. Phys. Lett. **84**, 1922 (2004).

[6]   G. Springholz, V. Holý, M. Pinczolits, G. Bauer, Science **282**, 734 (1998).

[7]   Zh. Zhong *et al.*, Physica E **21**, 588 (2004).

[8]   J. Stangl, V. Holý, G. Bauer, Rev. Mod. Phys. **76**, 725 (2004).

[9]   T. Roch *et al.*, Phys. Rev. B **65**, 245324 (2002).

[10] J.H. Li *et al.*, Phys. Rev. B **66**, 115312 (2002).

[11] O. Caha *et al.*, J. Appl. Phys. **96**, 4833 (2004).

[12] J. Novak *et al.*, to be published.

[13] U. Denker, M. Stoffel, O.G. Schmidt, Phys. Rev. Lett. **90**, 196102 (2003).

Ballistic Electron Emission Microscopy (Posters)

Cross-Sectional Ballistic Electron Emission Microscopy for Schottky Barrier Height Profiling on Heterostructures

D. Rakoczy, G. Strasser, J. Smoliner

Institut für Festkörperelektronik & Mikrostukturzentrum der TU-Wien Floragasse 7, A-1040 Wien, Austria

In this work, Cross-Sectional Ballistic Electron Emission Microscopy (= "XBEEM") is introduced to determine a Schottky barrier height profile of a GaAs-AlGaAs multi heterostructure in cross-sectional geometry. Ballistic electron spectra measured across the heterostructure with nm resolution indicate that the measured Schottky barrier height profile is smeared out compared to the conduction band profile calculated from the sample growth parameters. We attribute this behavior to lateral band bending effects along the heterojunction. In addition, we have evidence that the barrier height profile is influenced by single impurities in the AlGaAs layers.

Introduction

Ballistic Electron Emission Microscopy (BEEM) [1], [2] is a three terminal extension of Scanning Tunneling Microscopy (STM) [3] – [5] where the STM tip is used to inject hot electrons into a semiconductor via a thin metallic base layer evaporated onto a semiconductor surface. If the electron energy is high enough to overcome the Schottky barrier height at the metal-semiconductor interface, the electrons can penetrate into the semiconductor. The corresponding current, measured vs. the tunneling bias using a backside collector contact, is called BEEM spectrum. By mapping the BEEM current for a constant tip bias while scanning the sample surface, images can be taken with a spatial resolution of about 1 nm. Presently, BEEM is a well established technique to determine Schottky barrier heights (SBH) and subsurface band offsets. An overview of this technique can be found in several review articles [6] – [8].

Cross-sectional STM techniques are widely used in surface physics. During the last years, it was found that cross-sectional STM techniques (XSTM) are especially helpful for the characterization of MBE (Molecular Beam Epitaxy) grown heterostructures. XSTM measurements, e.g. have resolved atomic features of segregated interfaces [9], [10]. More recently, special attention was given to XSTM on InAs-GaAs heterostructures, since they are the base material for self assembled quantum dots. On such samples, the local composition of the InAs dots and the wetting layer [11], [12] was studied by XSTM.

Surprisingly, and although it is a quite straightforward idea to combine cross-sectional STM techniques and BEEM, no cross-sectional BEEM (XBEEM) experiments have been reported in the literature until now. In our opinion, the reason for this is not a lack of application possibilities, but notable technical difficulties, e.g. the precise sample positioning and, especially for profile measurements, a state of the art compensation of piezo creep. Once these problems are overcome, XBEEM turns out to be a very useful technique to determine profiles of various band structure related features, e.g. the conduction band offsets of GaAs-AlGaAs multi heterostructures.

Experimental

In this paper, cross-sectional BEEM measurements are reported on the cleaved [011] surface of a GaAs-AlGaAs multi-heterostructure covered with gold. To test XBEEM as a new method for cross-sectional SBH profile measurements, we used an MBE grown GaAs-AlGaAs multiple barrier structure with relatively thick layers: On a semi insulating substrate (GaAs [100]), a 3 µm thick layer of n-type GaAs (silicon doped, $N_D = 8 \times 10^{16}$ cm^{-3}) was grown as a spacer. On top of this layer we grew 6 periods of an AlGaAs-GaAs heterostructure (d_{AlGaAs} = 20 nm, d_{GaAs} = 50 nm) followed by a 200 nm thick GaAs spacer. This layer sequence was repeated three times, however, with layer thicknesses of (d_{AlGaAs} = 50 nm, d_{GaAs} = 20 nm) and (d_{AlGaAs} = 50 nm, d_{GaAs} = 50 nm), respectively. The aluminum content was 30% for all AlGaAs layers. In order to use the sample in a BEEM configuration one has to provide means to collect the injected ballistic current. This was achieved by doping all GaAs layers with silicon ($N_D = 8 \times 10^{16}$ cm^{-3}) and the AlGaAs layers with $N_D = 5.6 \times 10^{16}$ cm^{-3}, which guarantees a sufficient collector conductance as well as a good Schottky contact.

To prepare the samples for BEEM, InSn pellets were alloyed into the sample to establish the collector contact. After that, the samples were cleaved in air and immediately transferred into a vacuum chamber. As base layer, a 7 nm thick gold film was evaporated onto the cleaved [011] surface at base pressures $<1 \times 10^{-7}$ mbar using shadow evaporation techniques. After the evaporation process, the samples were glued on edge onto a sample transfer plate with conductive silver, which also provides the contact to the InSn pellets. An indium covered gold wire was attached to the gold covered [011] surface as a base contact. Finally, the sample was transferred as fast as possible into an Omicron Cryo SFM head. The scanning head is operated in helium atmosphere in a variable temperature inset of a cryostat. In this way, an undesired oxidation of the AlGaAs layers is suppressed. For all STM and BEEM measurements presented here, Au-coated ($d_{AU} \approx 10$ nm) non-contact AFM-tips were used. All measurements were carried out at a temperature of T = 200 K. This temperature is a very good compromise in meeting the requirements of minimizing piezo drift and sample degradation on the one hand and of a sufficiently large scan field and an optimal duty cycle of the bath cryostat on the other hand.

Results

The left hand side of Fig. 1 (a) shows a topographic image of the active region of our sample. The image was recorded at a tunneling current of I_T = 2 nA and a bias of V_T = 1.6 V. Underneath the Au covered surface, the AlGaAs barriers are slightly visible as horizontal lines. The AlGaAs regions appear a little bit higher (≈ 0.5 nm) than the GaAs regions, which is due to weak strain effects between the GaAs and the AlGaAs layers. The right hand side of Fig. 1 (a) shows the corresponding BEEM image. Here, the AlGaAs barriers are clearly visible as dark horizontal lines. Note that the samples are not stable and start to degrade after being stored in air for some days. A typical example for this can be seen in Fig. 1 (b): Here, the Au layer appears to be broken into fragments and in the corresponding BEEM image (Fig. 1 (b), right), the AlGaAs barriers are no longer clearly resolved and appear to have intermixed with the GaAs layers. In addition, the overall transmission is reduced approximately by a factor of 5 compared to a fresh sample. We attribute this behavior to an oxidation of the AlGaAs layers.

Figure 2 shows typical BEEM spectra acquired on a GaAs (curve (1)) and an AlGaAs region (curve (2)) on the cross-section of our sample. To show the onsets more clearly, we zoomed into the interesting data range. As common practice in BEEM, the current onsets were determined by a Bell Kaiser fit and are at $V_{b,GaAs}$= 0.97 V and $V_{b,AlGaAs}$ = 1.235 V, respectively. The difference $e\Delta V_b$ = 265 meV is larger than the conduction band offset between GaAs and AlGaAs, which is ΔE_c =230 meV for x = 30% according to the literature. Further note that these onset positions are about 50 meV higher com-

pared to values commonly reported for conventional BEEM on [100] GaAs and AlGaAs samples. Possible explanations for this lie in the properties of the cleaved [011] surface and in the fact that the surface was not treated with HCl as it is usually done in conventional BEEM for oxide removal.
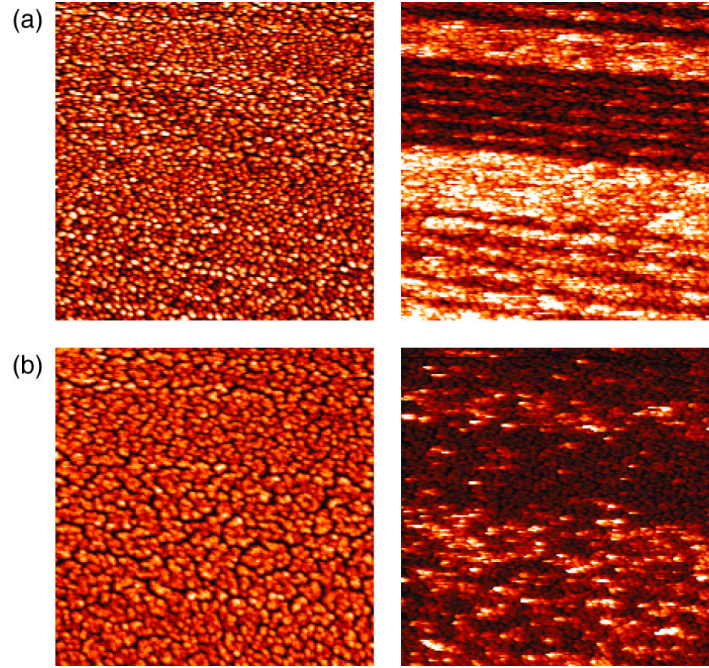

Fig. 1: (a), Left: Topographic STM image of the active region of our sample. Scan size is 1400 nm x 1400 nm. The z-scale is 4 nm. Tunneling current: I_T = 2nA, bias V_T = 1.6 V. Right: Simultaneously recorded BEEM image. The color scale corresponds to BEEM currents of 0…2.5 pA. (b), Images of a degraded sample, same scan size as in (a). I_T = 5nA, V_T = 1.6 V. Left: STM topography. The z-scale is 8 nm. Right: Simultaneously recorded BEEM image. The color scale corresponds to BEEM currents of 0…1.25 pA.
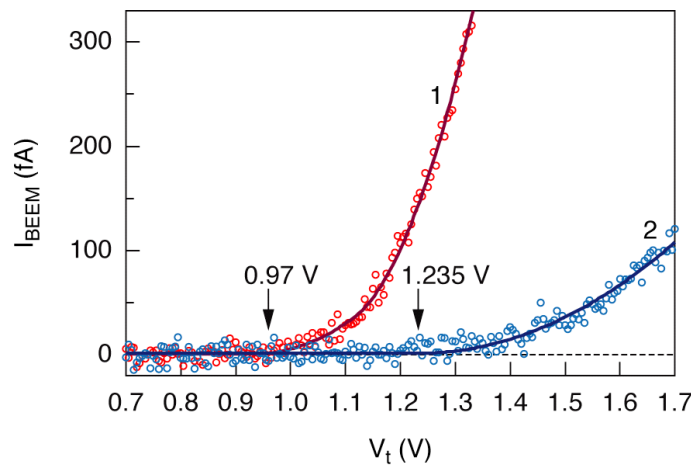

Fig. 2: Typical BEEM spectra acquired on a GaAs (curve (1)) and an AlGaAs region (curve (2)). The tunneling current was I_T = 2nA and the temperature was T = 200K. The onset bias is at 0.97 V and 1.235 V, respectively.

Figure 3 (top) shows a 143 nm x 45 nm large BEEM image taken in the area of an Al-GaAs barrier. The barrier region is visible as dark area in this image, embedded by two brighter regions of GaAs. As typical for BEEM, the Au grains have a significant influence on the transmission. The total transmission is a convolution of the transmission of the granular Au layer and the barrier underneath, which makes it difficult to depict the sharp MBE grown GaAs-AlGaAs interface precisely. However, a different Au-coverage of the base layer does not influence the onset of the BEEM spectra, which is merely determined by the Schottky barrier height.
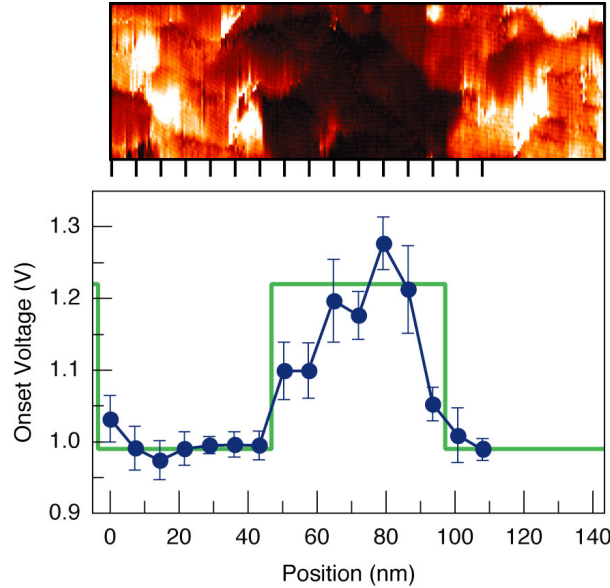

Fig. 3:   Top: BEEM image of a AlGaAs barrier region, Scan size: 143 nm x 45 nm. I_T = 2 nA, V_T = 1.7 V. The color scale corresponds to current values from 0 pA … 4 pA. Along the bottom line of this image, a series of BEEM spectra was recorded. The distance between the single points is 7.2 nm. Bottom: Measured Schottky barrier height profile determined from the BEEM spectra and the conduction band profile of the sample as calculated from the MBE growth parameters.

For a quantitative profile of the SBH across the heterostructure, a number of BEEM spectra (I_T = 2nA) were recorded at the marked spots along the bottom line of the image in Fig. 3. From the onset of these spectra, the local barrier heights were determined using a Bell-Kaiser fit. The result of this procedure can be seen in the lower part of Fig. 3 together with a conduction band profile based on the heterostructure design parameters. For comparison with the GaAs-AlGaAs band offsets, this band profile was aligned with the measured SBH in the GaAs regions. Each data point of the measured curve represents an average over the onsets of several spectra taken at the same position. The error bars indicate the standard deviation in the measured onset at each position. The lateral distance between the single data points is 7.2 nm.

As one can see, the barrier is depicted clearly in the profile. The barrier width is consistent with the BEEM image as well as with the growth parameters. However, the barrier height profile is not rectangular, as it would be expected from a conduction band profile obtained from the MBE growth parameters, and also exhibits a certain asymmetry. In addition, the maximum barrier height difference between GaAs and AlGaAs differs notably from the expected conduction band offset between GaAs and AlGaAs. Furthermore, the noise in the barrier height profile is significantly larger in the AlGaAs regions than in the GaAs areas on our sample.

Before the origins of the above features are discussed, we would like to point out that we can definitely exclude two possible experimental artifacts: First of all, the smeared out barrier height profile is not due to the limited lateral resolution of BEEM. As already confirmed in previous measurements, the typical resolution of BEEM is about 1nm. This is also verified by Fig. 3 (a), where BEEM contrast is achieved on such length scales. In contrast to that, the smeared out region in the barrier height profile is significantly larger.

Second, the higher noise in the barrier height profile in the AlGaAs regions is definitely not due to improper tunneling conditions. As one can see in Fig. 1 (a), the sample is very flat and the image quality is good everywhere. Also the noise in the BEEM spectra is equal for all regions (see Fig. 2) and the noise in the barrier height profile in the GaAs regions is comparable to what we are used from earlier measurements on reference samples. Thus, we conclude, that this effect is a genuine feature of the local properties of the AlGaAs layer.

In our opinion, the smeared out barrier height profile is most likely due to lateral band bending effects across the heterojunctions based on the following arguments: In general it can not be expected that the GaAs-AlGaAs conduction band offset is exactly mirrored by the difference in the SBH of the two materials. This is confirmed by our data, where the SBH on some points of the AlGaAs layers is notably larger than the SBH on GaAs plus the band offset between GaAs and AlGaAs. On the other hand, the Fermi level must be constant all over the sample surface and thus lateral band bending effects are unavoidable. A quantitative analysis of this behavior, however, requires extensive simulation as well as additional systematic measurements and is beyond the scope of this paper.

While lateral band bending can explain the amount of broadening on the right edge of the barrier profile seen in Fig. 3, it does not explain the rather gradual increase on the left edge of the profile. Also the increased noise in the AlGaAs regions is still an open issue. However, a look on earlier measurements, where we investigated the local influence of single impurities in AlAs barriers in BEEM [13], can shed light on this behavior. In that work we found that in the vicinity of an impurity the onset of the BEEM current was reduced from the Schottky barrier height of AlGaAs to the energetic level of the impurity.

Considering the design of our present sample, the AlGaAs barriers are doped with $N_D = 5.6 \times 10^{16}$ cm^{-3}, which means that the average distance between two impurities is ≈33 nm. Thus, on average, one to four impurities are present in the vicinity of any cross-section through a 50 nm thick AlGaAs barrier.

While in GaAs silicon impurity levels are close to the conduction band edge, they act as deep donors in AlGaAs. As shown in our previous work, the local influence of these impurities on the current onset position is quite dominant, which probably is the reason why the corresponding AlGaAs barrier height depends so strongly on the position on our sample. In contrast to that, the donor levels on GaAs are just 5 meV below the conduction band edge and therefore have almost no influence on the local barrier height. This is consistent with our experimental observation that the barrier height shows just little variations throughout the GaAs regions of our sample.

Summary

In summary, cross-sectional BEEM measurements were introduced to determine a Schottky barrier height profile on the cleaved [011] surface of a GaAs-AlGaAs multi-heterostructure. The measured data exhibit indications of lateral band bending effects at the GaAs-AlGaAs interfaces. Furthermore, an influence of deep impurity levels in the AlGaAs barriers on the measurements was observed.

Acknowledgements

References

[1]   W.J. Kaiser and L.D. Bell, Phys. Rev. Lett. 60, 1406 (1988)

[2]   L.D. Bell and W.J. Kaiser, Phys. Rev. Lett. 61, 2368 (1988)

[3]   G.Binnig, G.Rohrer, Ch.Gerber, E.Weibel, Phys. Rev. Lett. 49, 57 (1982)

[4]   R.Wiesendanger, Scanning Probe Microscopy and Spectroscopy, Cambridge University Press (1994)

[5]   C. Julian Chen, Introduction into Scanning Tunneling Microscopy, Oxford Series in Optical and Imaging Sciences, Oxford University Press (1993)

[6]   M.Prietsch, Physics Reports 253, 163 (1995)

[7]   V.Narayanamurti and M.Kozhevnikov, Physics Reports 349, 447 (2001)

[8]   J.Smoliner, D.Rakoczy, M.Kast, Rep. Prog. Phys. 67, 1863 (2004)

[9]   J.Harper, M.Weimer, D.Zhang, C.H.Lin, S.S.Pei, J.Vac. Sci. Technol. B16, 1389 (1998).

[10] R.Magri, A.Zunger, Phys. Rev. B64, 081305/1-4 (2001)

[11] D.M.Bruls, P.M.Koenraad, M.Hopkinson, J.H.Wolter, H.W.M.Salemink, Appl. Surf. Sci. 190, 258 (2002)

[12] S.L.Zuo, E.T.Yu, A.A.Allerman, R.M.Biefeld, J.Vac. Sci. Technol. B17, 1781 (1999)

[13] D.Rakoczy, G.Strasser, J.Smoliner, Phys. Rev. B68, 073304 (2003)

Organic Semiconductors (Posters)

High-Mobility n-Channel Organic Field Effect Transistors based on Epitaxially Grown C$_{60}$ Films

Th. B. Singh, N. Marjanović, G. J. Matt, S. Günes and N. S. Sariciftci

Linz Institute for Organic Solar Cells (LIOS),
Physical Chemistry, Johannes Kepler University Linz, Austria

A. Montaigne Ramil, A. Andreev, and H. Sitter

Institute of Semiconductor and Solid State Physics,
Johannes Kepler University Linz, Austria

R. Schwödiauer and S. Bauer

Soft Matter Physics, Johannes Kepler University Linz, Austria

Introduction

Organic thin-film electronics has developed to a promising technology in the last two decades with demonstrated prototypes of organic thin film transistors, organic integrated circuits for radio frequency identification tags (RFID-tags) [1], [2] and active matrix displays [3]. Organic field effect transistors (OFETs) have also been fabricated in arrays to drive electrophoretic display pixels [4]. The performance of the individual transistor limits the switching speed in an integrated circuit, which can be roughly estimated by the ratio of mobility and channel length of the transistor [3]. To obtain higher switching speed, the search for higher mobility materials is therefore important along with the effort to downscale the transistor geometry.

In this paper, we present results on OFETs fabricated using hot wall epitaxy (HWE) grown C$_{60}$ films on top of an organic insulator. HWE, working close to thermodynamical equilibrium, is well known as appropriate technique to grow highly ordered organic thin films, including C$_{60}$ films. The relatively smooth surface of the organic insulating film interfaced with a highly ordered HWE grown C$_{60}$ film resulted in mobilities of 0.4 – 1 cm^2/Vs and an on/off ratio >10^4. The obtained mobility is found to be nearly gate voltage independent with a normalized sub-threshold slope of 8 V·nF/decade·cm^2. Furthermore, the field effect mobility has been found to be thermally activated with an activation energy of ~100 meV within the temperature range of 90 – 300 K.

Experimental

A scheme of the device geometry is shown in Fig. 1 (a). The device fabrication starts with the etching of the indium tin oxide (ITO) on the glass substrate. After patterning the ITO and cleaning in an ultrasonic bath, a BCB layer is spin coated at 1500 rpm resulting in a 2 µm thick film. BCB was used as received from Dow Chemicals and curing was done according to the standard procedure. BCB is an excellent dielectric material with a rather low dielectric constant ε_{BCB}= 2.6 and a small, nearly temperature independent thermal expansion coefficient [5]. A 300 nm thick C$_{60}$ film was grown by HWE on top of the dielectric at a substrate temperature of 130 °C. The top source and drain electrodes (LiF/Al 0.6 / 60 nm) were evaporated under vacuum (2x10^{-6} mbar) through a shadow mask. LiF / Al is expected to form ohmic contacts on fullerenes [6]. The chan-

nel length L of the device is 35 µm and channel width W = 1.4 mm, which results in a W/L ratio of ≈40. From the measurement of the BCB film thickness, d = 2 µm and the dielectric constant of BCB, ε_{BCB} = 2.6, a dielectric capacitance C_{BCB} = 1.2 nF/cm^2 was calculated. In our devices we have a d/L ratio ≈0.05 acceptable not to screen the gate field by the source drain contacts. Device transportation from the HWE chamber to the glove box and further electrical characterization (using Keithley 236 and Keithley 2400 instruments) were carried out under argon environment. The surface morphology and thickness of the dielectric was determined with a Digital Instrument 3100 atomic force microscope (AFM) and a Dektak surface profilometer respectively. Device characterization at various temperatures was performed in a He flow cryostat (Cryo Industries) using a Lakeshore 331 as temperature controller.
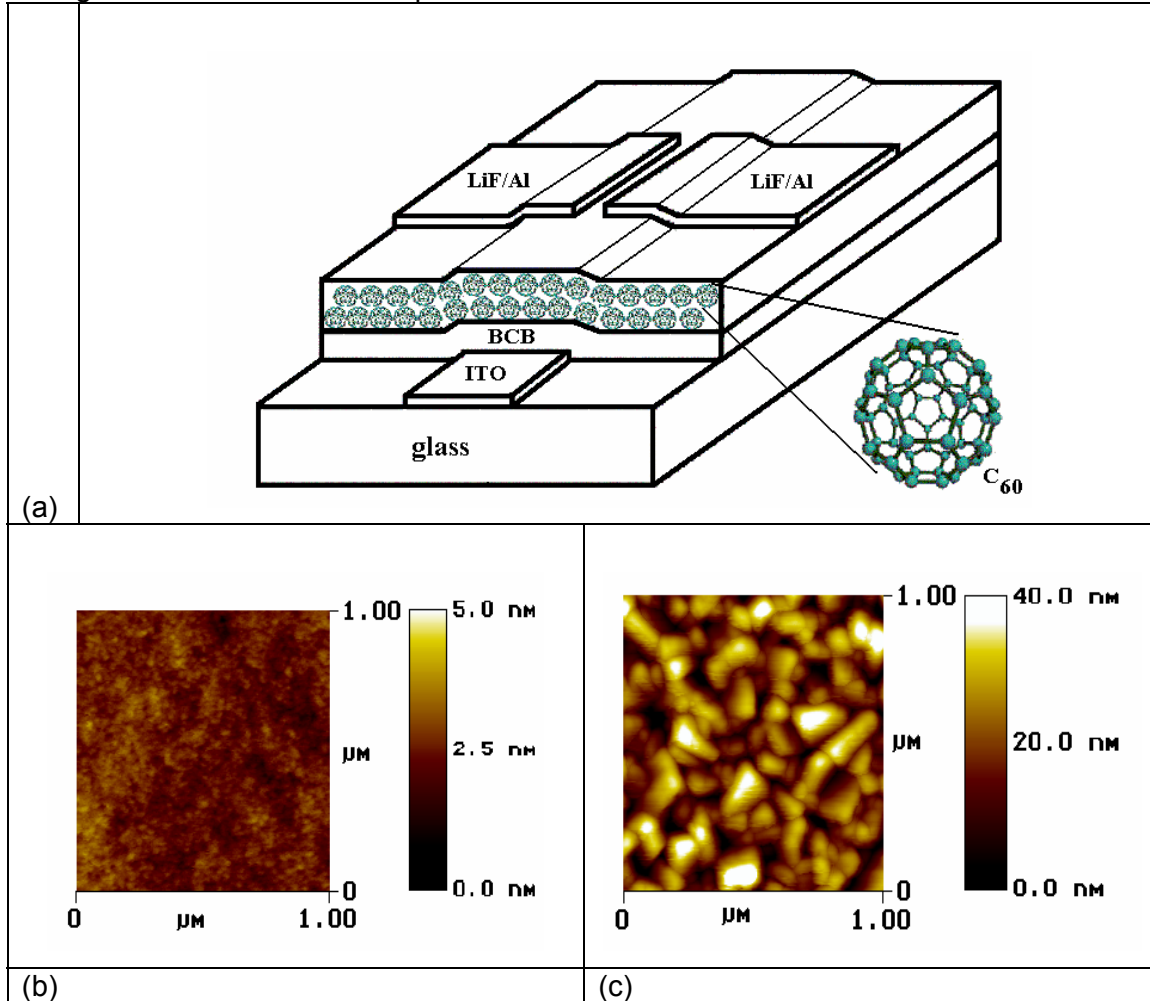

Fig. 1:   (a) Scheme of the staggered n-channel OFET device structure; (b) AFM image of the BCB dielectric surface; (c) AFM image of the C$_{60}$ surface in the channel region of the fabricated OFET.

Results

As shown in Fig. 1 (b), the dielectric layer showed a very smooth surface with a roughness <5 nm. This enables us to grow the next layer (C$_{60}$) with a very good control of the film morphology (Fig. 1 (c)). A recent study shows that the first couple of monolayers next to the dielectric dominate the charge transport in an organic semiconductor layer.
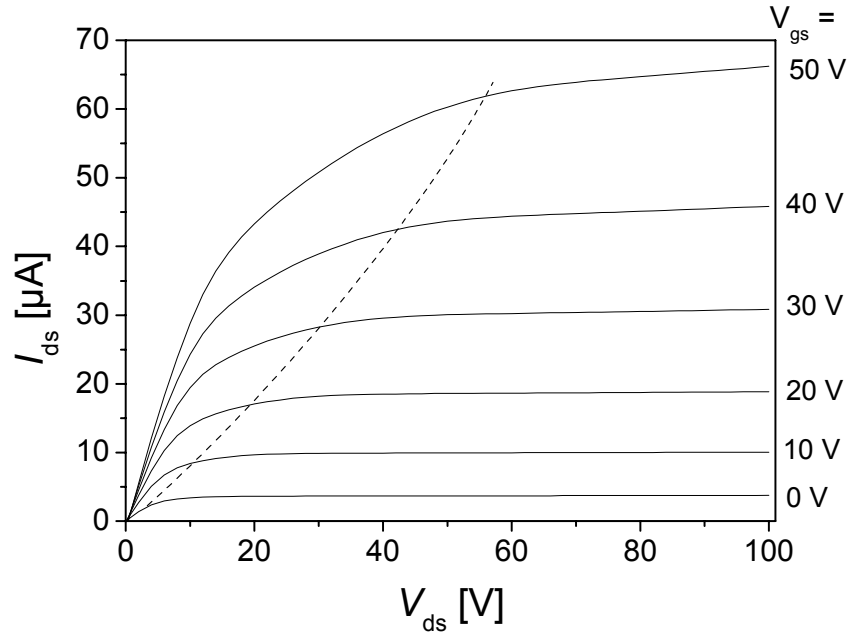
Fig. 2: I$_{ds}$(V$_{ds}$) curve of the OFET in the accumulation mode. The dotted line is a guide for the eye for saturated I$_{ds}$. The data shown here are taken in ascending V$_{gs}$ mode with integration time of 1s

Figure 2 shows the transistor characteristics of a device with a well saturated curve occurring pinch off at drain source voltage $V_{ds} \geq V_{gs}$ (gate Voltage). From the slope at V_{ds}= 0 V of the curve V_{gs} = 0 V, we evaluated a conductivity of 5 x 10^{-6} Scm^{-1}. For the same device (see Fig. 3) we measured the transfer characteristics. The data presented in Fig. 3 hold for V_{ds} = 60 V. One can see that the transistor turns on at an onset voltage of V_t = -35 V without significant hysteresis and drain-source current I$_{ds}$ increases quadratically. The device shows an on/off ratio >10^4 which is calculated as a ratio of I_{ds} at V_{gs} = 60 V and I_{ds} at V_{gs} = V_t. We have observed consistently the effect of having large drain-source current even when V_{gs} = 0 V. This effect is minimized when the dielectric layer is preheated at high temperature prior to the deposition of the active layer. This results in the shift of V_t. This effect is proposed to the presence of unintentional dopants at the interface of the untreated dielectric. Interfacial effects seem to play a major role in these devices. From $V_t = -(qn_0d_s/C_{BCB}) + V_{fb}$, where V_{fb} = 0.1 V is the flat band potential (which accounts for the work function difference between the semiconductor and the gate electrode without considering fixed charges at the dielectric and at the interface), d_s is the thickness of the semiconductor, q is the elementary charge and C_{BCB} is the capacitance of the gate dielectric, we were able to estimate the density of free carriers at equilibrium n_o. This yields a relatively high electron density of ~10^{17} cm^{-3}.

As shown in Fig. 3, from the fit to the data using equation (1) [7]:

$$I_{ds} = \frac{\mu W C_{BCB}}{2L}\left(V_{gs} - V_t\right)^2 \tag{1}$$

we extract a field effect mobility of 0.63 cm^{2}V^{-1}s^{-1} in the saturation regime for V_{ds} = 60 V (note the fitting line used for the mobility extraction fits the data over a wide range of V_{gs}). However, while we calculated field effect mobility, contact resistance of LiF/Al and C$_{60}$ is not taken into account assuming contact resistance is fairly low. Our studies of the dependence of field effect mobility on metal work functions on soluble methano-fullerene based OFETs have shown a highest μ of 0.2 cm^{2}V^{-1}s^{-1} with LiF/Al as drain-

source electrode. Use of higher work function metal electrodes viz. Cr, Au etc. in these OFETs leads to slightly reduced mobilities. Similarly we have also observed the slight decrease in field effect mobility in C_{60} OFETs with higher work function electrode (not shown here). To our best understanding of OFETs, the device performance and mobility strongly depend on the choice of the dielectric layer mainly due to a different surface energy of the dielectric layer. The sharp turn on of I_{ds} is a measure of the quality of the dielectric/semiconductor interface which is defined by the normalized subthreshold slope, $S = C_{BCB}dV_{gs}/d(\log I_{ds})$ [7]. As usually observed in organic FETs, subthreshold slope of 8 V·nF/decade·cm^2 obtained by us is very high which can be reduced by reducing the thickness of the dielectric layer. We presume, the most important factor in achieving this high mobility OFET is the combination of a smooth organic dielectric surface and a highly ordered C_{60} film grown by HWE.
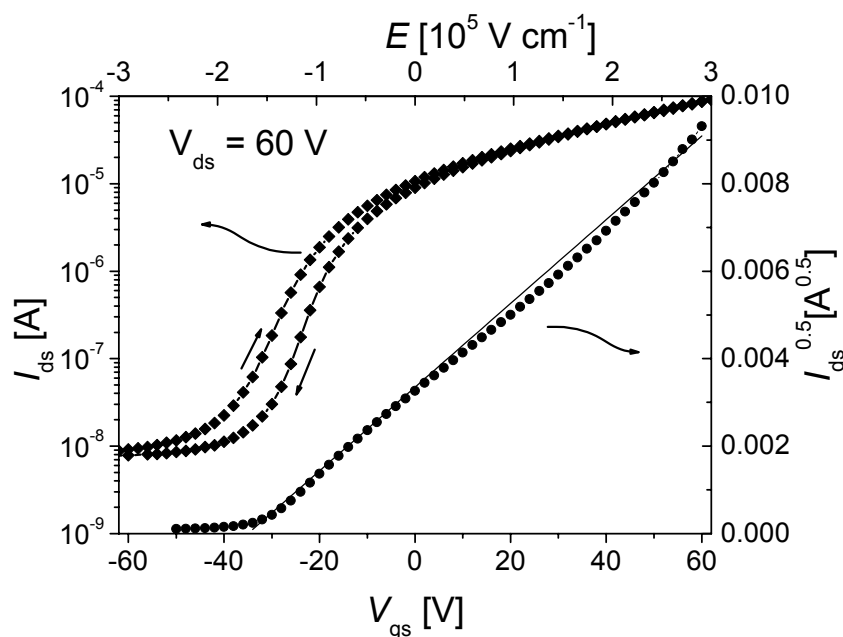

Fig. 3:   Semilogarithmic plot of Ids vs. Vgs (left scale) and plot of Ids0.5 vs Vgs (right scale) for the same C60 OFET as in Fig. 2. The full line shows a fit to the data (return curve) using equation (1) from which a field-effect mobility μ = 0.63 cm2/Vs is obtained. Each measurement was carried out with an integration time of 1 s.

Conclusion

In conclusion, we have demonstrated an n-channel OFET with an electron mobility of 0.4 – 1 cm^{2}V^{-1}s^{-1} along with an on/off ratio >10^4 using a solution based organic dielectric BCB film in combination with HWE grown C_{60} films. The obtained mobility is nearly gate voltage independent. Very few studies have been done so far on growing highly ordered organic thin films on top of organic dielectrics partly due to low glass transition temperature and unwanted hysteresis. Use of BCB among other organic dielectrics is based on the fact that its low hysteresis and high glass transition temperature which is an additional advantage for optimizing the film growth condition at high substrate temperatures.

Acknowledgements

References

[1]   Two most recent review articles, (a) W. Clemens, W. Fix, J. Ficker, A. Knobloch and A. Ullmann, J. Mat. Res. 19, 1963 (2004); (b) G. Horowitz, J. Mat. Res. 19, 1946 (2004) and reference there in.

[2]   B. Crone, A. Dodabalapur, Y. -Y. Lin, R. W. Filas, Z. Bao, A. Laduca, R. Sarpeshkar, H. E. Katz and W. Li, Nature 403, 521 (2000).

[3]   H. E. A. Huitema, G. H. Gelinck, J. B. P. H. van der Putten, K. E. Kuijk, C. M. Hart, E. Cantatore, P. T. Herwig, A. J. J. M. van Breemen and D. M. de Leeuw, Nature 414, 599 (2001).

[4]   L. -L. Chua, P. K. H. Ho, H. Sirringhaus and R. H. Friend, Appl. Phys. Lett. 84, 3400 (2004).

[5]   R. Schwödiauer, G. S. Neugschwandtner, S. Bauer-Gogonea, S. Bauer and W. Wirges, Appl. Phys. Lett. 75, 3998 (1999).

[6]   (a) V. D. Mihailetchi, J. K. J. van Duren, P. W. M. Blom, J. C. Hummelen, R. A. J. Janssen, J. M. Kroon, M. T. Rispens, W. J. H. Verhees and M. M. Wienk, Adv. Func. Mater. 13, 43 (2003)

[7]   G. Horowitz, R. Hajlaoui and F. Kouki, Eur. Phys. J. AP 1, 361 (1998).

ESD Protection (Posters)

Thermal Imaging at Multiple Time Instants for Study of Self-Heating and ESD Phenomena

V. Dubec, S. Bychikhin, M. Blaho, M. Heer, D. Pogany, E. Gornik
Institute of Solid State Electronics, Vienna University of Technology,
A-1040 Vienna, Austria

M. Denison, M. Stecher
Infineon Technologies, D-81617 München, Germany

G. Groos
University of Federal Armed Forces, D-85577 Neubiberg, Germany

A 2D backside transient interferometric mapping (TIM) method for nanosecond thermal energy imaging at multiple time instants during a single stress event is introduced. The method is based on fringe interferometry and the interferograms are analyzed using the Fast Fourier Transform technique. The method is applied to investigate moving current filaments in smart power DMOS transistors and in electrostatic discharge (ESD) protection devices exhibiting non-repeatable triggering behavior under ESD-like stress. The method additionally allows the extraction of instantaneous 2D power dissipation density (P_{2D}), which represents the current density distribution in the devices.

Introduction

Protection against electrostatic discharge (ESD) is an important requirement in automotive electronics [1]. For optimization of ESD protection devices (PDs) and for verification of device simulation models it is important to have an experimental access to the internal device behavior. Since self-heating is the main device failure cause [2], the temperature monitoring is especially important in device inspection.

Recently a 2D backside transient interferometric mapping (TIM) technique based on fringe interferometry has been introduced for ns thermal energy imaging at single time instants during a single stress event [3]. However, measurements of devices with complex unrepeatable current filament dynamics are time consuming to perform. An extended version of the 2D TIM method suitable for imaging at two time instants during a single stress event has been therefore developed [4], which overcomes the above limitation. In this article, smart power technology high power DMOS [5] and ESD protection devices [6] developed for automotive applications are investigated by this method. In addition, the current density distribution in the devices is extracted from the measurements.

Experimental Setup and Theory

The backside 2D TIM technique is based on the thermo-optical and plasma-optical effect. During the electrical pulse, the temperature and the free carrier density variation cause a change in the optical length of the laser beam. The optical path difference is measured in a Michelson interferometer, see Fig. 1. For imaging at two time instants, two orthogonally polarized laser beams produced by two high energy pulsed laser sources (λ = 1.3 µm, 5 ns pulses), combined by a polarizing beam splitter cube (PBS1)

are led into the Michelson interferometer. The parallel beams reflected from the device (DUT) (see detail on the right in Fig. 1) and from the reference mirror (M) are split according to their polarization (PBS2) and create the interference fringe patterns on two infrared (IR) cameras. The laser pulse positions relative to the stress pulse can be chosen independently. The image and waveform acquisition is synchronized and computer controlled.
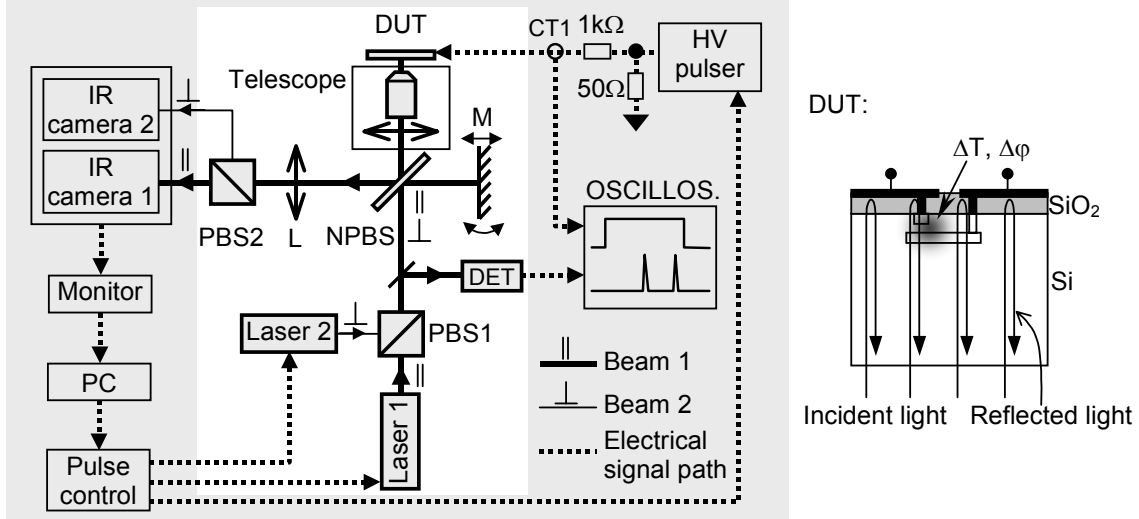

Fig. 1: Schematic drawing of the setup: PBS – polarizing beam splitter, NPBS – non-polarizing beam splitter, M – mirror, L – lens, DET – optical detector, CT1 – current probe, DUT – device under test (after [4]). On the right side the cross section of a DUT, the probe laser beam and the heat source ΔT is depicted.

The temperature-related phase distribution in the device at a particular time instant is extracted using a FFT-based method [7]. For elimination of the phase profile arising from the device the reference phase related to the interferogram without heating is subtracted. This removes also the phase tilt introduced by the reference mirror. The phase calculation results in phase modulo 2π, and the unwrapping is necessary. For unwrapping the pixel queue method or the minimum spanning three method are performed [8], [9]. Before the unwrapping is done, a pre-processing procedure is developed [7].

As two images during a single pulse are possible to record, the method allows extraction of the instantaneous 2D power dissipation density P_{2D}, which represents the current density distribution in the devices. Neglecting the heat transfer to the top device layers (normal component of the heat flow vector), P_{2D} is given by [6]:

$$P_{2D}(x,y,t) = \lambda \left(4\pi \frac{dn}{dT} \right)^{-1} \left(c_V \frac{\partial \varphi(x,y,t)}{\partial t} - \kappa \frac{\partial^2 \varphi(x,y,t)}{\partial x^2} - \kappa \frac{\partial^2 \varphi(x,y,t)}{\partial y^2} \right) \qquad (1)$$

where λ is the laser beam wavelength, *dn/dT* is the temperature coefficient of the refractive index, c_V is the volume specific heat, $\varphi(x,y,t)$ is the measured phase shift, κ is the thermal conductivity, *x, y* and *t* are the spatial coordinates and time, respectively. The time derivative in Eq. (1) is approximated using the phase difference between two images $\varphi(x,y,t)$ and $\varphi(x,y,t-\Delta t)$ recorded during the same ESD pulse at times *t* and *t–Δt*, respectively. The value of Δ*t* = 30 ns is a good compromise taking into account the phase and space resolution of the setup.

Results

The method is applied to the study of moving current filaments in ESD protection devices and DMOSes during a bipolar snapback mode where the current distribution in the device is strongly inhomogeneous. The backside IR image of the ESD PD is shown in Fig. 2 (a) and its cross section in Fig. 2 (f). Figures 2 (b) – (e) and (g) – (j) show the measured phase images and the extracted P_{2D} at four time instants, respectively. Due to the negative differential resistance a current filament, represented by a spatially localized P_{2D}, is formed in the middle of the device, see Fig. 2 (g). Later, due to the reduction of the impact ionization coefficient with increasing temperature, the filament starts to move towards a cooler region (to the corner) of the device, see Fig. 2 (h). When the filament reaches the corner, it is "reflected" back (Fig. 2 (i)) and moves again to the middle and toward the opposite corner of the device (Fig. 2 (j)). The initial direction (right or left) of the movement is random. The current filament amplitude is about 30 mW/μm^2, which is consistent with the results obtained previously using the time-consuming scanning TIM method [10].
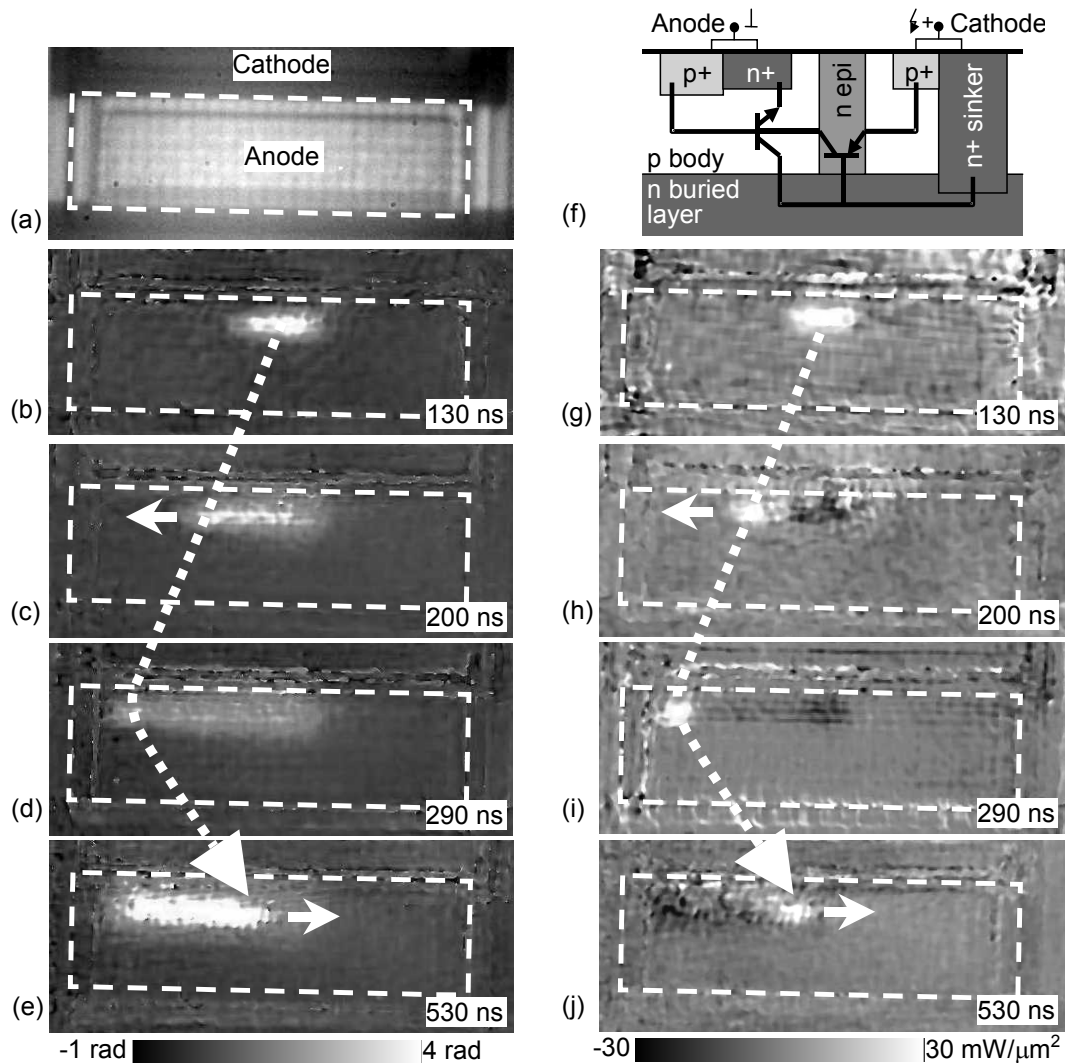

Fig. 2: (a) Backside IR image of the ESD PD and (f) device cross section. (b) – (e) Phase shift distribution $\varphi(x,y,t)$ in the ESD PD at four time instants during current pulses of 0.25 A, 600 ns duration. The heating is displayed by light color. (g) – (j) show the P_{2D}, representing the current filament position. The dashed arrow and the small white arrows denote the movement direction (after [4]).

The backside IR image of the DMOS device is shown in Fig. 3 (a) and its cross section in Fig. 3 (b). At snap back, when the parasitic bipolar transistor (see Fig. 3 (b)) of the DMOS turns on, a few cells take over the current and localized current filaments are formed along the source field termination. With time the filaments penetrate into cooler regions. The trigger position, number of the filaments, and direction of their movement vary randomly and non-repeatedly from pulse to pulse [4], [5].

In order to localize the active cell at a particular time instant in the DMOS, the P_{2D} is necessary to extract. For this the two imaging laser beams were positioned at time instants 120 ns and 150 ns, see Figs. 3 (c), (d). The P_{2D} calculated by Eq. (1) corresponding to $t = 150$ ns is shown in Fig. 3 (e). At this particular case, DMOS cells marked by the circles inside of the source field are active and there are no more active cells along the termination line.
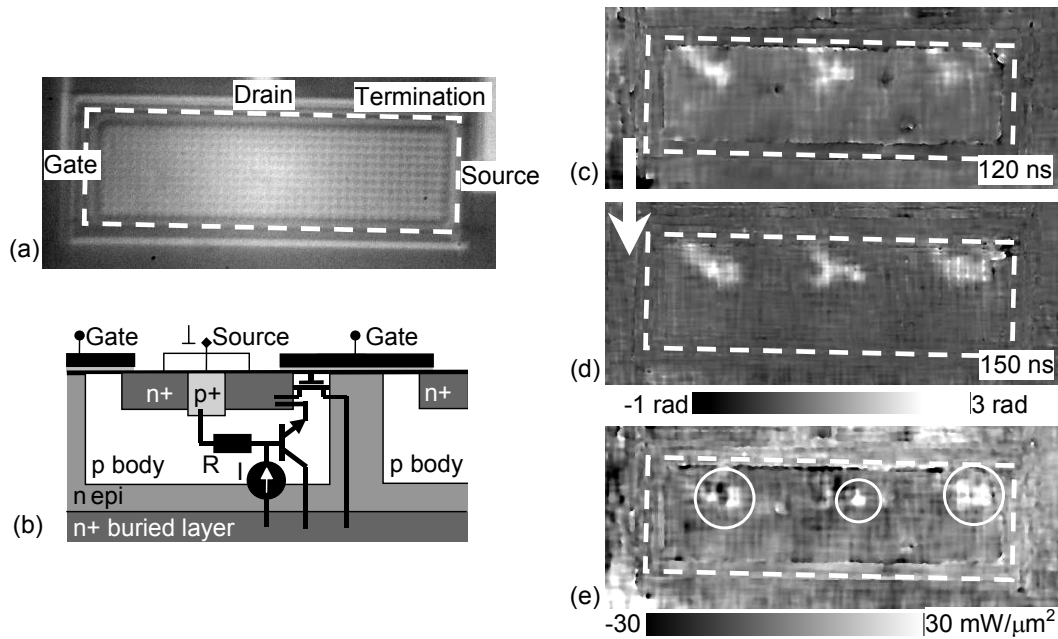

Fig. 3: (a) Backside IR image of the vertical DMOS, (b) device cross section.
(c, d) Phase shift distribution in the DMOS at 120 ns and 150 ns during a 3 A, 250 ns stress pulse and (e) corresponding P_{2D} (after [4]).

Conclusion

With the presented method, the position and direction of the filament movement can unambiguously be extracted from few single-shot measurements. Using the two-time-instant measurement the instantaneous power dissipation density can be obtained. This allows investigation of current dynamics in devices exhibiting complex unrepeatable behavior, which is not possible by any other method. The method has a potential for time-efficient studies of destructive phenomena in semiconductor devices including thermal run-away effects in the ns to ms time range and study of surface displacement of MEMS, bio-membranes, sensors and microfuidics.

Acknowledgements

References

[1]   B. J. Baliga: "Modern power devices", John Wiley, New York, 1987.

[2]   V. M. Dwyer, A. J. Franklin, D. S. Campbell: "Thermal failure in semiconductor devices", Solid-St. Electron., Vol. 33, 1990, pp. 553-560.

[3]   D. Pogany, V. Dubec, S. Bychikhin, C. Fürböck, M. Litzenberger, G. Groos, S. Stecher, E. Gornik: "Single-shot thermal energy mapping of semiconductor devices with the nanosecond resolution using holographic interferometry", IEEE Electron Dev. Lett., Vol. 23, 2002, pp. 606-608.

[4]   V. Dubec, S. Bychikhin, M. Blaho, M. Heer, D. Pogany, M. Denison, N. Jensen, M. Stecher, G. Groos, E. Gornik: "Multiple-time-instant 2D thermal mapping during a single ESD event", (ESREF 2004), Microel. Reliab. 44, 2004, pp.1793-1798.

[5]   M. Denison, M. Blaho, P. Rodin, V. Dubec, D. Pogany, D. Silber, E. Gornik, M. Stecher: "Moving current filaments in integrated DMOS transistors under short-duration current stress", IEEE Trans. Electron Dev., Vol. 51, 2004, pp. 1695-1703.

[6]   D. Pogany, S. Bychikhin, M. Litzenberger, E. Gornik, G. Groos, M. Stecher: "Extraction of spatio-temporal distribution of power dissipation in semiconductor devices using nanosecond interferometric mapping technique", Appl. Phys. Lett., Vol. 81, 2002, pp. 2881-2883.

[7]   V. Dubec, S. Bychikhin, D. Pogany, E. Gornik, G. Groos, M. Stecher: "Error analysis in phase extraction in a 2D holographic imaging of semiconductor devices", Proc. SPIE: Practical Holography XVIII: Materials and Applications, Vol. 5290, 2004, p. 233-242.

[8]   T. Kreis: "Holographic interferometry", Berlin, 1996.

[9]   H. A. Vrooman: "Quaint: quantitative analyses of interferograms", Delft Univ. Pr., 1991.

[10] D. Pogany, S. Bychikhin, M. Denison, P. Rodin, N. Jensen, G. Groos, M. Stecher, E. Gornik: "Thermally-driven motion of current filaments in ESD protection devices", Solid-St. Electron., Vol. 49, 2005, pp. 421-429.

Degradation Mechanisms in AlGaN/GaN HEMTs under Electrostatic Overstress

J. Kuzmík, M. Blaho, S. Bychikhin, D. Pogany, E. Gornik

Institute of Solid State Electronics
Vienna University of Technology, A-1040 Vienna

P. Javorka, P. Kordoš

Institute of Thin Films and Interfaces, Research Centre Jülich, Jülich
D-52425, Germany

We study degradation mechanism in AlGaN/GaN HEMTs under 100 ns long rectangular current pulses applied on the drain contact. Devices were dc characterized after consecutive current stresses. We observed a sudden increase of source and drain resistances after the stress of 1.65 A. We used a backside transient interferometric mapping technique to localize the current path in the device during stresses. We revealed a current filamentation during stresses and dark spots formation in the position corresponding to filaments occurrence. We assume electron injection into the device buffer layer and an electromigration on contacts.

Introduction

Devices may face electrical overstress events (EOS) during manufacturing, handling or device operation. Typical current pulses are in the ampere range with duration between nanoseconds and microseconds. The importance of a failure mechanism study in III-nitride transistors is given by their potential usage as power devices in many defense and commercial applications where harsh environment conditions can be expected. It was previously suggested that the electrical conduction mechanism in AlGaN/GaN HEMTs during EOS might be linked to the avalanche-injection processes in the GaN buffer layer [1]. On the other hand, the device's ohmic and Schottky barrier contacts degradation was revealed as the main mechanism responsible for the failure of AlGaN/GaN HEMTs after EOS [2].

Experimental

The AlGaN/GaN HEMT structures used in this study were grown on both-sides polished sapphire wafer by MO-VPE. The device processing included e-beam lithography [2], the gate geometry was 50 µm width, 450 nm length. We used a transmission line pulser (TLP) to stress the device. In the TLP technique a coaxial cable (TL) with a 50 Ω characteristic impedance is charged by a voltage source and afterwards is discharged by closing a relay, providing rectangular current pulses for our devices. Devices were characterized after consecutive current stresses of increasing level. Ohmic contact and open channel resistances were extrapolated from the functional dependence of the source-drain resistance on gate voltage [3]. We used backside interferometric mapping (TIM) technique [4] to localize the current path (dissipated power) in HEMTs during TLP stresses. The mapping was performed using an infrared laser beam scanning the device from the backside. The measured phase shift, caused by the temperature-induced change in the refractive index, is directly proportional to a local 2D energy density in the device [4].

Results and Discussion

The HEMT drain-source high-current pulsed *I-V* characteristics exhibit S-shape with three regions (see Fig. 1): A low-current / high-impedance region A, a NDC region B, and a high-current / low-voltage region C. A parasitic bipolar effect [1] may be linked to the S-shape.
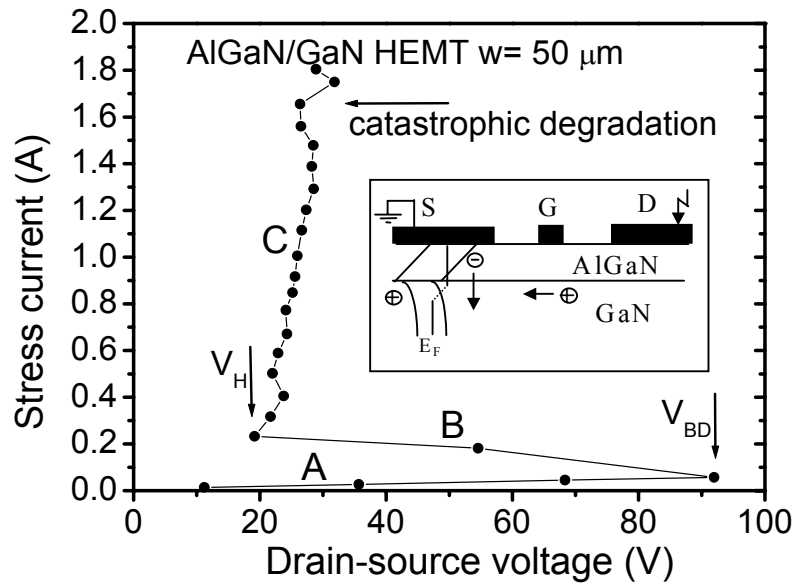

Fig. 1: Typical drain-source high-current pulsed *I-V* curve of the HEMT. The inset illustrates the band diagram and assumed process of the hole accumulation and electron injection into the GaN buffer (after [1]).
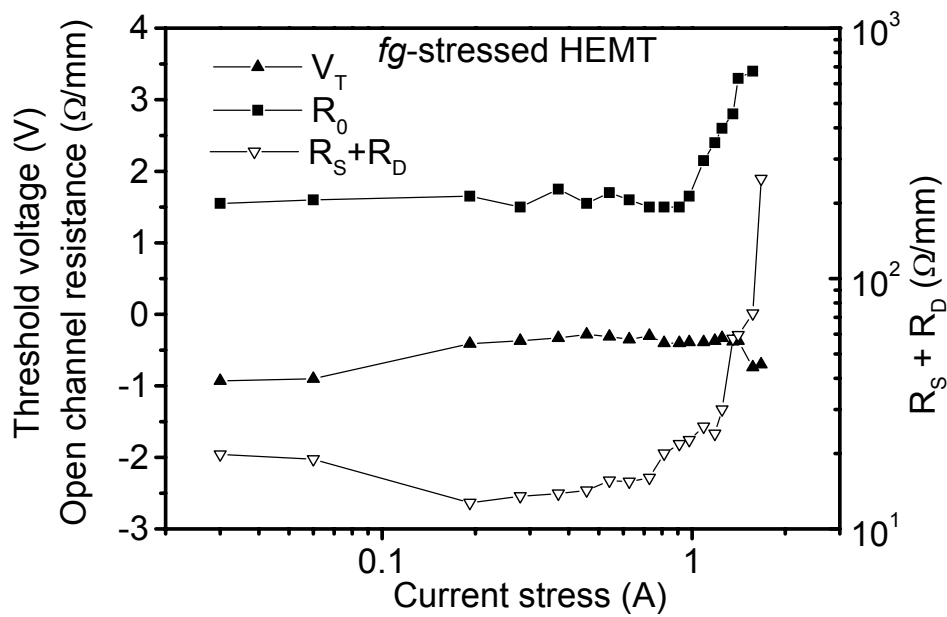

Fig. 2: Evolution of the AlGaN/GaN HEMT threshold voltage, open channel resistance and source + drain resistances values in dependence of previous current stress level (after [2]).

Transistor threshold voltage V_T, open channel resistance R_0, and the sum of the source R_S and drain R_D ohmic contact resistances as a function of the current stress level are shown in Fig. 2. The ohmic contacts' catastrophic degradation (ten-fold increase from the nominal value) was recorded at I_{stress} = 1.65 A. The abrupt $R_S + R_D$ increase is accompanied with a partial increase of the open channel resistance R_0. However, R_0 becomes marginal in comparison to $R_S + R_D$ at this point.
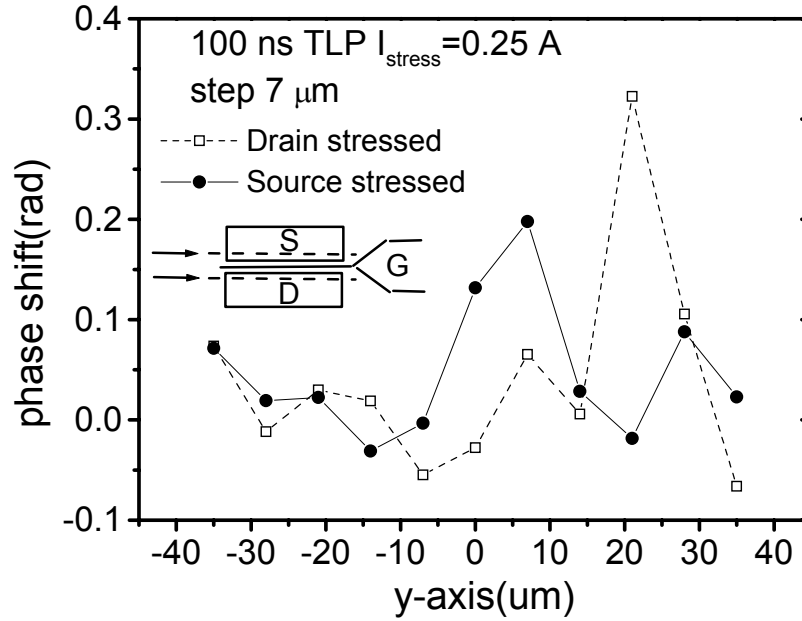

Fig. 3: Phase shift distributions of the AlGaN/GaN HEMT along the drain and source at I_{stress} = 0.25 A at the end of the pulse. Source was grounded for a scan along the drain and vice versa. Inset: Schematic device layout with indicated scan lines (after [2]).

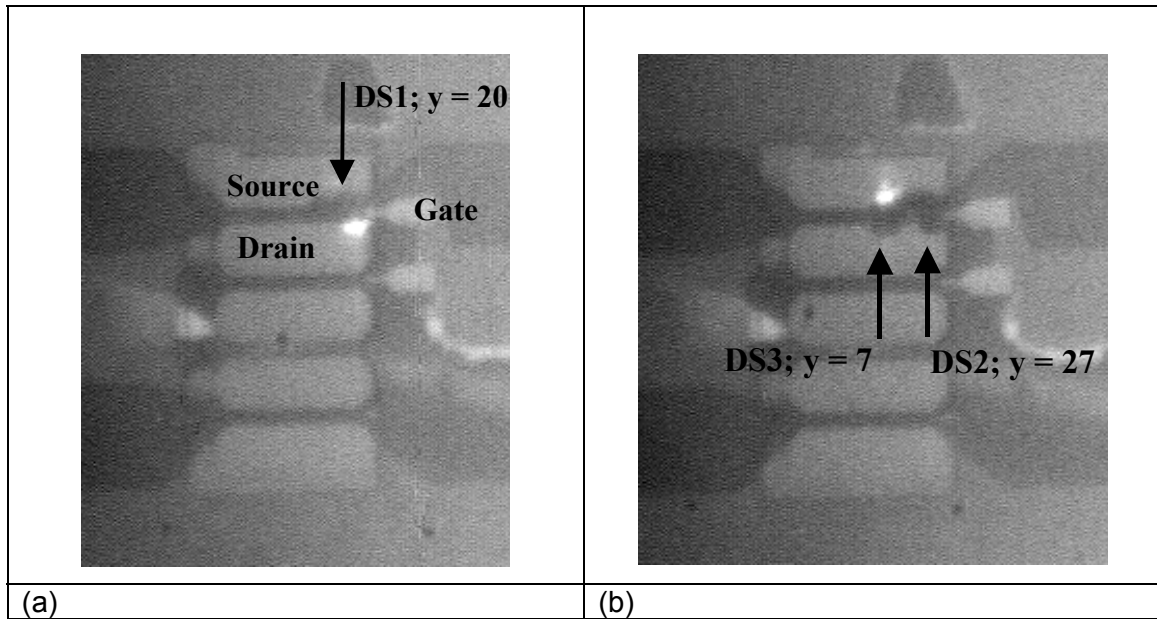(a)   (b)

Fig. 4: Backside infrared camera view of the AlGaN/GaN HEMT after I_{stress} = 0.25 A on the (a) drain, (b) source. Arrows mark dark spot (DS1 – 3) appearance, laser beam indicates the position of the maximal phase shift signal (after [2]).

Results of the TIM technique are presented in Fig. 3. The device was scanned along the stressed contact with a step of 7 µm. First, the source was grounded and the drain was stressed with a positive pulse. The phase shift characteristics show a fair local maximum at the right edge of the HEMT. Following the change of the stress polarity (drain grounded, source stressed), two new maxima appeared in new positions close to the previous one. These observation correlates with the backside infrared images of the device (Figs. 4 (a), (b)) where dark spot positions correspond to the phase shift maxima on the grounded (opposite) contact.

Conclusion

The AlGaN/GaN HEMT behavior and degradation mechanisms under pulsed overstress conditions have been investigated. The current filament formation and the electromigration effect were shown to be responsible for the *ohmic* contact dark spot formation. Dark spots may be considered as a precursor of the *ohmic* contact degradation. Semiconductor material parameters are not changed substantially during the EOS event.

References

[1]   Kuzmík J., Pogany D., Gornik E., Javorka P., Kordoš P., "Electrostatic discharge effects in AlGaN/GaN HEMTs", Applied Physics Letters, Vol. 83, 2003, pp. 4655 – 4657.

[2]   Kuzmík J., Pogany D., Gornik E., Javorka P., Kordoš P., "Electrical overstress in AlGaN/GaN HEMTs: study of degradation processes", Solid-State Electronics, Vol. 48, 2004, pp. 271-276.

[3]   Shur M., GaAs Devices and Circuits, New York and London: Plenum Press, 1987. p.369-372.

[4]   Pogany D., Bychikhin S., Fürböck C., Litzenberger M., Gornik E., Groos G., Esmark K., Stecher M., "Quantitative internal thermal energy mapping of semiconductor devices under short current stress using backside laser interferometry", IEEE Trans. Electron Dev Vol.49, 2002 pp. 2070-2079.

Electron and Ion Beam Processes (Posters)

Direct-Write Deposition Utilizing a Focused Electron Beam

M. Fischer, J. Gottsbachner, S. Müller, W. Brezna, and H.D. Wanzenboeck

Institute of Solid State Electronics, Vienna University of Technology, A-1040 Vienna, Austria

Local deposition of material can be induced by a focused electron beam delivering materials with a high purity and a clear interface to the substrate. Based on a commercial variable-pressure scanning electron microscope custom-tailored equipment was developed that allows introducing precursor gases through a nozzle system directly to the spot of deposition. For the deposition of material tetraethylorthosilicate (TEOS) was chosen, yielding a silicon oxide based material. The deposition process was investigated and optimized for high deposition rates. Variation of acceleration voltage and dwell time was performed, by depositing the material with a univariat parameter change. A higher deposition rate was obtained for lower electron energies. This result suggests a deposition mechanism based on the interaction with secondary electrons. Also effects of dwell time were discussed.

Introduction

The locally confined direct-write deposition is a new, maskless nanostructuring technique that is capable of fabricating 3-D structures within a single process step. The conventional fabrication of nanostructured devices with cutting-edge optical lithography requires the use of cost-intensive phase-shift masks and the processing time for several process steps including blanket deposition of the material, lithographic structuring and etch-back to obtain the desired structures. For prototyping a novel approach using direct-write deposition has been acknowledged as a promising alternative. The energy of a focused particle beam is used to locally induce a chemical vapor deposition. No mask is required and the structures can be deposited within a single process step. A frequently used approach is the deposition of a focused ion beam (FIB) [1], [2]. However, the ion contamination originating from the ion source and the atomic mixing of deposited material put a serious constraint on this method. An alternative technique could be the focused electron beam induced deposition. This technology delivers materials with a higher purity and a clear interface to the substrate.

In this article, tetraethoxysilane (TEOS) was used as a precursor for electron beam insulator deposition. The effects of several process parameters were studied. The variation of parameters was performed by depositing arrays of material with a univariat parameter change. The aim of the present work is to investigate the deposition process and to optimize the deposition parameters.

Experimental

Experiments have been performed using a variable-pressure scanning electron microscope LEO 1530 VP with a sophisticated gas inlet system. With a nozzle system the gas was introduced directly to the focus point of the electron beam. The energy of the electrons could be adjusted via the acceleration voltage in a range from 0.1 to 30 kV. The scanning operation of the electron beam could be controlled with a RAITH ELPHY PLUS pattern generator. The pattern generator allowed varying the pixel spacing of the

scan array, the dwell time of the beam on a single spot, and the number of scan repetitions.

For the deposition of material, tetraethylorthosilicate (TEOS) was chosen as exemplary precursor. The vapor pressure of TEOS is about 2 mbar at 20 °C and is sufficient for an accurate control of the gas flux via a dosing valve of the gas injection system. The acceleration voltage was varied in arrange from 5 to 30 kV. The maximum beam current was 3 to 4.3 nA (depending on the acceleration voltage), results of the use of the 120 µm aperture. In order to investigate the deposition process 50 x 20 µm SiOx pads were deposited. The height of the deposition was determined by a DEKTAK profilometer. The surface morphology of the deposited material patches was investigated by atomic force microscopy in tapping mode.

Results and Discussion

For the deposition of silicon oxide a focused electron beam was used. The electron beam was scanned in a rectangular area.

First experiments should demonstrate that depositions of silicon oxide are feasible with the used set-up. Figure 1 shows an AFM-image of a deposited 6 x 6 µm area of silicon oxide. For this deposition an acceleration voltage of 5 kV, a pixel spacing of 46 nm, and a dwell time of 0.5 µs were adjusted.
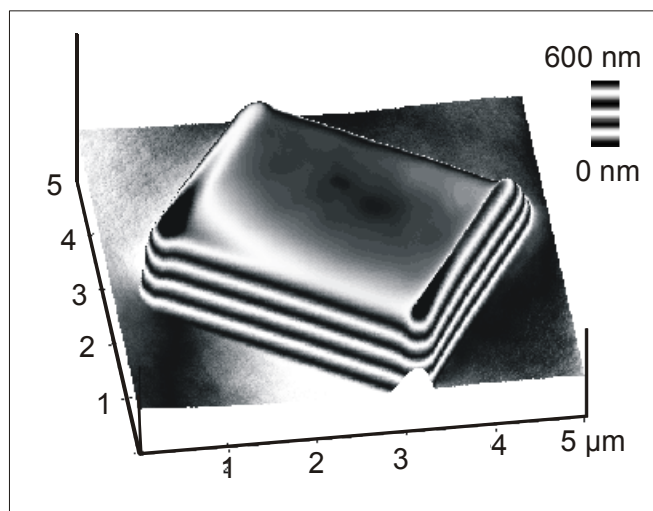

Fig. 1:   AFM – image of a silicon oxide deposition on a 6x6 µm area

In the AFM-image (Fig. 1) a 6 x 6 µm deposition is seen. The deposited field has a total height of about 630 nm. The thicker material at the rim results from the longer dwell time at the left and right edge of the scan pattern, which is generated by the pattern generator. In the area between the rims the roughness of the surface is very low. This is of special interest in combination with optical applications. These findings prove that an electron beam may be used as a local probe for the deposition of well-defined structures. Investigations of the correlation between acceleration voltages and deposition thickness were performed with acceleration voltages from 30 kV down to 5 kV. All other process parameters were kept constant. The thickness of the deposited material was measured with a Dektak profilometer.
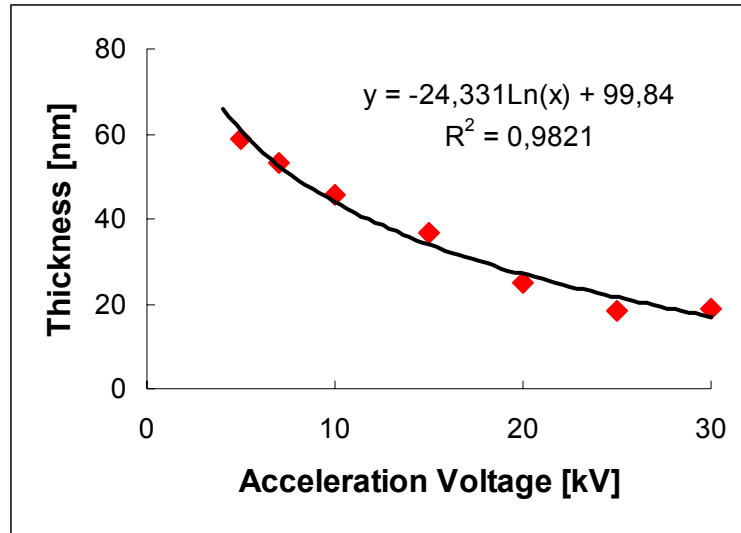
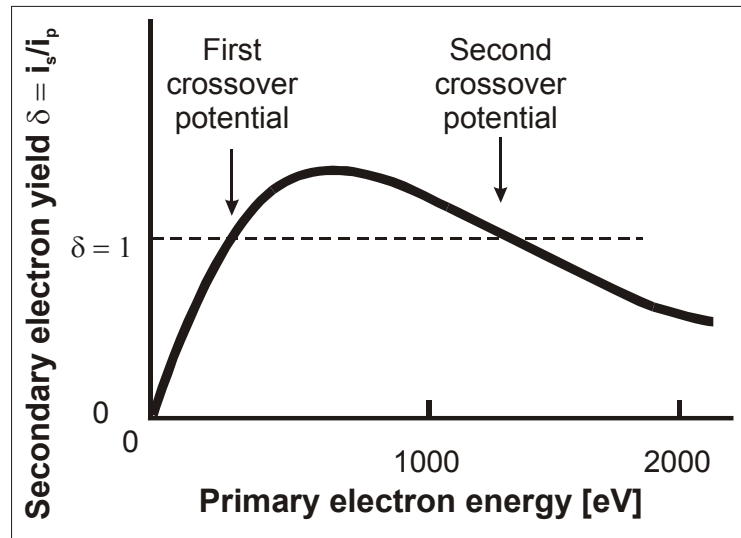Fig. 2: Deposited thickness to acceleration voltage

Fig. 3: Secondary electron yield correlated depending on the acceleration voltage from Hearle [4]

The dependence of the deposited thickness against the acceleration voltage is illustrated in Fig. 2. The graph indicates that the deposition rate increases at lower beam energies. This result correlates with the hypothesis that the deposition reaction is potentially induced by interaction of the adsorbed precursor with the secondary electrons [3], [4]. The yield of the secondary electrons (SE) depends on the energy of the primary electrons as it is illustrated in Fig. 3. Towards lower beam energies down to 600 V the penetration depth of electrons is reduced and the secondary electrons yield increases. The problem with low primary electron energy is the loss of beam stability.

The effect of the dwell time on the deposition thickness was analyzed by fabricating an array of 50 x 20 µm areas in a 3 x 6 matrix (Fig. 4) with increasing dwell times. The default value for the shortest dwell time was set at 0,375 µs. Other dwell times were obtained with a multiplier (= 1 + 2n) resulting in a 3-, 5-, 7-, …- fold longer dwell time. Within the array (Fig. 4) the dose for every deposited field was different. The thickness was measured by Dektak profilometer. To compare the deposited thickness the meas-

ured values were calibrated against the exposure dose. The deposited structures in Fig. 4 are well defined with sharp edges and excellently aligned. This array demonstrates that electron beam lithography is a serious technique for maskless direct-write lithography and for prototyping in the sub µm microelectronic technology.
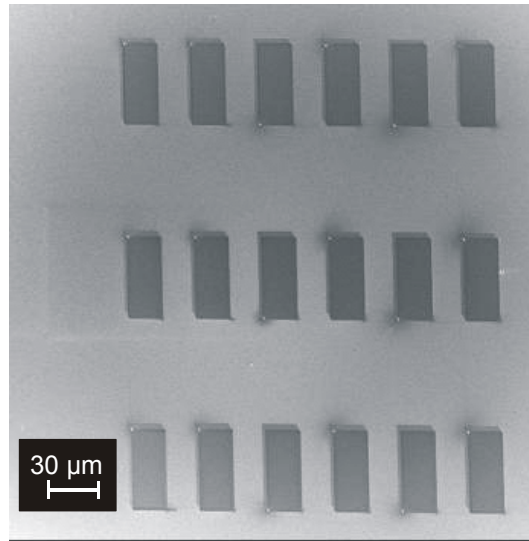

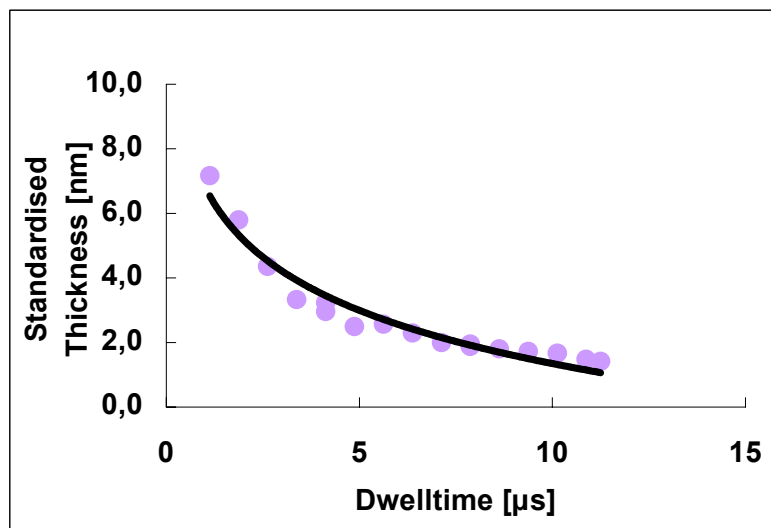Fig. 4: Array of deposited material by electron beam induced deposition

Fig. 5: Standardized thickness against dwell time

The evaluation of the dwell time influence is shown in Fig. 5. It is shown that the deposition thickness increased at lower dwell times. This indicates that the deposition reaction is faster than the surface saturation. A further decrease of the dwell time will result in a rise of the deposition rate.

Conclusions

It has been successfully demonstrated that an electron beam may be used as a local probe for the deposition of well-defined structures. This technique is an essential tech-

nology for repairing and preparing sub-µm feature sized structures. It has been shown that a higher deposition rate was obtained for lower electron energies. A deposition mechanism based on the interaction of the adsorbed precursor molecules with secondary electrons is leads to the assumption. These findings are considered a solid bias for the better understanding of electron-induced surface reactions and path the way to a further process optimization of this innovative nanofabrication technique.

Acknowledgement

References

[1] H.D. Wanzenboeck, M. Verbeek, W. Maurer, E. Bertagnolli, Proceedings of the SPIE – The international Society for Optical Engineering, 4186, 148-57 (2001)

[2] S. Lipp, L. Frey, C. Lehrer, B. Frank, E. Demm, S. Pauthner, H. Ryssel, J. Vac. Sci. Technol. B 14(6), 3920-3, (1996)

[3] R. R. Kunz and T. M. Mayer, Appl. Phys. Lett. 50, 962 (1987)

[4] J.W.S. Hearle, J.T Sparrow, and P.M. Cross, The Use of the Scanning Electron Microscope, Pergamon Press, Oxford, New York, Toronto, Sidney, Braunschweig (1972)

A New Approach for the Formation of Size and Site Controlled Metallic Nano Dots Seeded by Focused Ion Beams

A. Lugstein, W. Brezna, E. Bertagnolli
Institute of Solid State Electronics
Vienna University of Technology, A-1040 Vienna, Austria

We present a new approach for the generation of uniform metallic nano dots, which in contrast to conventional bottom up or top down processes is based on a subtractive self organization process relying on material decomposition induced by focused ion beam exposure and subsequent rapid thermal annealing.

The nanometer sized Ga and In dots that can be formed in a size and position controlled fashion were fabricated on GaAs (100), InAs (100), Si (100) and SiO_2 using focused ion beam techniques. Two dimensional ordered arrays of embedded as well as freestanding metallic dots were fabricated by a site control technique relying on preformed craters and an irradiation mediated migration. The diameters of the dots range from 60 to 850 nm.

The formation of these dots is discussed in terms of selective etching of arsenic due to the local energy injection by the ions and further agglomeration. Due to the high energy injection during FIB milling and the low melting point of the metal the precipitations behave like a liquid under milling conditions. Thus, the minimization of surface energy at the enhanced temperatures during FIB exposure calls for a spherical shape of the small droplets, as we did observe.

The morphological evolution of the sample surface was investigated by in-situ FIB-SEM, and AFM, and the chemical composition of the pattern was analyzed using high resolution AES. We completed these many-facetted experimental studies with optical microscopy and electrical measurements.

This technique is a promising way to obtain quantum dot arrays with small and uniform dot sizes and high packaging densities. Since GaAs quantum dot formation from Ga droplets has been reported, our technique is considered to be a candidate for the fabrication of highly ordered quantum dot array structures. Furthermore, this method is expected to apply to various metals apart from Ga and In.

Plasma Processing (Posters)

Inductively Coupled Plasma Reactive Ion Etching of GaN

S. Golka, W. Schrenk, G. Strasser

Zentrum für Mikro- und Nanostrukturen, Technische Universität Wien, Floragasse 7, A-1040 Wien

We investigate in deep etching recipes for GaN based compound semiconductors. For nitride semiconductors wet chemistry does not work, therefore plasma etching is required. For deep structures of wavelength scale in GaN, a good etchant to mask selectivity and vertical etch profiles is needed. We present an inductively coupled plasma recipe that can etch 6 µm deep with smooth sidewalls with a SiNx hard mask.

Introduction

Since etching of GaN [1] cannot be accomplished by wet chemistry to a satisfactory degree, reactive ion etching (RIE) becomes very important, as it is the only means of obtaining vertical structuring. The only practical wet etch [2] is KOH at 50 …100 °C. The inability to find a mask that will hold up to such aggressive chemistry makes it more or less useless for accurate transfer of patterns. Unlike for other III-V semiconductors this is also valid for shallow structures for electronics. Demands on etch quality become even more stringent for deeper optically waveguided structures; especially where lithographic resolution needs to be on the micrometer scale. In that mask thickness will be limited by some lithographic technique; here selectivity plays a significant role.

With respect to the demands in optically integrated circuits a RIE recipe is needed to produce vertical or at least overcut sidewalls. Undercut would not be compatible with subsequent metallization steps. Preferably this sample preparation technique should be fast and reliable, which is not a matter of course for the nitrides, since etch rates are generally slow [1]. Smoothness of sidewalls becomes a crucial issue for optoelectronic devices operating at 1.55 µm or less. In rough sidewalls scattering will take place and hence will boost the waveguide losses. Additionally cleavage of waveguide facets is difficult or even impossible in the GaN/InGaAlN system if grown on commonly used sapphire substrate; therefore cleaved facets for in-plane fiber coupling are no option. Etched facets [3] are an excellent solution but this again demands vertical and smooth etches, in this case even in excess of 5 µm in order to make space for fiber tapers.

So far most groups used chlorine based RIE techniques, mainly because these provide the highest etch rates for GaN in the order of 50 nm/min for capacitively coupled plasma (CCP) RIE [4]. Going to higher plasma densities with inductively coupled plasma (ICP) RIE [5] enhances rates to the order of 600 nm/min. In this work we are mainly concerned with developing such an ICP process for very large etch depths.

Sample preparation

For advanced structures like tightly guiding rib waveguides a better mask to etchant selectivity is needed than the one obtained for GaN versus photo resist, which was smaller then 1:1 in favor of the photo resist. The use of an intermediate mask does not only enhance selectivity but also improves the sidewall smoothness which will be important for etched mirrors. Since SiN$_X$ is available in almost any processing lab and has

very good adhesive properties to GaN/AlN it is a good choice. Remaining SiN_X can easily be removed by HF after etching. We used a two step fabrication scheme as outlined in Fig. 1. The photo resist to SiN_X selectivity is only slightly better than 1:1, but the expected selectivity of GaN to SiN_X in an ICP RIE process step is well above 1:1 as will be shown later. Also, the process utilizing SiNx masks has the advantage of being totally free of organic substances during the deep etch process. Remaining photo resist is stripped by plasma oxidizing and KOH. By this additional cleaning procedure we avoid any micro masking [6] effects and wall roughening by contaminants.

Experiment

In ICP-RIE a $N_2/SiCl_4$ based chemistry, as compared to commonly used Ar/Cl_2, has proved itself due to two reasons: Nitrogen has less than half the atomic weight than Argon and therefore does much less damage the masking material. Concerning the acceleration voltage acting on the inert gas atoms normally there is an onset voltage where sputter removal of the mask just starts to be efficient. If one manages to stay below that only very slightly, etch selectivity is very much improved. This fine tuning works especially nice with nitrogen. Second, the $SiCl_4$ [7] is split in the plasma and provides silicon compounds that are again not reluctant to react with chlorine; these compounds can serve as passivation layers that stick on sidewalls were sputtering does not take place. So at the end it can act as a chemical underetch inhibitor. This inhibitor is still efficient at very high chlorine flow. Furthermore, $SiCl_4$ is much more compatible with residual water in the etch chamber. In contrary, the use of Cl_2 gas causes major troubles with residual water vapors and needs additional cleaning steps to prevent hydrogen-chlorine based erosion.
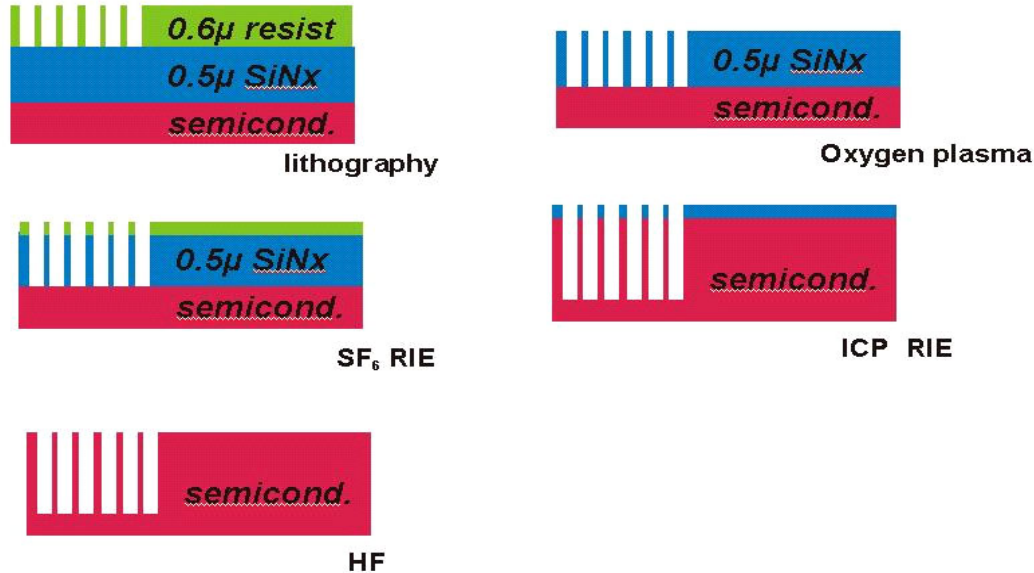

Fig. 1: Fabrication scheme for deep GaN/AlN structures

Initially processes with high flow of chemically reactive gas species have been tried assuming that this will enhance selectivity in any case. Unlike in, e.g., GaAs etching, where it represents an annoying problem, apparently chemical underetching of sidewalls is unlikely in GaN at least in the parameter range investigated within this study. Therefore it was thought that more $SiCl_4$ than N_2 flow would be advantageous. This resulted in an ultimate etch depth of about 2 µm (Fig. 2). But surprisingly the opposite ratio, namely 20:10 $N_2:SiCl_4$ had almost double the selectivity, which we believe to be

due to better etch product sputter removal, since the etch process is not flow limited at all, if in excess of 10 sccm $SiCl_4$. There is an additional argument supporting this gas mixture that was mentioned already: the $SiCl_4$ sputter rate of the SiN_x mask is about 50% higher than the mask sputter rate achieved by using N2 only.
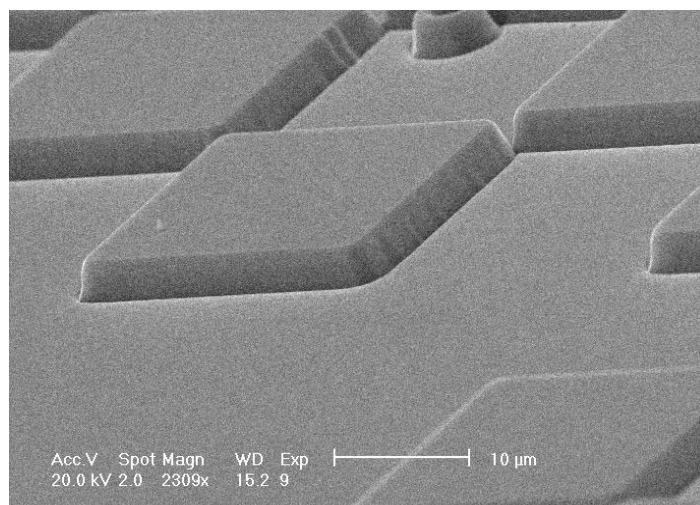

Fig. 2: Typical result of the first set of process testing obtained by etching thick intentionally undoped C-GaN layers on sapphire susbstrates. DC bias set to 200 V, $SiCl_4$:N_2 ratio was 20:10.
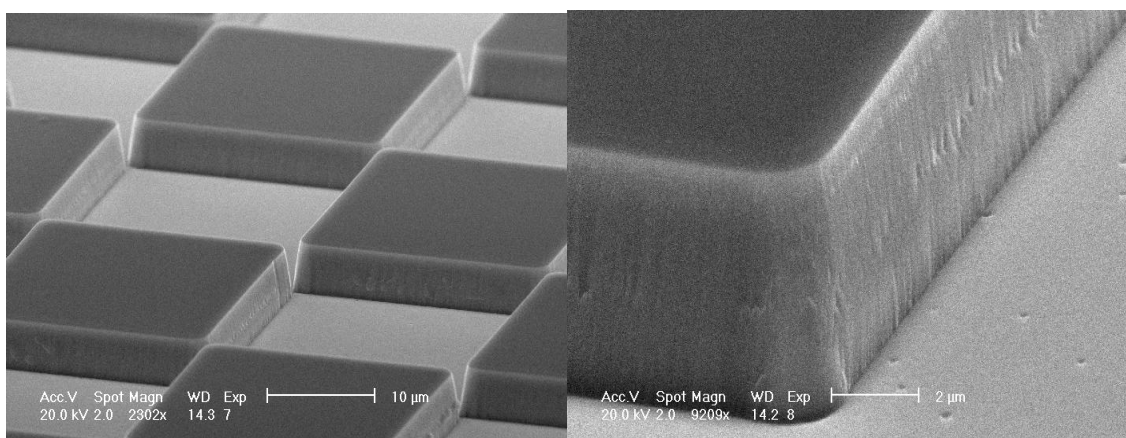

Fig. 3: SEM picture of the 20:10 N_2:$SiCl_4$ process with magnified sidewalls in the picture on the right. The surface roughness is well below a critical roughness for 1.55 µm light. Note that deviations from the verticality are well below 5°.

During optimization it also turned out that very low DC bias does give much better selectivity as well. This might seem somewhat contradictory to the above assumption about sputter removal, but even at room temperature the energy typical $GaCl_x$ compounds need for removal are very low. Thus, there is no additional enhancement in the sputter rate by increasing the ion energy via the applied DC bias. Higher ion energy on the other hand sputters the mask faster and, therefore, reduces the total achievable thickness for a given mask thickness. More reactive species are much more effectively supplied by high powers to the ICP coil, which should break up the $SiCl_4$ in larger amounts. The resulting etch rates we found in our optimized process are about 106 nm/min for GaN and 13 nm/min for the SiN_x mask. This should be sufficient selec-

tivity to prepare waveguides as well as deep etched mirrors. As can be seen in Fig. 3 the sidewall roughness is low and verticality <5° sufficient not to refract light off plane. This small angle deviation from rectangular sidewalls originates from mask erosion, which is always a little bit faster at the edges than in the center of large areas. The etch rate of both, the SiN_X mask and the GaN epilayers did not scale with temperature notably in the investigated temperature range spanning from 150 °C to 300 °C. This is exactly the temperature window in which $InCl_3$ evaporates at pressures around 10 mtorr. The consequence of this particular finding is that it will be easy to obtain smooth but still not underetched profiles of InGaN of any Indium content.

Conclusions

We developed and optimized an etch recipe to perform deep etching of GaN-based materials with a low surface roughness. The process employing inductively coupled plasma reactive ion etching (ICP-RIE) with N_2 and $SiCl_4$ allows an etch depth exceeding 5 µm, sidewalls deviate <5° from verticality. A SiN_X mask gives a selectivity of about 7:1. No trenching occurs at the bottom or into Al containing layers. This process can be readily used for processing of rib waveguides for 1.55 µm wavelength as well as etched reflecting facets.

References

[1]   S. J. Pearton, J. C. Zolper, R. J. Shul, and F. Ren, J. Appl. Phys. 86(1) Appl. Phys. Reviews 1-78 (1999)

[2]   C.B. Vartuli, S.J. Pearton, J.W. Lee, C.R. Abernathy, J.D. Mackenzie, J.C. Zolper, R.J. Shul, and F. Ren, J. Electrochem. Soc. 143, 3681 (1996)

[3]   F.A. Khan, L. Zhou, A.T. Ping, and I. Adesida, , J. Vac. Sci. Techn. B 17(6), 2750-2754 (1999)

[4]   I. Adesida, A. Mahajan, E. Andideh M. Asif Khan, D. T. Olsen, and J. N. Kuznia, Appl. Phys. Lett. 63(20), 2777-2779 (1993)

[5]   R. J. Shul, G. B. McClellan, S. A. Casalnuovo, D. J. Rieger, S. J. Pearton, C. Constantine, C. Barratt, R. F. Karlicek, Jr., C. Tran, and M. Schurman, Appl. Phys. Lett. 69(8), 1119-1121 (1996)

[6]   Y. B. Hahn, Y. H. Im, J. S. Park, K. S. Nahm, and Y. S. Lee, J. Vac. Sci. Techn. A, 19(4), 1277-1281 (2001)

[7]   E. Zhirnov, S. Stepanov, W.N. Wang, Y. G. Shreter, D. V. Takhin, and N. I. Bochkareva, J. Vac. Sci. Techn. A, 22(6), 2336-2341 (2004)

Sensors and Sensor Technology (Posters)

Analytical 3D Hydrodynamical Analysis of Spurious Compressional Wave Excitation by Microacoustic TSM Liquid Sensors

R. Beigelbeck [1] and B. Jakoby [2]

[1] Research Unit for Integrated Sensor Systems
Austrian Academy of Sciences, A-2700 Wr. Neustadt

[2] Institute of Sensor and Actuator Systems
Vienna University of Technology, A-1040 Vienna

Piezoelectric thickness-shear-mode (TSM) resonators are well-established as viscosity and chemical liquid sensors. When immersed in the sample liquid, the resonator excites a strongly damped shear-polarized wave as well as spurious compressional waves in the liquid. The latter are scarcely damped, which can lead to disturbing interferences if they are reflected by obstacles close to the sensor. In order to analyze the spurious compressional wave excitation due to the non-uniform shear displacement across the resonator/liquid-interface, we developed a three-dimensional mathematical model utilizing solutions of the linearized Navier-Stokes equations in the spatial Fourier-domain, which govern the acoustic field in the liquid. We discuss the resulting solutions and illustrate these results by considering practical examples.

Basic Sensor Concept

A typical TSM-resonator for viscosity sensing applications is made of a thin AT-cut quartz disk, which is plated with metal electrodes on both sides of the disk (see Fig. 1). When applying an electric alternating voltage to the electrodes, the resonator starts to vibrate in thickness-shear-mode. The adjacent liquid is entrained by the shear movement of the immersed TSM-resonator, which leads to a change of the resonance frequency and the damping compared to the vibrating resonator in air. By detecting this shift, the viscosity-density product of the liquid can be determined [1], [2].
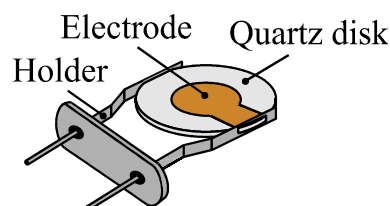

Fig. 1: Typical design of a TSM-resonator for viscosity sensing applications

In the ideal case, a pure and uniform shear displacement across the resonator surface leads to excitation of an evanescent shear wave in the adjacent viscous liquid. However, in the real case, spurious compressional waves are also excited because of

➢ small out-of-plane displacements due to mode conversion (at clamping points, electrode edges, ...),

➢ the uncompensated angular momentum of the dominant shear vibration of the quartz disk [3].

Method and Theory

This contribution deals with a generalization of a recently developed two-dimensional model [1]. We decouple the piezoelectric disk and the fluid region (see Fig. 2 (a)) by considering only the liquid and replace the resonator by impressing a non-uniform Gaussian-shaped shear displacement at the interface as it has been observed in practical measurements [1], [2]. Then, the linearized Navier-Stokes equation in the liquid

$$\nabla^2 \underline{\mathbf{u}} + \alpha \nabla (\nabla \cdot \underline{\mathbf{u}}) + \beta \underline{\mathbf{u}} = \mathbf{0} ,$$

where α and β are fluid parameters [4] and $\underline{\mathbf{u}}(x,y,z)$ is the displacement vector in the liquid, is solved by using a spectral method. The displacement components $\underline{u}_i(x,y,z)$ in the liquid ($i \in \{x,y,z\}$) are represented in terms of compact Fourier double-integrals

$$\underline{u}_i(x,y,z) = \frac{1}{(2\pi)^2} \int_{-\infty}^{\infty} \int_{-\infty}^{\infty} \underline{U}_i(k_x,k_y;z) \exp[-j(k_x x + k_y y)] \, dk_x \, dk_y .$$

Here, k_x and k_y are the lateral wave numbers and $\underline{U}_i(k_x,k_y;z)$ is the general solution ($i \in \{x,y,z\}$) in the spectral domain, which reads

$$\underline{U}_x\left(k_x,k_y;z\right) = \underline{U}_{x0} \left[\frac{\left(k_y^2 - \xi_1\xi_5\right)\exp(\xi_1 z)}{k_x^2 + k_y^2 - \xi_1\xi_5} + \frac{k_x^2 \exp(\xi_5 z)}{k_x^2 + k_y^2 - \xi_1\xi_5} \right],$$

$$\underline{U}_y\left(k_x,k_y;z\right) = -\underline{U}_{x0} \frac{k_x k_y \left[\exp(\xi_1 z) - \exp(\xi_5 z) \right]}{k_x^2 + k_y^2 - \xi_1\xi_5},$$

$$\underline{U}_z\left(k_x,k_y;z\right) = -\underline{U}_{x0} \frac{j k_x \xi_5 \left[\exp(\xi_1 z) - \exp(\xi_5 z) \right]}{k_x^2 + k_y^2 - \xi_1\xi_5} .$$

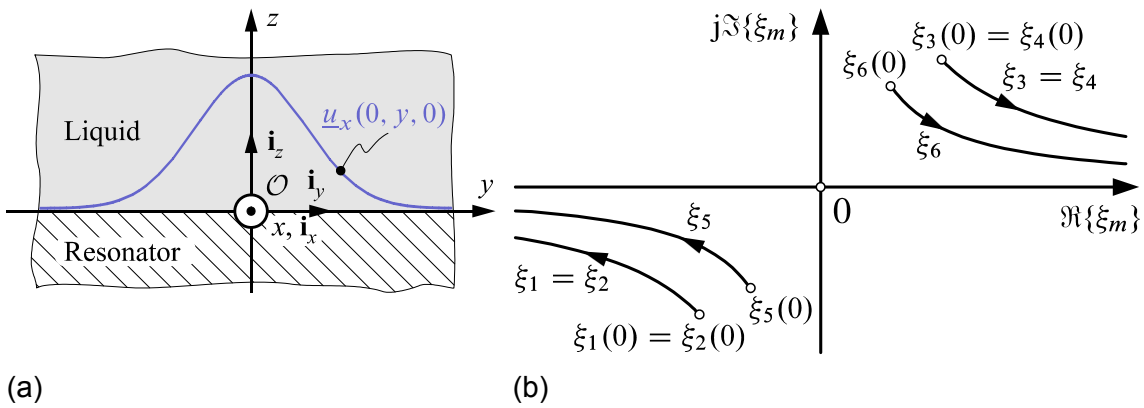(a)   (b)

Fig. 2: (a) Half space model to analyze the wave excitation mechanism of a vibrating TSM-resonator immersed into a liquid. The area $z > 0$ is filled with a linear viscous and adiabatic compressible liquid. The resonator is replaced by an appropriate boundary condition at $z = 0$. (b) Schematic locus of the eigenvalues ξ_m as function of $k = (k_x^2 + k_y^2)^{1/2}$. Note that the real parts of ξ_1, ξ_2, and ξ_5 are negative for any arbitrary value of k, while the real parts of ξ_3, ξ_4, and ξ_6 are always positive. For common liquids is $\left| \Re\{\xi_1\} \right| \Box \left| \Re\{\xi_5\} \right|$ resulting in a much lower damping for compressional waves.

$\underline{U}_{x0}$ is the 2D-Fourier transform of the boundary condition at $z = 0$. $\xi_1 = (k_x^2 + k_y^2 - \beta)^{1/2}$ and $\xi_5 = (k_x^2 + k_y^2 - \beta/(1 + \alpha))^{1/2}$ are the eigenvalues associated to the problem (see Fig. 2 (b)). The real parts of ξ_1 and ξ_5 are related to spatial damping in z-direction, while the imaginary parts correspond to a wave number in z-direction. For small k-values, ξ_5 corresponds to a dominantly longitudinal mode, whereas ξ_1 is related to a dominantly shear polarized mode.

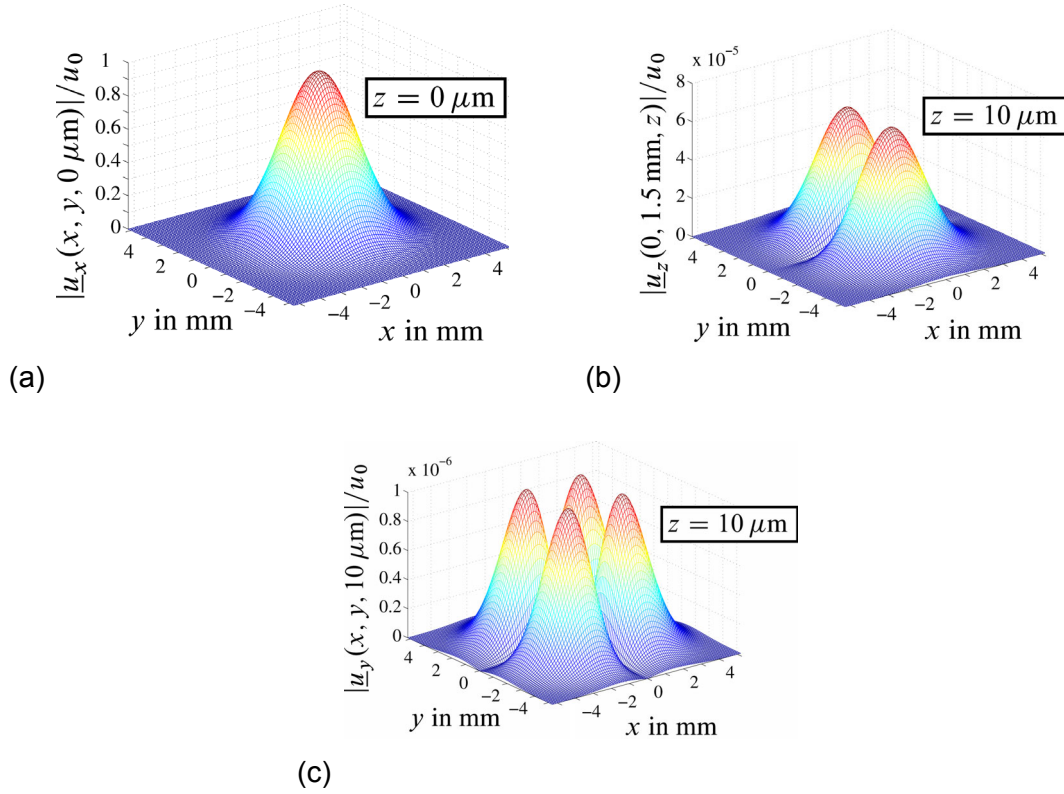(a)   (b)

(c)

Fig. 3: (a) Normalized shear displacement $\left|\underline{u}_x(x,y,0)/u_0\right|$ at the resonator surface $z = 0$ as prescribed by the boundary condition. (b) Normal displacement $\left|\underline{u}_z(x,y,10\,\mu\text{m})/u_0\right|$ at $z = 10\,\mu\text{m}$ above the resonator surface. Two major centers of scarcely damped compressional waves are built up above the resonator. (c) Secondary shear component $\left|\underline{u}_y(x,y,10\,\mu\text{m})/u_0\right|$ at $z = 10\,\mu\text{m}$ above the resonator surface. This component shows four major centers and is a by-product of the compressional wave beams.

Results

We consider a frequency of $6\,\text{MHz}$ and water as sample liquid. As a result, a dominantly shear polarized wave $\underline{u}_x$ is excited (see Fig. 3 (a)), which is highly damped in z-direction (see Fig. 4 (a)). Simultaneously, two major beams (see Fig. 3 (b)) of scarcely damped compressional waves (see Fig. 4 (b)), represented by normal displacements $\underline{u}_z$, are built up with increasing z. Due to their finite lateral extension, these pressure waves cause secondary shear components in x- and y-directions with amplitudes being typically two orders of magnitude smaller than the associated normal (see Fig. 3 (c)) components $\underline{u}_z$. At this height above the surface, the related secondary amplitudes in x-direction are still overshadowed by the primary Gaussian shear displacements. Their damping behavior is similar to one of the compressional waves (see Fig. 4 (c)).
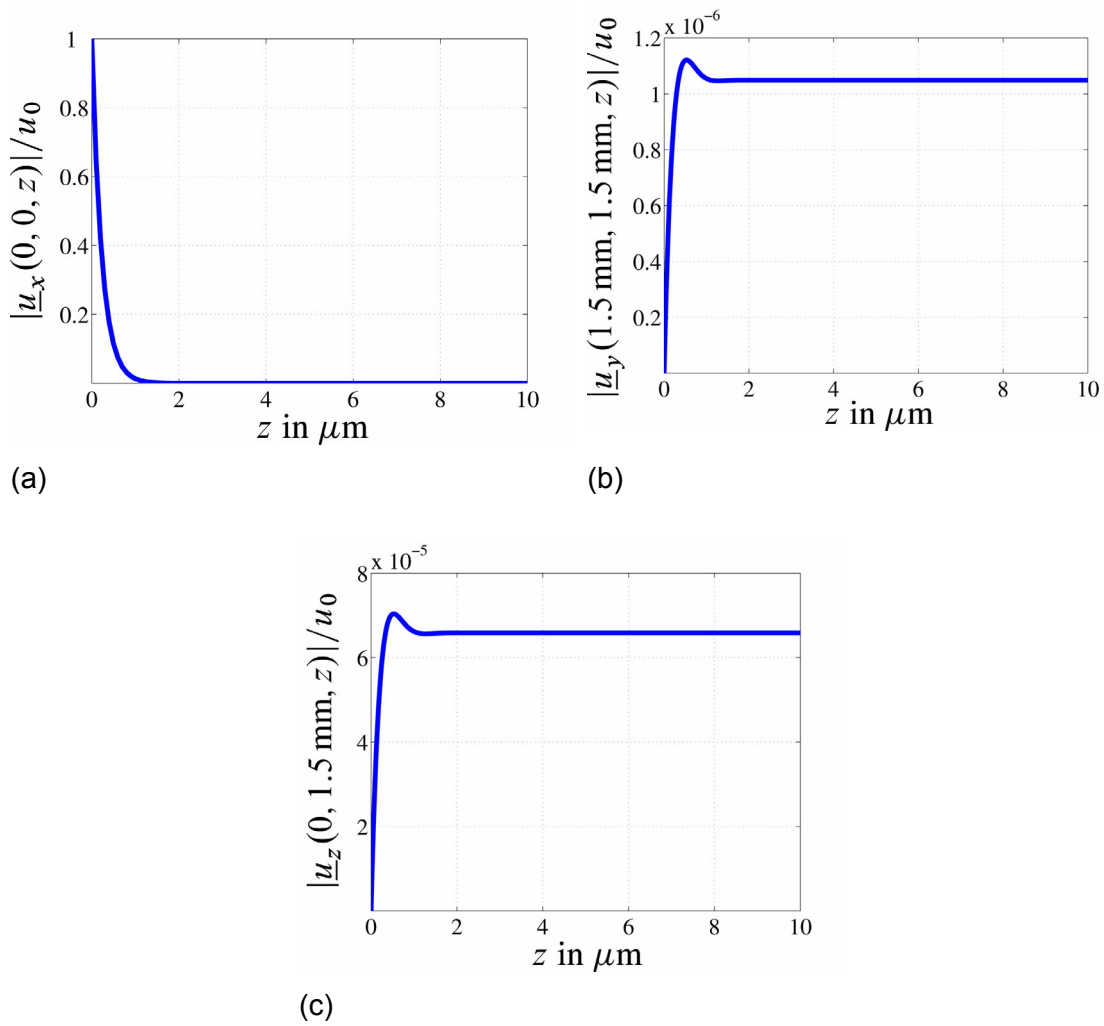
(a)

(b)

(c)

Fig. 4: Comparison of the major peaks of the displacement components with increasing distance z from the resonator surface.

References

[1] B. A. Martin and H. E. Hager: "Velocity profile on quartz crystals oscillating in liquids", Journal of Applied Physics, 65: 2627, 1989.

[2] B. A. Martin and H. E. Hager: "Flow profile above a quartz crystal vibrating in liquid", Journal of Applied Physics, 65: 2630, 1989.

[3] E. Benes et al.: "Sensors based on Piezoelectric Resonators", Sensors and Actuators A, 48:1, 1995.

[4] R. Beigelbeck and B. Jakoby: "A Two-Dimensional Analysis of Spurious Compressional Wave Excitation by Thickness-Shear-Mode Resonators", Journal of Applied Physics, 95(9):4989, 2004.

Simultaneous Measurement of Two Magnetic Field Components Using a Single U-Shaped MEM Cantilever Device

F. Keplinger [1], R. Beigelbeck [2], F. Kohl [2], and P. Loschmidt [2]

[1]Institute of Sensor and Actuator Systems
Vienna University of Technology, A-1040 Vienna

[2]Research Unit for Integrated Sensor Systems
Austrian Academy of Sciences, A-2700 Wr. Neustadt

A miniaturized sensor capable of measuring simultaneously two orthogonal components of the magnetic flux density is presented. These magnetic field components excite two different resonant modes of a single micromachined U-shaped cantilever. The cantilever vibrations are accomplished by the Lorentz force acting on an alternating electrical current, which flows through a thin film lead attached to the top surface of the silicon cantilever. This lead operates also as a deflecting mirror in an optical readout system which is used to detect the oscillations of the cantilever. By means of two lock-in amplifiers, the output of the readout is converted into two signals related to orthogonal components of the magnetic flux density. The feasibility of the system is proved by measuring contour plots of the magnetic flux distribution of a sample magnet.

Introduction

Micromachined cantilevers enable measurement of a variety of physical parameters such as magnetization or viscosity. These devices offer a high quality factor and achieve a high sensitivity when they are excited at or near a resonant frequency. To measure magnetic fields with cantilever structures, the Lorentz force is utilized on a current carrying lead. Cantilevers vibrating in the fundamental mode are typically used to measure the magnetic flux density in the direction parallel to the arms of the cantilever. The presented approach uses high order oscillation modes to measure the flux density components parallel to the base of the cantilever.

Sensor Principle and Theory

The Lorentz force is used to bend a micromachined cantilever (Fig. 1). Small deflections compared to the length of the cantilever are directly proportional to the applied force. To reach a high sensitivity, the cantilever is excited by a sinusoidal alternating current at the resonant frequency.

The investigated U-shaped cantilever can oscillate in various flexural vibration modes (Fig. 2), whereas the first four modes are of most practical importance. With respect to our design, these modes can be divided into two symmetrical (S1 and S2, where the cantilever arms are moving in parallel) and two antisymmetrical ones (A1 and A2, where the arms move in opposite directions).
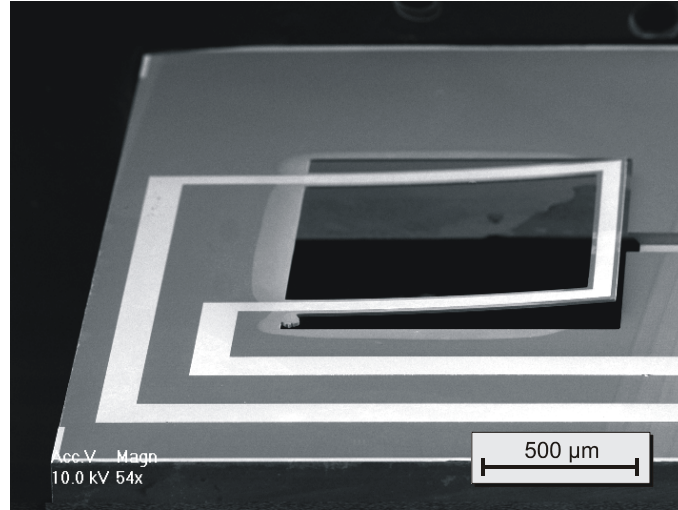
Fig. 1: Micromachined silicon cantilever with a thickness of 12 μm. The bright area represents the gold surface of the lead.
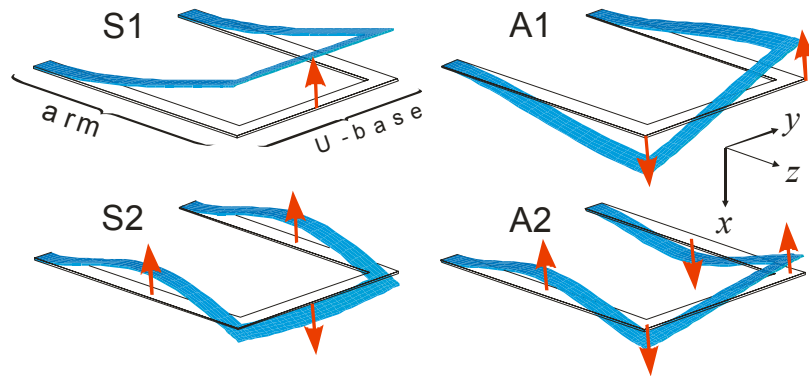

Fig. 2: Visualization of the first two symmetric (S1 and S2) and the first two anti-symmetric (A1 and A2) flexural vibration modes obtained by a finite element analysis.

The oscillating cantilever structure can be described by the classical Euler-Bernoulli beam dynamics theory leading to a set of three (one for each cantilever arm and one for the cantilever base) coupled linear 4th-order partial differential equations which read as

$$\frac{\partial}{\partial \zeta_i^{\,2}}\left(EI_i(z)\frac{\partial^2 \psi_i}{\partial \zeta_i^{\,2}}\right)-\left(f_i-\overline{m}_i(z)\frac{\partial^2 \psi_i}{\partial t^2}\right)=0$$

where $i = 1, 2$ indicates the arms and $i = 3$ the base. Regarding this, EI_i denotes the stiffness, ζ_i the coordinate along the cantilever ($\zeta_{1,2} = z$ and $\zeta_3 = y$), f_i the external forces, $\overline{m}_i$ the mass per unit length, t the time, and $\psi_i(\zeta_i, t)$ the deflection along the cantilever.

Experimental

Cantilever Excitation

Each mode can be excited by suitable Lorentz force distributions on different parts of the lead. The fundamental mode S1 is excited by a homogeneous magnetic field in z-direction. The field is parallel to the arms of the cantilever and therefore the forces are generated only at the base of the "U". The first antisymmetric mode A1 is excited by a homogeneous magnetic field in y-direction, where the Lorentz forces develop only along the arms of the cantilever. Due to the different orientation of the electrical current, the arms are bent in opposite directions.

Optical Readout

The vibrations of the cantilever are contact-free sensed using an optical readout. The IR-beam of a commercial available reflective sensor is returned partially by the surface of the gold lead on top of the cantilever and received by the photo transistor of the reflective sensor as shown in the experimental setup of Fig. 3.
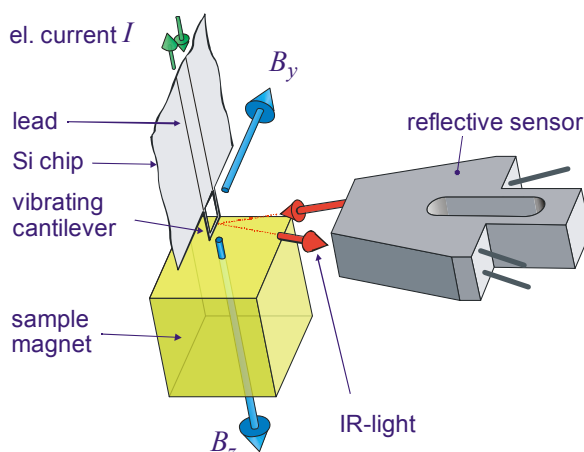

Fig. 3: Experimental setup: The oscillations of the cantilever caused by the Lorentz force modulate the intensity of an infrared beam emitted and detected by a reflective sensor.

Signal Generation for Dual Field Component Measurement

To excite the first symmetric (S1) and the first antisymmetrical mode (A1) simultaneously, the appropriate flux densities have to be present and the composite AC current should match to the resonant frequencies of the flexural vibration modes (Fig. 4). The amplified output signal of the reflective sensor is analyzed by two lock-in amplifiers. Their output signals are proportional to the magnetic flux densities to be measured. The phase information is used to determine the direction of the magnetic field.

Results

A typical measurement example is depicted in Fig. 5, where a permanent magnet of a voice coil actuator which moves the multiple read/write heads of a hard disk is scanned to create a contour plot of the magnetic flux distribution. The distance between magnet surface and cantilever tip is 2 mm.
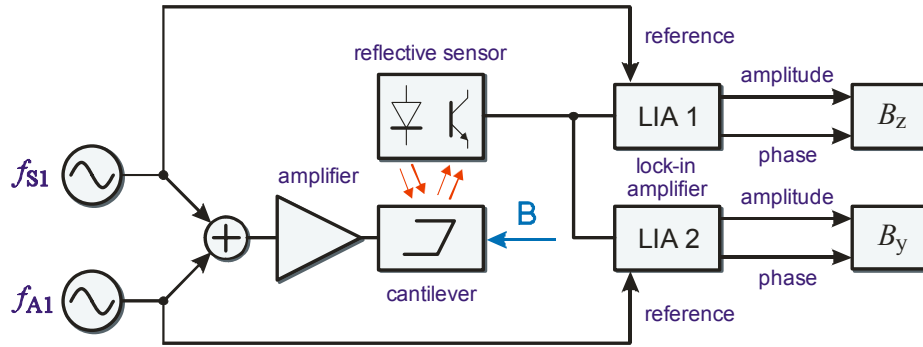
Fig. 4: To excite the symmetric (S1) and the antisymmetric (A1) oscillation modes of the cantilever simultaneously, two AC currents with frequencies according to the resonant frequencies (f_{S1} and f_{A1}) of these modes are added up and amplified. The magnetic flux densities (B_z and B_y) determine the amplitude of the cantilever oscillations and modulate the light reflected by the cantilever surface. The amplified output of the reflective sensor is analyzed by two lock-in amplifiers synchronized to the excitation frequencies. With amplitude and phase
information, strength and direction of the magnetic flux density in *z*- and *y*-direction can be calculated.
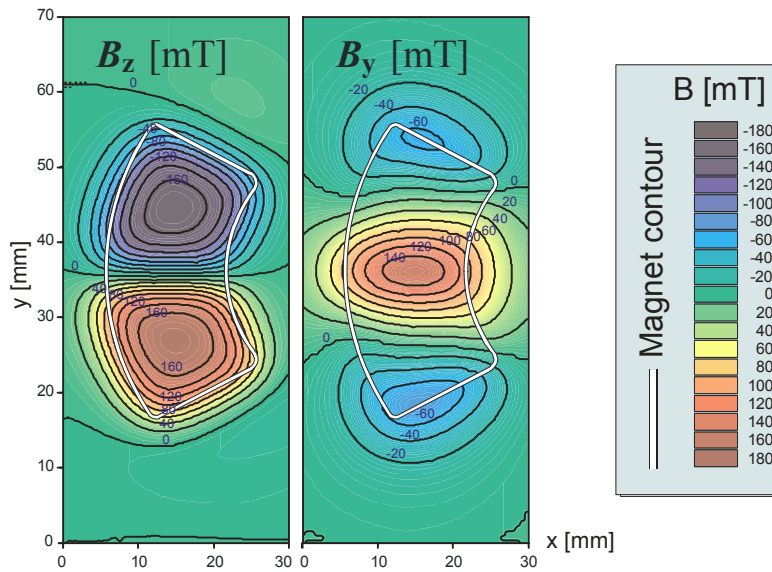

Fig. 5: Contour plots of the magnetic flux density in *z*- and *y*-direction of a kidney shaped permanent magnet of a voice coil actuator of a hard disk drive.

Conclusion

Utilization of two vibration modes of a U-shaped cantilever allows simultaneous measurement of two orthogonal flux density components with a single optical read out. The presented design is not feasible for measuring magnetic flux components in *x*-direction because modes sensitive to this direction have resonant frequencies far beyond 100 kHz and too low amplitudes. To measure all three components, a redesign of the vibrating structure has to be performed.

Oil Condition Monitoring Using a Thermal Conductivity Sensor

J. Kuntner, R. Chabicovsky, and B. Jakoby

**Industrial Sensor Systems, Institute of Sensor and Actuator Systems
Vienna University of Technology, Austria**

In recent years, the monitoring of oil-based liquids has gained increasing importance in various branches of the industry. In this contribution we discuss the application of a miniaturized thermal conductivity sensor for the monitoring of water contamination and deterioration processes in mineral oil. The sensor, which utilizes the hot film principle, features a molybdenum resistive structure simultaneously serving as heater and sensing element. The experimental results show that both, water contamination and deterioration processes in mineral oil lead to an increased thermal conductivity, indicating the potential of thermal conductivity sensors in the field of oil condition monitoring. Finally we analyzed the sensor's performance numerically in order to further evaluate its applicability and possible design modifications.

Introduction

In recent years, the monitoring of oil-based liquids has gained increasing importance in various branches of the industry. A prominent example is the condition monitoring of lubrication and insulating oils. In both cases the water contamination of oil often cannot be avoided which seriously influences its performance if certain levels are exceeded. In the case of lubrication oil, excessive water content leads to insufficient lubrication and subsequently to abrasive wear and corrosion. In case of insulation oils, increased water content results in a considerable reduction of the breakdown voltage. Thus, the detection of water content in the oil is of major importance.

Comparing the thermal transport properties of mineral oil and water, it turns out that the latter features a five times higher thermal conductivity. This indicates that thermal conductivity is a potential parameter for the detection of water content in mineral oils. In this contribution we investigate the thermal transport properties of W/O emulsions and artificially aged oils using a resistive hot film microsensor.

	ϑ	ρ	c_p	λ
	°C	$\frac{kg}{m^3}$	$\frac{J}{kgK}$	$\frac{W}{mK}$
Water	20.0	998	4183	0.598
Engine Oil	60.0	868	2010	0.140
Insulation Oil	60.0	842	2090	0.120

Table 1: Thermal properties of selected liquids [1].

Theory

During the last four decades many different techniques for measuring the thermal conductivity of liquids, solids, and gases have been developed. For the characterization of the thermal transport properties of fluids, in particular the transient hot-wire method is widely-used (see, e.g., [2]). This technique is based on a thin metal wire, mostly made of platinum, simultaneously serving as both, heater and sensing element. By applying a transient electrical current, the wire and the surrounding medium under investigation start heating up. Recording the corresponding temperature response of the wire enables the determination of the thermal conductivity and diffusivity of the surrounding fluid. Instead of a wire, other heater geometries have also been utilized. In case of the classical transient hot-strip technique a thin metal sheet is used (see e.g., [3]). In micro technology, this sheet is replaced by a thin film structure deposited on a substrate. In order to minimize the influence of this substrate on the sensor's performance various geometries like thin membranes, cantilevers, or micro-bridges can be utilized. However, regarding the applicability in harsh industrial environments, a trade-off has to be found between sensitivity and mechanical robustness. In this contribution we consider a hot film microsensor, which is operated using an adapted transient method.

Considering the small dimensions of the sensor compared to the used sample volumes (15 ml) of the investigated liquids, the corresponding temperature field in some distance from the sensor can be approximated by solving the heat diffusion equation for a thermal point source switched on at $t = 0$:

$$\vartheta(r, t) = \frac{\Phi}{4 \pi \lambda\, r}\, \text{erfc}\left(\frac{r}{\sqrt{4at}}\right) \tag{1}$$

Here Φ denotes the heating power, λ the thermal conductivity, a the thermal diffusivity, and r the radial distance from the point source [1]. Note that for small r, this approximation becomes inaccurate and even yields a non-physical singularity for $r = 0$. The diffusivity is related to the heat capacity c_p by

$$a = \frac{\lambda}{\rho \cdot c_p}, \tag{2}$$

where ρ denotes the mass density. For $t \to \infty$ the complementary error function erfc in Eq. (1) approaches unity such that in the steady state, the temperature distribution depends on the thermal conductivity and the heating power only:

$$\vartheta(r)\Big|_{t \to \infty} = \frac{\Phi}{4 \pi \lambda\, r} \tag{3}$$

Sensor Design and Fabrication

Figure 1 shows the basic layout of the thin film microsensor. The device consists of a glass substrate (5 mm x 2.6 mm x 0.4 mm) with a resistive loop made of molybdenum as resistive sensing and heating element. Molybdenum is known for its linear resistance characteristics, which is valid over a wide temperature range. The shape of the resistive loop is especially designed to allow digital laser trimming. To avoid any chemical interaction between the resistor and the fluid, the molybdenum is covered with a silicon nitride protective layer. The bonding pad area is additionally coated with a nickel chromium adhesive layer and a gold layer. All films have been deposited by RF-sputtering in a Perkin Elmer 4400 diode system. The system allows the deposition of the nickel chromium and gold films without a vacuum interruption, which ensures the production of solderable contacts.

The film patterning has been carried out by lift off photolithography techniques. The connecting wires are bonded to the contact pads by soldering. The temperature coefficient of the resistive loop was measured to be 0.956×10^{-3}/°C and its resistance was 112.55 Ω at 22.1°C.

Resistive loop

Protective layer
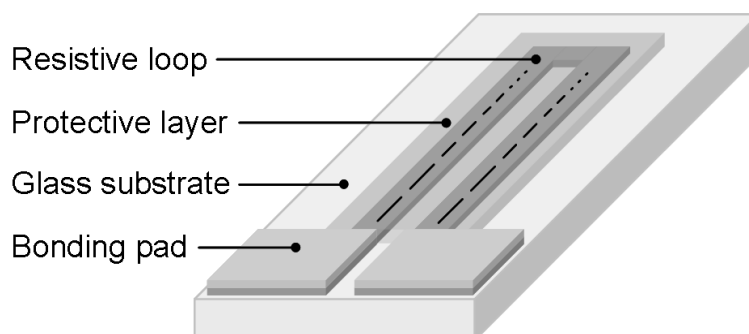
Glass substrate

Bonding pad

Fig. 1: Design of the hot film sensor.

Measurement Setup

The sensor was inserted into a beaker containing the sample liquid and was electrically connected to a measurement bridge as shown in Fig. 2. The differential bridge output voltage is amplified by an instrumentation amplifier (gain = 25) and recorded by means of a digital oscilloscope. By switching on the power supply (12 V), the heater current is turned on and the temporal evolution of the resistance (and thus the sensor temperature) can be monitored by recording the bridge output voltage. As long as the temperature at the walls of the beaker does not increase significantly, the assumption of an infinitely extended medium, which is also underlying Eq. (1), is approximately valid. In this case the sensor response is basically determined by the thermal material parameters of the surrounding liquid.
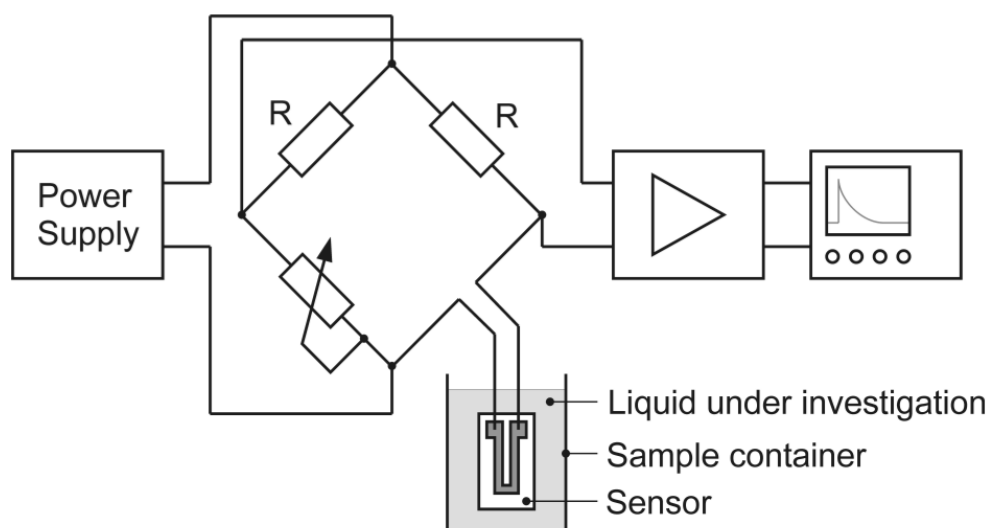
Power Supply

R   R

Liquid under investigation

Sample container

Sensor

Fig. 2: Measurement Setup (R=470 Ω).

Results and Discussion

First we investigated water contamination in engine oils, where we deliberately contaminated a standard engine oil (SAE 15W40) with DI water, which leads to the formation of an emulsion. Figure 3 shows the resulting temperature rise $\Delta\vartheta$ above ambient (room) temperature versus the time t after switching on, for emulsions featuring a water content of 7%, 15% and 18% by volume compared to the pure oil sample. After the initial transient, the excess temperature becomes essentially determined by the thermal conductivity (see also Eq. (1)). It can thus be seen, that for increasing water contents the thermal conductivity of the emulsions increases, which leads to lower excess temperatures. Compared to pure oil, the excess temperature at $t = 20$ seconds is reduced by 4.7%, 10.5%, and 13.6%, for the W/O emulsions containing 7%, 15%, and 18% of water by volume, respectively.
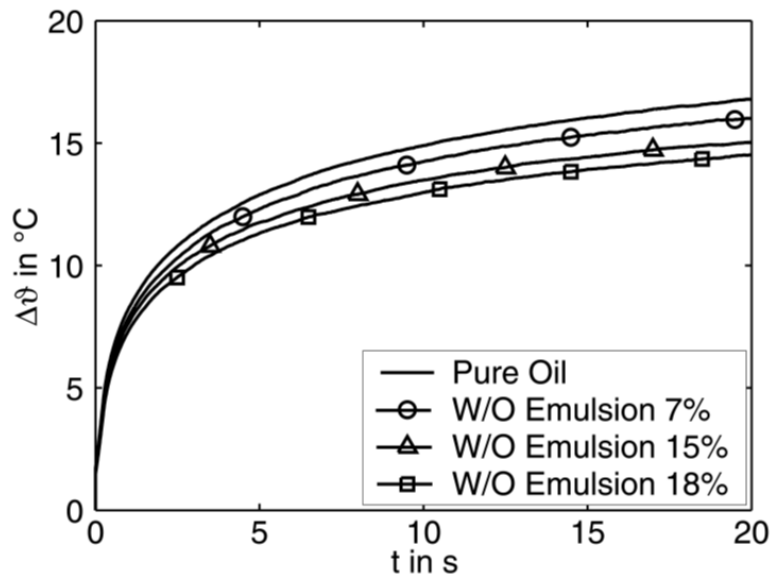

Fig. 3: Temperature rise $\Delta\vartheta$ vs. time t for W/O emulsions of 7%, 15%, 18% b.v. and the corresponding pure oil (SAE 15W40).
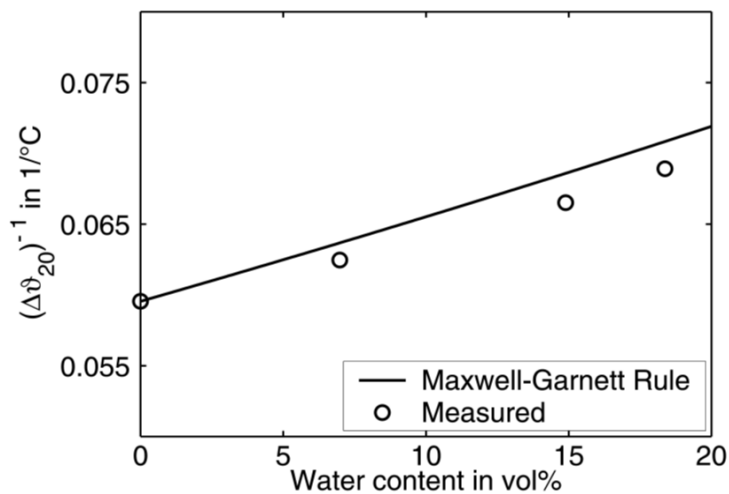

Fig. 4: Inverse of $\Delta\vartheta$ @ $t=20$ seconds (which is approximately proportional to λ) vs. water content in % b.v.

Figure 4 shows the inverse of the excess temperature, $1/\Delta\vartheta$, at $t = 20$ seconds versus the water content. At this time the disturbing influence of the boundary is still negligible and the excess temperature has virtually reached its steady state. Thus we can assume that $1/\Delta\vartheta$ will be approximately proportional to the thermal conductivity λ (see also Equ. (1) for $t \to \infty$).

In further experiments we investigated the effect of oxidative deterioration. Figure 5 shows the resulting temperature rise $\Delta\vartheta$ above ambient (room) temperature versus the time t after switching on, for engine oil (SAE 15W40) which was artificially aged at 160°C for 7 days according to a standardized method. It can be observed that the deteriorated oil features an increased thermal conductivity which could be related to water formation due to thermal oxidation processes in the engine oil. We observed a total increase of about 3.4% for the above mentioned ageing conditions.
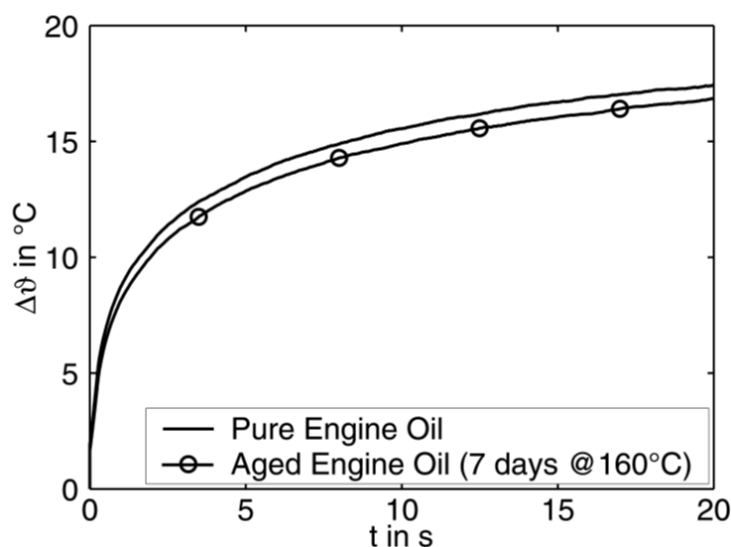

Fig. 5: Temperature rise $\Delta\vartheta$ vs. time t for pure engine oil (SAE 15W40) and artificially aged engine oil (7 days @ 160°C).

According to theoretical considerations, for the steady state the excess temperature of the sensor becomes essentially determined by the thermal conductivity of the surrounding fluid. This mechanism allows to clearly detect water deterioration in mineral oil, but underlies the restriction of a maximum measuring time that must not be exceeded to avoid the disturbing influence of the liquid boundary. To overcome this problem a transient measurement lasting several hundred milliseconds could be utilized, which would correspond to the concept of the above-mentioned hot-wire and hot-strip methods. However, as can be seen, e.g., from the measurement shown in Fig. 3, within this time frame a deviation between different samples can hardly be observed. By considering the sensor design, we find that the initial transient to a certain extent will be determined by the specific heat of the sensor substrate and the liquid. Glass features a specific heat comparable to that of mineral oil and moreover shows a very high thermal conductivity (typically 10 times higher than that of oil). Hence it can be assumed that due to the relatively thick glass substrate, the sensitivity in the initial transient regime is decreased accordingly. However, at the same time the thickness of the sensor increases its physical robustness.

To further investigate on these assumptions, a Finite Element (FE) simulation has been conducted. Figure 6 (a) depicts the simulated temperature rise $\Delta\vartheta$ within the initial transient of 500 milliseconds for an emulsion featuring a water content of 20% by volume compared to the pure oil sample. In order to evaluate the impact of the substrate thick-

ness on the initial temperature slope, we calculated the initial transient for the same sample liquids but for a sensor structure with a reduced thickness of 5 microns instead of 400 microns. Figure 6 (b) shows the resulting excess temperature and the initial temperature slope. As expected reducing the thermal mass of the sensor results in a steeper slope and in an increased sensitivity with respect to water contamination of the oil. Compared to the pure oil sample, the initial transient slope, $d\Delta\vartheta/dt$, for the emulsion was -13.0% and -24.5% smaller for the thick and the thin glass substrate, respectively. This indicates the increase in sensitivity for the transient measurement method that can be obtained by reducing the influence of the glass substrate by making it thinner. Thus the sensitivity generally increases if a thinner glass substrate is used. In practical applications, the mechanical robustness of the sensor has to be considered as well, which accordingly requires a trade-off in choosing the thickness.
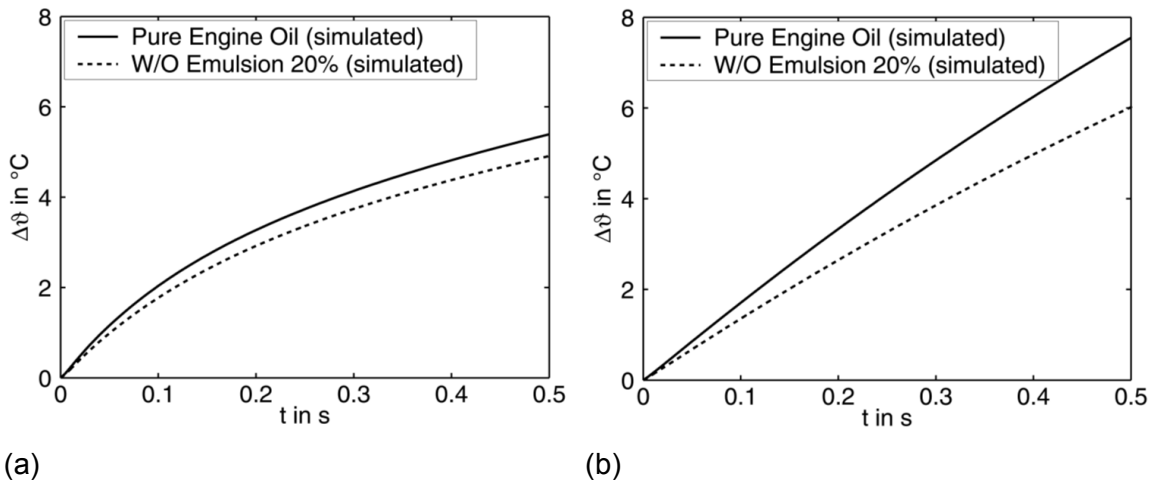

(a)   (b)

Fig. 6: (a) Simulated temperature rise $\Delta\vartheta$ vs. time t of the initial transient for W/O emulsions of 20% b.v. and the pure oil. (b) Simulated temperature rise $\Delta\vartheta$ vs. time t for a glass substrate with a reduced thickness of 5 µm.

Conclusion

In this contribution we discussed the applicability of thermal conductivity sensing for liquid condition monitoring. As sample applications we considered the water contamination and the deterioration of mineral oils. For this purpose we performed experiments with a hot film sensor using a resistive thin-film molybdenum structure on a glass substrate. It could be shown that not only water-in-oil emulsions but also aged oils feature increased thermal conductivities compared to the base oils, which indicates that monitoring the thermal conductivity by means of miniaturized sensors could be utilized in oil condition monitoring systems. By means of numerical simulations it was furthermore found that the sensitivity of the sensing approach in the transient regime could be significantly increased by utilizing a thinner substrate, which, however, would reduce the mechanical robustness of the sensor.

Acknowledgements

References

[1]   U. Grigull, and H. Sandner, "Wärmeleitung", 2nd edition, Springer, 1990.

[2]   J.J. Healy, J.J. de Groot, and J. Kestin, "The theory of the transient hot-wire method for measuring thermal conductivity", Physica C, Vol. 82, 1976, pp. 392 - 408.

[3]   S.E. Gustafsson, E. Karawacki, and M.N. Khan, "Transient hot-strip method for simultaneously measuring thermal conductivity and thermal diffusivity", J. Phys. D: Appl. Phys., Vol. 12, 1979, pp. 1411 - 1421.

Microsensor for the Measurement of the Transepidermal Water Loss of Human Skin

M. Mündlein [1], R. Chabicovsky [1], J. Nicolics [1], B. Valentin [1], P. Svasek [2],
E. Svasek [2], T. Komeda [3], H. Funakubo [3], T. Nagashima [3], M. Itoh [3]

[1]Institute of Sensor and Actuator Systems, Vienna University of Technology, A-1040 Wien

[2]Ludwig Boltzmann Institute of Biomedical Microtechnique, A-1040 Wien

[3]Shibaura Institute of Technology, Faculty of Systems Engineering, Saitama-City, 330-8570 Japan

We have developed a novel microsensor to measure the emission of water from human skin. Measurement of the transepidermal water loss (TEWL) is used for studying the water barrier function of the skin. The microsensor consists of a ceramic substrate carrying a thin film interdigital electrode system covered with a highly hygroscopic salt film. The change of capacitance of the electrode system per unit of time is a measure for the TEWL value. We demonstrate the different measuring results with normal skin and atopic skin.

Introduction

The protective function of the human skin shields the body not only from external influences (e.g. germs) but also prevents it from drying up. The stratum corneum (outer part of the skin) is flexible as long as it contains more than 10% water, but it becomes hard and brittle when dehydrated. Dermatologists universally recognize the unaffected skin of patients with atopic dermatitis by the fact that it tends to be dry and slightly scaly [1]. Different techniques have been developed to measure the skin properties that are influenced by the water content. Among the most widely used techniques are those involving the measurement of the skin impedance [2] – [5]. In this case the sensor chip must be brought into direct contact with the skin and therefore, a completely flat front surface of the sensor chip is necessary [6], [7]. One disadvantage of this type of sensor is the pollution of the chip caused by the skin.

A further possibility to investigate the skin health is the measurement of the transepidermal water loss (TEWL) expressed in grams per square meter and per hour [8] – [10]. This is an important parameter for evaluating the efficiency of the water barrier function. The more perfect the skin protective coat is, the higher the water content and the lower the TEWL. Disorders such as atopic dermatitis arise when the barrier function does not work properly. TEWL measurements allow the discovery of disturbances in the skin protective function in an early stage. By this way the onset of dermatological therapies can be accomplished in good time.

Different methods for TEWL measurement from local skin sites have been described: closed chamber methods and open chamber methods [9]. In this work we use a new type of sensor in a closed chamber arrangement. This arrangement offers the advantage of reduced influence of the environment resulting in more stable and reproducible measurements.

Measuring Principle and Sensor Technology

When the sensor device touches the skin a small hermetically closed measuring chamber is formed. A miniaturized humidity sensor is located on the top of this chamber in a distance of about 1.4 mm away from the skin surface (Fig. 1). The water vapor emitted from the skin fills the measuring chamber and causes an increasing relative humidity inside the chamber. A part of this humidity condenses on the comparable cold humidity sensor surface causing there a growing film of water. The growing rate of this film can be expressed by the change of the sensor impedance within a defined time interval.
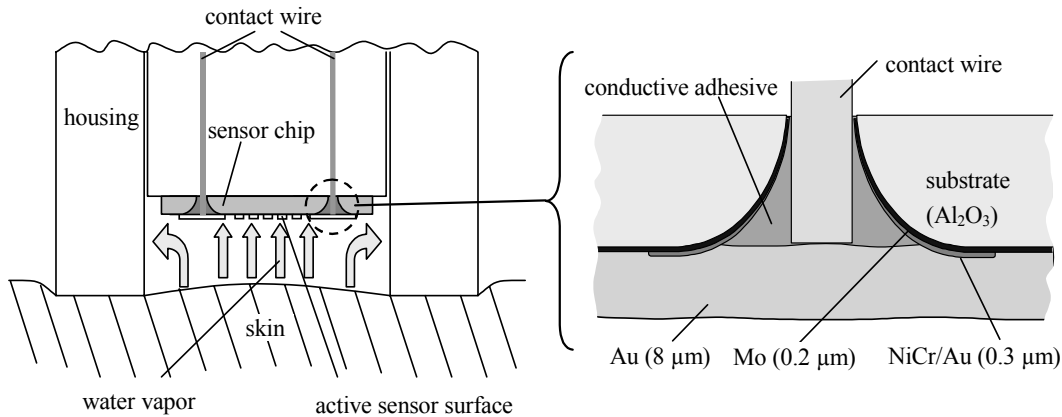

Fig. 1: Schematic cross sectional view of the TEWL-sensor with closed measuring chamber (increasing concentration of water vapor in the chamber after touching the skin). The funnel-shaped holes are produced by a special laser drilling process. The thick gold layer is deposited by electroplating.
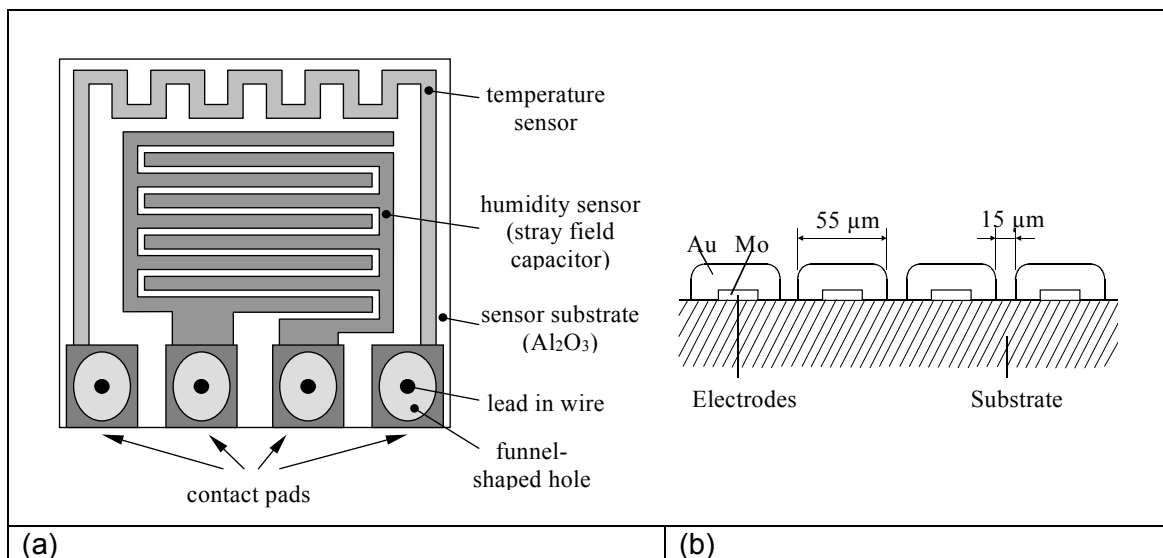

Fig. 2: (a) Schematic structure of the thin film microsensor. The chip dimensions are 5 mm x 5 mm x 0.6 mm. (b) Schematic cross sectional view of the electrode system.

The novel microsensor used in this work consists of a small ceramic substrate (5 mm x 5 mm x 0.6 mm) carrying a metallic interdigital electrode system (Fig. 2). We have used a double-layer system of molybdenum and gold for the sensor electrodes. The molybdenum film has been deposited by rf-sputtering; the rather thick gold film (8 μm) has

been produced by electroplating. The width of the electrodes is about 55 µm; the gap between them is approximately 15 µm. The active moisture sensing area is 1.75 mm x 3.15 mm. The contacts of the electrodes are made of a sputtered layer system of molybdenum, nickelchrome and gold. The lead-in wires are guided through funnel-shaped holes to the rear substrate surface (Fig. 1). These holes were laser-drilled into the ceramic substrate using a CO_2-laser. The lead-in wires are bonded to the contacts by using an isotropically conductive adhesive. The result is a completely flat front surface of the sensor [6], [7]. This fact is important for the application as a TEWL-sensor. The sensitivity is significantly improved by covering the active area of the sensor chip with a hygroscopic inorganic salt film. All technological work has been carried out in the Institute of Sensor and Actuator Systems of the Vienna University of Technology.

Measurements and Results

The measurements have been carried out in the Shibaura Institute of Technology in Japan. We have used an LCR-meter HP 4285A connected to a computer. The measuring frequency was 500 kHz and the measuring voltage was 100 mV. We have used an equivalent circuit R parallel C and the capacitance C was chosen as the output quantity (Fig. 3). However, for further measurements carried out at the Vienna University of Technology we have used the conductance as the output quantity [10].
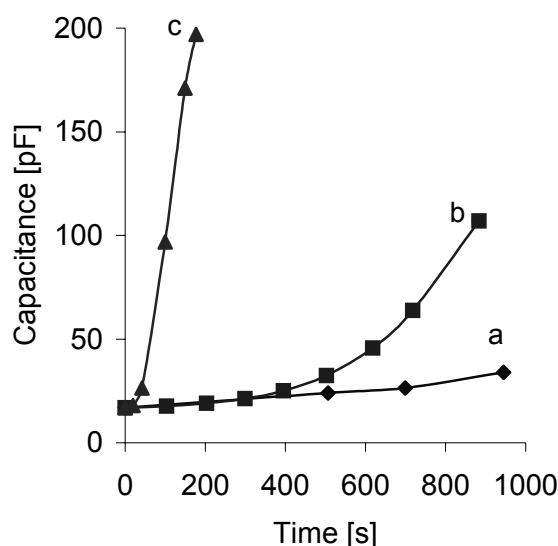

Fig. 3: Capacitance as a function of time. Curve a: normal skin of an elderly male person. Curve b: normal skin of a young male person. Curve c: atopic skin of a young male person. Measurements have been carried out at 500 kHz and 100 mV on the right forearm in a room with stable conditions (relative humidity 30%, temperature 23 °C).

Conclusion

The transepidermal water loss is an important factor for characterizing the health condition of human skin. TEWL measurements allow the discovery of dysfunctions of the skin even before they are visible. A measuring device with a novel moisture sensor in a closed chamber configuration has been introduced. The slope of the capacitance vs. time characteristic of the sensor can be used as a measure for the TEWL-value of the investigated skin.

Acknowledgements

References

[1]   M. Watanabe, H. Tagami, I. Horii, M. Takahashi, A.M. Kligmann: "Functional analyses of the superficial stratum corneum in atopic xerosis", Arch. Dermatol. 127, 1991, pp. 1689-1692.

[2]   M. Mündlein, J. Nicolics, R. Chabicovsky, N. Sekiguchi, T. Komeda, H. Funakubo, G. Stangl: "Innovative packaging concept of a miniaturized skin moisture sensor and first measuring results", Proc. 2nd European Medical and Biological Engineering Conference-EMBEC 2002, Vienna, Austria, December 4-8, 2002, pp. 968-969.

[3]   N. Sekiguchi, T. Komeda, H. Funakubo, R. Chabicovsky, J. Nicolics, G. Stangl: "Microsensor for the measurement of water content in the human skin", Proc. 14th European Conference on Solid-State Transducers (EUROSENSORS XIV), August 27-30, 2000, Copenhagen, Denmark, pp. 407-410.

[4]   M. Mündlein, A. Brunner, J. Nicolics, R. Chabicovsky, N. Sekiguchi, T. Suzuki: "Prototype of a skin humidity sensor and initial experiments", Proc. 25th International Spring Seminar on Electronics Technology (ISSE 2002), Prague, Czech Republic, May 11-14, 2002, pp. 95-99.

[5]   N. Sekiguchi, T. Komeda, H. Funakubo, R. Chabicovsky, J. Nicolics, G. Stangl: "Microsensor for the measurement of water content in the human skin", Sensors and Actuators B 78 (2001), pp. 326-330.

[6]   M. Mündlein, A. Brunner, R. Chabicovsky, G. Stangl, J. Nicolics: "A new interconnection technology for the attachment of sensors", Proc. 24th International Spring Seminar on Electronics Technology (ISSE 2001), Calimanesti-Caciulata, Romania, May 5-9, 2001, pp. 277-281.

[7]   G. Hanreich, J. Nicolics, M. Mündlein, H. Hauser, R. Chabicovsky: "A new bonding technique for human skin humidity sensors", Sensors and Actuators A 92 (2001), pp. 364-369.

[8]   J. Serup, G. Jemec: "Handbook of non-invasive methods and the skin", Chapter 9.1, J. Pinnagoda, R.A. Tupker, "Measurement of the Transepidermal Water Loss", CRC Press Inc., 1995, pp. 173-178.

[9]   M. Mündlein, J. Nicolics, R. Chabicovsky, P. Svasek, E. Svasek, T. Komeda, H. Funakubo, T. Nagashima, M. Itoh: "Packaging of a thin film sensor for transepidermal water loss measurements", Proc. 26th International Spring Seminar on Electronics Technology, May 8-11, 2003, Stara Lesna, Slovak Republic, pp. 328-333.

[10]   B. Valentin, M. Mündlein, R. Chabicovsky, J. Nicolics: "Evaluation of a novel transepidermal water loss sensor", CD-ROM Proceedings of the IEEE Sensors 2004 Conference, Vienna, Austria, October 24-27, 2004, pp. 115-118.

Particle Discrimination with an Improved Projection Cytometer

J.H. Nieuwenhuis [1], P. Svasek [2], P.M. Sarro [3], M.J. Vellekoop [1]

[1] Institute of Sensor and Actuator Systems, Center for Micro and Nanostructures, Vienna University of Technology, Austria

[2] Ludwig Boltzmann Institute of Biomedical Microtechnology, Vienna, Austria

[3] Laboratory of ECTM – DIMES, Delft University of Technology, Delft, The Netherlands

An integrated cytometer is presented based on optical projection. A sheath flow focuses the particles closely over an integrated optical sensor capable of counting, sizing and measuring the shape of particles. Measurements demonstrate good repeatability and the ability to discriminate between particles based on their optical properties.

Cytometers are instruments for particle analysis based on the optical properties of the particle. In literature different integrated sheath-flow chambers have been presented (some early ones can be found in [1], [2]), but the optical sensors are often located off-chip. In this paper an integrated projection cytometer is presented that has a built-in optical sensor.
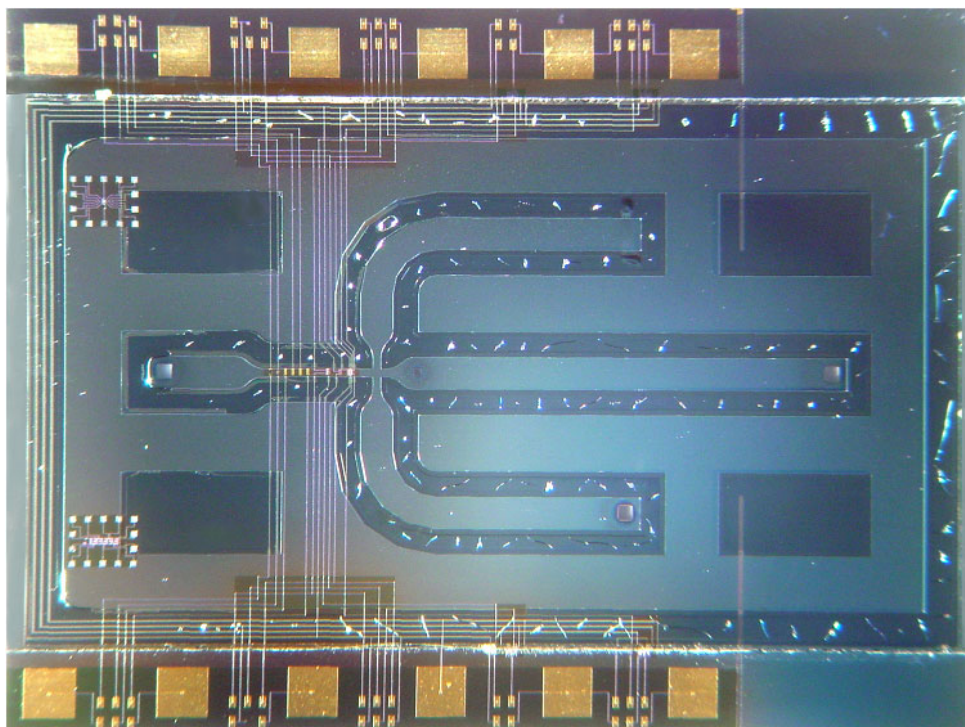

Fig. 1: The cytometer chip (1.5 x 2 cm^2)

The device (Fig. 1) consists of a transparent flow-channel that has an elongated photo-diode (1 x 50 µm^2) integrated in the bottom of this channel, aligned perpendicular to the direction of flow. By means of a non-coaxial sheath flow the sample liquid containing the particles is focused over the optical sensor. The chip is illuminated from the top and when a particle now passes over the sensor its optical properties are registered. The small projection distance realized by the sheath-flow minimizes the optical distortion of the particle projection, without the need for any additional optical components.

The shape of the sensor signal, caused by a passing particle, depends on the optical properties of the particle (Fig. 2). Since the sensor only consists of a single photodiode the optical properties of the particle are integrated along a line perpendicular to the direction of flow.
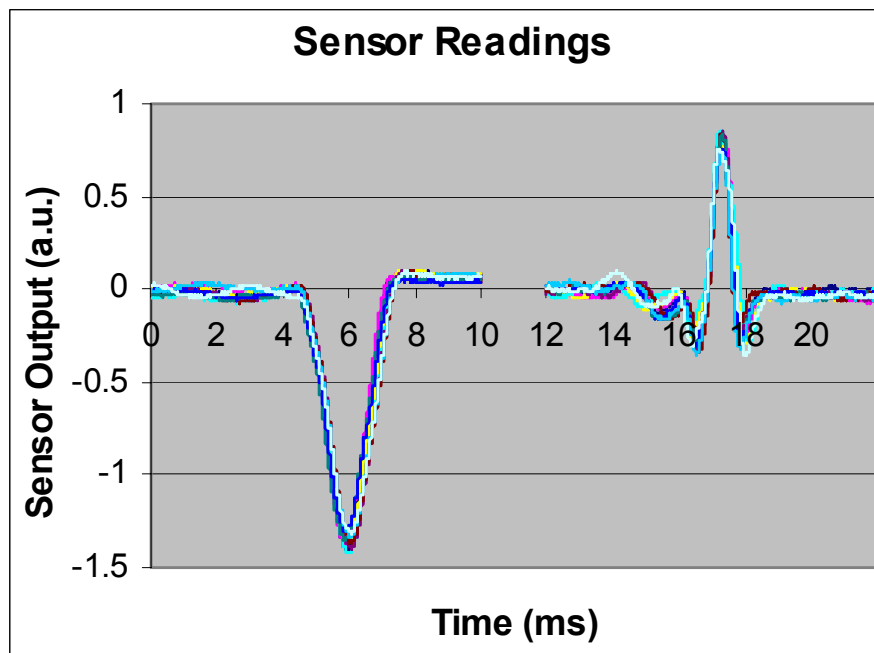

Fig. 2: Ten measurements printed on top of each other for 10 µm radius silver coated particles (left) and 12 µm radius plain particles (right) demonstrate the repeat-ability

References

[1]   R. Miyake, H. Ohki, I. Yamazaki, R. Yabe, A Development of Micro Sheath Flow Chamber, proc. of MEMS '91, 1991, pp. 265-270.

[2]   D. Sobek, A.M. Young, M.L. Gray, S.D. Senturia, "A microfabricated flow chamber for optical measurement in fluids", proc. MEMS '93, 1993, pp. 219-224.

SU-8-Based Fluidic Devices

P. Svasek [1], E. Svasek [1], B. Lendl [3], M. Vellekoop [2]

[1] Ludwig Boltzmann Institute of Biomedical Microtechnology, Gusshausstrasse 27-29, A-1040 Vienna, Austria

[2] Institute of Sensor and Actuator Systems, Vienna University of Technology, Austria

[3] Institute of Chemical Technology and Analytics, Vienna University of Technology, Austria

Introduction

During the last years SU-8 has become a widely used material for MEMS and miniaturized fluidic devices. It can be deposited by spin- or spray coating in a wide range of layer thicknesses. Because of the low UV absorption of the resist a standard UV mask aligner can be used for exposure, even for thick layers. Processing of SU-8 includes the following steps:

1. Deposition of the resist by spray- or spin coating

2. Drying at 95 °C on a hotplate

3. Exposure

4. Post exposure bake (PEB): Crosslinking of exposed resist

5. Development: unexposed resist is dissolved

6. Hardbake: The remaining structures are completely crosslinked. The resist gets its final mechanical strength and chemical stability.

Flow cell for Infrared Detection in Capillary Electrophoresis Systems

To use FTIR-spectroscopy as a powerful detection method in capillary electrophoresis an infrared transparent flow cell had to be designed because the fused silica capillaries normally used in CE are not transparent to IR. An appropriate material for infrared transparent devices is CaF_2. It shows very good optical properties, i.e. high transmittance in the mid-IR range (wavenumber 4000...700).

Fabrication of the CE cell

The cell consists of two plates of CaF_2, each 1 mm thick (see Fig. 1). On one of these plates there is a Titanium layer which acts as an optical aperture. This is necessary because with the given optical setup the IR-beam cannot be focused inside the flow channel only. The 200 nm thick titanium layer is deposited by evaporation and patterned by conventional lift-off technique. This metal structure must be completely isolated from the flow channel, otherwise gas bubbles would be produced by electrolysis.
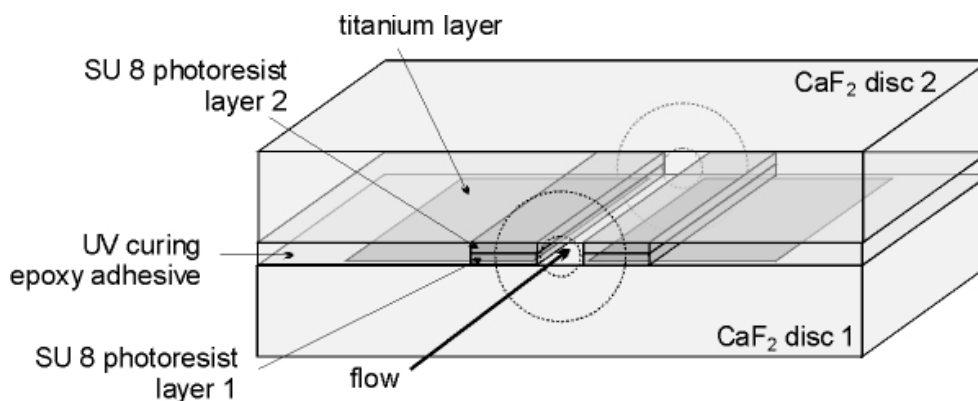
Fig. 1 Schematic drawing of the CE-cell

The channel is formed by two lines of SU-8 on each CaF_2 plate, each of them 100 µm wide. The distance between these two lines and thus the width of the channel is 150 µm. The height of the SU-8 lines is 7.5 µm, half of the desired height of the cell. The CaF_2 wafers (diameter 30 mm, thickness 1 mm) are spin-coated with SU-8 and softbaked. After UV-exposure using a SUSS MJB3 mask aligner and an appropriate photomask the resist is post-exposure-baked (90 °C for 10 min.) and developed. The unexposed and therefore not crosslinked areas are dissolved during the development process. The developer used is PGMEA (propylene glycol monomethyl ether acetate).

Two wafers (one with and one without metal structure) are superimposed, aligned and pressed against each other during the hardbake process. Consequently a bond is established between corresponding SU-8 structures because the hardbake temperature of 200 °C induces the complete crosslinking of the SU-8. This hardbake is necessary to achieve the full mechanical strength and chemical resistance of the SU-8.

Finally the area outside the SU-8 lines is filled with UV-curing epoxy adhesive (Delo Katiobond 4653) and the waferstack is diced with a dicing saw. We get 40 devices from one waferstack with a diameter of 30 mm. The final dimension of the cell is $2 \times 5 \times 2$ mm^3. The capillaries (I.D. 50 µm, O.D 360 µm) are coupled to the cell by means of a metal support and an elastic gasket that is applied to the tip of each capillary [1].

The two surfaces of each cell where the capillaries are coupled (inlet and outlet of the flow channel) are polished with 3 µm lapping film to achieve a tight connection between the capillaries and the cell. Results obtained with the help of this setup are discussed elsewhere [1], [4].

Micromixer for FTIR-Spectroscopy

This mixing device is used for the investigation of chemical reactions by FTIR-spectroscopy combined with in-situ mixing of two reactants. The IR-beam directly passes the mixing chamber. The optical pathlength (the height of the mixing chamber) is 10 µm (see Fig. 2). The optical pathlength should not exceed 20 µm because of the strong absorption of water and organic solvents in the mid-IR region, which otherwise would result in a bad signal-noise-ratio.

The mixing device is Y-shaped. Two sheets of liquid are superimposed inside the mixing chamber and mixed by diffusion. Because of the cross-section of the mixing chamber (1 mm wide, 10 µm high) the mixing time is approx. 50 ms. The mixer is used in the "stopped-flow-mode", i.e. the two liquids are injected by means of a double syringe pump. The two streams are separated by the separation membrane until they meet inside the mixing chamber. This membrane is a 2 µm thick silver membrane. During the

injection there is hardly any premixing. Then the flow is stopped, the reactants are mixed by vertical diffusion and the chemical reaction takes place. This reaction is investigated by time resolved FTIR-spectroscopy [2], [3]. The micromixer is fabricated by means of a 2-layer lithography, which combines SU-8 and metal, together with a polymer-based wafer bonding technique.
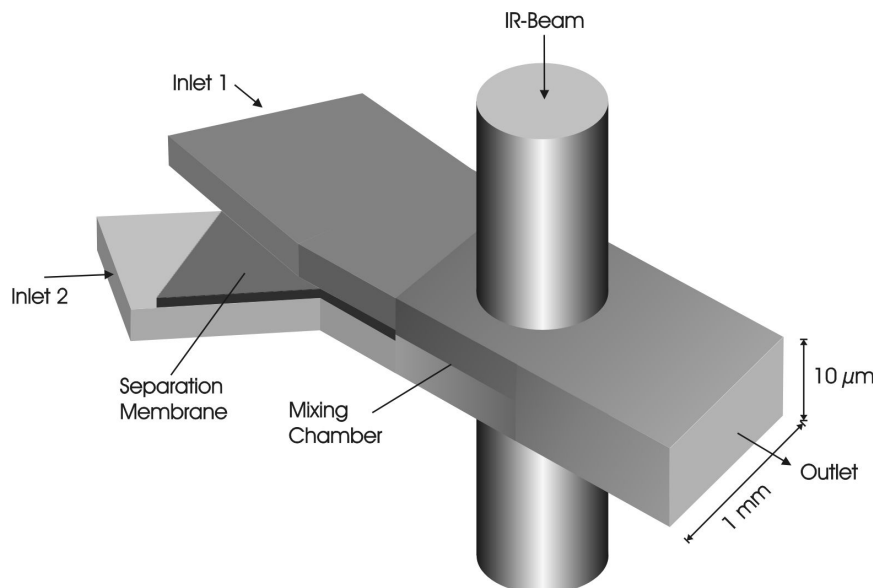

Fig. 2: Principle of the Micromixer (drawing not to scale)

Preparation of the Micromixer

As mentioned above, Calcium Fluoride is used as substrate material. The wafers which are used have a diameter of 100 mm, a thickness of 1 mm and are double side polished. A 4 µm thick layer of SU-8 is deposited by spin-coating onto both wafers. To achieve this layer thickness, the SU-8-50, which has a rather high viscosity, has to be diluted 4:1 (vol.) with GBL (gamma-butyro-lactone). Spin coating is done at 5000 rpm. After spin-coating the wafers are softbaked at 90 °C for 30 min. Exposure of wafer #1 is done by means of a SUSS MA 150 mask aligner. Wafer #1 is the bottom wafer. It carries the structures for inlet 2 and the separation membrane (see Fig. 2). Exposure is followed by a post-exposure bake at 90 °C for 10 min. The baking processes are performed using a hotplate.

To form the separation membrane a 2 µm thick metal layer is deposited by evaporation on top of the exposed (but undeveloped) SU-8 layer. We choose Ag as a material for this layer for two reasons: Evaporated Ag layers show no internal stress and therefore they do not bend when released. Additionally, it is possible to deposit Ag by thermal evaporation with relatively low power at a temperature well below 1000 °C. Consequently no UV light is generated, which would otherwise expose the wafer during the evaporation process, because the SU-8 layer is still sensitive to light. Evaporation is done in a Balzers BAK 550 evaporation system.

The Ag layer is then covered by positive photoresist AZ 1512 HS. The photoresist is processed as usual and the Ag layer is wet etched to form the structure of the separation membrane. As an etchant a 45% (WT) solution of $Fe(NO_3)_3$ in water is used. This solution does not attack the SU-8. The photomask for the Ag layer is compensated for the underetch of the Ag structure.

Finally the AZ positive resist is removed by undiluted developer AZ 400k and the SU-8 structure is developed with PGMEA. To dissolve unexposed SU-8 underneath the

metal structure takes quite some time (approx. 2 hours for channels of 1 mm length). Wafer #1 now carries the structures of inlet 2 and the separation membrane (see Fig. 3). The narrow SU-8-lines inside the flow channel are necessary to guide the flow and to keep the Ag membrane in place.

On wafer #2 (the top wafer) the structure of inlet 2 is fabricated as usual from a 4 µm thick layer of SU-8. Subsequently the holes for 2 inlets and 1 outlet per mixer are drilled by means of a high speed spindle and diamond tools. So far the SU-8 structures on both wafers are not hardbaked and therefore the polymer is still able to establish a bond to other materials during hardbake.
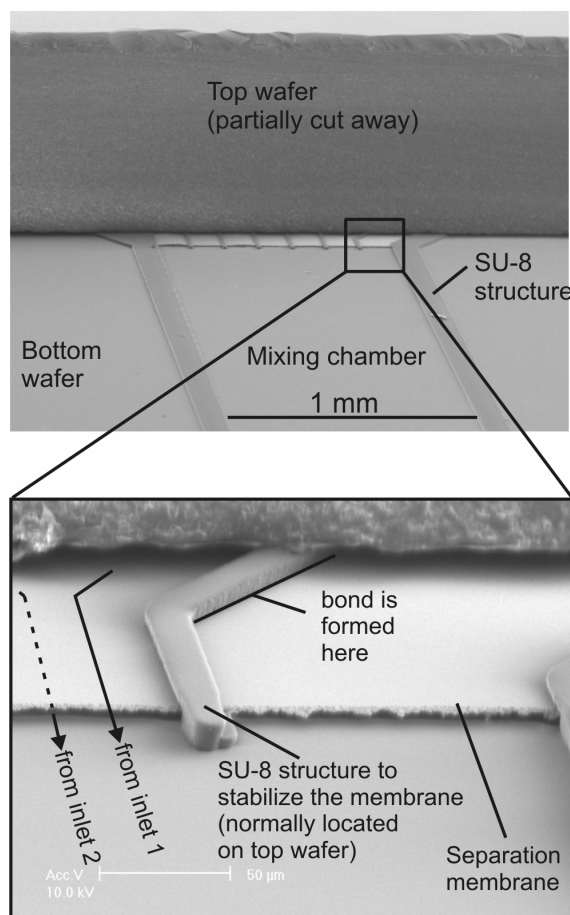

Fig. 3: SEM micrograph of the mixing device with the top wafer partially cut away

To complete the production process of the micromixer both wafers need to be bonded together in order to form a closed fluidic structure. The simple bonding process which was described in this paper for bonding of the CE cell wafers can be applied for the micromixer as well, but shows a poor yield in this case.

SU-8 Wafer Bonding

Both wafers are superimposed to form a sandwich configuration, and aligned. Hardbaking is done in an EVG 501 wafer bonder. The wafers are pressed against each other with a contact force of 2000 N and heated to 180 °C for 1 hour. Because of this high temperature the SU-8 is hardbaked and a bond is established between the SU-8 structure on the top wafer and the SU-8-Ag-structure on the bottom wafer (see Fig. 3).

A drawback of this bonding method is the fact that the layer thickness uniformity of spin-coated SU-8 layers is limited. For a layer thickness of approx. 4 µm we were able

to achieve thickness differences as low as 0,05 µm. Due to these differences the corresponding structures are not completely in close contact. Therefore some voids remain after bonding.

To overcome this problem it is possible to increase the contact force. SU-8-structures which are not hardbaked are plastic and can be deformed. Consequently some gaps or voids can be closed if a higher contact force is applied. The required force depends on the contact area as well as on the aspect ratio of the structures to be bonded. For this reason this method is feasible for the CE-cell (higher structures, smaller wafers), but not for the micromixer (lower structures, larger wafers). If the structures are deformed too much, the desired shape and height of the fluidic structures can not be maintained and will vary throughout the wafer area.

Another way to avoid insufficient bonding is to add some soft "adhesive" which fills the gaps caused by non-uniform layer thickness. Again the material of choice is SU-8, but this time without UV exposure. Unexposed SU-8 is thermoplastic, and it even fills gaps because of capillary forces. SU-8 is crosslinked when heated to 150...200 °C – it behaves like thermally cured epoxy adhesive.

If SU-8 is used for building fluid structures and – in unexposed form – for waferbonding, the unexposed SU-8 has to be patterned. This method is described in Fig. 4:

a. exposure of SU-8 layer

b. post exposure bake

c. deposition of metal layer

d. metal patterned by wet etching

e. SU-8 structure developed

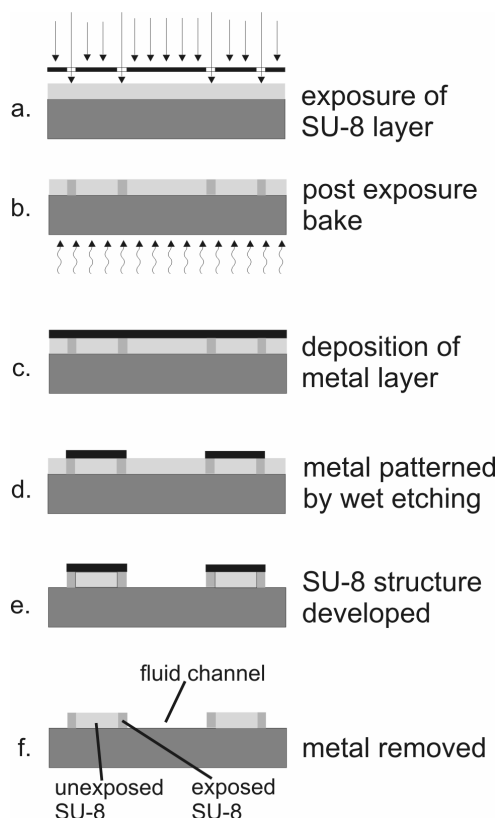f. metal removed

fluid channel

unexposed SU-8   exposed SU-8

Fig. 4: Preparation of the top wafer for bonding. The drawing shows the cross-section of a channel and its sidewalls

After exposure and PEB (see Fig 4 (a) and (b)) a metal layer is deposited on top of the SU-8 layer by evaporation. This metal layer (1 µm Ag) is patterned by wet etching (see Fig. 4 (c) and (d)). Now the areas where unexposed SU-8 is necessary for bonding are surrounded by narrow lines of exposed (hard) SU-8 and covered by metal. After development of SU-8 and removal of the metal layer (see Fig. 4 (e) and (f)) the wafer is ready for bonding.

With this bonding method it is not necessary to apply a high contact force, because remaining gaps are closed by the unexposed (soft) SU-8. Therefore the structures are not deformed and their correct height and shape is maintained during the bonding process.

Alignment of the wafers for bonding is done in an EVG AL6 mask aligner. Then the waferstack is clamped to the bond tool and inserted into an EVG 501 wafer bonder.

Bond parameters are as follows:

1. Contact force of 1000 N is applied. Temperature of top and bottom heaters is ramped up to 180 °C with a ramp of 3 °C/min.

2. Temperature of 180 °C is maintained for 1 h

3. Temperature is ramped down to room temperature with a ramp of 2 °C/min.

4. Contact force is removed

Conclusion

With the method described in this paper it is possible to manufacture miniaturized fluidic devices in a batch process. The combination of SU-8 and metal layers allows building up structures which contain fluid channels in more than one plane.

Wafer bonding with SU-8 is a method for the batch fabrication of closed fluidic devices. If infrared transparent wafers are used these devices can be used for IR spectroscopy.

If hard and soft (i.e. exposed and unexposed) SU-8 is used in combination, this wafer bonding method is a means to overcome the problem of non-uniform layer thickness of the SU-8 layers. Additionally, this method allows the bonding of wafers which contain e.g. conducting lines or other structures that cause a topographic surface.

References

[1]   M. Kölhed, P. Hinsmann, P. Svasek, J. Frank, B. Karlberg, B. Lendl: On-Line Fourier Transform Infrared Detection in Capillary Electrophoresis; Anal. Chem., 74 (2002), 3843 - 3848.

[2]   P. Hinsmann, J. Frank, P. Svasek, M. Harasek, B. Lendl: Design, Simulation and Application of a new Micromixing Device for Time Resolved Infrared Spectroscopy of Chemical Reactions in Solution; Lab on a Chip, 1 (2001), 16 - 21.

[3]   B. Lendl, P. Hinsmann, P. Svasek, J. Frank: Device for Label-Free Bio-Ligand Interaction Studies based on Time resolved Fourier Transform Infrared Spectrometry; Proceedings of the µTAS 2002 Symposium; (2002), ISBN: 1-420-1009-5; 221 - 223.

[4]   B. Lendl, M. Kölhed, P. Hinsmann, M. Haberkorn, P. Svasek, B. Karlberg: Online Mid-IR (Quantum Cascade Laser and FTIR Spectrometric) Detection in Capillary Based Separation Systems; Proceedings of the µTAS 2002 Symposium; (2002), ISBN: 1-4020-1009-5; 599 - 601.